

**School of Electrical Engineering,
Computing and Mathematical Sciences**

**Department
of
Physics & Astronomy**

**Development of metal hydride systems
for thermal energy storage applications**

Lucas Michel Dominique POUPIN

**This thesis is presented of the Degree of
Doctor of Philosophy
at
Curtin University**

August 2020

Declaration

To the best of my knowledge and belief this thesis contains no material previously published by any other person except where due reference and acknowledgement has been made.

This thesis contains no material which has been accepted for the award of any other degree or diploma in any university.

Lucas Michel Poupin

Abstract

Concentrated solar thermal power (CSP) complimented with suitable thermal energy storage are efficient and cost effective methods of harnessing renewable energy in large scale operations. Molten salts are commonly used for heat storage in the CSP operations but storage of thermal in metal hydrides has enhanced effects. In this research, Mg_2FeH_6 and $NaMgH_3$ metal hydrides are investigated as candidates for suitability in large scale high temperature thermal energy storage systems. The concept is that the high temperature metal hydrides (HTMH) are heated by solar energy from the CSP during the day that results in an endothermic release of hydrogen from the hydride that must be stored in tank or another low temperature (LTMH) hydride. In this research, we performed research on thermal energy storage in Mg_2FeH_6 and $NaMgH_3$ which enhanced high temperature energy storage by 20 times as compared to conventional systems. This thesis is divided into three part study:

Part (i), Feasibility study of pairing a HTMH ($NaMgH_3$) with a LTMH (intermetallic $TiMn_{1.5}$): In this case, small masses of Mg_2FeH_6 (40 g) and $TiMn_{1.5}$ (89 g) were used mainly to evaluate effective storage of hydrogen released from HTMH in the LTMH as compared to the volumetric H_2 storage in a standard gas cylinder. Studies are performed for specific tuning of the HTMH and LTMH operating specified temperatures in an effort to reach 90 % of the HTMH hydrogen capacity. The intermetallic LTMH gas storage has issues with hysteresis between desorption and absorption hydrogen pressure that significantly influences the hydrogen capacity. Secondly, the LTMH thermodynamics induces a significant thermal excursion of the HTMH ($150^\circ C$) to attain the 90 wt% of hydrogen capacity. Finally, the absorption kinetics of the HTMH was studied to optimize the hydrogen flow rate. Experiments were performed to determine overall small system properties.

Part (ii) $NaMgH_3$ as thermal energy storage media:

In the second part of the thesis, the $NaMgH_3$ is investigated as thermal energy storage material with pressurised water as a heat transfer fluid (HTF). Details of issues related to the management of a 2 steps decomposition material are presented; particularly the conditions for mitigating the irreversible decomposition of NaH into $Na + \frac{1}{2} H_2$. The total hydrogen capacity of the 150 g HTMH mixture is 2.6 wt% H_2 , and in this experimental study,

1.4 wt% H₂ is achieved to avoid NaH decomposition. Thermal cycling performance was then determined in the reactor between 450 °C and 370 °C that revealed consistent reversibility. Issues related to heat energy generation during the hydrogen absorption at moderate pressures are observed; to mitigate this, the hydrogen flow was enhanced by increased supply pressure. This did improve the thermal power generation but thermal energy balance was in question. However, despite heat loss the heat transfer fluid was able to extract up to 12 kJ.gH₂, which is ~28% of the energy available to the thermal system. In these small scale experiments the heat generated is lost to the steel reactor, as the mass of vessel is 20 times greater than the mass of the heat storage metal hydrides. It is expected that these losses will be significantly minimized with much larger systems. This study of NaMgH₃ as heat storage material determined that it was not suitable for large scale applications.

Part (iii) Mg₂FeH₆ as thermal energy storage media

This part investigates thermal energy storage in a 900 g Mg₂FeH₆ reactor that has a theoretical energy capacity of 1.8 MJ (500 Wh_{th}). Pressurised water was used to supply and retrieve energy in an operating temperature range between 400 °C and 450 °C. The system displayed consistent hydriding/dehydriding cycles involving 1.65 MJ, which is 90 % of the theoretical value. The thermal gradient observed within the reactor during operations was shown to be a hindrance to reach optimal hydrogen capacity during absorption. Mitigation of the thermal gradient was obtained by controlling the HTF flow and supplying hydrogen gas pressure above the Mg₂FeH₆ equilibrium pressure. Variations of the hydrogen pressure supplied were particularly profitable to control the power generated by the exothermic hydrogen absorption. During these studies, an automated control of hydrogen supply for specific gas pressure supply and HTF flow allowed to extract levelised power that could be used by a thermoelectric engine to generate base load electric power.

Finally, Mg₂FeH₆ is revealed to be a suitable material to pursue investigations toward an industrial use as a high temperature thermochemical energy storage.

Acknowledgements

I wish to acknowledge everyone that have supported me through this PhD project, all have been instrumental in the completion of this manuscript. First, I would like to express the most exothermic acknowledgement to Professor Craig E. Buckley for giving me the opportunity to work towards the development of an innovative energy storage technology in a skilful team of expert researchers on hydrogen. I would like to thank Dr. Terry Humphries, his guidance through this journey was unique and invaluable in many ways. His training, availability and many chats allowed me to reach the confidence required to perform the research presented hereafter. My deep acknowledgement also goes to Associate Professor Mark Paskevicius whose ideas, knowledge and support were essential to the completion of this project. I also thank Dr. Brendan McGann for being a patient committee chair.

A special mention goes to my former housemate and researcher at Curtin, Dr. Guillaume Drouart who informed me of the very existence of such an interesting research project in such an attractive region of the globe.

These three years of research brought forth many questions, technically, scientifically and sometimes more personally. Information can be found in the written literature, but it is sometimes more efficient to ask 'those who know'. Therefore, I would like to thank all the researchers of the Hydrogen Storage Research Group at Curtin University: Drew Sheppard, Veronica Sofianos, Dehua Dong and Kasper Möller, who were considered peers and with whom scientific discussions were always enriching. A big thankyou also goes to the PhD students of the group, Arnaud, Marianna, Enrico, Sruthy, Diego, Amanda, Kyran and Tom who shared the ups and downs of this journey and constituted an invaluable group of friends with whom discussions, scientific or otherwise, were always a great addition to the day. I would like to take the opportunity to thank as well the other PhD students of the building 120 (so called "the dungeon") who shared their experiences and knowledge, and put life into our PhD student building.

To my family and friends (in Australia and overseas), I would like to express my gratitude, as their support was crucial to achieve this journey and see further. Especially my mother, Elisabeth, and Father, Patrick who always had confidence in me and my abilities to complete this project.

I would like to acknowledge the team of technicians Glen, Mark, Kettesse, Kate, Ming, Luke and Andy who keep the laboratory, workshop and building 301 running smoothly to allow research work to be performed. I would like to thank Matthew Rowles and Veronica Avery from the Microscopy and Microanalysis Research Facility at John de Laeter Research Centre, who taught me the necessary knowledge to conduct and understand X-ray diffraction experiments.

Finally, I would like to acknowledge the financial support of the Australian Research Council for granting me a research scholarship through the ARC linkage grant LP150100730: "Metal hydride reactors for high temperature thermochemical heat storage".

Statement of contribution by others

Chapter 1, Energy storage, hydrogen and metal hydrides, presents the context of the following work. It is original writing by myself, suggestions and corrections were made by T.D.Humphries, M.Paskevicius and C.E.Buckley.

Chapter 2, Experimental, presents the materials and apparatus used to perform the different investigations discussed in the following chapters. It is original writing by myself, greatly inspired by some inputs from T.D.Humphries, M.Paskevicius and C.E.Buckley.

Chapter 3, Metal hydrides used for heat storage presents the state of art of metal hydrides. This chapter is general review written by myself with amendements and corrections from T.D.Humphries, M.Paskevicius and C.E.Buckley.

Chapter 4, High temperature metal hydride paired with a low temperature metal hydride, is based on a published paper by L.Poupin et al. An experimental high temperature thermal battery coupled to a low metal hydride for solar thermal energy storage (Sustainable Energy & Fuels, 4(1), 285-292). It is my own work. Discussions were contributed to by members of the Hydrogen Storage Research Group, such as T.D.Humphries, M.Paskevicius and C.Buckley.

Chapter 5, A sodium magnesium hydride reactor prototype to store thermal energy, is based on a published paper by L.Poupin et al. A thermal energy storage prototype using sodium magnesium hydride (Sustainable Energy & Fuels, 3(4), 985-995). It is my own work. Design and prototype assembly were assisted by T.D.Humphries and M.Paskevicius. Discussions were contributed to by members of the Hydrogen Storage Research Group, such as T.D.Humphries, M.Paskevicius and C.Buckley.

The content of Chapter 6, An operational prototype to store thermal energy using magnesium iron hydride, is yet unpublished. M.Paskevicius provided support to supply prototype components and with T.D.Humphries assisted the prototype assembly and troubleshooting. Discussions were contributed to by members of the Hydrogen Storage Research Group, such as T.D.Humphries, M.Paskevicius and C.Buckley.

Poupin Lucas
(Candidate)

C.E.Buckley
(Supervisor)

Table of contents

Chapter 1	Energy storage, hydrogen and metal hydrides.....	21
1.1.	Introduction	22
1.2.	Energy storage	22
1.2.1.	Mechanical.....	23
1.2.1.1.	Pumped hydro energy storage.....	23
1.2.1.2.	Compressed air	25
1.2.1.3.	Flywheel	26
1.2.2.	Electrical.....	27
1.2.2.1.	Electrochemical batteries	27
1.2.2.2.	Capacitors.....	28
1.2.2.3.	Superconducting magnetic energy storage	28
1.2.3.	Thermal energy storage	29
1.2.3.1.	Sensible thermal energy storage	31
1.2.3.2.	Phase change materials for thermal energy storage	32
1.2.3.3.	Thermochemical thermal energy storage.....	33
1.3.	Hydrogen.....	36
1.3.1.	History.....	36
1.3.2.	Production and sources	37
1.3.3.	Applications.....	38
1.3.4.	Storage	38
1.4.	Metal hydrides	41
1.4.1.	Principle	41
1.4.2.	Metal hydrides categories	42
1.4.2.1.	Ionic hydrides.....	43
1.4.2.2.	Covalent hydrides	43
1.4.2.3.	Metallic hydrides.....	44
1.4.3.	History.....	44
Chapter 2	Experimental	46
2.1.	Introduction	47
2.2.	Materials	47
2.3.	General instrumentation	48
2.4.	Synthesis	48

2.4.1.	Planetary ball mill.....	48
2.4.2.	Shaker mill.....	49
2.5.	Characterisation.....	50
2.5.1.	Differential scanning calorimetry.....	50
2.5.2.	X-ray powder diffraction.....	52
2.5.3.	Sieverts apparatus.....	56
2.5.3.1.	Volume calibrations	57
2.5.3.2.	Pressure composition Isotherms (PCI or PCT).....	58
2.5.3.3.	Small scale gas cycling.....	62
2.5.3.4.	Absorption kinetics of hydrogen.....	63
2.5.4.	Transient plane source for thermal conductivity.....	64
2.6.	Differential pressure manometer	66
2.7.	Experimental setup for metal hydride coupling	68
2.8.	Design and setup of high temperature thermal energy storage prototype (TES150)	69
2.8.1.	Heat transfer fluid line	69
2.8.2.	Hydrogen manifold	72
2.9.	Design and setup of high temperature thermal energy storage prototype (TES900)	74
2.9.1.	Heat transfer fluid circuit.....	75
2.9.1.1.	Fluid pump	76
2.9.1.2.	Dampener	77
2.9.1.3.	Pre-heater	77
2.9.1.4.	The reactor heat transfer fluid line.....	78
2.9.1.5.	Heat sink.....	80
2.9.1.6.	Backpressure regulator	81
2.9.1.7.	The HTF flow meter.....	81
2.9.2.	Hydrogen circuit.....	81
2.9.2.1.	Pressurised storage.....	82
2.9.2.2.	The compressor.....	83
2.9.3.	The furnace and controller	84
2.9.4.	Monitoring, acquisition and control system.....	84
2.9.4.1.	Software	84
Chapter 3	Metal hydrides used for high temperature heat storage.....	87
3.1.	Introduction	88
3.2.	Main considerations.....	88

3.2.1.	H ₂ safety	88
3.2.2.	Material compatibility.....	89
3.2.3.	Abundancy / Cost	90
3.2.4.	Thermodynamics.....	91
3.2.4.1.	Operating temperature and pressure.....	91
3.2.4.2.	Enthalpy of reaction and energy density	91
3.2.5.	Reversibility.....	92
3.2.6.	Kinetics.....	92
3.2.7.	Thermal losses.....	93
3.2.8.	Heat supply/ exchange.....	93
3.3.	Potential metal hydrides.....	94
3.3.1.	Calcium based	95
3.3.2.	Sodium based.....	98
3.3.3.	Magnesium based.....	98
3.3.3.1.	NaMgH ₃	99
3.3.3.1.1.	Introduction	99
3.3.3.1.2.	Synthesis	100
3.3.3.1.3.	Thermodynamics	102
3.3.3.1.4.	Kinetics.....	Error! Bookmark not defined.
3.3.3.1.5.	Thermal conductivity	108
3.3.3.1.6.	Summary.....	109
3.3.3.2.	Mg ₂ FeH ₆	110
3.3.3.2.1.	Introduction	110
3.3.3.2.2.	Synthesis	110
3.3.3.2.3.	Thermodynamics	112
3.3.3.2.4.	Kinetics.....	114
3.3.3.2.5.	Thermal conductivity	116
3.3.3.2.6.	Summary.....	116
Chapter 4	High temperature metal hydride paired with a low temperature metal	
hydride	118	
4.1.	Introduction	119
4.2.	Coupling principle	119
4.3.	Literature review.....	120
4.4.	Material election.....	121
4.4.1.	High temperature metal hydride (HTMH)	121
4.4.2.	Low temperature hydride for storing hydrogen from HTMH.....	122

4.5.	Cycling investigations.....	126
4.5.1.	Cycling HTMH thermally with LTMH at ambient temperature.....	126
4.5.2.	HTMH working temperature optimisation	128
4.5.3.	Effect of free gas volume	129
4.5.4.	Cycling HTMH thermally with elevated LTMH temperature	131
4.5.1.	Cycling thermally the LTMH with the HTMH maintained ≈ 450 °C.....	133
4.6.	Summary	136
Chapter 5 A sodium magnesium hydride reactor prototype to store thermal energy		
137		
5.1.	Introduction	138
5.2.	Operating parameter tuning.....	139
5.3.	Lab scale thermal battery operation.....	142
5.3.1.	Temperature cycling	142
5.3.2.	Temperature driven desorption.....	143
5.3.3.	Temperature driven absorption.....	145
5.3.4.	Over pressurised absorption.....	147
5.3.5.	Energy consideration	152
5.3.5.1.	Heat transfer fluid energy.....	152
5.3.5.2.	Metal hydride energy.....	154
5.3.5.3.	Stainless steel reactor energy.....	155
5.3.5.4.	The environmental losses	156
5.3.5.5.	Synopsis.....	156
5.3.6.	Post cycle analysis.....	157
5.3.7.	Summary	158
Chapter 6 An operational prototype to store thermal energy using magnesium iron hydride		
160		
6.1.	Introduction	161
6.2.	Operating investigation.....	161
6.2.1.	Thermal energy charging	161
6.2.2.	Thermal energy discharge.....	166
6.2.3.	Operating pressure variations.....	171
6.2.3.1.	Operating at $T = 430$ °C.....	171
6.2.3.2.	Operating at $T = 410$ °C.....	173
6.2.4.	Operating temperature variations.....	174
6.2.5.	HTF flow variations	176
6.2.6.	Thermal battery supplying consistent power	179

6.2.6.1.	HTF outlet temperature regulation between 430 °C – 425 °C with 40 bar H ₂ , HTF flow of 50 ml/min.....	179
6.2.6.2.	HTF outlet temperature regulation between 430 °C – 425 °C with 35 bar H ₂ , HTF flow of 50 ml/min.....	183
6.2.6.3.	HTF outlet temperature regulation between 430 °C – 425 °C with 35 bar H ₂ , HTF flow of 65 ml/min.....	186
6.3.	Summary	188
Chapter 7	Conclusions and future work	190
Appendices	195	
References	209	

List of figures

Figure 1-1 - Electrical power capacity of main operational storage technologies (2017). ⁷ ...	23
Figure 1-2 - (a) Layout of a pumped hydroelectric storage plant and (b) a picture of the Kidston pumped storage facility in an abandoned gold mine in Queensland (Australia) storing ~2 GWh (Reprinted from Genexpower.com). ⁸	24
Figure 1-3 - Simple schematic of an isothermal Compressed Air Energy System. ¹⁸	25
Figure 1-4 - Schematic view of a flywheel energy storage device (Copyright © 2007, IEEE). ²⁶	26
Figure 1-5 - (a) Chemical energy discharging concept, (b) charging, (c) schematic typical design of lead-acid battery. ³¹ (Reprinted with permission from Elsevier)	28
Figure 1-6 - Typical layout of a superconducting magnetic energy storage. ⁴³	29
Figure 1-7 - TES methods: (a) sensible (b) latent (c) thermochemical.....	30
Figure 1-8 - Heat storage capacity for various phase change materials. ⁵⁵ (Reprinted with permission from Elsevier)	32
Figure 1-9 - Details of a high pressure hydrogen tank. ¹³² (reprinted with permission from Elsevier).....	39
Figure 1-10 - Schematic of hydrogen cycle through LOHC. Reprinted with permission from ACS	40
Figure 1-11 - Conventional MOF synthesis. ¹⁴⁸	41
Figure 1-12 - Schematic of hydrogen absorption and desorption process. ¹⁴⁹	42
Figure 1-13 – Table of the binary hydrides and the Allred–Rochow electronegativity. Most elements react with hydrogen to form ionic, covalent, or metallic binary hydrides. ¹⁵¹	43
Figure 2-2 (a) A custom made ball milling canister with 650 cm ³ internal volume and balls of 7.9 mm and 12.7 mm diameter (b) A Glen Mills Turbula T2C shaker mixer.	50
Figure 2-3 - Typical DSC curve showing a peak of additional power required to achieve hydrogen desorption with a heat rate of 2 °C/min.....	52
Figure 2-4 - Bragg-Brentano geometry used in XRD. ¹⁷⁷	54
Figure 2-5 –Typical XRD pattern with raw data (blue), Rietveld refinement (red) and the difference curve (grey).....	55
Figure 2-6 - Schematic view of the custom made Sieverts apparatus at the HSRG laboratory. Courtesy of M.Paskevicius.	57

Figure 2-7 – Typical PCT for the hydrogen absorption in a typical intermetallic compound is shown on the left hand side. The construction of the van 't Hoff plot is shown on the right hand side. ¹⁸⁴	61
Figure 2-8 - Temperature cycling example between 450 °C and 530 °C and the associated pressure change in the Sieverts apparatus volume.....	63
Figure 2-9 - Absorption kinetics for NaMgH ₃ at 410 °C and different pressures.....	64
Figure 2-10 - (a) Kapton sensor, (b) a schematic of the experimental set up and (c) a picture of set up in glove box.	65
Figure 2-11 - (a) Schematic gathering geometric constant used to determine fluid flow through a diaphragm and (b) a picture of mounted Rosemount 3051, differential manometer.	67
Figure 2-12 - Schematic of the experimental set up with the HTMH in a furnace (left) and LTMH in agitated water bath (right).	69
Figure 2-13 - Schematic of the heat transfer line in the system with a detail of the reactor's interior.	70
Figure 2-14. Water phase diagram. ²¹⁷	71
Figure 2-15 - Picture of the custom made pre-heater with the stainless steel tube, the brass plate and heat tape wrapped around.....	72
Figure 2-16 - The heat transfer coil which was similarly embedded in both reactors.	72
Figure 2-17 - Schematic view of the hydrogen gas line set up with instrumentation.....	74
Figure 2-18 - Picture of the "Red Sparrow" apparatus built to perform automated tests of thermochemical batteries.....	75
Figure 2-19 - Schematic of the overall HTF circuit.....	76
Figure 2-20 - Picture of the equipped Lewa [®] metering pump with digital manometer and pressure relief valve.....	77
Figure 2-21 - Schematic and picture of (a) the tubing, (b, and c) coiled around a steel pipe, and (d) embedded in high temperature heat transfer paste.	78
Figure 2-22 - Pictures of the Parr reactor: (a) the bottom and cap equipped the HTF coil, (b) the cap's different connections, (c) the whole reactor, and (d) the collar that closes the reactor tight.	78
Figure 2-23 - Pictures of the custom made reactor assembly. (a) The two tubes of the middle line wrapped in the HTF coil; (b) the eight tubes with the middle line embedded in thermal paste; (c) the eight tubes wrapped in the external HTF coil; (d) the reactor encased in its insulating jacket.....	80

Figure 2-24 - Picture of a part of the heat sink equipped with aluminium fins.....	81
Figure 2-25 - Schematic of the hydrogen circuit setup that allowed control of the gas absorption and desorption.	82
Figure 2-26 - Picture of the hydrogen compressor on its dedicated support with safety valve and compressed air supply port. (a) Front side, (b) back side.....	83
Figure 2-27 - Picture of the Labview [®] program user window with live monitoring and different operating modes.....	86
Figure 3-1- Hydrogen permeability of potential envelope materials. ^{200, 201}	89
Figure 3-2 - Element abundancy available for mining. ²⁰⁹	91
Figure 3-3 - . X-ray diffraction pattern of synthesised NaMgH ₃ after milling and annealing. (a) Ball-milled with a MgH ₂ precursor, (b) Ball-milled with a Mg precursor, (c) hand-ground with a Mg precursor; $\lambda = 1.5418 \text{ \AA}$	101
Figure 3-4 - Pressure composition isotherm of RM between 418 °C and 466 °C.	103
Figure 3-5 - van 't Hoff plot of the Reactor Mix compared with pristine NaMgH ₃	104
Figure 3-6 - Pressure - composition isotherms of NaMgH ₃ with additives upon desorption and absorption between 418 °C and 459 °C.....	105
Figure 3-7 - Differential scanning calorimetry pattern of (a) pure NaMgH ₃ and (b) Reactor Mix.	106
Figure 3-8 - Kissinger plot for the Reactor Mix (black circle) and pure NaMgH ₃ (blue stars).	107
Figure 3-9 - Hydrogen absorption kinetic plots for the reactor mix at various supplied pressures for temperatures: (a) 390 °C, (b) 410 °C, (c) 430 °C and (d) 450 °C.....	108
Figure 3-10 - X-ray diffraction pattern of different Mg ₂ FeH ₆ annealing parameters; (a) 500 °C - 80 bar, (b) 460 °C - 60 bar, (c) 450 °C- 40 bar; $\lambda = 1.5418 \text{ \AA}$	112
Figure 3-11 - Van 't Hoff plot of hydrogen absorption for Mg ₂ FeH ₆	114
Figure 3-12 - Pressure-composition isotherms of Mg ₂ FeH ₆ upon hydrogen absorption for temperature from 410 °C to 490 °C.....	114
Figure 3-13 - Mg ₂ FeH ₆ absorption kinetics for different hydrogen supply pressure at (a) 430 °C and (b) 450 °C.	115
Figure 3-14 - Kinetics of Mg ₂ FeH ₆ absorption at (a) 430 °C and (b) 450 °C for the pure hydride and with 10 wt% ENG added.	115
Figure 4-1 - Example of intermetallic metal hydrides for near- ambient hydrogen storage. ¹⁵⁵	122
Figure 4-2 - Equilibrium pressure for Mg ₂ FeH ₆ as the HTMH and operational target.....	124

Figure 4-3 - Pressure composition isotherm of $\text{TiMn}_{1.5}$. ³⁰¹ (Reprinted with permission of Elsevier).....	125
Figure 4-4 - Equilibrium pressure curves for Mg_2FeH_6 as HTMH and $\text{TiMn}_{1.5}$ as LTMH. ³⁰¹ ..	125
Figure 4-5 - (a) Cycling of HTMH between 350 °C and 450 °C, (b) associated temperature excursion of LTMH and (c) associated system pressure evolution.....	126
Figure 4-6 - (a) HTMH temperatures, (b) LTMH temperatures, (c) system pressure, (d) hydrogen flow 3 cycles when HTMH temperature oscillate between 350 °C and 450 °C...	127
Figure 4-7 - HTMH cycling between ≈ 350 °C and ≈ 500 °C (left) and LTMH (right) with original and added volume; with their respective calculated equilibrium pressure plots. (Blue line: fully hydrogenated, blue dash: half hydrogenated, red line: fully dehydrogenated, red dash: half dehydrogenated).....	130
Figure 4-8 - HTMH (right) and LTMH (left) for different LTMH regulated temperatures (ambient, 30 °C, 40 °C). (Blue line: fully hydrogenated, blue dash: half hydrogenated, red line: fully dehydrogenated, red dash: half dehydrogenated). (a) points an anomaly caused by the water heater.	132
Figure 4-9 - HTMH (right) and LTMH (left) for different HTMH maximum temperatures (450 °C and 520 °C). (Blue line: fully hydrogenated, blue dash: half hydrogenated, red line: fully dehydrogenated, red dash: half dehydrogenated).....	133
Figure 4-10 - Temperature evolutions of the LTMH and HTMH along with the system pressure and the HTMH equilibrium pressure (P_{eq} , averaged and minimum).....	134
Figure 4-11 - System pressure evolution along with the LTMH equilibrium pressure when fully hydrogenated and fully dehydrogenated. Hydrogen flow and hydrogen mass flowing from the LTMH.....	135
Figure 5-1 - (a) calculated equilibrium curves for NaH decomposition (Black circles) and NaMgH_3 decomposition (squares). (b) Hydrogen capacity versus cycle number for varying initial pressure and operating temperatures.....	141
Figure 5-2 - Hydrogen absorption and desorption cycles with HTF flowing at 8 ml/min between 480 °C and 380 °C.	143
Figure 5-3 - Detailed view of various measurements in the system during desorption.....	144
Figure 5-4 - Temperature driven absorption for HTF temperature dropping from 480 °C to 380 °C with a 8 ml/min flow.	146
Figure 5-5 - Absorbed hydrogen flow for a range of initial hydrogen pressure	148
Figure 5-6 - Thermal response of the reactor set up for an absorption initially at 5 bar H_2	150

Figure 5-7 - Thermal response of the reactor set up for an absorption initially at 4 bar H₂.
..... **Error! Bookmark not defined.**

Figure 5-8 - Thermal response of the reactor set up for an absorption initially at 4 bar H₂.
..... 150

Figure 5-9 - Thermal response of the reactor set up for an absorption initially at 8 bar H₂.
..... 151

Figure 5-11 - Power extracted by the HTF during hydrogen absorption with various initial pressures..... 154

Figure 5-12 - Thermal energy distribution during hydrogen absorption in the 4 subsystems (HTF, SS316 reactor, hydride and losses) for various initial hydrogen pressures..... 157

Figure 5-13 - Quantity analysis of the Reactor Mix at various places across the length of the reactor..... 158

Figure 6-1 - Gas store and reactor hydrogen pressure during desorption, along with the hydrogen mass desorbed from the hydride. Average reactor temperature 430 °C, HTF flow of 35 ml/min, and hydrogen pressure set to 10 bar..... 162

Figure 6-2 - Temperature of inlet and outlet HTF as well as inside the reactor during desorption. Average reactor temperature 430 °C, HTF flow of 35 ml/min, and hydrogen pressure set to 10 bar. T1 to T6 follow the HTF flow direction (T inlet was 10 cm before T1 and T outlet was 10 cm after T6). 163

Figure 6-3 - Energy and power required for hydrogen desorption. Average reactor temperature 430 °C, HTF flow of 35 ml/min, and hydrogen pressure set to 10 bar..... 165

Figure 6-4 - Gas store and reactor hydrogen pressure evolution, along with the hydrogen mass absorbed by the hydride. Average reactor temperature 430 °C, HTF flow of 35 ml/min, and hydrogen pressure set to 45 bar..... 167

Figure 6-5 - Temperature of inlet and outlet HTF as well as inside the reactor during H₂ absorption. Average reactor temperature 430 °C, HTF flow of 35 ml/min, and hydrogen pressure set to 45 bar. T1 to T6 follow the HTF flow direction (T inlet was 10 cm before T1 and T outlet was 10 cm after T6). 168

Figure 6-6 - Energy and power generated by the hydrogen absorption. Average reactor temperature 430 °C, HTF flow of 35 ml/min, and hydrogen pressure set to 10 bar..... 169

Figure 6-7 - Energy losses fraction versus energy storage capacity based on the thermal resistivity and apparent hydride density determined in this setup. Three different heights (H) are displayed. 171

Figure 6-8 - Hydrogen absorption kinetics for varied H ₂ supply pressures for an operating temperature of 430 °C.	172
Figure 6-9 - Hydrogen absorption kinetics for different supply pressures for an operating temperature of 410 °C. HTF flow of 35 ml/min and hot background temperature regulated at 380 °C.	174
Figure 6-10 - Absorption kinetics at varied operating temperatures and a hydrogen supply pressure of 17 bar over the equilibrium pressure. The HTF flow was 35 ml/min.	175
Figure 6-11 - Reacted fraction evolution for various HTF flow at the operating temperature of 430 °C with 40 and 50 bar H ₂ supplied.	177
Figure 6-12 - Power generated and harvested for various HTF flow rates at the operating temperature of 430 °C with 40 and 50 bar H ₂ supplied.	178
Figure 6-13 - Inlet and outlet HTF temperature history during thermal energy charge and discharge when the flow rate is 50 ml/min.	180
Figure 6-14 - History of hydrogen cylinder pressure, reactor pressure and mass of hydrogen absorbed by the hydride during thermal energy charge and discharge. (HTF flow rate 50 ml/min, hydrogen pressure 40 bar)	181
Figure 6-15 - Power exchanged between the HTF and the thermal battery during thermal cycles (HTF flow 50 ml/min, hydrogen pressure 40 bar).	182
Figure 6-16 - Energy generated and absorbed by the hydrogen reaction along with the energy harvested and supplied by the HTF (HTF flow 50 ml/min, hydrogen pressure 40 bar)	182
Figure 6-17 - (a) Temperature measured at each thermocouple and (b) related gas store pressure during one of the cycles presented in Figure 6.14, 6.15, 6.16.	183
Figure 6-18 (a) Inlet and regulated HTF outlet temperature between 430 and 425 °C and flowing at 50 ml/min, (b) Hydrogen mass absorbed and desorbed and (c) power extracted and supplied by the HTF , with 35 bar H ₂ supplied.	185
Figure 6-19 - Energy generated and absorbed by the hydrogen reaction along with the energy harvested and supplied by the HTF (HTF flow 50 ml/min, hydrogen pressure 35 bar).	186
Figure 6-20 - (a) Inlet and regulated HTF outlet temperature between 430 and 425 °C with flow rate of 65 ml/min, (b) Hydrogen mass absorbed and desorbed, and (c) power extracted and supplied by the HTF), with 35 bar H ₂ supplied.	187

Figure 6-21 - Energy generated and absorbed by the hydrogen reaction along with the energy harvested and supplied by the HTF (HTF flow 65 ml/min, hydrogen pressure 35 bar)
..... 188

List of tables

Table 1-1 - Different type of CSP plants, adapted from ^{48, 50, 51}	30
Table 1-2 - Favourable reversible thermochemical materials.	34
Table 2-1 - List of chemicals used thorough the project.	47
Table 2-2 - LynxEye detector parameters used for analysis in TOPAS.....	55
Table 3-1 - Significant properties of possible heat transfer fluids from NIST database. ²¹⁷ ..	94
Table 3-2 - Recapitulative main characteristic table of promising metal hydrides.	95
Table 3-3 - Comparison of enthalpy and entropy of hydrogen desorption.....	104
Table 3-4 - Thermal conductivity of pristine NaMgH ₃ and Reactor Mix, measured by TPS (Section 2.5.4). (Reprinted from co-authored paper ²⁷⁶)	109
Table 3-5 - Thermal conductivity for mixtures of Mg ₂ FeH ₆ measured by TPS (Section 2.5.4). (Partly reprinted from co-authored paper ²⁷⁶).....	116
Table 4-1 - List of potentially suitable LTMH.	123
Table 4-3 - Comparison of variables affected by variations in a free gas volume. (Temperatures and pressures have a 2% uncertainty; hydrogen masses have a 5% uncertainty).....	130
Table 4-4 - Effect of average LTMH temperature change on the system variables.	132
Table 5-1 - Hydrogen desorption optimisations, inlet HTF at 480 °C and 8 ml/min.....	145
Table 5-2 - Time required for absorption, maximum hydrogen flow for a range of initial hydrogen pressures and subsequent theoretical maximum power generated.	149
Table 6-1 - Energy breakdown (kJ) of the different supplies (with 10 % uncertainty). Hydride and vessel energy are based on their specific heat, furnace energy was estimated from PID control, HTF energy from temperature and mass flow, and required energy was determined from hydrogen mass and enthalpy.	166
Table 6-2 - Energy breakdown (kJ) of the different components (with 10 % uncertainty). Hydride and vessel energy are based on their specific heat, furnace energy was estimated from PID control, HTF energy from temperature and mass flow, and required energy was determined from hydrogen mass and enthalpy.	169
Table 6-3 - Energy breakdown at an operating temperature of 430 °C and HTF flow of 35 ml/min for different hydrogen pressure supplies (uncertainty of 10 %). Hydride and vessel energy are based on their specific heat, the furnace energy was estimated from PID control,	

HTF energy from temperature and mass flow, and required energy was determined from hydrogen mass and enthalpy..... 173

Table 6-4 - Local temperatures measured in a steady state reactor (no chemical reaction, with 0.75% uncertainty)..... 176

Table 6-5 - Energy generated and harvested for thermal energy discharge at 430 °C with 40 and 50 bar H₂ supplied for various HTF flows (uncertainty on energy calculation is 10%). Hydride and vessel energy are based on their specific heat, the furnace energy was estimated from PID control, HTF energy from temperature, mass flow and required energy were determined from hydrogen mass and enthalpy..... 178

Chapter 1 Energy storage, hydrogen and metal hydrides

LEONARD : “Debout disciple !”

“Wake up lackey!”

BASILE : “Je sers la science et c’est ma joie”

“I serve science and it’s my joy”

[Bob De Groot and Turk] *Extract from comic “Leonard le genie”.*

1.1. Introduction

This research project falls within the major technological challenge of energy storage; hence, some of the leading energy storage technologies are presented. In this project, the utilisation of hydrogen gas is a key thread throughout the study, which justifies a brief history and overview of hydrogen usage. The technology investigated and developed herein uses the ability of hydrogen to react with certain metals to form metal hydrides. A detailed literature review is given to identify the advantages offered by such energy storage technology, and the remaining challenges to address towards successful industrialisation.

1.2. Energy storage

Sustainable energy storage is paramount for management of energy supply and demand, since it reduces energy wastage and can increase utilisation efficiency.¹ As a result, the consumption of energy made from fossil fuels can be lowered and therefore, greenhouse gas emissions reduced. Efficient energy storage would assist in increasing the slow penetration of renewable energy.² As most of the renewable energy sources are discontinuous, storage is instrumental in stabilising a baseload supply demanded by the grid. Efficient energy storage also enables the development of off-grid power stations using renewable sources for remote areas that often rely on diesel generators.³

The inventory of energy technologies is vast and ever-growing, although it is possible to distinguish three main energy storage techniques: mechanical, electrical and thermal.⁴⁻⁶ As displayed in Figure 1-1, pumped hydro storage is, by far, the most wide-spread technology in terms of power capacity.⁷ However, other technologies should not be neglected and present attractive advantages that forecast them to play an essential role in the compelling future storage technology mix. Therefore, a brief state-of-the-art is presented to give the reader a basic understanding of the significance of this project.

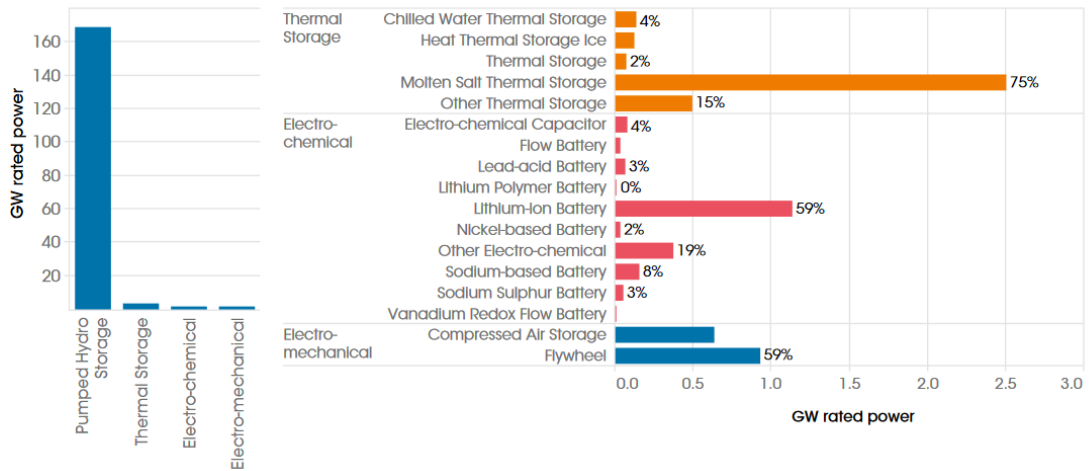


Figure 1-1 - Electrical power capacity of main operational storage technologies (2017).⁷

1.2.1.Mechanical

Mechanical energy storage involves displacement of a mass. The mass displacement can accumulate potential or kinetic energy that can be converted into electricity on demand via a converter or a turbine. Some examples are provided below.

1.2.1.1. Pumped hydro energy storage

Pumped Hydro Energy Storage (PHES) is amongst the most simple energy storage technologies. It consists in filling an elevated reservoir with water using excess energy available from the grid or other sources. If energy production is required, the stored water is released to a lower basin. The fall is directed by a capillary through a turbine, which converts water flow into electricity. The height difference between the two basins and the volume of stored water dictates the quantity of stored energy. Figure 1-2 presents a simple schematic and a photo of an Australian facility in Queensland.⁸

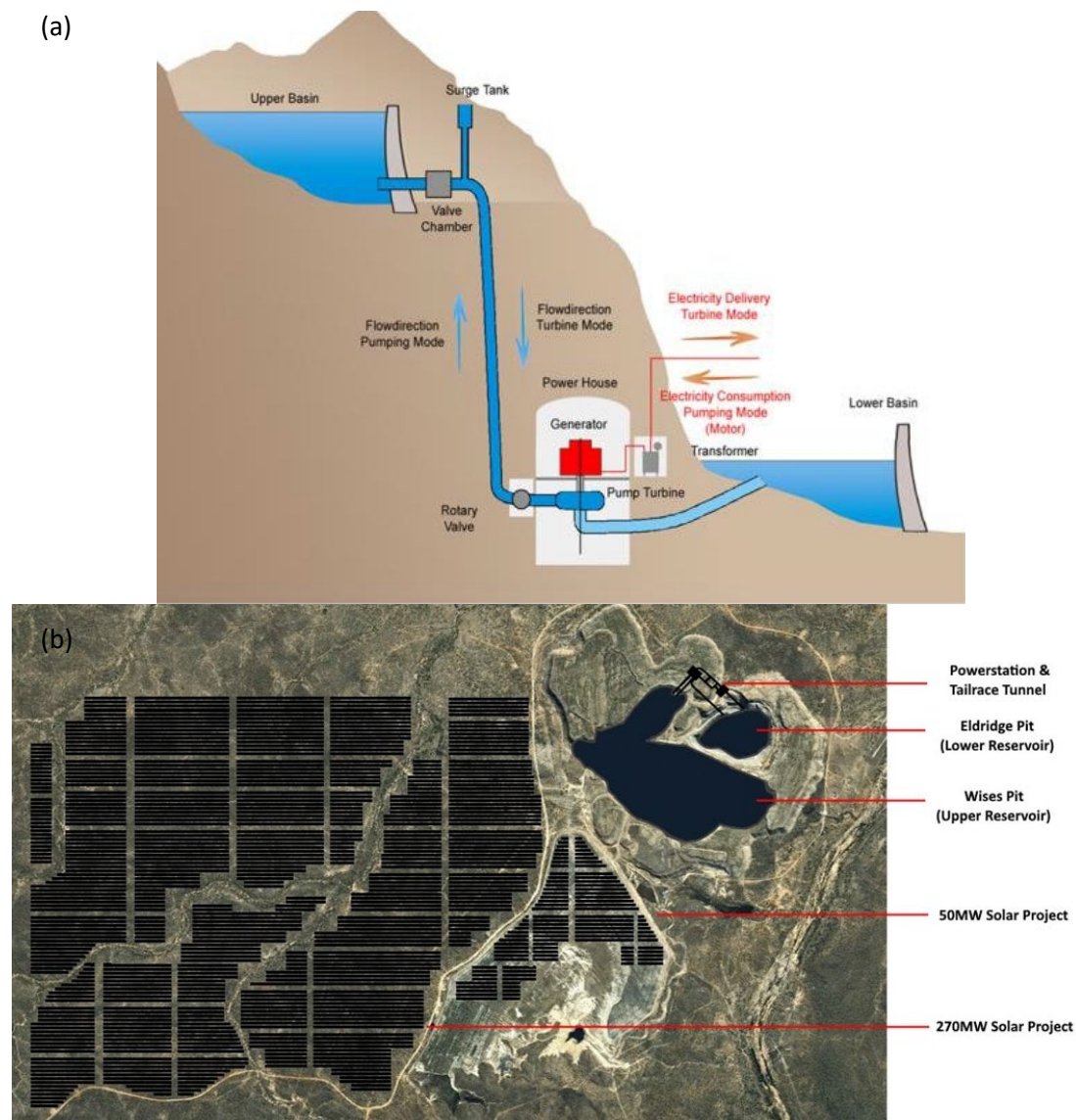


Figure 1-2 - (a) Layout of a pumped hydroelectric storage plant and (b) a picture of the Kidston pumped storage facility in an abandoned gold mine in Queensland (Australia) storing ~2 GWh (Reprinted from Genexpower.com).⁸

This type of storage can offer an energy density of 1 kWh/m³ for a fall of 360 m, with recovery efficiency from 70 % to 85 %.⁹ It presents several advantages for the electric grid: a fast response speed with the flexibility to start and stop, the capacity to modulate the frequency and maintain voltage stability.^{10, 11} Despite substantial geographical constraints, such as large area occupancy and local landform elevation differential, recent studies have identified numerous eligible locations.¹² In 2017, more than 150 GW of power capacity was operational worldwide, producing approximately 4 000 TWh/y.⁷ China has the most extensive pumped hydro storage with 32 GW of power capacity and has recently (January 2019) announced another 6 GW to come online in 2026.¹³ Kear and Chapman revealed that

pumped hydroelectric plants are mostly seen as prohibitively expensive,¹⁴ potentially due to high upfront costs, difficulties to determine the financial revenue generated and to obtain necessary permits to flood a promising site. A staggering 22 000 TWh of energy storage potential using pumped hydro is thought to be feasible worldwide.¹⁵ The development of PHES is forecasted to continue to grow as new projects are announced or commenced. For example, “Snowy 2.0” in New South Wales, Australia, which would provide an additional 2000 MW and 250 GWh of electrical energy storage.¹⁶

1.2.1.2. Compressed air

Compressed air energy storage (CAES) was first developed in the 1940’s,¹⁷ although it wasn’t until the late seventies that the first CAES plant was commissioned.⁷ In general, it uses an electrical air compressor to store pressurised air in a cavity or a tank. This air can then be released at any time to power a turbine generator. Figure 1-3 below shows a simple schematic of the process.¹⁸

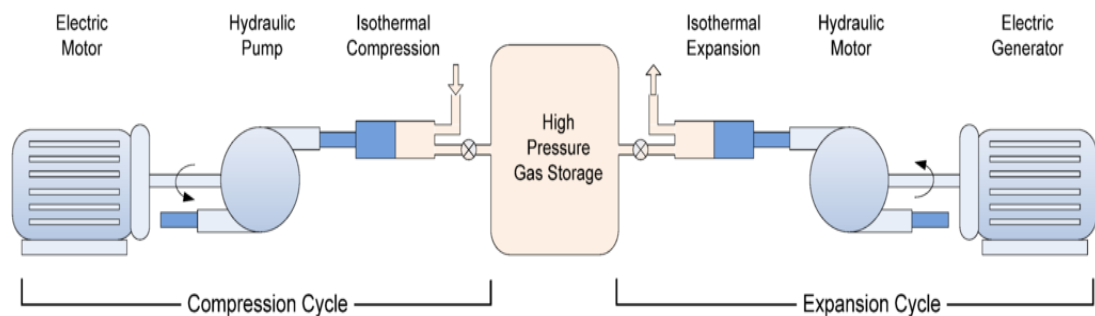


Figure 1-3 - Simple schematic of an isothermal Compressed Air Energy System.¹⁸

As with pumped hydroelectric storage, this technology is typically used in the high power range: 50 to 300 MW with a storage efficiency between 70 and 89 %.¹⁹ However, basic CAES technology needs a natural gas source to increase the temperature of the stored compressed air before expansion to counteract cooling and ensure adiabatic expansion.¹⁸ Despite the simplicity of the idea, many CAES projects were abandoned for various reasons

hindering an effective penetration of CAES.²⁰ Two plants built in the 20th century, a 290 MW in Huntorf (Germany) and a 110 MW plant in McIntosh (Alabama, USA), are still operating.²¹ In 2012, a third CAES plant, coupled with wind turbines generating 2 MW, became operational in Texas, USA.²² This plant avoided the use of polluting gas that was required for heating the air after expansion. Since then a few projects have commenced, but have not yet been completed. It is noted that South Australia has recently (July 2019) approved a proposal to deploy a 10 MWh CAES system in a former zinc mine.²³

1.2.1.3. Flywheel

Flywheel technology is one of the oldest mechanical energy storage systems. In the 18th century, their use in steam engines was instrumental in the industrial revolution.²⁴ Flywheels can store energy through a high speed rotating disk. The accumulated kinetic energy can be conveyed to a shaft driving conventional electromagnetic generators. The main advantages of this technology are the fast response speed and the ability to provide intense and instantaneous electrical loads.²⁵ Figure 1-4 illustrates the flywheel technology for energy storage.²⁶

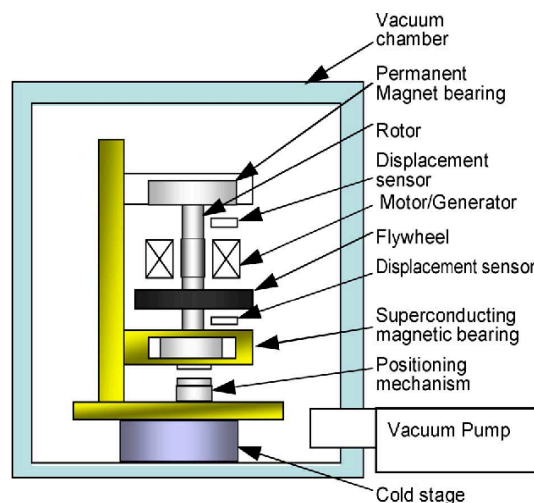


Figure 1-4 - Schematic view of a flywheel energy storage device (Copyright © 2007, IEEE).²⁶

Even if this technology is antique, recent improvements position it as one of the viable solutions in grid power stabilisation.²⁷ However, the high power losses over time significantly reduce its use to niche applications.²⁸

1.2.2. Electrical

1.2.2.1. Electrochemical batteries

The work of Alessandro Volta in 1800 sets the common ground of all electrochemical batteries.²⁹ He demonstrated the possibility of generating electricity by alternatively stacking slices of zinc and copper, separated by saltwater saturated fabric.

In the 1860s, Gaston Planté described the first rechargeable electrochemical battery using the pair: lead and acid, which remains in use today.³⁰ Figure 1-5 shows the workings of a lead-acid battery. Since then, this technology has been developed to reduce device sizes, optimise electrode materials and design, leading to high flexibility and versatility.³¹ In the 1970s, Dr Goodenough *et al.* proposed a much-improved solution with their lithium-ion battery that resulted in the team being awarded a Nobel Prize in 2019.³² Li-ion batteries play a crucial role in our modern society, allowing the emergence of portable electronic devices such as smartphones. Electrochemical batteries are probably the most commonly used technology for energy storage. However, despite tremendous efforts of development, electrochemical batteries suffer from an inherent insufficient energy density (< 756 kJ/kg), and a high price.³³⁻³⁵ In 1970, the discovery of a solid polymer material able to transport ions opened a new field of research on solid-state batteries.³⁶ Solid-state (or solid electrolyte) batteries could offer higher energy densities and increased safety that could make them attractive for large scale energy storage, but challenges such as charge transfer resistance at interfaces are yet to be overcome.³⁷

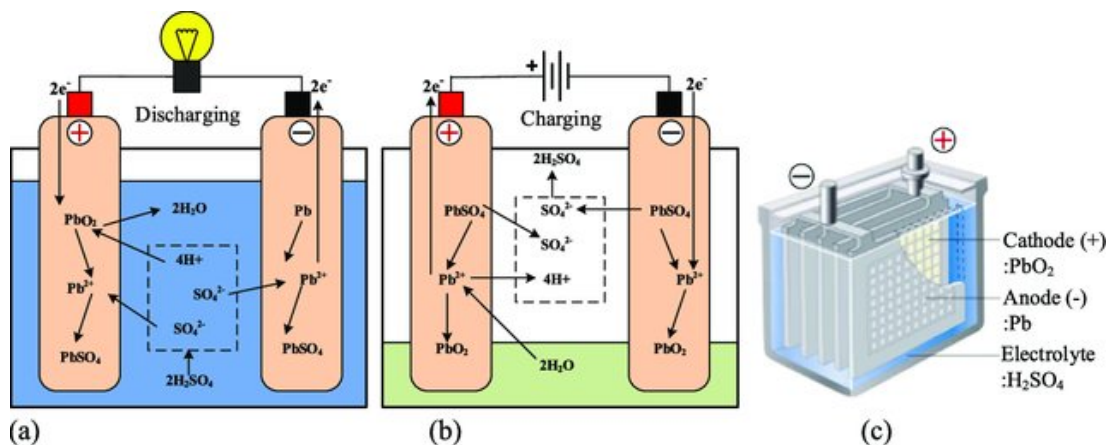


Figure 1-5 - (a) Chemical energy discharging concept, (b) charging, (c) schematic typical design of lead-acid battery. ³¹ (Reprinted with permission from Elsevier)

1.2.2.2. Capacitors

A capacitor is a basic electrical component that stores direct electric charges on two segregated conductive plates. Invented in 1745 by E.G. von Kleist, it is now a great asset to many electrical and electronic circuits.³⁸ The main advantage of capacitors is that they offer sizeable electric storage in a short time and small volumes, but they typically operate with low voltage and provide direct current.³⁹ They are thus not suitable for large scale energy storage, but are thought to assist in the mobility market.⁴⁰ For example, this technology can be used by a subway train to retrieve the energy generated while braking to reinject it directly into the supply chain.⁴¹

1.2.2.3. Superconducting magnetic energy storage

Certain materials become superconducting when cooled to extremely low temperatures, at which point their electrical resistivity becomes nonexistent.⁴² At these temperatures, it is possible to generate a current by magnetic induction and electricity can be stored in a coiled inductor so that current can circulate indefinitely. The auto discharge time is approximately 100 000 years, meaning that, on a human scale, the current remains consistent. This process allows a device to store and deliver large power over a short

timeframe, a basic schematic is displayed Figure 1-6. The number of charge/discharge cycles doesn't impact the lifetime of such devices or the depth of discharge.⁴³ This system is thus ideal for grid stabilisation. However, expensive cryogenic equipment is required for this technology, which can dramatically increase the energy price. Development of superconductive materials that operate under higher temperature, such as when cooled to - 77 °C by liquid nitrogen, could assist in price cost-effectiveness.⁴⁴

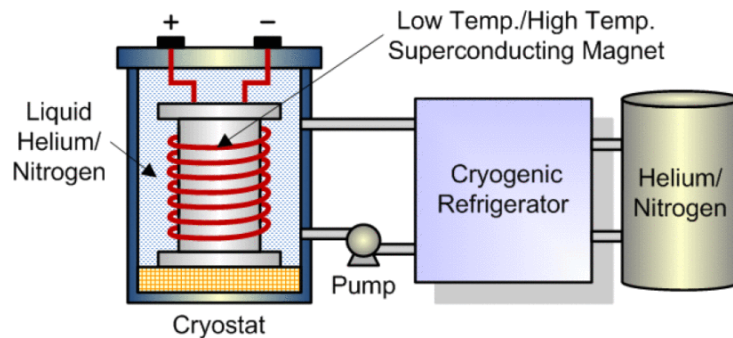


Figure 1-6 - Typical layout of a superconducting magnetic energy storage.⁴³

1.2.3. Thermal energy storage

Thermal energy storage (TES) is based on heating or cooling a well-insulated storage medium in order to retrieve the heat for later applications. Thermal energy can be stored and used in many processes: individual, industrial or for electricity generation. Operational temperatures can range from 60 °C to 1000 °C and the stored energy can be used months later, for example, seasonal thermal energy storage (storing summer heat for the following winter). TES is a highly regarded technology to assist the penetration of renewable energies and waste heat recovery.⁴⁵

Waste heat recovery offers a wide variety of sources and potentially billions of MWh.⁴⁶ Despite this, concentrated solar power (CSP), as a renewable energy source is a driving force for current research, as it is forecasted to reach 7% of the global electricity generation by 2030.⁴⁷ As thermal storage is an essential addition for this technology to supply baseload power and compete with conventional fuels, efforts are ongoing towards

optimisation or new technology development.⁴⁸ Heat storage is currently achieved by molten salts that operate between 290 °C and 565 °C and offer 153 kJ/kg for a 100 °C of temperature variation.⁴⁹ Figure 1-1 presents energy storage in molten salts as the second most deployed storage in terms of power capacity. However, other thermal energy storage technologies could soon replace it with better efficiency. The four different types of CSP plants are detailed in Table 1-1.^{48, 50, 51} Their broad range of potential operating temperatures offer the possibility to adapt a thermal energy storage technology to the technology that best suits the operating temperature and energy densities required.

Table 1-1 - Different type of CSP plants, adapted from ^{48, 50, 51}.

Type	Operating temperature range (°C)	Capacity range (MW)	Efficiency Solar to electricity (%)	Production share (%)
Parabolic trough collectors (PTC)	20 - 400	10 - 250	≈ 15	> 82
Solar power towers (SPT)	300 - 1000	10 - 100	≈ 20	≈ 13
Linear Fresnel reflectors (LFR)	50 - 300	5 - 250	≈ 10	≈ 4
Parabolic dish collectors (PDC)	120 - 1500	0.01 - 1	≈ 25	< 1

Many thermal energy storage technologies exist.⁴⁶ As shown in Figure 1-7, TES technologies are distinguished by three methods with decreasing technological maturity: sensible thermal energy storage, latent thermal energy storage, and thermochemical energy storage.

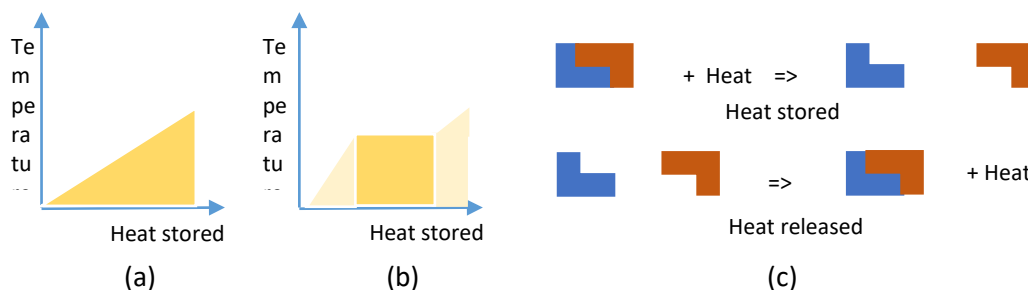


Figure 1-7 - TES methods: (a) sensible (b) latent (c) thermochemical.

1.2.3.1. Sensible thermal energy storage

Sensible thermal storage is the most common thermal energy storage process. It is based on the internal energy of a substance due to particle agitation also known as specific heat, with the reference being the amount of energy required to elevate the temperature of 1 gram of water by 1 °C. It follows the first thermodynamic principle:

$$\Delta E = \Delta E_k + \Delta E_p + \Delta U \quad \text{eq. 1-1}$$

where ΔE_k and ΔE_p (kinetic and potential energy, respectively) equal to zero in a static process, and ΔU (internal energy), which can be written, for an isochoric and isobaric system as:

$$\Delta U = m \cdot C_p \cdot \Delta T \quad \text{eq. 1-2}$$

where m , the storage material mass; C_p , its specific heat capacity; ΔT , is a temperature differential.

Many households possess a heated water tank as thermal energy storage (TES) that provides hot water on demand. But depending on the final application and operating temperature, different materials can be used to store heat, i.g., cast iron or concrete.⁵² A recent review of TES systems by Alva *et al.* reveals the bulk of TES usage is currently performed through sensible storage.⁴⁵ The TES review presents a variety of usable storage materials that are usually low-cost materials such as water, thermal oils, molten salts, liquid metal (Lead bismuth eutectic can operate at temperatures up to 1533°C), or concrete blocks. Notably, a French company Ecotechceram[®] developed and commercialised a low-cost thermal energy storage solution using ceramics to add value from waste heat from industry. The company claims to store 2 MWh_{th} from 600 °C to ambient temperature, using ceramics in a 6 m sea cargo container. However, the thermal energy storage at high temperature based on specific heat has a typically low gravimetric energy density of ≈ 100 kJ/kg per 100 °C and therefore, involves large temperature excursions.⁵³ Despite the maturity of this simple technology, future alternative technologies may offer better cost efficiency for storing energy at high temperatures.

1.2.3.2. Phase change materials for thermal energy storage

Phase change thermal energy storage uses the aptitude of a substance to change phase, typically melting or solidifying at a specific temperature with a high amount of thermal energy involved (i.e. latent heat of fusion). The range of potential materials is broad and is distinguished into three categories: Organic, inorganic (as single material) and eutectic (as compounds).⁵⁴ As shown in Figure 1-8, they cover a vast spectrum of operating temperature and thus a wide range of possible applications.⁵⁵

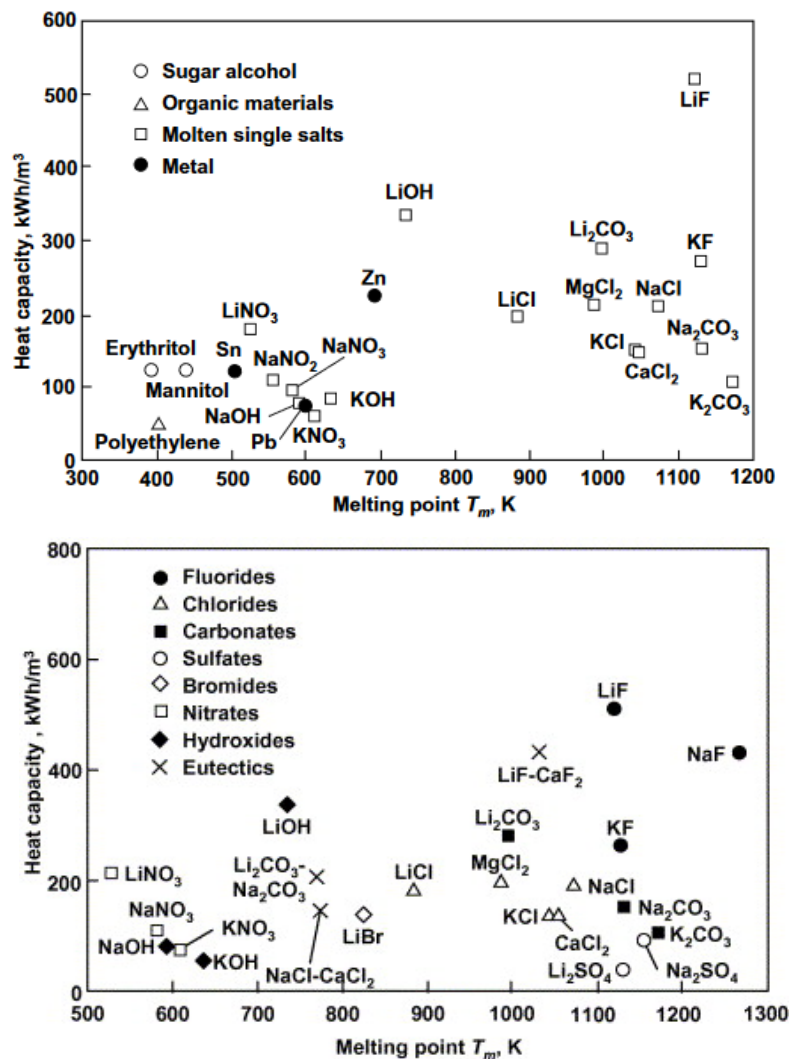


Figure 1-8 - Heat storage capacity for various phase change materials.⁵⁵ (Reprinted with permission from Elsevier)

Compared to existing sensible thermal energy storage systems, these materials have the potential to reduce the volume of storage material by an order of magnitude. Nevertheless, they suffer from large structural deformation which induces poor thermal conductivity.⁵⁶ This challenge needs to be addressed in order to be successful in commercial applications. For this purpose, numerous investigations are conducted such as material improvement and encapsulation.^{57, 58}

1.2.3.3. Thermochemical thermal energy storage

Thermochemical energy storage describes the process of storing heat by means of a compound decomposing under specific conditions of pressure and temperature into two (or more) substances during an endothermic reaction.⁵⁹ The energy supplied breaks the chemical bond between atoms. This reaction is necessarily reversible, so the stored thermal energy can be retrieved during the reverse exothermic reaction. The enthalpy of reaction (ΔH) dictates the energy storage density of the system. A chemical reaction that occurs in a potentially negligible temperature excursion and offers high enthalpy of reaction is the prime advantage of such technology. There are two major types of reactions: gas - gas and solid-gas. The gas to gas reaction principle can be mainly summarised by the ammonia synthesis/dissociation reaction that offers a theoretical gravimetric energy density of 3950 kJ/kg.⁶⁰ It has already been implemented onto a solar dish system by the Australian National University (ANU) and offers a total energy storage efficiency of 52%.⁶¹ Recent studies demonstrated the feasibility of such technology for thermochemical energy storage, but this requires several MPa of gas pressure to operate. Hence, it is still under a development and optimisation phase.⁶² The solid-gas reaction concept offers broader possibilities, 4 different reversible reactions are commonly under investigation: carbonates, reacting with carbon dioxide; metal oxides, reacting with oxygen; hydroxides, reacting with water and metal hydrides, reacting with hydrogen.

For example, hydrogen chemical bonding with lithium to form a lithium hydride offers a staggering theoretical heat storage capacity of 8397 kJ/kg, however the high material cost, is prohibitive for large scale usage.⁶³ A reaction between calcium oxide and carbon dioxide can form calcium carbonate with a gravimetric energy density of 1657 kJ/kg.⁶⁴ Magnesium hydride is also an attractive potential thermal energy storage material which offers a higher

theoretical capacity of 2814 kJ/kg and the base metal, magnesium, is widely available in the earth crust.⁶⁵ The second attractive characteristic involved in utilising the enthalpy of reaction lies in the absence of losses when there is no reaction occurring. This allows the storage of thermal energy during extended periods and also to consider the transportation of storing material. Once the material is heated up to its operational temperature, the bulk of the stored energy can be retrieved.

As solar thermal energy storage is driving heat storage investigations, the majority of development on this type of storage concerns high-temperature reactions. Table 1-2 details the four most investigated thermochemical reaction types and the associated attractive materials due to their gravimetric energy densities and operating temperatures.

	Materials	Operating temperature range (°C)	Equilibrium temperature at 1 bar (°C)	Gravimetric energy density (kJ/kg)	Volumetric energy density (kJ/L)	ref
Carbonates	CaCO ₃	> 880	873	1657	4639	64
	MgCO ₃	≈ 450	350	1147	3383	66
	CaMg(CO ₃) ₂	≈ 590	630	682	1977	64, 67
Metal Oxides	Co ₃ O ₄	885 - 1050	885	826	2124	68, 69
	Mn ₃ O ₄	> 650	650	≈ 160	≈ 1150	70
Hydroxides	Ca(OH) ₂	400 - 600	500	≈ 2000	≈ 3100	71
	Mg(OH) ₂	200 - 500	250	≈ 900		72
Metal hydrides	CaH ₂	> 1020	1020	3857	6550	64
	NaMgH ₃	350 - 683	380	1721	2950	73
	Mg ₂ FeH ₆	300 - 600	330	2100	5757	74
	CaAl ₂ H _x	≈ 600	≈ 500	865	1860	75
	Mg ₂ CoH ₆	250 - 400	≈ 320	≈ 2000	≈ 4000	76, 77

Table 1-2 - Favourable reversible thermochemical materials.

Carbonates offer typically high operating temperatures and attractive energy densities.^{64, 67} However, Benitez-Guerrero *et al.* reported high potential of pore plugging issues and identified the constraints involved with the high thermal expansion of these materials.⁶⁷ Investigations on dolomite revealed attractive results with impurities ensuring a consistent

porosity, hence CO₂ capacity, but the slow kinetics of their reaction remains the prime challenge to address.⁶⁴

Metals oxides also display a high operating temperature range and offer the advantage of using compressed air as a heat transfer fluid.⁷⁸ Cobalt-based oxides have been designated as the best candidate for thermal energy storage using oxygen as the reactant, due to acceptable kinetics and stable reversibility.^{68, 70} However, a recent techno-economic assessment by Bayon *et al.* exposed the high cost involved with the use of cobalt.⁷⁹

Metal hydroxides such as CaO/Ca(OH)₂ offer a high gravimetric energy density and display reliable reversibility in the 500 °C vicinity.^{80, 81} Further investigations remain to address particle aggregations and volume change during reaction, resulting in an increased thermal resistivity.^{82, 83}

Metal hydrides offer a wide range of high-temperature operations and appealing energy densities, as shown in Table 1-2. Since the 1990's, a renewed interest appeared for metal hydride used to store high temperature thermal energy (350 °C and above) due to the identification of low-cost magnesium hydride by Bogdanović *et al.*⁸⁴⁻⁸⁶ These metal hydrides absorb and release hydrogen at specific temperatures and pressures. The van 't Hoff equation describes the temperature and pressure correlation with the change of enthalpy (ΔH) during the hydrogen desorption:

$$\ln \left(\frac{P(H_2)}{P_0} \right) = \frac{-\Delta H}{RT} + \frac{\Delta S}{R} \quad \text{eq. 1-3}$$

where

$P(H_2)$ = the system pressure (bar)

P_0 = 1 bar

T = the temperature (K)

R = the gas constant (8.314 J/(K.mol))

ΔS = the entropy of the reaction (J/K.mol)

Magnesium hydride has attracted a multitude of studies due to its enthalpy of reaction of 74 kJ/mol H₂ and high hydrogen capacity, leading to a thermal energy density of 2814 kJ/kg.^{53, 87} These studies were focused on improving synthesis yields, reaction kinetics and thermal conductivity.⁸⁸⁻⁹² Overall, a sintering process that occurs around 470 °C limits the reversible hydrogen uptake capacity.⁹³ Various magnesium-based hydrides, have been developed to improve thermal energy density, lower the operating pressure associated

with high temperature, or increase the operating temperature with the aim of using them as high temperature metal hydrides (HTMH).^{87, 94} For example, sodium magnesium hydride (NaMgH_3) can decompose into sodium hydride and magnesium and release 4 wt% of hydrogen at stable pressure of approximately 3 bar at 430 °C.⁹⁵ The addition of fluorine has been shown to stabilise MgH_2 and allow an operating temperature increase of 80 °C.⁹⁶ The addition of small quantities of iron to MgH_2 can lead to a reduced activation energy by half and full hydrogen release in less than 5 minutes at 300 °C.⁸⁸ A mixture of 2 moles of magnesium and one of iron leads to the formation of a magnesium iron hexahydride (Mg_2FeH_6), which occurs at lower hydrogen pressure than a pristine magnesium hydride. Despite the favourable characteristics of these materials, it is only recently that the technology has been up-scaled experimentally to explore the constraints involved with thermal energy storage and reversibility using such chemistry.⁹⁷⁻⁹⁹ The research project herein, aims at further exploring the feasibility of this thermal energy storage technology by scaling tanks up to 900 g of material and exploring the limits involved in their operation. The storage of the hydrogen gas released is also considered by using a low temperature metal hydride (LTMH) or a compressed gas tank.

1.3. Hydrogen

1.3.1. History

Hydrogen (H_2) is the most common element in the universe and the primary fuel of our sun. On Earth, at ambient conditions, hydrogen is a low density gas. Henry Cavendish was granted the discovery of hydrogen in 1766. He originally called it “inflammable air”, to distinguish from the non-flammable nature of “normal air”.¹⁰⁰ It is only a century after that A. Lavoisier named the diatomic gas hydrogen, signifying in Greek: water generator. In 1839, the Swiss chemist Schoenbein discovered that combining hydrogen and oxygen could produce water and electricity. The lightest element of the periodic classification was first used for air transport. F. von Zeppelin developed a rigid airship able to cross the Atlantic Ocean, although, a tragic accident in 1937, caused by the flammable nature of this gas, terminated its exploitation.¹⁰¹

After the First World War, hydrogen started to be considered for practical use, fuelling cars or trucks, as hydrogen has an energy density of 120 MJ/kg, which corresponds to 3 times that of the petrol.^{102, 103} This places hydrogen as a promising replacement for gasoline in the transport sector, aiming towards decarbonisation. Nowadays, despite various industrial applications, hydrogen is predominantly utilised in ammonia synthesis, which is intensively used in conventional agriculture.¹⁰⁴ The very low density of hydrogen induces large volume requirements for storage, which hinders applications. Nevertheless, various storage solutions are emerging to concentrate hydrogen into smaller volumes; these solutions are further developed in the following sections.

1.3.2. Production and sources

Hydrogen is available on Earth, but only in a bonded form. Sources of hydrogen are diverse and various production processes exist. Compounds that contain hydrogen, such as biomass, fossil fuels or water, can be base materials for hydrogen production.¹⁰⁵⁻¹⁰⁸

At the present time 70 million tons of hydrogen are consumed daily.¹⁰⁹ Steam reforming of natural gas is the most commonly used technique to generate hydrogen, which produces over 48 % of the annual world production.¹¹⁰ The carbon-hydrogen bonds in methane (CH₄) are broken when exposed to high-temperature steam (≈ 800 °C), producing hydrogen and carbon dioxide. This mature, efficient and financially attractive technique suffers from a high CO₂ production.¹¹¹ It is, therefore, likely to be a bridging technology, as various “greener” and economically viable production processes arise.^{108, 112} Hydrogen could be a renewable energy carrier, but only if it is produced via renewable sources such as hydroelectricity, solar or wind power. In the past decade, research projects have arisen to develop or improve technologies such as sun powered water electrolysis or biomass gasification. Water electrolysis is highly regarded as a sustainable way to generate hydrogen and can offer efficiencies up to 60 %, however it remains at a high cost, and technological development is required for it to be considered as a viable method for large scale hydrogen production.^{106, 113} Photo-electrochemical water splitting has been investigated to produce hydrogen from direct sunlight through the use of non-oxide semiconductors with a 2 step photo-excitation reaction.¹¹⁴ A recent review on this process emphasises the obstacles of charge recombination and mass transfer limitation, and underlines the interest of developing photo-catalysts that could be activated at a

wavelength of 600 nm and higher to improve solar-hydrogen conversion efficiency.¹¹⁵ Urea has also shown attractive characteristics to produce cheap 100% pure hydrogen.¹⁰³ In the long term, biomass gasification could offer both: an environmentally friendly resource at a competitive price.^{116, 117}

1.3.3. Applications

Currently, hydrogen is mainly used in the petroleum and chemical industry. Due to its high reactivity with various elements it is often used to refine or combine products, such as the reduction of iron ore.¹¹⁸ Ammonia synthesis uses ≈ 50 % of globally produced hydrogen. In this process hydrogen is combined with nitrogen through the Haber-Bosch process to produce ammonia.^{119, 120} Another 20 % is used in refineries for desulphurisation or oil cracking.¹²¹ Methanol production also uses a significant quantity of hydrogen resulting in 10 % of the hydrogen consumption. The remaining applications are less hydrogen intensive, but the gas plays a significant role in diverse applications such as rocket propellant in the aerospace industry, decreasing unsaturated fat levels in the food industry or scavenging oxygen in the metal production industry.¹²⁰ With the rising interest in hydrogen toward decarbonisation, many more applications are emerging. Mainly, the highly energetic combustion of hydrogen places it as a potential fuel replacement in the transport industry.¹²²⁻¹²⁴ It is also considered to assist renewables market penetration as an energy storage solution.^{125, 126}

1.3.4. Storage

Hydrogen storage is amongst the critical parameters to ensure development of the hydrogen economy.¹⁰³ Due to its light weight and gas phase under standard temperature and pressure conditions, hydrogen is a complex material to store cost effectively. An ideal hydrogen storage technology suitable for industrial applications should satisfy the requirements of high gravimetric and volumetric hydrogen storage density, long cycle life, and excellent safety performance. It shall be noted that the US Department of Energy

(DOE) has set a target of 45 g/kg (or 30 g/l) for 2020 and Europe is aiming at 48 g/l.^{127, 128} To date, hydrogen is most commonly stored compressed in high-pressure cylinders at pressures up to 700 bar, which leads to a hydrogen density of ≈ 38 g/L and can offer complete refueling of a car in less than 3 minutes.^{129, 130} However, as Figure 1-9 shows, several layers are necessary to form a reliable containment vessel and the composite materials used for the pressure vessel are expensive.^{131,132}

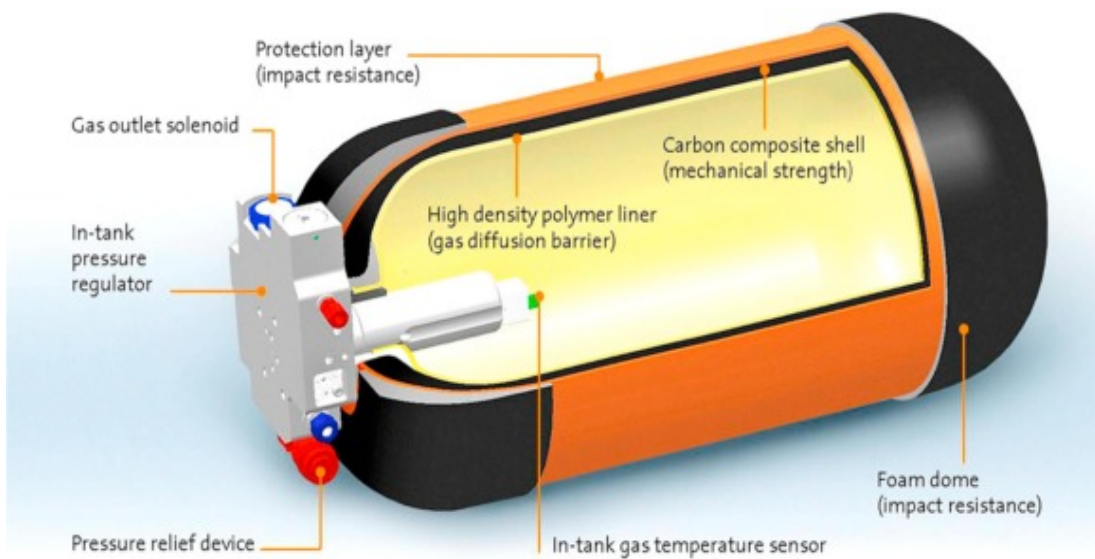


Figure 1-9 - Details of a high pressure hydrogen tank.¹³² (reprinted with permission from Elsevier)

Gaseous hydrogen can also be stored underground. The literature on underground hydrogen storage in geological structures is mainly based on analogies to the storage of natural gas and carbon dioxide. However, the light hydrogen particle possesses high diffusion capacity and a cavity suitable for CH₄, or CO₂ storage, doesn't necessarily offer adequate characteristics to store hydrogen.¹³³ In France, at Beynes, Gaz de France (GDF) stored manufactured gas containing 50 % of hydrogen in a saline aquifer with a capacity of 385 million cubic meters between 1956 and 1972. However, intense bacterial activity and subsequent gas transformation was observed.¹³⁴ Long term pure hydrogen storage was demonstrated at Teeside cavern (UK) commissioned in 1972 offering 210,000 cubic meters of storage volume at a maximum pressure of 48 bar.¹³⁵ Specific properties of salt can guarantee long-term stability and a leak tight storage.¹³⁶ Investigations are continuing to find eligible locations, as demonstrates, for example, a recent study by Le Duigou *et al.*, to identify feasible sites in France.¹³⁷

Hydrogen can also be stored in a liquid form to reach a density of 70 kg/m^3 .¹³⁸ Although, it requires liquefaction at $-253 \text{ }^\circ\text{C}$, which is achieved at high cost and containers require considerable insulation, which are also expensive. It is therefore mainly used for space applications. Cape Canaveral, Florida, hosts one of the largest tanks for storing liquid hydrogen with a capacity of $3,800 \text{ m}^3$ (245 tons).¹³⁹

Liquid organic hydrogen carriers (LOHC) are promising hydrogen storage technologies receiving attention from scientific community.¹⁴⁰ With gravimetric hydrogen capacities ranging between 6 wt% and 8 wt%,¹⁴⁰ LOHC allow hydrogen to be stored in a liquid form at ambient temperature whilst using existing infrastructure for transportation.¹⁴¹ Figure 1-10 illustrates the typical hydrogen storage cycle with LOHC. The technological challenge of this storage solution resides in a dehydrogenation of the liquid typically occurring between $200 \text{ }^\circ\text{C}$ and $450 \text{ }^\circ\text{C}$.^{142, 143}

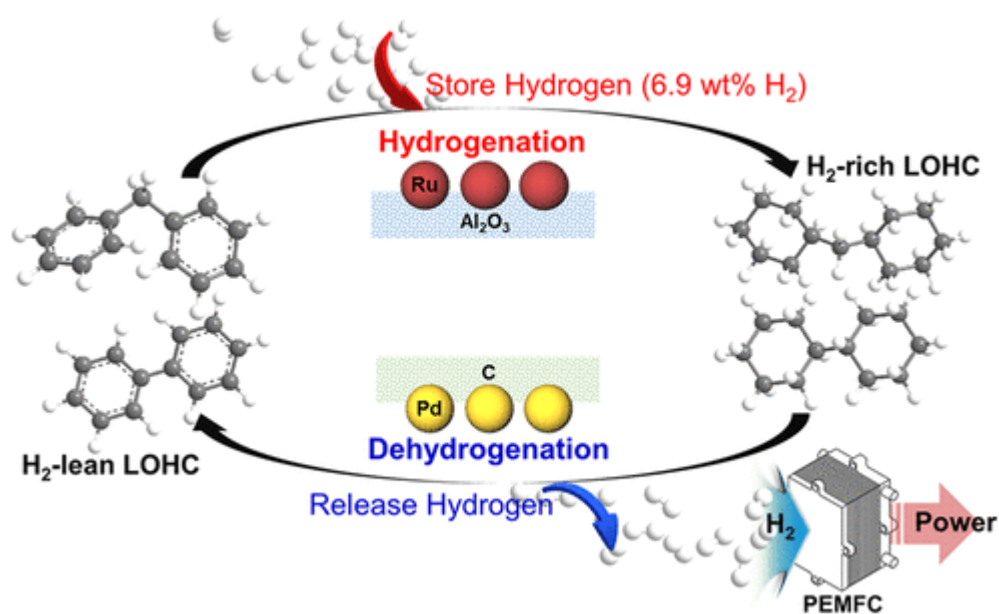
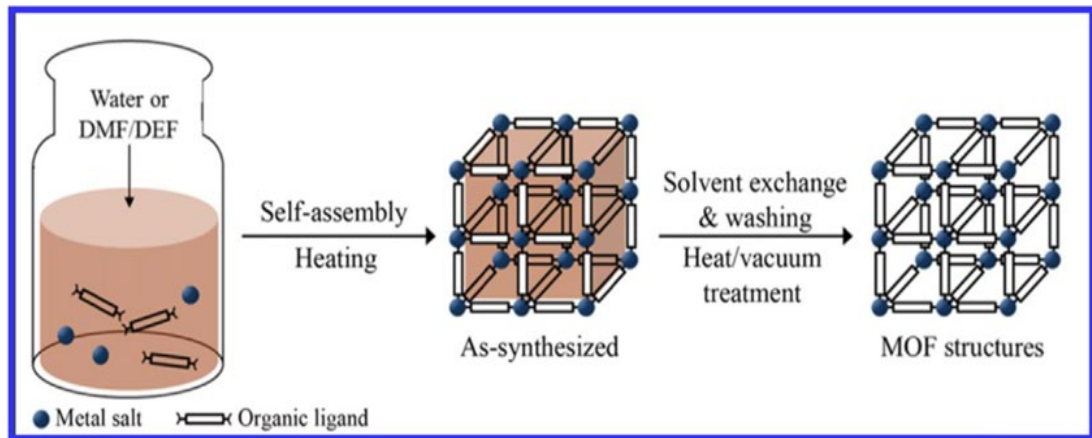


Figure 1-10 - Schematic of hydrogen cycle through LOHC. Reprinted with permission from ACS

Sustainable Chemistry & Engineering. Copyright (2019) American Chemical Society.¹⁴³

Crystalline porous materials such as metalorganic frameworks (MOF) display attractive adsorption capacity. They are made of metal ions linked by organic substance offering a network of channels and pores offering high specific surface up to $7140 \text{ m}^2/\text{g}$.^{144, 145} MOFs have received tremendous attention as hydrogen storage materials since the pioneering work of Rosi *et al.*, in 2003, that reported hydrogen adsorption on porous MOFs.¹⁴⁶ Their hydrogen capacity ranges from 6 wt% to 15 wt% which meets the DOE target.¹⁴⁷ However, these values are reached at temperatures of $-196 \text{ }^\circ\text{C}$ and research is required to optimise

hydrogen adsorption near room temperature to avoid an expensive cooling system. Moreover, the synthesis procedure requires several steps (Figure 1-11) and can demand



extended time.¹⁴⁸ As a consequence, MOFs are expensive materials.

Figure 1-11 - Conventional MOF synthesis.¹⁴⁸

1.4. Metal hydrides

1.4.1. Principle

Metal hydrides are another attractive and promising way to store hydrogen. In the past few decades, researchers have been unravelling the characteristics of these materials. Many metals can chemically bond with hydrogen and form solid chemical compounds. Commonly called absorption, the association process can be separated into different steps. As shown in Figure 1-12, the hydrogen molecule contacts the metal surface and dissociates into hydrogen atoms. These atoms can then penetrate the crystal structure of the material and may change it to form a new compound known as a metal hydride. During this absorption stage, thermal energy is generated via an exothermic reaction.

A thermal decomposition can allow a release of the hydrogen following the reaction:



where

M = a metal or an intermetallic compound

X = the quantity of hydrogen able to react with the metal

Q = the reaction's heat

The dissociation of hydrogen and its host metal, may result from a thermal energy supply. The energy breaks the bonds of hydrogen atoms which combine to reform a gaseous hydrogen molecule.

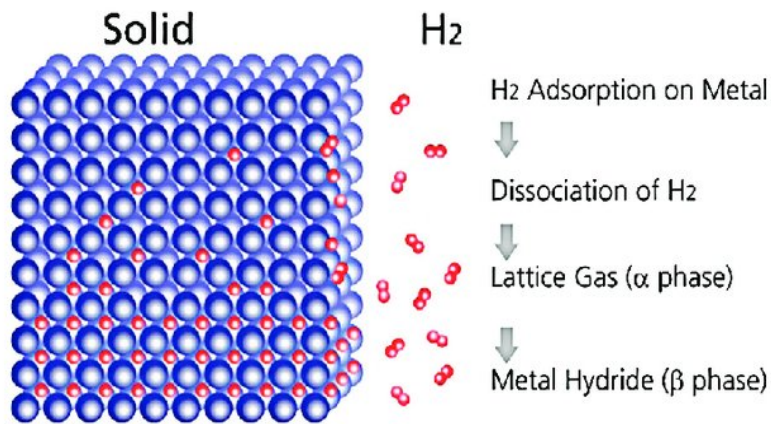


Figure 1-12 - Schematic of hydrogen absorption and desorption process.¹⁴⁹

1.4.2. Metal hydrides categories

Metal hydrides for hydrogen storage can be divided into distinct categories including ionic, covalent and metallic, as shown in Figure 1-13.^{150, 151} Each of them is briefly presented.

1		2												13	14	15	16	17	18
H																		He	
2.20																			
LiH	BeH ₂												BH ₃	CH ₄	NH ₃	H ₂ O	HF	Ne	
0.97	1.47												2.01	2.50	3.07	3.50	4.10		
NaH	MgH ₂												AlH ₃	SiH ₄	PH ₃	H ₂ S	HCl	Ar	
1.01	1.23												1.47	1.74	2.06	2.44	2.83		
KH	CaH ₂	ScH ₂	TiH ₂	VH VH ₃	CrH (CrH ₂)	Mn	Fe	Co	NiH ₄	CuH	ZnH ₂	(GaH ₃)	GeH ₄	AsH ₃	H ₂ Se	HBr		Kr	
0.91	1.04	1.20	1.32	1.45	1.56	1.60	1.64	1.70	1.75	1.75	1.66	1.82	2.02	2.20	2.48	2.74			
RbH	SrH ₂	YH ₂ YH ₃	ZrH ₂	(NbH ₂)	Mo	Tc	Ru	Rh	PdH ₄	Ag	(CdH ₂)	(InH ₃)	SnH ₄	SbH ₃	H ₂ Tc	HI		Xe	
0.89	0.99	1.11	1.22	1.23	1.30	1.36	1.42	1.45	1.35	1.42	1.46	1.49	1.72	1.82	2.01	2.21			
CsH	BaH ₂	LaH ₂ LaH ₃	HfH ₂	TaH	W	Re	Os	Ir	Pt	(AuH ₃)	(HgH ₂)	(TlH ₃)	PbH ₄	BiH ₃	H ₂ Po	HAt		Rn	
0.86	0.97	1.08	1.23	1.33	1.40	1.46	1.52	1.55	1.44	1.42	1.44	1.44	1.55	1.67	1.76	1.90			
Fr	Ra	AcH ₃																	
		1.00																	

CeH ₂	PrH ₂ PrH ₃	NdH ₂ NdH ₃	Pm	SmH ₂ SmH ₃	EuH ₂	GdH ₂ GdH ₃	TbH ₂ TbH ₃	DyH ₂ DyH ₃	HoH ₂ HoH ₃	ErH ₂ ErH ₃	TmH ₂ TmH ₃	(YbH ₂) YbH ₃	LuH ₂ LuH ₃
1.06	1.07	1.07		1.07	1.01	1.11	1.10	1.10	1.10	1.11	1.11	1.05	1.14
ThH ₂	PaH ₂	UH ₃	NpH ₂ NpH ₃	PuH ₂ PuH ₃	AmH ₂ AmH ₃	Cm	Bk	Cf	Es	Fm	Md	No	Lr
1.11	1.14	1.22	1.22	1.22	1.2								

Figure 1-13 – Table of the binary hydrides and the Allred–Rochow electronegativity. Most elements react with hydrogen to form ionic, covalent, or metallic binary hydrides.¹⁵¹

1.4.2.1. Ionic hydrides

Ionic hydrides are compounds, usually binary, based on alkali metals (group I) or alkaline earth (group II). The negatively charged hydrogen atom bonds with the electropositive metal to form a hydride such as LiH or NaH.¹⁵² However, this class of hydride is highly reactive with water and generally too thermally stable to be eligible for hydrogen storage. Note that this thermal stability points this class of hydride as potentially eligible for high temperature thermal energy storage.

1.4.2.2. Covalent hydrides

Covalent hydrides represent all elements covalently bonded to the hydrogen atom. It implies an electron is shared from each atom acting as a ligand and the hydrogen is in the

lattice as an anion. Covalent hydrides encompass a wide range of compound such as hydrocarbons, ammonia, borohydrides, boranes or alanes. They can be solids, liquids or gases and usually present weak bonding energy. As a consequence, they can be unstable or volatile at standard temperature and pressure.

This class also contains the large group of complex metal hydrides which are formed by, at least, a pair of elements, metal or non-metal. They follow the chemical formula $A(BH_x)_y$, with A, an alkali metal or alkaline earth as cation; and B, a light element such as boron or aluminum. $(BH_x)_y$ is a complex anion, with x and y an integer. The high gravimetric hydrogen content of complex hydrides points them as favourable materials for hydrogen storage.¹⁵³ One of the most investigated hydride of this group is $NaAlH_4$ (also called sodium alanate) which releases 5.5 wt% of hydrogen reversibly at ≈ 230 °C when pure.^{153, 154}

1.4.2.3. Metallic hydrides

Metallic hydrides, also called interstitial metal hydrides, are formed when hydrogen bonds with a metal from group III to VIII. Hydrogen is present in the lattice as a proton filling interstitial crystallographic sites of the structure. The hydride formation changes the structure and lattice parameters of the original metal.¹⁵² These materials can generally react with hydrogen reversibly at ambient temperature, which makes them attractive for hydrogen storage. However, the high molar mass of the original atom induces a low gravimetric density of hydrogen typically less than 3 wt%.¹⁵⁵

1.4.3. History

The interaction of hydrogen with metals was discovered at the beginning of the 20th century with studies of systems such as palladium-hydrogen or nickel-hydrogen.^{156, 157} In 1958, Libowitz *et al.* revealed a reversible hydrogen storage through an intermetallic alloy, zirconium-nickel.¹⁵⁸ As early as the 1980's metal hydrides were seen as an attractive means to store hydrogen. Mercedes had developed a TiFe hydride tank capable of fueling a 2.4 ton experimental van for 130 km at 60 km/h.¹⁵⁹ The hydrogen reloading took 45 minutes

due to the external cooling requirement and hindered further industrial developments. Extensive investigations are ongoing to discover and develop suitable hydrides to improve the safety of hydrogen storage and reach the U.S. department of energy (DOE) target for mobile applications.^{160, 161} Critical material properties such as thermal conductivity and enthalpy of reaction remain the most difficult challenges since heat is released during hydrogen absorption and the hydride temperature elevation can hinder the absorption process. A few companies, typically spin-offs from research groups, have emerged such as the French company McPhy energy[®], created in 2008, which developed and commercialised a hydrogen storage solution based on optimised magnesium hydride pellets.⁹¹ In 2010, Australian company Hydrexia[®] developed a solid-gas storage device based on the investigations led by Nogita *et al.* on a low cost production technique of a Mg-Ni alloy.¹⁶²

In parallel, investigations of metal hydrides as a potential high temperature thermal energy storage have arisen, following the work of Bogdanović *et al.* on magnesium hydride for high temperature heat storage earlier this century.¹⁶³ This application will be further developed in chapter 3 of this manuscript.

Chapter 2 Experimental

« J'ai inventé une lampe de poche qui fonctionne à l'énergie solaire...
Elle n'a qu'un dernier défaut : elle ne marche qu'en plein soleil. »

« I invented a torch that works with solar energy...
One last issue: it works only when exposed to the sun. »

[André Franquin] *Extract from comic "Gaston Lagaffe".*

2.1. Introduction

During the course of this research project, various materials were synthesised and analysed through a number of different techniques. These techniques have generally been optimised to suit the best possible data acquisition. In this chapter, each method that has been employed for sample preparation and characterisation is described in detail. The basic principles and theories are also presented to give the reader some fundamental knowledge of the different techniques.

2.2. Materials

Table 2-1 presents a list of chemicals used during this thesis project and states their purity and supplier.

Table 2-1 - List of chemicals used through the project.

Chemical	Chemical formula	State	Purity (%)	Supplier
Argon	Ar	Gas	99.997	BOC until 11/2018, then Coregas
Hydrogen	H ₂	Gas	99.9995	BOC until 11/2018, then Coregas
Helium	He	Gas	99.999	BOC until 11/2018, then Coregas
Nitrogen	N ₂	Gas	99.99	Coregas
Magnesium hydride	MgH ₂	Powder	>95	Sigma-Aldrich
Sodium hydride	NaH	Powder	>95	Sigma-Aldrich
Magnesium	Mg	Powder	>98	Sigma-Aldrich
Iron	Fe	Powder	>99	Sigma-Aldrich
Titanium manganese alloy (TiMn _{1.5} alloy)	Ti _{0.97} Zr _{0.019} V _{0.439} Fe _{0.097} Cr _{0.045} Al _{0.026} Mn _{1.5}	Powder		Sigma-Aldrich
Expanded natural graphite	C	Flakes (<1 cm)		SGL carbon
Titanium boride	TiB ₂	Powder (<10 μm)		Sigma-Aldrich

2.3. General instrumentation

A series of sensors were used to acquire temperatures, pressures, gas or liquid flow. Here, they are presented with their supplier and main specifications. Varying diameter K-type thermocouples (from 100 μm to 2 mm diameter), supplied by Omega[®] or RS Components[®], were used to monitor temperatures based on the Seebeck effect (the ability of two different metals joined to create a potential difference function of the temperature).¹⁶⁴ Piezo-resistive sensors supplied by Omega[®] (PX series with accuracy of 0.5%) and a coplanar differential pressure manometer from Rosemount[®] (3051 SMV with DP reading accuracy of 0.04%) were used to record system pressure from 0 to 300 bar and pressure differentials when fluid flow was undertaken. Details on the use of differential manometer to determine a flow is further given in section 2.6. Sensors were connected to a computer via acquisition cards (OMB-DAQ from Omega[®] or DT80 from Datalogic[®]) using appropriate software such as Labview[®] or Pactware[®]. Some more specific instrumentation and devices are used for investigations in chapter 4, 5 and 6. Details of the developed experimental setups are further described in sections 2.7, 2.8 and 2.9 of this chapter.

2.4. Synthesis

Metal hydrides are sensitive to moisture and oxygen, therefore, all manipulation of chemicals were performed inside an argon filled glovebox (Unilab Glovebox, mBraun, Germany). The atmosphere inside the glovebox is controlled by an automatic gas purifier which traps oxygen and moisture, the levels of $\text{H}_2\text{O}/\text{O}_2$ were typically kept below 1 ppm.

A metal hydride is formed through the reaction of a metal with hydrogen. A variety of synthetic procedures can be used to form a metal hydride from solvent based to cryogenic milling.¹⁶⁵⁻¹⁶⁷ The most accessible remains ball milling, which is also used for particle size reduction or powder blending.¹⁶⁸ Further details for each material milling process and synthesis are given in sections 3.3.3.1.2 and 3.3.3.2.2.

2.4.1. Planetary ball mill

All materials synthesised throughout this project were conducted using planetary ball mill and annealing (heating under hydrogen pressure). The powder mixture was typically placed in a 316 stainless steel canister with a set weight and/or amount of stainless steel balls. The stainless steel has a high hardness advantage (around 6 on Mohs scale) compared to the bulk of other metals, which prevents sample contamination.¹⁶⁹ The mill is then put into rotation creating a centrifugal force resulting in the powder mixture being subjected to high energy collisions. If the duration and ball to powder weight ratio is correct, the result of a ball milling process is a fine homogenous powder (crystal size of nanometres) of merged materials. Figure 2-1 displays a picture of the PQ-N04 planetary ball mill, canister and balls used to perform the first synthesis step for a few grams of sample.

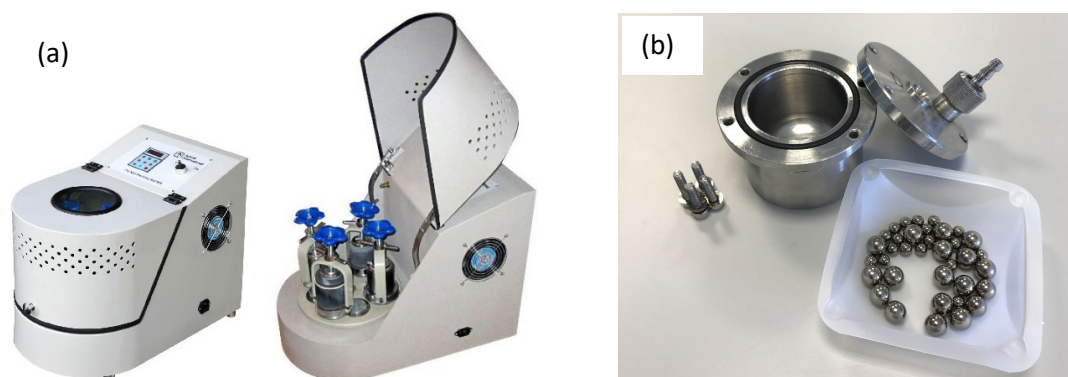


Figure 2-1 (a) PQ-N04 planetary ball-mill. (b) 316 stainless steel ball-milling canister and balls (diameter of 6 and 10 mm).

2.4.2. Shaker mill

In order to prepare batches of more than a few grams, a custom made 316 stainless steel canister, shown in Figure 2-2, was used. The internal available volume is 650 cm³ and the design avoids any powder to be trapped in a corner. This canister enables milling up to 100 g of material with 500 g of balls (diameter of 10 and 6 mm). After sealing, the canister was inserted in a Glenn Mills Turbula T2C shaker-mill which provides a combined rotation on two axes.

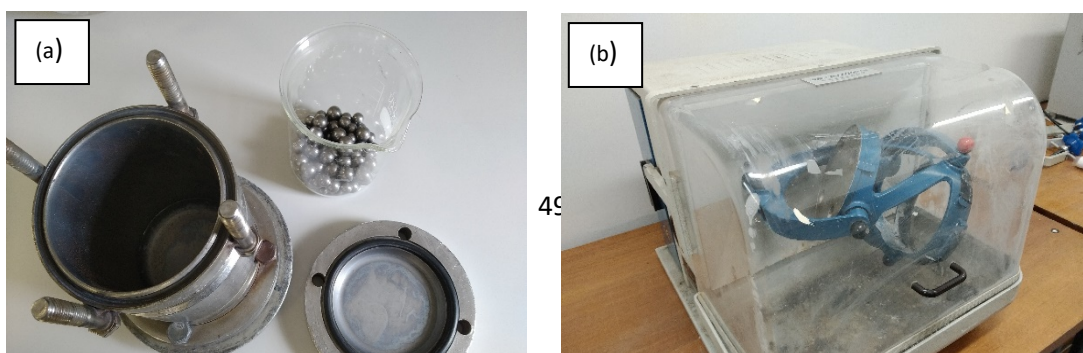


Figure 2-2 (a) A custom made ball milling canister with 650 cm³ internal volume and balls of 7.9 mm and 12.7 mm diameter (b) A Glen Mills Turbula T2C shaker mixer.

2.5. Characterisation

2.5.1. Differential scanning calorimetry

Differential scanning Calorimetry (DSC) initially measures the heat flow required to rise a sample temperature at a constant set rate. i.e. it measures the heat capacity of a sample.¹⁷⁰ It is typically used to investigate physical transformations such as glass transitions, melting or crystallisation. The heat flow required to elevate the temperature of a sample is compared to that of a known reference. The heat flow necessary to rise the empty sample holder (or crucible) temperature is generally used as the reference. A small mass, approximately 10 mg of material, is inserted in the crucible and heated under the same rate as the reference. The difference of electric power required is recorded as a function of time and the integration of the curve results in the heat required for the transition to occur. The procedure to extract the activation energy from tests conducted at different heating rates was developed by Kissinger.¹⁷¹ This energy relates to the energy required to break bonds and overcome repulsion forces that hinder two material to react. It is derived from the reaction rate expression for solid state transformation proposed by Arrhenius:¹⁷²

$$\frac{d\alpha}{dt} = A \cdot e^{-E/RT} \cdot f(\alpha) \quad (\text{eq. 2-1})$$

where

α = the reacted fraction

A = the pre-exponential factor of Arrhenius

E = the activation energy (kJ/mol)

T = the temperature

R = the gas constant (kJ/mol.K)

$f(\alpha)$ = the reaction kinetic model

Under constant heating rate, with $\beta = dT/dt$, eq. 2-1 becomes:

$$\frac{d\alpha}{dT} = \frac{A}{\beta} e^{-E/RT} \cdot f(\alpha) \quad (\text{eq. 2-2})$$

Kissinger showed that at the maximum reaction rate, the derivation over time of the transformed Arrhenius equation is equal to zero, allowing to transform the equation into:

$$\frac{d^2\alpha}{dt^2} = A e^{-\frac{E}{RT}} \cdot f'(\alpha) \frac{d\alpha}{dt} + A \cdot f(\alpha) \cdot \left(\frac{-E}{R}\right) e^{-\frac{E}{RT}} \cdot \left(\frac{-1}{T^2}\right) \cdot \frac{dT}{dt} = 0 \quad (\text{eq. 2-3})$$

or

$$\frac{E\beta}{RT^2} = -A f'(\alpha) e^{-E/RT} \quad (\text{eq. 2-4})$$

Considering the reaction kinetic model as a first order reaction (the reaction rate is directly proportional to the concentration of the reactants), $f'(\alpha)$ is typically equal to - 1. Hence, the equation, eq. 2-4, can be written in the following form:

$$\frac{\beta}{T^2} = \frac{AR}{E} e^{-E/RT} \quad (\text{eq. 2-5})$$

The insertion of logarithms into equation Eq. 2-5, gives:

$$\ln\left(\frac{\beta}{T^2}\right) = \ln\left(\frac{AR}{E}\right) - \frac{E}{RT} \quad (\text{eq. 2-6})$$

Plotting values of $\ln(\beta/T^2)$ as a function of $1/T$, where T relates to the peak onset temperature, results in a Kissinger plot. It gives a straight line for which the slope is equal

to E/R , from which the activation energy is easily extracted. The lower the activation energy, the faster will be the reaction rate.

In the case of a metal hydride, the sample is immersed in a light flow of argon (20 ml/min) to prevent contact with air. The sample remains at a negligible hydrogen partial pressure, therefore, the energy needed for desorption can be obtained at ≈ 0 bar H_2 . It is therefore mostly utilised to comparatively determine the effect of an additive on the activation energy or the reaction rate. The procedure can be applied for hydrogen absorption during cooling. However, the replacement of the argon flow by a hydrogen pressure requires a more specific apparatus, not available during this project. Thus, it is necessary to carry out different procedures to investigate the reaction rate for hydrogen absorption.¹⁷³ A Mettler Toledo[®] TGA/DSC 1 was used to acquire DSC signals. The acquired signal typically resembles the plot presented in Figure 2-3.

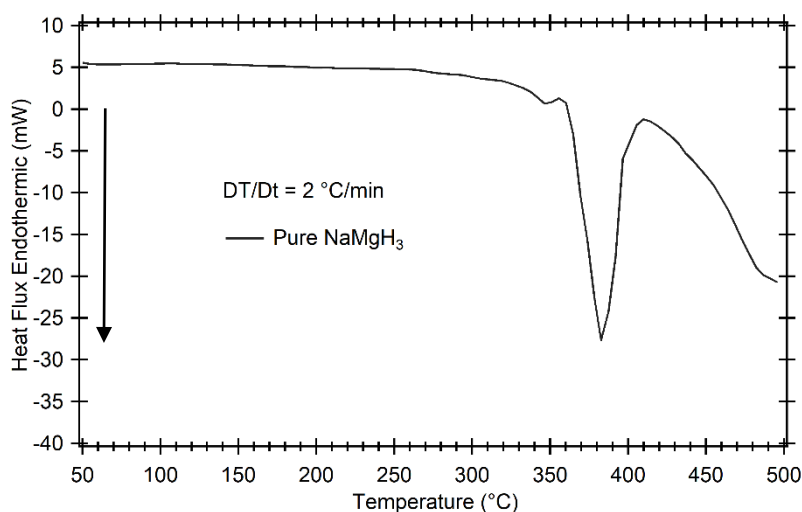


Figure 2-3 - Typical DSC curve showing a peak of additional power required to achieve hydrogen desorption with a heat rate of 2 °C/min.

2.5.2. X-ray powder diffraction

The main use of X-ray powder diffraction is to identify the crystalline compounds present in a sample. An X-ray powder diffractometer collects X-ray beams scattered by the atoms in the crystal structure of the powder under analysis. The detector receives the scattered waves with a relative phase shift and measures intensity related to an angle of incidence.¹⁷⁴ This angle, 2θ , represents the angle between the beam source and the scattering plane. Bragg's law (eq. 2-7) allows the determination of the distance between atomic layers within the crystal structure d_{hkl} :^{175 176}

$$n \lambda = 2d_{hkl} \cdot \sin\theta \quad (\text{eq. 2-7})$$

with

n = an integer

λ = the wavelength of the incident X-ray beam

d_{hkl} = the distance between atomic layers

2θ = the angle of incidence between the incident ray and the scattering planes.

This distance between layers expressed with a set of lattice planes: h , k and l , is also known as the Miller indices, they determine the peaks position on a diffraction profile. Every crystal possesses a specific set of peaks at specific positions and can therefore be identified through this technique. A schematic of the experimental setup is presented in Figure 2-4.

177

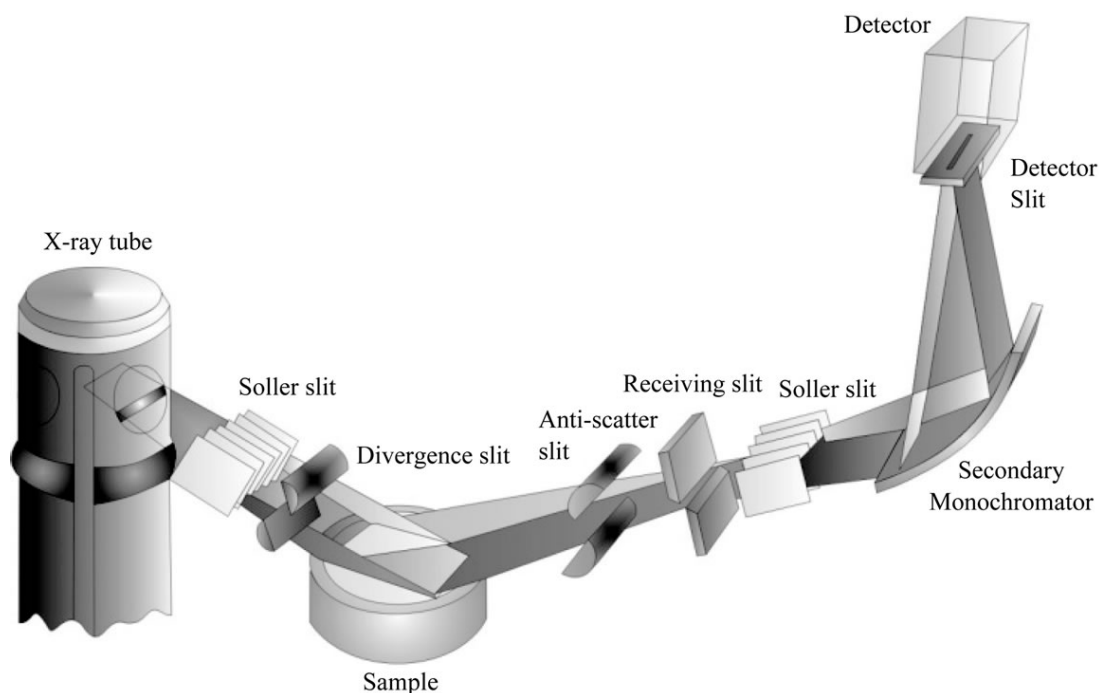


Figure 2-4 - Bragg-Brentano geometry used in XRD.¹⁷⁷

A Bragg-Brentano Bruker D8 Advance X-ray diffractometer was used to perform the experiments with a typical 2θ range of 20° - 80° using 0.02° steps with 0.9 s of count time per steps. A Cu- $K\alpha_{1+2}$ anode tube ($\lambda = 0.1542$ nm) produces the unpolarised radiation beam which impinges on the sample under analysis. A 192 channel LynxEye detector was used to receive the acquired scattered wave intensity. Table 2-2 details the detector parameters used during data acquisition. The samples were loaded under argon atmosphere, onto a custom sample holder made of polymethylmethacrylate, then flattened to prevent any preferential orientations. A hemispherical cap is used to clamp a rubber gasket onto the sample holder to ensure that oxidation of the sample does not occur during data acquisition. The sample holder material induces a broad hump at $2\theta \approx 20^\circ$, therefore each XRD pattern is subtracted by a background plot to analyse the peaks and their intensity originating from the sample only.

Table 2-2 - LynxEye detector parameters used for analysis in TOPAS.

Parameter	Value
Radiation source	Copper
Wavelength (Å)	1.5418 Å
Operating voltage	40 kV
Operating current	40 mA
Detector	Linear PSD (lynxeye)
Monochromator	-
Goniometer radius	250 mm
Source length	12 mm
Sample length	25 mm
Receiving slit length	17 mm
Motorised divergence slit angle	0.3°
Primary Soller slit angle	2.5°
Secondary Soller slit angle	2.5°

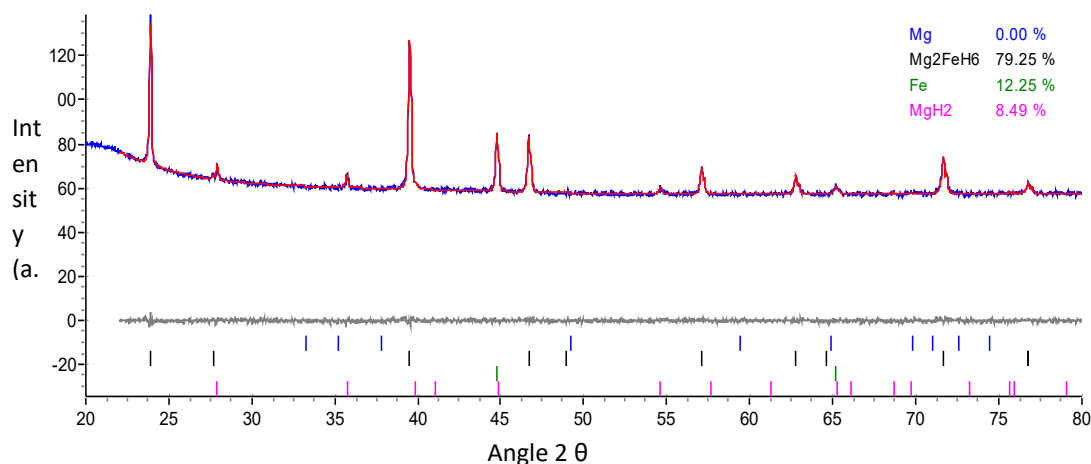


Figure 2-5 –Typical XRD pattern with raw data (blue), Rietveld refinement (red) and the difference curve (grey).

From an XRD profile, as shown Figure 2-5, it is possible to quantitatively determine the elements or compounds present in the sample. This is performed using phase identification software such as EVA[®] (Bruker software) which gathers a library of lattice parameters of a multitude of known phases. When all phases in a sample are identified, they can be analysed quantitatively by means of the Rietveld method.¹⁷⁸ It is a refinement technique which uses the non-linear least squares method to fit a model to the entire XRD profile.¹⁷⁹

It refines the initial intrinsic parameters of each phase, such as lattice parameters, until the calculated values best match the acquired XRD pattern.¹⁸⁰

The software Topas[®] V-5 (Bruker AXS) was used to carry out such a refinement and quantify each phase. This software was typically used to determine the yield of a synthesis method.

2.5.3. Sieverts apparatus

A Sieverts apparatus was used to study gas sorption of a material, by performing pressure composition isotherms as well as sorption kinetics. They can be determined through a manometric technique or thermogravimetric technique.¹⁸¹ The pressure change, in an accurately calibrated volume, has been reported to be more precise than a small mass variation.¹⁸² It allows continuous determination of the transfer of hydrogen between a hydrogen loaded reference volume and the sample. At room temperature, a pressure change in the closed system depicts a number of moles of gas desorbed or absorbed by the material through the ideal gas law:

$$PV = nRT \quad (\text{eq. 2-8})$$

where

P = pressure (Pa)

V = volume (m³)

n = number of moles

T = temperature (K)

R = universal gas constant (8.314 J/(K.mol))

When the conditions of temperature or pressure increase away from an atmospheric reference point, hydrogen gas behaviour cannot be considered ideal (typically when $P > 10$ bar). It is necessary to take into account the compressibility of hydrogen. Noted Z , the compressibility factor, is a dimensionless term that is temperature and pressure dependent. It represents the deviation from the ideal gas law.

$$PV = ZnRT \quad (\text{eq. 2-9})$$

A manometric custom made Sieverts apparatus was used in the Hydrogen Storage Research Group (HSRG) laboratory at Curtin University. It is made of a series of volumes separated by valves connected to a high purity hydrogen gas bottle (Figure 2-6). All tube fittings are made from SS316 and connected with Swagelok® VCR fittings sealed by silver plated gaskets. A Rosemount 3051S pressure transducer with a 0.02 % accuracy and a K-type thermocouple with a 1.5°C accuracy are used to collect pressure and temperature of the apparatus reference volumes.

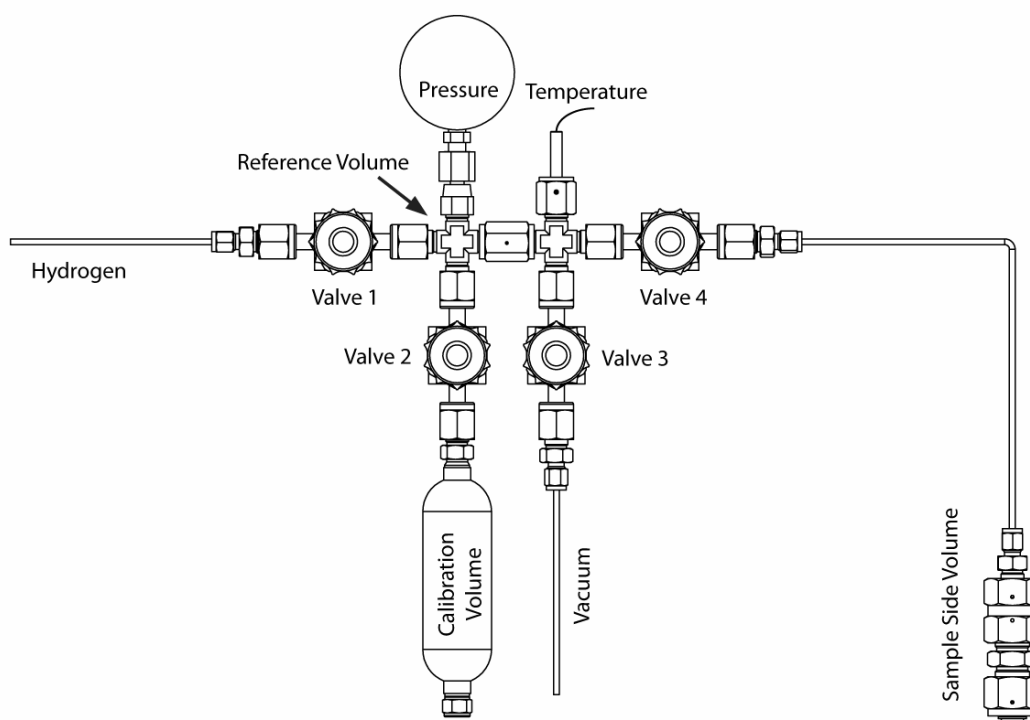


Figure 2-6 - Schematic view of the custom made Sieverts apparatus at the HSRG laboratory. Courtesy of M.Paskevicius.

2.5.3.1. Volume calibrations

The reference volume (V_r) was calibrated with an accuracy of 0.1 cm^3 using an ethanol filled calibration volume. As the sample side volume was placed in a furnace to study high temperature hydrogen sorption, it was partly at ambient temperature and partly at high temperature. It was, therefore, deconvoluted into two different volumes: ambient sample side volume (V_s) and non-ambient sample side volume (V_{sna}).

The ambient sample side volume was calibrated using the following procedure according to Figure 2.6:

Valve 3 and 4 are opened to evacuate the whole system volume for about 5 minutes, then closed. Valve 1 is opened to load the reference volume (V_r) with a known hydrogen pressure (P_r) at a known temperature (T_r), then closed. After 10 minutes, valve 4 is opened to let the hydrogen fill the sample side volume. The system volume is left to stabilise for about 30 minutes until equilibrium pressure (P_e) and temperature (T_e) are reached.

The ambient sample side volume is determined by (eq. 2-10):

$$V_s = V_r \frac{\frac{P_r}{Z_r T_r} - \frac{P_e}{Z_e T_e}}{\frac{P_e}{Z_e T_e}} \quad (\text{eq. 2-10})$$

To calibrate the non-ambient sample side volume (V_{sna}), it was necessary to place it into a furnace and heat it to the desired temperature of experiment (typically 450°C), and then left to stabilise for ≈ 30 minutes. A similar procedure is used to calibrate the ambient sample volume. The non-ambient sample side volume is determined from (eq. 2-11):

$$V_{sna} = \frac{V_r \left(\frac{P_r}{Z_r T_r} - \frac{P_e}{Z_e T_e} \right) - V_s \left(\frac{P_e}{Z_e T_e} \right)}{\frac{P_e}{Z_{ena} T_{ena}} - \frac{P_e}{Z_e T_e}} \quad (\text{eq. 2-11})$$

where

T_{ena} = the non-ambient temperature of the non-ambient sample volume and

Z_{ena} = the hydrogen compressibility at the non-ambient temperature.

2.5.3.2. Pressure composition Isotherms (PCI or PCT)

Pressure composition isotherm experiments give important knowledge on the thermodynamics of a material. Based on the Blach and Gray method, it allows the determination of the equilibrium pressure at which a sample absorbs or desorbs hydrogen at a set temperature.¹⁸³ For absorption, a step by step increase of the system pressure reveals a decrease in pressure as the sample is absorbing gas. Since all volumes are known in the system a change in pressure can relate to the number of moles of gas absorbed or desorbed by the sample.

At each step, the number of moles of hydrogen sorbed by the sample is given by:

$$n_{sor} = n_r + n_s - n_e \quad (\text{eq. 2-12})$$

where

$$n_r = \frac{P_r \cdot V_r}{Z_r \cdot R \cdot T_r} \quad (\text{eq. 2-13})$$

$$n_s = \frac{P_s(V_s - V_{na})}{Z_s RT_s} + \frac{P_s(V_{na} - V_{sample})}{Z_{na} RT_{na}} \quad (\text{eq. 2-14})$$

$$n_e = \frac{P_e V_r}{Z_e RT_e} + \frac{P_e(V_s - V_{na})}{Z_e RT_e} + \frac{P_e(V_{na} - V_{sample})}{Z_{e,na} RT_{na}} \quad (\text{eq. 2-15})$$

where:

n_r = the initial number of moles in the reference side volume

n_s = the initial number of moles in the sample side volume

n_e = the number moles at equilibrium

R = the universal gas constant

P_r = the initial reference side volume pressure

P_s = the initial sample side volume pressure

P_e = the final equilibrium volume pressure

V_r = the reference side volume

V_s = the sample side volume

V_{na} = the sample side volume at non-ambient temperature

V_{sample} = the solid volume of sample based on sample mass and density

T_r = the initial reference side volume temperature (K)
 T_s = the initial sample side volume temperature (K)
 T_e = the equilibrium temperature (K)
 T_{na} = the non-ambient temperature (K)
 Z_r = the compressibility value associated with P_r and T_r
 Z_s = the compressibility value associated with P_s and T_s
 Z_e = the compressibility value associated with P_e and T_e
 Z_{na} = the compressibility value associated with V_{na} and T_{na}
 Z_{ena} = the compressibility value associated with P_e and T_{na}

As the sample is precisely weighed, it is simple to calculate the mass of hydrogen uptake per mass of material with:

$$wt\% = \frac{n_{sor} \cdot M_{H_2}}{m_{sample}} \quad (\text{eq. 2-16})$$

where

n_{sor} = the number of moles calculated previously

M_{H_2} = the molar mass of hydrogen gas

m_{sample} = the mass of sample in the non-ambient sample side volume

The number of hydrogen gas moles absorbed by the sample can be plotted as a function of hydrogen pressure in the system and typically resembles

Figure 2-7, (on the left) in which three PCTs are drawn (for 0 °C, 25 °C and 100 °C). The Figure 2-7 presents, on the right, the associated van 't Hoff plot that represents the equilibrium pressure (typically the pressure reached for half the hydrogen capacity of the sample) as a function of its corresponding inverse equilibrium temperature. This plot is a linear fit of each unique data point retrieved from each PCT.

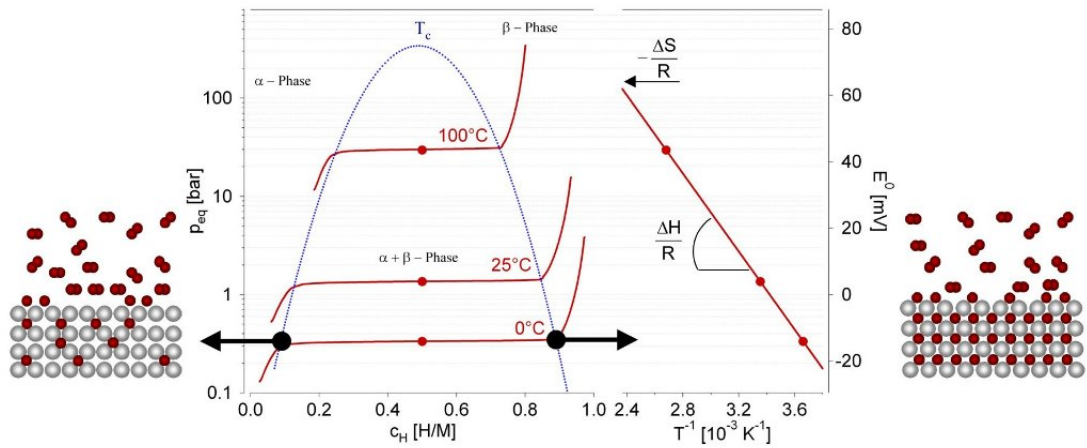


Figure 2-7 – Typical PCT for the hydrogen absorption in a typical intermetallic compound is shown on the left hand side. The construction of the van 't Hoff plot is shown on the right hand side. ¹⁸⁴

Based on the van 't Hoff equation under standard conditions, the linear fit can be related to the variation of enthalpy as follows:¹⁸⁵

$$\frac{d(\ln \frac{P_{eq}}{P_0})}{dT} = \frac{\Delta H}{RT^2} \quad (\text{eq. 2-17})$$

where

P_{eq} = the equilibrium pressure (bar)

ΔH = the variation of enthalpy (kJ/mol H₂)

R = the gas constant related to Boltzmann constant (J/K.mol)

T = the temperature of reaction (K).

Which is developed from the definition of Gibbs free energy when a system is isotherm:¹⁸⁶

$$\Delta G = -RT \cdot \ln \left(\frac{P_{eq}}{P_0} \right) = \Delta H - T\Delta S \quad (\text{eq. 2-18})$$

to

$$\ln \left(\frac{P_{eq}}{P_0} \right) = -\frac{\Delta H}{RT} + \frac{\Delta S}{R} \quad (\text{eq. 2-19})$$

where

ΔS = the variation of entropy (J/mol H₂.K)

$P_0 = 1$ bar

It is possible to calculate the variation of enthalpy and entropy of the hydrogen sorption reaction from the plot $\ln(P_{eq}/P_0)$ versus $1/T$. The slope allows to calculate the enthalpy of reaction:

$$\text{slope} = - \frac{\Delta H}{R} \quad (\text{eq. 2-20})$$

and the y-axis intercept, when the inverse temperature is null, allows for the calculation of the change in entropy:

$$\text{intercept} = \frac{\Delta S}{R} \quad (\text{eq. 2-21})$$

2.5.3.3. Small scale gas cycling

When the sample is heated in a furnace, it is possible to use the Sieverts apparatus to induce hydrogen desorption and absorption by cycling the sample at temperature (between a low minimum temperature and a high temperature), if the thermodynamics and the hydrogen capacity of a hydrogenated sample are known. The hydrogen equilibrium pressure of the material, for the minimum operating temperature, is loaded into the whole volume and the temperature is increased to a higher temperature level that is typically few tens of degree higher than the minimum operating temperature. The temperature increase induces a hydrogen desorption as long as the equilibrium pressure corresponding to the high temperature level is not reached. The versatility of the custom made Sieverts apparatus allows the reference volume to be adapted so that a full dehydrogenation can be attained.

After the sample has fully dehydrogenated and temperature and pressure are stabilised, the furnace can be set to the lower temperature. The sample may absorb the hydrogen previously released. The repetition of these temperature variations is termed temperature cycling. It allows for the investigation of the capacity of the material to absorb and desorb

hydrogen several times. This capacity, also known as the reversibility, is a crucial parameter for a material to be used for thermal storage thousands of times.¹⁸⁷ Figure 2-8 presents a typical temperature cycling experiment with the resulting hydrogen system pressure evolution due to desorption and absorption.

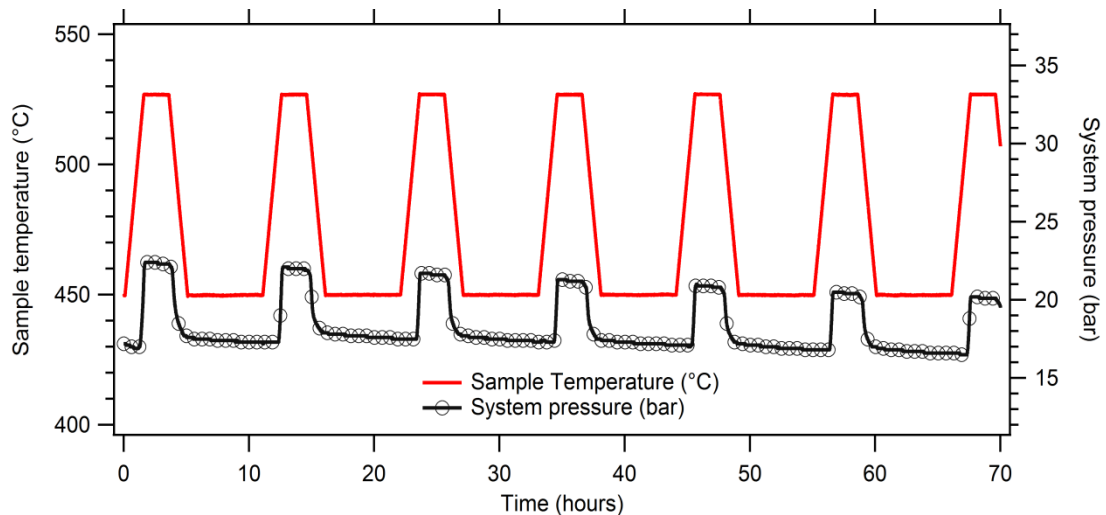


Figure 2-8 - Temperature cycling example between 450 °C and 530 °C and the associated pressure change in the Sieverts apparatus volume.

2.5.3.4. Absorption kinetics of hydrogen

The versatility of a Sieverts apparatus also allows one to conduct absorption kinetic studies at operating temperatures. As for thermal energy storage in metal hydrides, the absorption kinetics directly relates to the rate of thermal power generation. The Sieverts apparatus is valuable to investigate this reaction rate and the eventual limitations from the material. It is based on the same principle described in the pressure composition isotherm section, but the sample mass is calculated so that the hydrogen contained in the system volume can be absorbed with a minimum pressure change (< 1bar) to be able to consider the system isobaric. From the number of hydrogen moles absorbed over time, it is possible to plot a comparative reacted fraction at a given operating temperature, as shown for example in Figure 2-9.

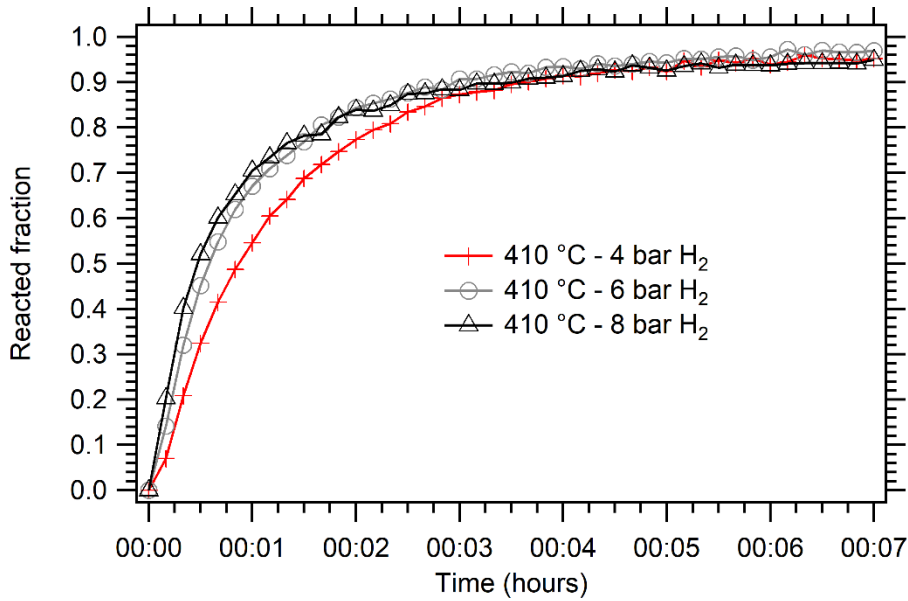


Figure 2-9 - Absorption kinetics for NaMgH₃ at 410 °C and different pressures.

2.5.4. Transient plane source for thermal conductivity

The transient plane source (TPS) method is a common technique to measure thermal properties of a material. Developed by Gustaffson, a sensor embedded in the sample is powered to generate heat that is diffused through the tested material.¹⁸⁸ The temperature increase in the sensor changes its resistivity and the thermal conductivity of the sample can be estimated by monitoring of the sensor's electrical resistance over a specific time function from the following expressions (eq. 22-23-24).^{189,190} Made of a spiral reinforced by an electrically insulating layer on each side, the sensor is clamped between two sample pellets identical in diameter, height and weight. The diameter of the pellets must at least double the diameter of the sensor to consider the sample as radially infinite.

$$R(t) = R_0 \{1 + \psi(\Delta T_i + \Delta T(\tau))\} \quad (\text{eq. 2-22})$$

And

$$\tau = \sqrt{\frac{t_0 \alpha}{r^2}} \quad (\text{eq. 2-23})$$

where

t = the relative time

R_0 = the resistance of the sensor at $t = 0$.

τ = the constant time

ΔT_i = the temperature difference across the sensor

$\Delta T(\tau)$ = the temperature difference of the sample

ψ = the temperature coefficient of resistivity (1/K)

a = the thermal diffusivity of the sample (m^2/s)

r = the radius of the sensor (m)

the solution of the thermal conductivity equation is: ¹⁹⁰

$$\Delta T(\tau) = \frac{P_0}{\pi^2 \cdot r \cdot \lambda} E(\tau) \quad (\text{eq. 2-24})$$

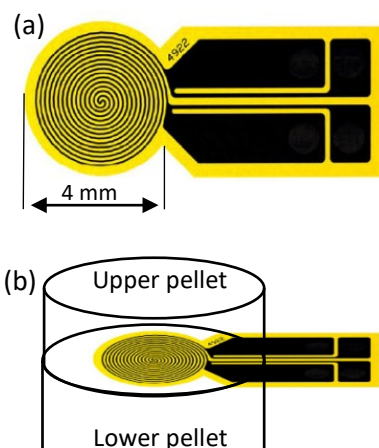
where

P_0 = the power output of the sensor (W)

λ = the thermal conductivity of the sample ($\text{W m}^{-1} \text{K}^{-1}$)

$E(\tau)$ = the dimensionless time function

For the results presented in this thesis, a TPS 500S from Hot Disk was used with a 4 mm radius nickel coil (Kapton insulated) sensor and a probing depth set to 4 mm. The sensor was calibrated using a stainless steel reference. The samples, in powder form, were pelletised using an 8 mm diameter die, pressed under 950 MPa. Each pellet mass was approximately 1.4 g. Figure 2-10 presents a schematic and a picture of the apparatus placed in an argon glovebox.



Sensor

Pellets

2.6. Differential pressure manometer

A Rosemount™ 3051 Coplanar™ Pressure transmitter was used to monitor the differential pressure across a diaphragm (laser pierced from Lenox®) of a set diameter between 100 μm and 500 μm, produced by a hydrogen flow. The size of these diaphragms were determined using equation 2-27, an estimation of the gas flow expected and the measurement range of the manometer. This device was employed to calculate the hydrogen gas flow during absorption and desorption for large-scale experiments. The monitoring of differential pressure, ΔP , presents the advantage of a non-invasive technique achieving high repeatability and accuracy.

It is based on Bernoulli's equation on energy conservation, and refers to Figure 2-11:¹⁹¹

$$P_1 + \frac{1}{2}\rho_1 v_1^2 = P_2 + \frac{1}{2}\rho_2 v_2^2 = \text{constant} \quad (\text{eq. 2-25})$$

Considering a negligible density variation between ρ_1 and ρ_2 , the differential pressure can be written as:

$$P_1 - P_2 = \frac{\rho}{2} (v_1^2 - v_2^2) = \Delta P \quad (\text{eq. 2-26})$$

where

P_1 and P_2 = Pressure before and after diaphragm

ρ_1 and ρ_2 = Density of fluid

v_1 and v_2 = velocity of fluid

Replacing the velocity term by geometric measures (i.e. D = fluid stream diameter before and after the diaphragm) allows the fluid mass flow q_m to be introduced as:

$$v^2 = \frac{16 \cdot q_m^2}{D^4 \pi^2 \rho^2} \quad (\text{eq. 2-27})$$

Gives

$$q_m^2 = \frac{1}{\left(1 - \frac{D_2^4}{D_1^4}\right)} \cdot \frac{\pi^4}{16} \cdot D_2^4 \cdot 2\Delta P \cdot \rho \quad (\text{eq. 2-28})$$

As the diameter D_2 , the fluid stream diameter after the diaphragm is not known, Reader-Harris Gallagher proposed to introduce a discharge coefficient C relating D_2 to d (the diaphragm diameter) and ϵ the expansion coefficient for the compressible fluid (details in appendix).¹⁹² Since the discharge and expansion coefficient only depends on intrinsic fluid properties such as volumetric mass, temperature and viscosity. The calculation of the fluid mass flow becomes a function of these properties at operating conditions and the differential pressure, given by:

$$q_m = \frac{C}{\sqrt{1-\beta^4}} \cdot \epsilon \cdot \frac{\pi}{4} \cdot d^2 \cdot \sqrt{2\Delta P \cdot \rho_1} \quad (\text{eq. 2-29})$$

Where $\beta = d/D$

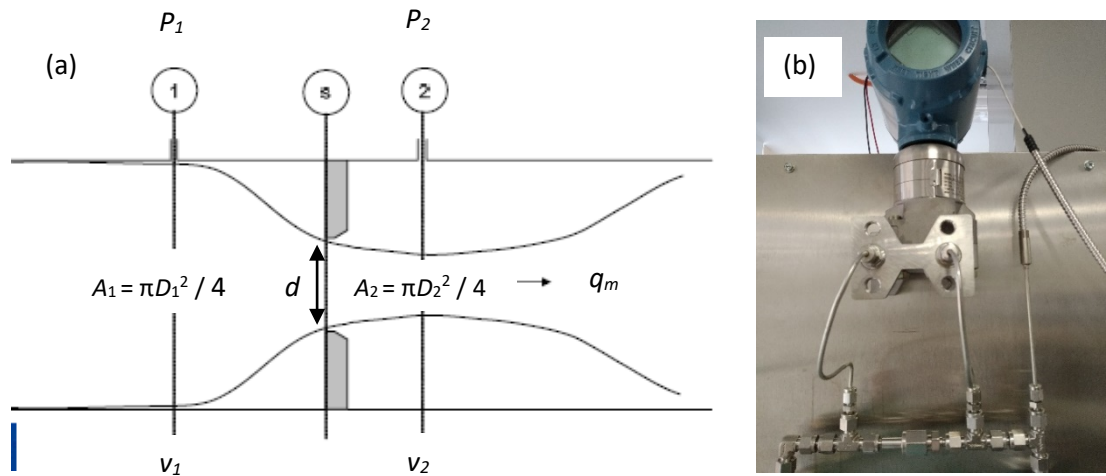


Figure 2-11 - (a) Schematic gathering geometric constant used to determine fluid flow through a diaphragm and (b) a picture of mounted Rosemount 3051, differential manometer.

2.7. Experimental setup for metal hydride coupling

This section presents the first of three experimental setups investigated during this research project. The results and findings from this first setup are detailed in Chapter 4 of this manuscript, which reports the investigation of a high temperature metal hydride (HTMH) coupled with a low temperature metal hydride (LTMH), which acts as a hydrogen store. The apparatus designed for this investigation consisted of two separate metal hydride vessels linked by a 0.31 cm outer diameter stainless steel tubing to transport the gas. A schematic is shown in Figure 2-12. The line was equipped with a pressure transducer (Rosemount 3051 SMV), which was able to monitor the system pressure as well as a differential pressure across a 100 μm diaphragm. As described in section 2.6, this pressure differential allows one to determine the instant hydrogen mass flow. 40.7 g of high temperature metal hydride (HTMH), a ball milled 2:1 molar ratio mixture of Mg and Fe, was encapsulated in a 2.54 cm outer diameter 316 stainless steel cylinder (0.2 cm of wall thickness). The 20 cm long vessel was equipped with a thermocouple embedded in the powder and another mounted on the outer side of the cylinder. This allowed for the observation of temperature excursions when cycling. The entire HTMH reactor was fixed inside an insulated furnace to provide isothermal heating, therefore the entire powder bed was assumed isothermal. The LTMH reactor filled with 85.5 g of titanium manganese alloy (alloy 5800) was 7 cm long and 2.54 cm in external diameter. It was placed into a stirred water bath, which allowed for the minimisation of temperature excursions during hydrogen uptake and release. This vessel was equipped with one embedded thermocouple in the centre. A 0.6 cm diameter porous rod made of stainless steel (pore size = 1 μm , SIKA-R IS, GKN Sinter Metals Filters GmbH) was incorporated in the centre of both vessels to guarantee even hydrogen diffusion through the bed. The system also comprised of a volume of gas, called free gas volume, which was determined to be 93 ± 0.5 ml using an external calibrated volume.

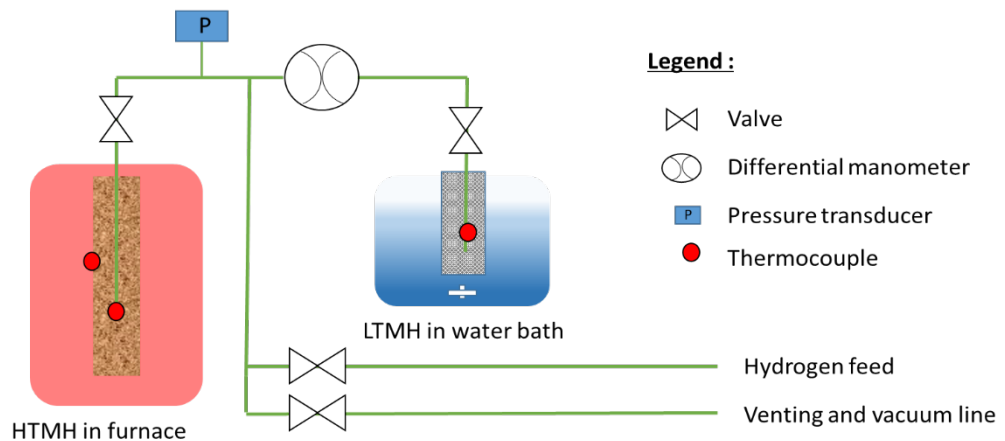


Figure 2-12 - Schematic of the experimental set up with the HTMH in a furnace (left) and LTMH in agitated water bath (right).

2.8. Design and setup of high temperature thermal energy storage prototype (TES150)

To investigate the feasibility of a NaMgH_3 based hydride for high temperature thermal energy storage, the developed Reactor Mix (RM, $\text{NaH/Mg/0.02 TiB}_2/ 20 \text{ wt\% ENG}$) presented in Section 3.3.3.1 was inserted into a custom made reactor. Investigations on this reactor are presented in Chapter 5. The hydride synthesis was performed following the procedure described in section 3.3.3.1.2: six hours at $380 \text{ }^\circ\text{C}$ under 20 bar of hydrogen.

Two stainless steel tubes, 40 cm in length and 2.54 cm external diameter were used to contain 150 g of Reactor Mix. The powder was manually compacted while poured inside the reactor. The tubes were mounted vertically, in close contact with each other and their ends were sealed with Swagelok[®] tube fittings. The empty mass of the reactor was measured to be $\approx 3 \text{ kg}$. Both tubes were encapsulated in a total of 6 ceramic bricks to provide thermal insulation. These bricks supplied by Bellis[®] were 5 cm thick and provided a low thermal conductivity of 0.65 W/m.K . A 5 m thermo-regulated heating tape of 1500 W was coiled around the bricks to further limit heat losses by acting as a “hot background” (HB). For additional insulation, the heating tape was covered by an approximately 5 cm thick layer of aluminosilicate wool with a thermal conductivity of 0.1 W/m.K (Insulfrax LTX blanket).

2.8.1. Heat transfer fluid line

The purpose of the heat transfer fluid (HTF) line is to transfer the high temperature thermal energy from a source, which can be from concentrated solar power (CSP) or waste heat, to be stored into the metal hydride reactor. This line also recovers the heat stored to transfer it to the user end, i.e. a thermo-electric generator or simply a heat exchanger. As water has previously been shown to be a convenient HTF, it was preferred in this setup.⁹⁸

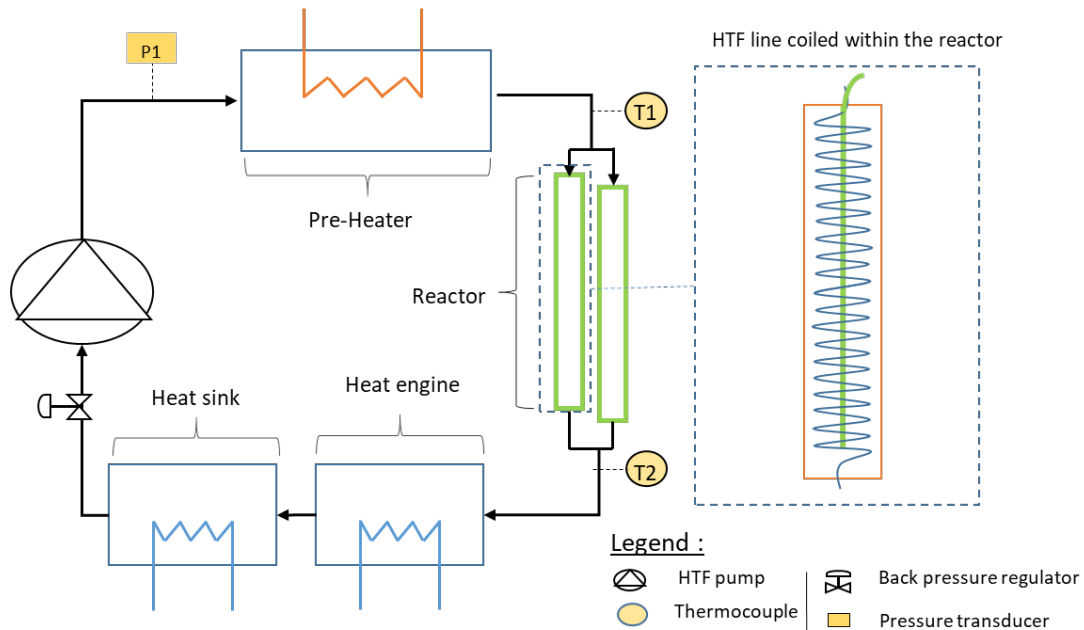


Figure 2-13 - Schematic of the heat transfer line in the system with a detail of the reactor's interior.

A Gilson water pump was used to provide pressurised water at a maximum flow rate of 8 ml/min. A back pressure regulator was used to pressurise the water to 140 bar and maintain a superheated vapour state throughout the circuit, As shown by the “operational range” in Figure 2-14.

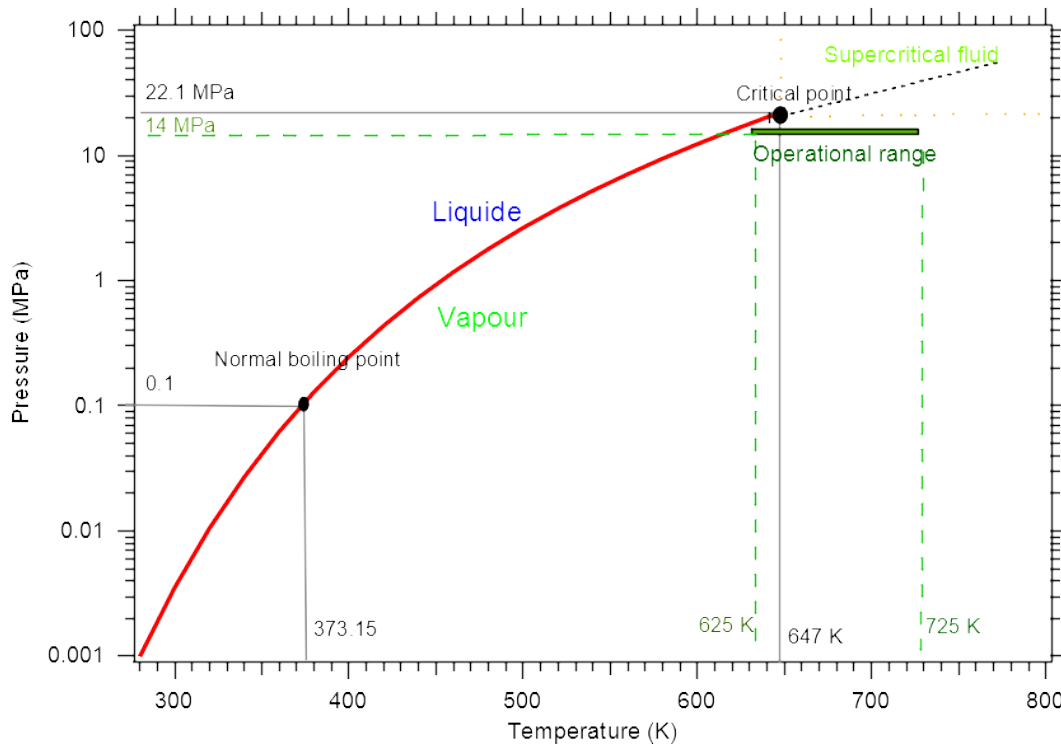


Figure 2-14. Water phase diagram.²¹⁷

As presented in the schematic **Error! Reference source not found.**, the water flowed through a pre-heater to provide high temperature thermal energy to the subsequent thermal battery. The heat was then used to power a small Stirling engine before being withdrawn by a heat sink comprised of aluminium fins to cool down the HTF and avoid damage to the backpressure regulator and the pump.

To simulate the heat source, a pre-heater device was designed and built. It was made of 0.6 cm external diameter, 80 cm length stainless steel tube. As shown in Figure 2-15, the tube was formed into an elbow shape and encapsulated by two 20 cm square brass plates that weighed approximately 1.5 kg, which provided thermal mass to avoid temperature fluctuations. A heating tape of 1500 W was wrapped around the HTF pipe and equipped with a K-type thermocouple to perform thermo-regulation of the thermal energy storage inlet. The heat exchanger was encapsulated in the previously mentioned aluminosilicate wool for thermal insulation.



Figure 2-15 - Picture of the custom made pre-heater with the stainless steel tube, the brass plate and heat tape wrapped around.

The HTF line external diameter was reduced to 0.31 cm to enter the thermal battery, that line was then coiled as shown in Figure 2-16. This heat transfer solution was shown to be efficiently transferring thermal energy between the HTF and the powder bed, providing enhanced surface exchange and diminishing thermal resistance compared to a simple straight tube.⁹⁸ However, this solution has limited space for the storage material and also caused many technical challenges during construction, as it multiplies the need for specific fittings and the associated potential hydrogen leakage points.



Figure 2-16 - The heat transfer coil which was similarly embedded in both reactors.

2.8.2. Hydrogen manifold

The hydrogen manifold was designed according to the mass of NaMgH_3 and its expected hydrogen capacity. As will be shown in section 3.3.2.2.3, the reactor mix offered 2.6 wt% of

hydrogen capacity, which results in a total hydrogen mass of 3.9 grams expected to flow from the 150 g thermal energy storage reactor. As presented in Figure 2-17, to store this hydrogen, a G-type gas bottle, providing 50 standard litres of storage volume, equipped with a refilling pin was connected to both reactor cylinders in parallel. This volume was chosen so that for an operating pressure around 5 bar H₂, the pressure variations induced by the uptake and release of 3.9 grams of hydrogen wouldn't exceed 1 bar. The manifold was made of 0.31 cm in external diameter Swagelok® tubes and fittings. Each reactor was equipped with an isolating valve to avoid air or moisture contamination during assembly. A hydrogen porous rod (pore size = 1 µm, SIKA-R IS, GKN Sinter Metals Filters GmbH) was placed in the centre of each cylinder to ensure a homogenous gas diffusion through the entire cylinder's height. A Rosemount® 3051S manometer was inserted between the metal hydride reactor and the gas storage tank to monitor system gas pressure and differential pressure caused by the hydrogen flow, across a 1 µm diaphragm.

Additionally, as shown in Figure 2-17, three K-type thermocouples (0.2 mm diameter) were embedded in the powder within one of the reactor cylinders to monitor the axial temperature gradient, while two others were placed on the external skin.

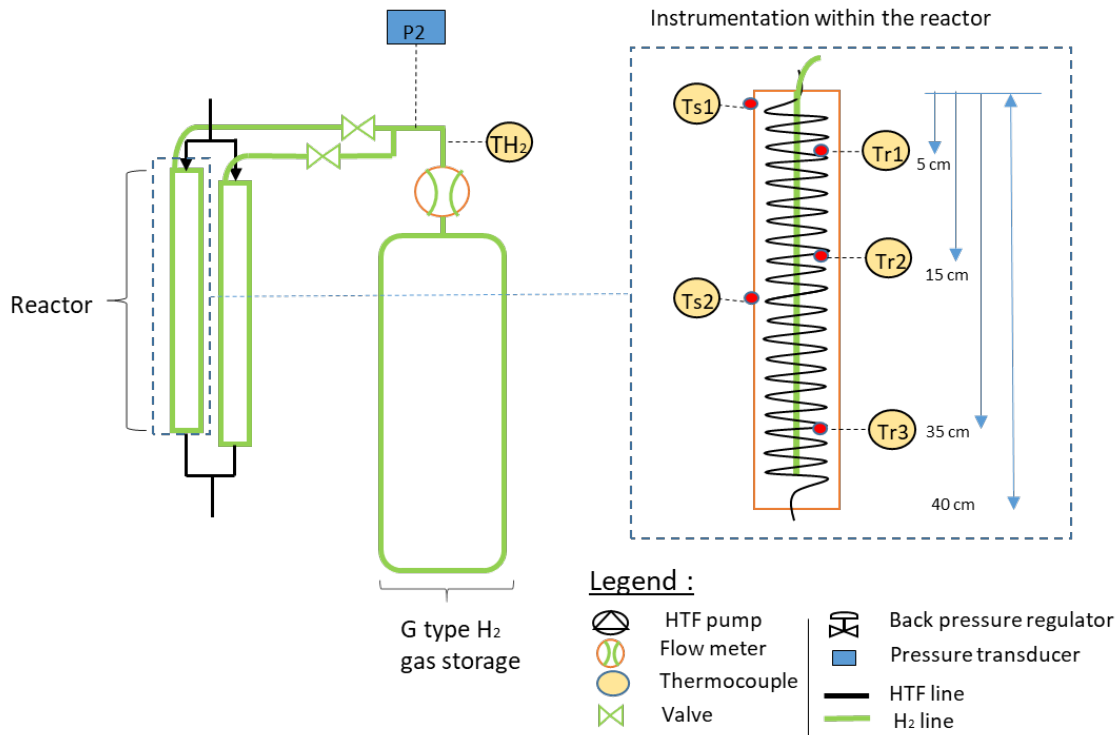


Figure 2-17 - Schematic view of the hydrogen gas line set up with instrumentation.

2.9. Design and setup of high temperature thermal energy storage prototype (TES900)

A custom-made apparatus (aka “Red Sparrow”, Figure 2-18) was specifically built to study thermal storage materials on a larger scale (up to 2 kg of material) and approach the autonomous operating conditions of an industrial scale prototype.

It incorporates a heat transfer fluid circulation system, with a heat recovery system and pre-heater device, a thermal energy storage material reactor, a furnace, a hydrogen compressor, gas bottle, and a hydrogen gas circuit automated using LabVIEW[®] software.

The apparatus was designed to simulate an industrial scale thermal energy storage battery using metal hydrides as a heat storing media. In essence, a pressurised heat transfer fluid was heated, then passed through a heat exchanger embedded in the reactor that hosts the thermal storage material. This delivers thermal energy to the battery.

A gas manifold was attached to the reactor to provide hydrogen gas to the inside of the reactor and allow chemical reactions (gas sorption) to occur. This circuit was connected to a G-size gas bottle that stores the amount of gas required for the experiment (≈ 50 L at standard temperature and pressure conditions); the whole system was therefore isolated, forming a closed loop. The developed concept has the potential to be implemented in a

remote area. A pneumatic compressor was used to fill the gas bottle up to a maximum pressure of 150 bar, enabling a large quantity of gas to be stored for the experiment (up to 600 g H₂). The following sections describe the different components, as well as the whole design and setup. Further details are supplied when necessary to provide the reader with explanations for the chosen design.

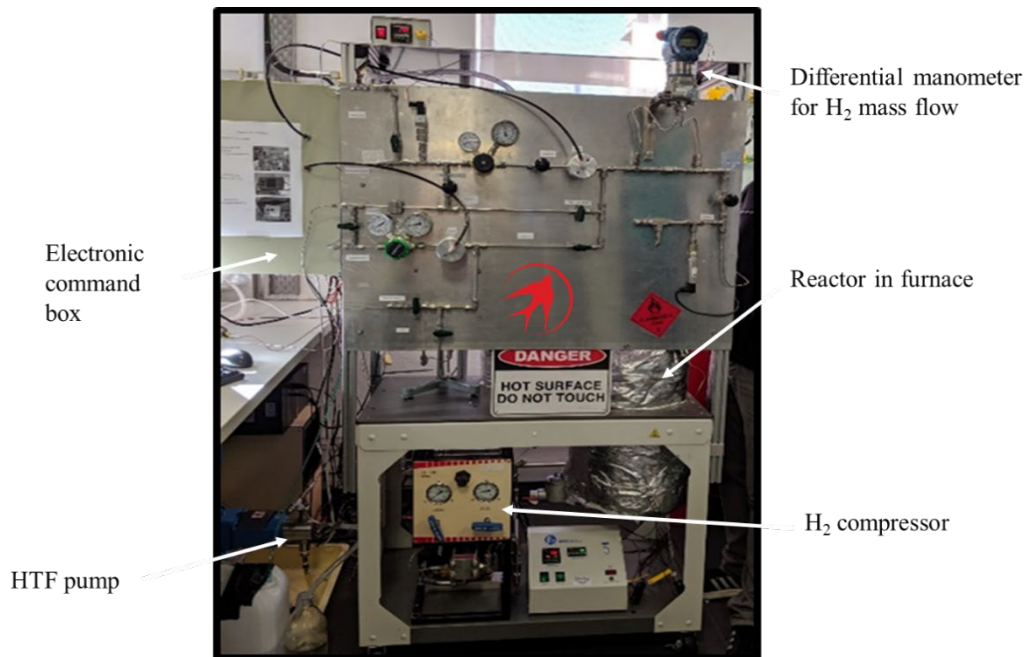


Figure 2-18 - Picture of the "Red Sparrow" apparatus built to perform automated tests of thermochemical batteries.

2.9.1. Heat transfer fluid circuit

The heat transfer fluid (HTF) circuit is a crucial aspect of the high temperature thermal battery as it distributes the thermal energy, to be stored and collected when required. The HTF has to provide sufficient power to maintain the reactor at a high temperature level (between 400 °C and 600 °C), supply thermal energy to be stored by inducing hydrogen desorption and retrieve that energy when generated by the exothermic hydrogen absorption. Figure 2-19 illustrates a schematic of the entire heat transfer fluid loop; a metering pump initiates a fluid flow (milliQ water) that enters a pre-heater to elevate the temperature up to 600 °C before entering the thermal battery. A back pressure regulator maintains the HTF at a pressure of 200 bar to preserve a substantial fluid density between 400 and 600 °C. The HTF outlet was connected to an active heat sink that dropped the fluid

temperature below 80 °C to protect the HTF pump head that is designed to handle fluid temperatures up to 80 °C. Once the HTF has been cooled and depressurised, a flow meter was mounted in the circuit to provide HTF flow measurement that allowed the determination of the thermal energy and power stored. The HTF then flows back into a reservoir to be pumped again. Each component is further detailed in the following sections.

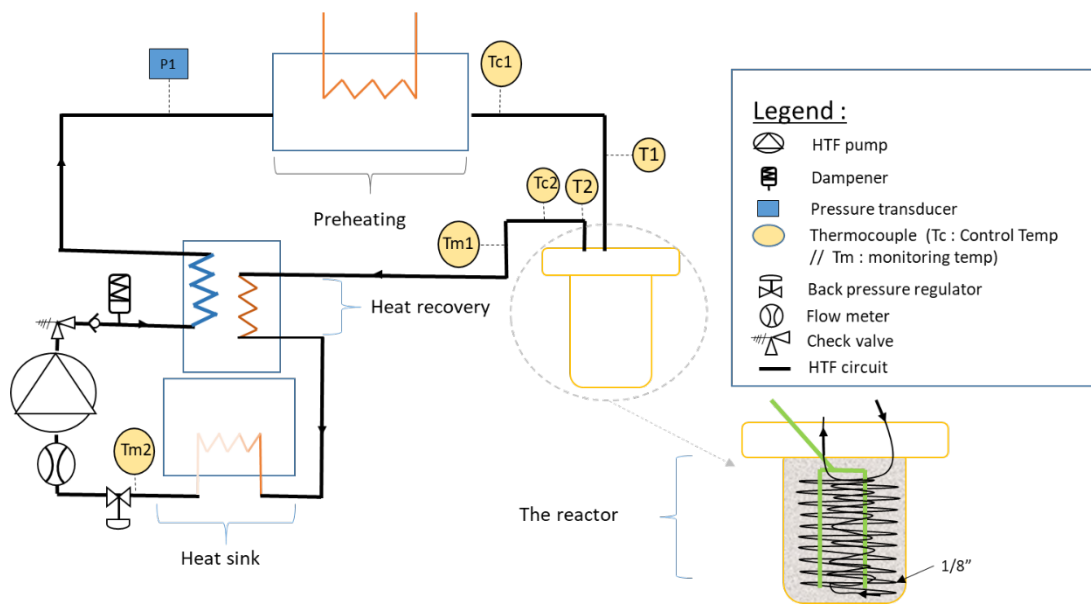


Figure 2-19 - Schematic of the overall HTF circuit.

2.9.1.1. Fluid pump

The fluid pump allows the heat transfer fluid to flow through the high temperature thermal battery and charge or discharge the thermal energy stored. The pump is a “Unit LEWA Metering Pump Type LDB1 high pressure pump”. Its specifications allow for a HTF pressurisation up to 400 bar at 80 °C, with an adjustable flow from 0 to 150 mL/min. A digital manometer was connected to the pump outlet to monitor the pressure in the circuit. A check valve is also mounted for safety, providing a possible HTF release path if the pressure builds up to a set level, in this case, 300 bar. A rotary Vernier allows adjustment of the volume of the compression chamber mechanically, hence changing the HTF flow. Figure 2-20 displays a picture of the equipped HTF pump.



Figure 2-20 - Picture of the equipped Lewa® metering pump with digital manometer and pressure relief valve.

2.9.1.2. Dampener

As the HTF pump periodically delivers a specific fluid volume, the HTF pressure can fluctuate substantially, making it difficult to maintain a constant fluid flow regime and cause damage to the tubing and fittings. To temper the hydraulic shock, a dampener (Pipeguard®, PiG-TW/0.1Lt/B44x75) loaded with 200 bar of nitrogen was mounted near the pump outlet, as shown in Figure 2-19. This provided a much more uniform HTF pressure.

2.9.1.3. Pre-heater

A pre-heater was used to raise the heat transfer fluid to a set temperature level of up to 600 °C before entering the reactor. It was made of 12 m of stainless tube SS316 with an outer diameter 0.31 cm. As pictured in Figure 2-21, the tube was coiled around a 7.5 cm diameter steel pipe (Figure 2-21 (a-c)) and coated in thermally conductive paste (Figure 2-21(d), Thermon®). 3.75 kW heating tapes (STH052-120, Omega®) were then wrapped around the coil. A thickness of ≈ 10 cm of insulating aluminosilicate wool ensured the 0.05 cm thin steel outer jacket would not reach more than 100 °C and therefore diminished heat losses.

A 'command' thermocouple was enclosed in the thermal paste to provide information to the proportional–integral–derivative (PID) regulator E5CN-H (Omron®). This allowed the programming of the temperature level, heating rate, and soaking time of the heat transfer fluid.

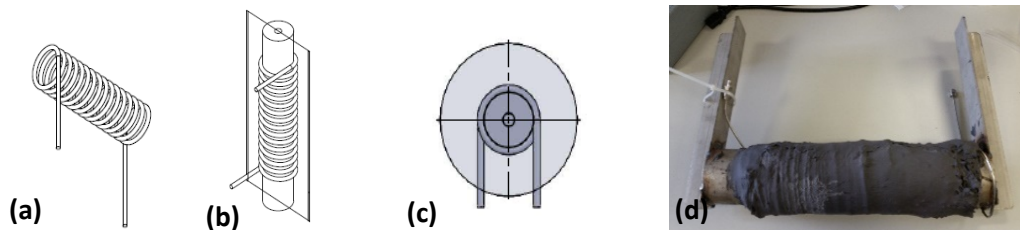


Figure 2-21 - Schematic and picture of (a) the tubing, (b, and c) coiled around a steel pipe, and (d) embedded in high temperature heat transfer paste.

2.9.1.4. The reactor heat transfer fluid line

2.9.1.4.1. Hydride reactor TES 1500

The first reactor was supplied by Parr®. This reactor was manufactured from 35 kg of stainless steel, with dimensions of 28 cm high by 9 cm of internal diameter, with a total volume of 1.8 litres for the HTMH (Figure 2-22 (a)).

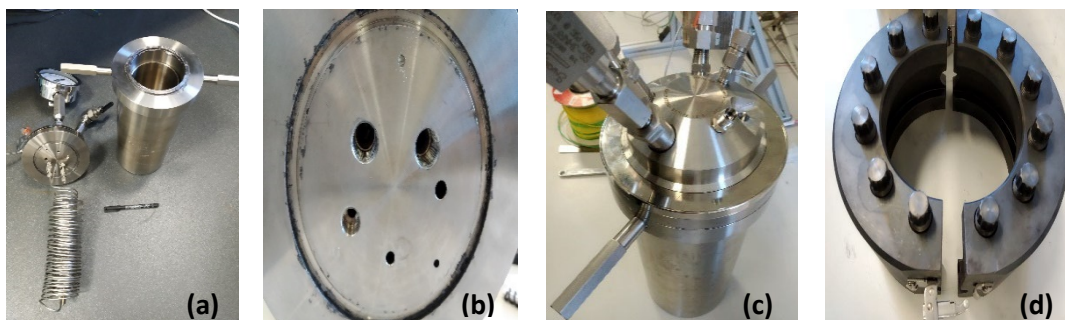


Figure 2-22 - Pictures of the Parr reactor: (a) the bottom and cap equipped the HTF coil, (b) the cap's different connections, (c) the whole reactor, and (d) the collar that closes the reactor tight.

The reactor head (Figure 2-22 (b, c)) was fitted with a Hydrogen port (inlet/outlet), a digital manometer, a rupture disk (rated to 150 bar) and two ports for heat transfer fluid circulation (inlet and outlet). Two additional ports allowed insertion of thermocouples to

monitor the temperature inside the reactor during thermal energy charge and discharge. The heat exchanger embedded inside the reactor was made of two concentric coils using 1/8" stainless steel 316 tubing. In this design, the coil measured 12 m in length. The tightening of the bolts (Figure 2-22 (d)) to 50 Nm allowed the crown to compress a graphite gasket between the head and the reactor and ensured a hydrogen leak tight closure. Unfortunately, despite several attempts, it wasn't possible to operate this Parr[®] reactor at 400 °C without major hydrogen leaks. The material of the cap was a "SA182 -F316" stainless steel, that had a slightly different composition from the SS316 of the tube fittings. A micrometric thermal expansion difference between the head fittings and the cap may have been the cause of hydrogen leakages upon the reactor cooling. As a consequence, this design had to be discarded, and a custom reactor was designed and built. A detailed description is given in the following section.

2.9.1.4.2. Hydride reactor TES 900

The custom-made reactor (TES900) was constructed of eight 28 cm long, 316 stainless steel tubes sealed by tube fittings (Swagelok[®]). The internal diameter was 2.11 cm, offering a total volume of ≈ 0.8 L. A total of 900 g of Mg_2FeH_6 was poured into this volume. In the centre of each tube, a 0.1 cm thick, 2 cm wide and 27 cm long iron sheet was inserted to promote hydrogen diffusion throughout the whole reactor length. The configuration of the eight tubes formed three lines of 3, 2 and 3 tubes, respectively (Figure 2-23(a, b)). A 6 m coil (ID= 0.175 cm) encircled the two tubes of the middle line and was covered in thermal paste (T-99, maximum temperature 1200 °C, 85 – 170 W/m², Thermon[®]). The six additional cells were then added, then another 6 m tube (ID = 0.175 cm) was coiled around the 8 tubes bundle (Figure 2-23(c)). Once connected to the primary coil, the total HTF tube length was 12 m. Finally, the reactor was covered in a thin layer of thermal paste to promote heat exchange between the HTF and the eight tubes. This was wrapped in a 1 cm layer of insulation (aluminosilicate wool, Insulfrax[®]) and a 0.05 cm thick aluminium jacket (Figure 2-23(d)). Three thermocouples (K-type, Omega[®]) were embedded into the thermal paste on the side of one of the two tubes in the middle line. The first was placed at the top of the tube, the second in the middle and the third at the bottom. Three additional thermocouples were identically placed onto the side of one of the six outer cells. The final

dimension of this thermal battery was 8 cm in diameter and 28 cm high, which implied an apparent hydride density of 640 kg/m³.

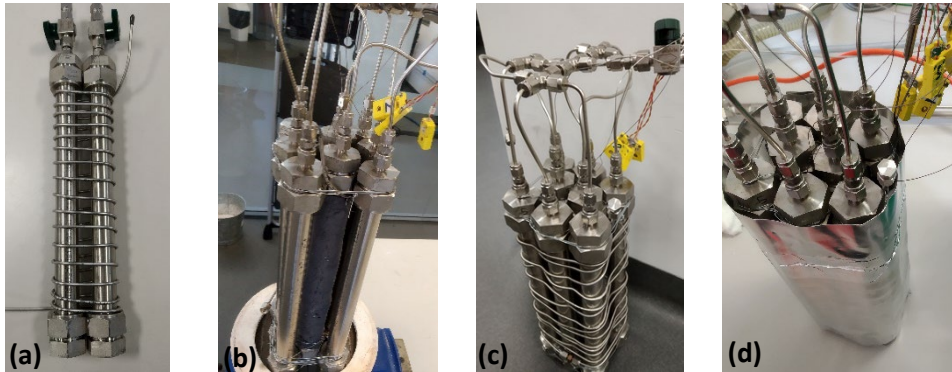


Figure 2-23 - Pictures of the custom made reactor assembly. (a) The two tubes of the middle line wrapped in the HTF coil; (b) the eight tubes with the middle line embedded in thermal paste; (c) the eight tubes wrapped in the external HTF coil; (d) the reactor encased in its insulating jacket.

2.9.1.5. Heat sink

A heat sink array was installed after the outlet of the thermal battery in the HTF loop to prevent the fluid from entering the backpressure regulator (discussed in section 2.9.1.6) and the pump at a temperature higher than 80 °C. It was made of 2 components: a heat recovery system that allows a portion of the heat delivered from the reactor to be transferred to the fluid before entering the pre-heater; and a heat sink made of 2 m of stainless steel tubing (OD = 6 cm) equipped with radial aluminum radiators (Figure 2-24). An electric fan was added to blow cold air at the radiator to extend heat power removal.



Figure 2-24 - Picture of a part of the heat sink equipped with aluminium fins.

2.9.1.6. Backpressure regulator

A back pressure regulator (Trident Australia[®], rated to 350 bar and 80 °C) was mounted after the heat sink to pressurise the system. A manual screw was used to adjust the desired pressure between 1 bar and 350 bar. During experimental investigations, the HTF pressure was set to 200 bar.

2.9.1.7. The HTF flow meter

A digital flow meter (Omega[®], FLR1008) was mounted after the outlet of the backpressure regulator to monitor the volumetric fluid flow. The meter was rated for a flow of 20 to 200 ml/min at atmospheric pressure, delivering a 0 to 5V signal over the whole scale (accuracy 1 %).

2.9.2. Hydrogen circuit

The hydrogen circuit allows gas transport from the G-type volumetric storage cylinder to the HTMH reactor for the hydride to undergo reversible hydrogenation during cycling. The circuit also allows the hydrogen released during dehydrogenation (or thermal energy storage) to be stored in the gas cylinder.

As shown in Figure 2-25, the setup was designed to provide hydrogen to the reactor (“absorption path”) with the possibility of manually regulating the inlet pressure using a

closed loop system. Therefore, a G-size bottle (B.O.C.[®], ≈ 50 NL) was attached to the rig, providing 150 bar (≈ 600 g) of hydrogen. This bottle was equipped with a reverse flow pin that allowed the cylinder to be refilled.

2.9.2.2. The compressor

A specialised hydrogen compressor, or gas booster (Haskell[®], model: AGT-30/75, two-stage gas booster single airhead, cooling jacket), was driven by a pressurised airflow.

The gas booster was mounted into a dedicated support cage incorporating valves and digital manometer at the inlet and outlet (Figure 2-26). A safety valve set to 120 bar, was mounted directly onto the compressor outlet to prevent the system from a hydrogen overpressure surge. The pressure of air supplied to the compressor was adjustable between 2 and 8 bar, through a pneumatic regulator, and a pneumatic cut-off valve was mounted onto the air inlet to stop the compression when no desorption occurred.

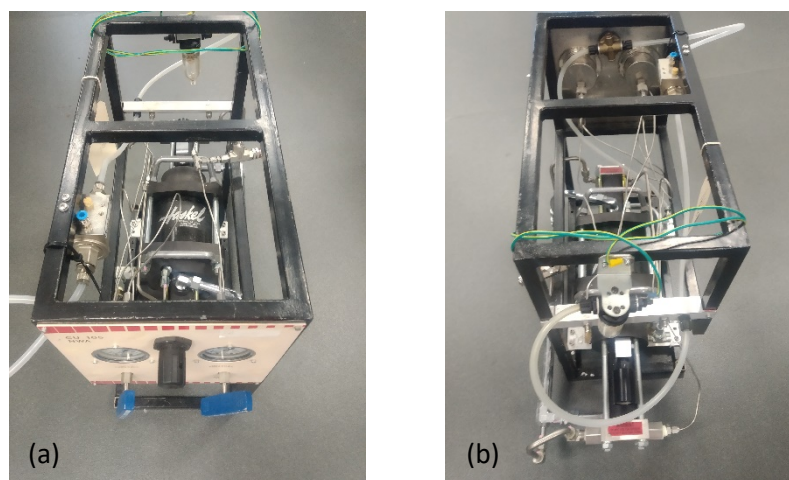


Figure 2-26 - Picture of the hydrogen compressor on its dedicated support with safety valve and compressed air supply port. (a) Front side, (b) back side.

Table 2-3- Technical specifications of the hydrogen compressor.

Model	Minimum hydrogen supply pressure (bar)	Maximum hydrogen outlet pressure (bar)	Static outlet stall pressure formula	Weight (kg)
AGT 7/30	1.7	620	$30 \text{ Pa} + 4 \text{ Ps}$	19

Ps : hydrogen supply pressure

Pa : compressed air drive pressure

2.9.3. The furnace and controller

The Parr[®] manufactured furnace was designed to heat the reactor Parr[®] 4683, 1.8 L reactor (TES1500). Temperature control was governed by two J-type thermocouples, which were mounted through the cap of the reactor allowing furnace temperature control according to the inner reactor temperature. In this experimental setup, the furnace was used to provide a simulated isothermal hot background (HB, 30 °C below the average operating temperature of the thermal battery) to diminish heat losses to the environment. Therefore, the thermocouples were placed in the furnace and surrounding the reactor's envelope, and an additional 5 cm thick layer of aluminosilicate wool was added to the furnace insulation to further reduce heat loss.

2.9.4. Monitoring, acquisition and control system

2.9.4.1. Software

2.9.4.1.1. LabVIEW[®]

A dedicated program was developed utilising LabVIEW[®] software. It enabled a large quantity of the data to be acquired during the experiments: temperature, pressure (hydrogen and HTF), and flow rate of the HTF and state of pneumatic valves (open or closed). It allowed for control of the pneumatic valves based on measurement states, and different triggering parameters were available (Figure 2-27):

- Manual: User can click on indicators on the “front window” located in the “Manual” tab to open each of the pneumatic valves.

- Temperature driven: User can set a temperature level, and if the reactor's temperature falls below this value, the absorption valve (V_{m1} , Figure 2-25) is opened. If the temperature measured is higher, the desorption valve (V_{m2}) is opened and V_{m1} is closed.
- Pressure driven: User can set a pressure level, if reactor's pressure is above this value, the absorption valve (V_{m1}) is opened, and on the contrary, desorption valve (V_{m2}) is opened.
- Time driven: User can set the amount of time allowed for the absorption mode to last. When the countdown is complete, the system automatically switches to desorption mode, and vice versa. For the desorption mode, a minimum reactor pressure can be set, so that when this pressure falls below this value the desorption valve (V_{m2}) is closed until the pressure rises higher. This prevents the compressor from over pumping hydrogen gas from the reactor and creating a vacuum inside that volume.
- Outlet driven: User can set a temperature level on the HTF outlet of the reactor, and if the data measured is lower than this value the absorption valve (V_{m1}) opens to promote hydrogen absorption and generate heat. On the contrary, the desorption valve (V_{m2}) opens to desorb hydrogen and store thermal energy.

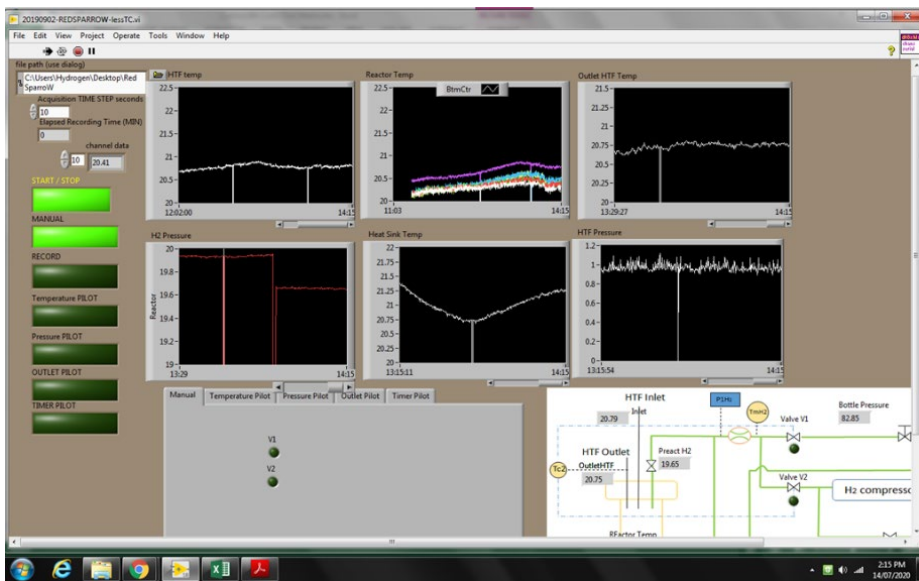


Figure 2-27 - Picture of the Labview® program user window with live monitoring and different operating modes.

2.9.4.1.2. Pactware®

Pactware® software was used for communication with the differential manometer through a Highway Addressable Remote Transducer (HART) protocol. This software gathered the hydrogen temperature flowing in or out of the reactor, as well as the pressure differential over the 500 μm aperture. This permitted the hydrogen mass flow between the reactor and gas cylinder to be calculated using the procedure and equation presented in section 2.6.

Chapter 3 Metal hydrides used for high temperature heat storage

“La chaleur pénètre, comme la gravité, toutes les substances de l’univers, ses rayons occupent toutes les parties de l’espace.”

“Heat, like gravity, penetrates every substance of the universe, its rays occupy all parts of space.”

Jean-Baptiste-Joseph Fourier.

3.1. Introduction

As metal hydrides offer high gravimetric energy density, they have potential to be a future high temperature energy storage technology. The list of candidates is virtually endless. However, some inherent constraints depending on application need to be taken into account. This chapter aims to describe the implications of using hydrogen at high temperature and the metal hydride characteristics for a suitable material as a high temperature thermal energy storage. Further, this chapter expands on investigations of a selected material, detailing thermodynamic, kinetic studies and their improvement.

3.2. Main considerations

3.2.1. H₂ safety

The main concern of working with hydrogen is its flammability at the low concentration of 4% in air. In a confined space, an explosion can be devastating, as per example, the explosion of Fukushima Daiichi's reactor was due to the leakage of hydrogen from its containment.¹⁹³ However, hydrogen gas, compressed or cryo-cooled, has already been used in industry for a long time and quality standards are in practice to provide safety. Industries generally equip facilities with hydrogen sensors for leak detection. In the continuous pursuit of improvement, two databases are gathering incident reports in the aim of sharing the identified reasons of incident occurrences and addressing them.¹⁹⁴ The storage of hydrogen in metal hydrides presents an improved safety feature: a significant reduction of storage pressure that inherently limits the effect of eventual failure in the storage tank.

3.2.2. Material compatibility

As the smallest molecule in the universe, hydrogen atoms have the ability to diffuse through many non porous materials. This effect can cause blistering, cracking or embrittlement that eventually leads to the failure of the vessel.¹⁹⁵ Since the phenomenon is part of the challenge of conventional fuel transport, the subject has been well studied over many decades.¹⁹⁶⁻¹⁹⁸ However, at high temperature, the mobility of hydrogen is increased and more hydrogen can diffuse through the material, as a consequence hydrogen atoms not only reside in preferred defect sites and the hydrogen embrittlement is lowered but hydrogen losses occur.^{199, 200} Detailed reviews present the hydrogen permeability through a wide range of materials, some example are drawn Figure 3-1.^{201, 202} For industry and specifically in nuclear applications, studies have pointed to a thin ceramic coating as an effective permeability hindrance.^{203, 204} Causey *et al.* have also identified silicon carbide as a suitable hydrogen barrier in a high temperature environment.²⁰⁵ Later, Forcey *et al.*, revealed that aluminised steel with a thin layer of Al_2O_3 decreases hydrogen diffusion by 3 orders of magnitude.²⁰⁶ SS316 was used for hydride reactors due its acceptable hydrogen

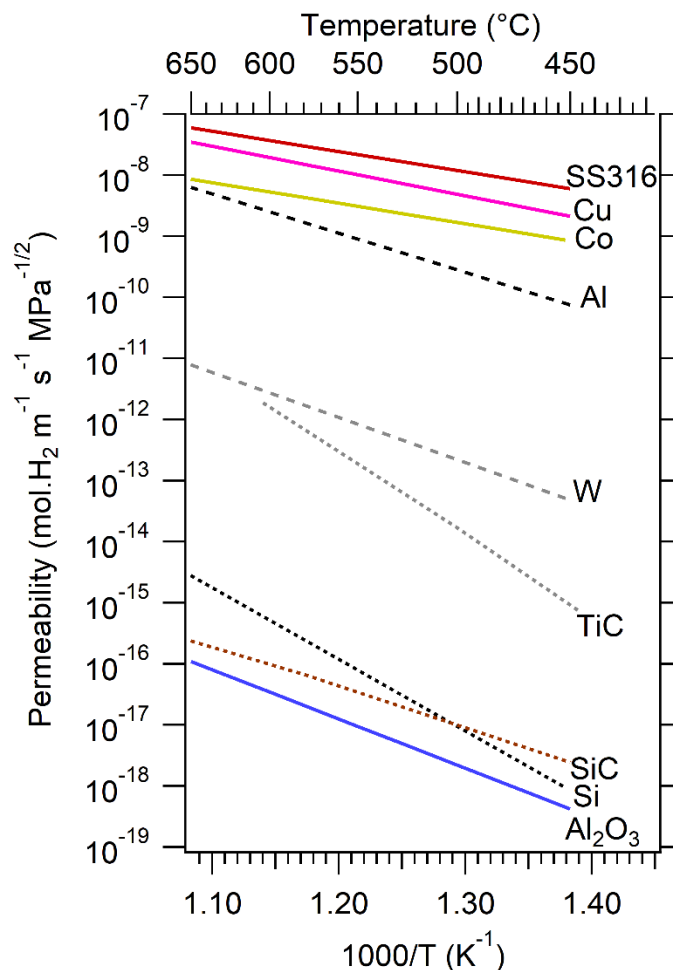


Figure 3-1- Hydrogen permeability of potential envelope materials.^{200, 201}

permeability. In the temperature regime (300 °C – 500 °C), hydrogen permeability ranges from $8 \cdot 10^{-10}$ and $1 \cdot 10^{-8} \text{ mol.H}_2 \text{ m}^{-1} \text{ s}^{-1} \text{ MPa}^{-1/2}$.²⁰¹ In the aim of improving the accuracy for the measurement of thermodynamic data of hydrides, Sheppard *et al.* developed a procedure to account for the hydrogen diffusion through steel at temperatures above 450 °C.²⁰⁷ This procedure was used in this research involving hydrogen sorption at high temperatures.

3.2.3. Abundance / Cost

Market competitiveness is a mandatory feature for a potential technology to be adopted by industry. Hence, thermal energy storage in metal hydrides must offer at least the same energy price than the existing industry standard. For that purpose, the office of energy efficiency and renewable energy of U.S. set up targets for the CSP power generation; it is set at 0.05 USD/kWh for 2030, assuming 12 hours of energy storage to ensure baseload supply.²⁰⁸ Since metal hydride technology is at an early stage of laboratory development, it is highly complex to accurately determine the energy price associated to the use of metal hydrides as high temperature thermal energy storage. Researchers often reflect the cost of raw material per energy storage capacity, as Manickam *et al.* presented in a recent review.¹²⁶

The cost of raw material is often driven by the laws of supply and demand. If the demand of a rare material increases, the price shall increase. On the contrary, if the material is abundant, the infrastructure for extraction can readily increase production, resulting in a decreased price. Therefore, a prime parameter to consider to develop thermal energy storage in metal hydrides is the abundance of raw materials. As presented in Figure 3-2, elements such as aluminium, magnesium or iron are available in large amounts and are therefore likely to be chosen as base metal hydride materials.²⁰⁹

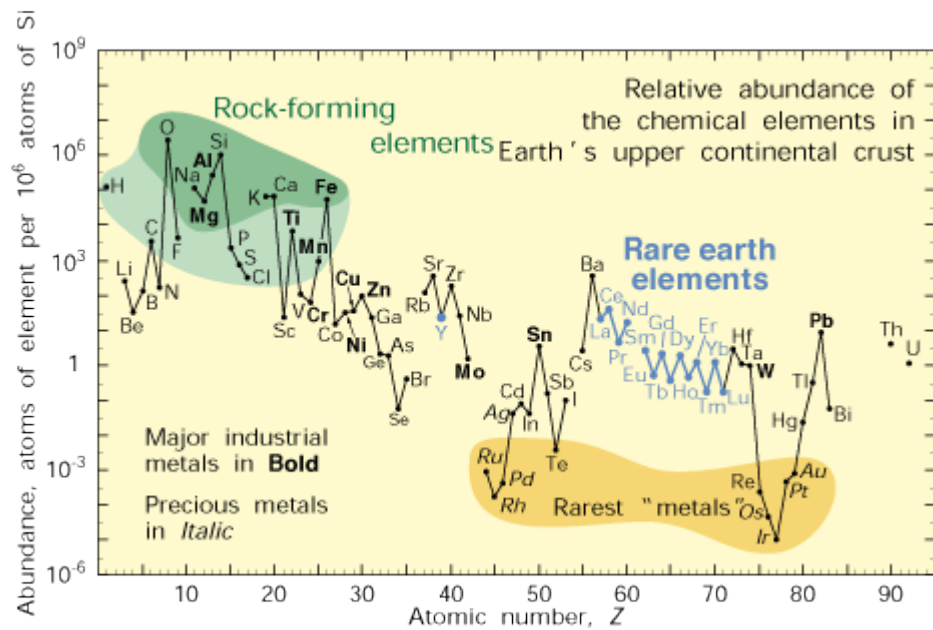


Figure 3-2 - Element abundance available for mining.²⁰⁹

3.2.4. Thermodynamics

3.2.4.1. Operating temperature and pressure

As explained in chapter 1, most metals can react with hydrogen. In order to be considered as a high temperature thermal energy storage material, the metal must display a hydrogen uptake and release at temperature above 400 °C, at an acceptable level of hydrogen pressure. As the high hydrogen pressure requirement may involve high cost of management and containment, an adequate level of hydrogen pressure would be as low as possible, but likely above 1 bar.

3.2.4.2. Enthalpy of reaction and energy density

The enthalpy of a reaction between hydrogen and a metal directly dictates, though the hydrogen capacity, the gravimetric or volumetric energy density of material.

$$Q = \frac{\Delta H \cdot m \cdot \text{wt}\%}{2.016 \cdot 1000} \quad \text{eq. 3-1}$$

where

Q = gravimetric energy density (kJ/kg)

ΔH = the enthalpy of the hydride (kJ/mol H₂)

m = the mass of hydride (kg)

$\text{wt}\%$ = the hydrogen capacity of the hydride (kg⁻¹)

Therefore, for an identical raw material price, materials offering high hydrogen uptake at high enthalpy of reaction are to be preferred in order to offer the best energy density.

3.2.5. Reversibility

A favourable metal hydride shall undergo hydrogen uptake and release to provide energy storage for many years. Hence, to be a successful candidate, it is mandatory for the elected material to display consistent hydrogen capacity over many cycles (as introduced in section 2.5.3.3).

3.2.6. Kinetics

When a metal is maintained in a hydrogen atmosphere at a temperature and pressure that exceeds the equilibrium pressure, the hydrogenation reaction occurs. The kinetics of hydrogen absorption relate to the rate of the hydrogen uptake or release. The generated power is driven by the kinetics and the mass of hydrogen involved. In order to offer the high thermal power required to operate a thermoelectric generator, hydrogen uptake should be as fast as possible. Small scale (less than a gram) kinetics studies on MgH₂ and other hydrides showed that the reaction speed was an intrinsic parameter related to the material structure and phase boundary movement.^{210, 211} Different additives have been investigated to improve absorption or desorption kinetics.^{212, 213} However, on a large scale,

other parameters such as hydrogen diffusion pathways or heat transfer may have an increasing impact on the reaction rate. This project evaluates this possibility.

3.2.7. Thermal losses

The low thermal losses involved in this technology are one of the attractive aspects of thermal energy storage using metal hydrides. When the storage device doesn't undergo a chemical reaction, it can remain at ambient temperature depleting only the sensible thermal energy stored. For example, the magnesium iron hydride, which offers an energy density close to 2100 kJ/kg would only lose around 530 kJ/kg from 400 °C to 25 °C. The bulk of the stored energy can be retrieved when the hydrogen absorption reaction occurs.

Nevertheless, the storage system is required to work at high temperature and hence adequate insulation is paramount during heat storage and release operations.

3.2.8. Heat supply/ exchange

For high temperature thermal energy storage devices, heat transfer is a crucial part of the system design. The heat storing material must efficiently transmit the heat to some media which conveys this energy to the user, a generator or another heat exchanger. Nowadays, three heat transfer fluids (HTF) are predominantly used when operating temperatures are above 350 °C: molten salts, air and water as pressurised steam.²¹⁴

Molten salts, as used today, are commonly made of 60% NaNO₃ and 40% KNO₃, irreversible decomposition of such mixture occurs at 565 °C and their operating temperature is limited to 550 °C to prevent fluid decomposition.²¹⁵ Vignarooban *et al.* recently reviewed potential heat transfer fluids for CSP, and revealed some attractive molten salt HTFs that could carry energy at temperatures up to 800 °C.²¹⁵ However, these salts are highly corrosive, and corrosion was responsible for an 8 month long close down of iconic Crescent Dunes CSP plant.²¹⁶ Leakage from the molten salt tank were detected and took time to get repaired. It is probable that the incident has had hindering repercussions on the CSP industry.

Water as a HTF offers undeniable advantages: virtually endless supply, easily available and low price; environmentally friendly and not hazardous. However, at such temperatures, water must be heavily pressurised to maintain usable steam density (as shown Table 3-1),

which may induce a hefty cost. Gases could provide an appealing alternative as their chemical stability inhibit pipe corrosion or decomposition at high operating temperature. However, their low densities and specific heat (Table 3-1) means that they would need to flow at a significantly high speed to enable a high energy transfer. Amongst these gases, carbon dioxide (CO₂) has a supercritical point as low as at 304.1 K and 74 bar. Operating with CO₂ pressurised at 100 bar would allow to increase the fluid density by almost two order of compared to the other mentioned gas and counteract the low thermal conductivity.²¹⁷ Nevertheless, CO₂ can be corrosive to steel and the elevated temperature acts as a corrosion catalyst,^{218, 219} hence, inhibitors or coating have to be implemented to prevent such reaction.²²⁰

Table 3-1 - Significant properties of possible heat transfer fluids from NIST database.²¹⁷

Fluid	Operating temperature (°C)	Operating pressure (bar)	Density (kg/m ³)	Specific heat, Cp (kJ/kg.K)	Specific heat, Cv (kJ/kg.K)	Thermal conductivity (W/m.K)
Supercritical water	450	250	107.9	5	2.44	0.106
Superheated steam	450	200	78	3.96	2.24	0.09
Superheated steam	450	100	33.45	2.74	1.89	0.072
Hydrogen gas	450	1	0.033	14.64	10.5	0.355
Hydrogen gas	450	100	3.35	14.64	10.5	0.356
Helium gas	450	1	0.066	5.2	3.11	0.288
Helium gas	450	100	6.6	5.2	3.20	0.288
Carbon dioxide gas	450	10	7.3	1.14	0.95	0.051
Carbon dioxide supercritical	450	100	542.6	1.36	0.96	0.085
Dry air	450	100	46.2	1.1	0.80	0.054

3.3. Potential metal hydrides

For a metal hydride to be successfully selected for high temperature thermal energy storage, it must comply with all the above mentioned constraints. Despite a large amount of materials already investigated, it is often that one or more of these parameters are not

satisfied, which limits the list of materials that are attractive for further investigations.

Table 3-2 presents a list of the most favourable metal hydrides.

Table 3-2 - Recapitulative main characteristic table of promising metal hydrides.

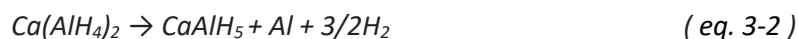
Material	Theoretical H ₂ capacity (wt%)	Theoretical operating temperature (°C)	Enthalpy (kJ/mol H ₂)	Gravimetric energy storage (kJ/kg)	Possible operating temp (°C)	Associated operating pressure (bar)	Ref
LiH	9.51	> 950	133.5	8397	930	1	63
TiH ₂	4	700 – 1100	165.3	2842	650	1	221,222
CaH ₂	4.9	990 - 1100	181.5	4198	1100	1.2	223
CaAl ₂	2.1	400 - 630	70.7	735	620	83.1	223,75
CaHCl	1.32	700 – 1000	x	x	650	12	224
CaH ₂ Si	2.87	413 - 1100	106.5	x	x	x	225
Ca ₂ NH	2.1	350 - 600	107.8	943	550	1	226
MgH ₂	7.6	282 - 534	74	2811	400	17	92,84,163
MgH ₂ Ni doped	7.4	290 - 500	74	2710			227,228
Mg ₂ NiH ₄	3.6	250 - 400	62.6	1117			229,230, 231
Mg ₂ CoH ₅	4.5	380 - 600	75	1674			232,76,77
Mg ₂ FeH ₆	5.47	380 - 600	77.4	2100	500	65	74,229,233
NaH	4.2	426 - 659	117	2437	600	53	234,235
NaBH ₄	10.7	511 - 890	100.4	5328	540	1	236
NaAlH ₄	5.6	31 - 181	38.4	740	120	60	237
K ₂ NaAlH ₆	2.2	380 - 631	98	1070	x	x	238,234
NaMgH ₃	4	382 - 683	86.6	1720	450	6	95,94,93
NaMgH ₂ F	2.5	431 - 738	96.8	1200	x	x	73

For example, lithium hydride has attracted attention for its light-weight, and hence, possesses a high gravimetric energy density of 8397 kJ/kg.⁶³ However, the liquid phase of the material at the extreme temperatures required for the reaction has been hindering investigations on this material.^{63, 239} Moreover destabilisation studies underlined the excessive cost of the base material.²⁴⁰ Otherwise, three metal hydride groups can be defined: calcium based, sodium based and magnesium based. Their state of art is further discussed below.

3.3.1. Calcium based

To date, calcium based hydride investigations have mainly been driven by the association of calcium and aluminium. The high temperature (around 1100 °C) required for pure calcium to react with hydrogen at 1 bar involves an adequate destabilisation to lower the operating temperature.²²³ Calcium aluminium hydrides have been studied for a long time with the first reported preparation in 1955.²⁴¹ Initially, it was synthesised from a reaction between aluminium bromide and calcium hydride in a solution of dimethyl-ether. Later in 1981, Veleckis investigated the thermodynamics of Ca-Al alloys, more precisely CaAl₄ and CaAl₂.²⁴² Their preparation was performed by melting calcium and aluminium at 1100°C followed by annealing at 875 °C overnight to form the CaAl₂ alloy, although the annealing process for CaAl₄ was significantly longer (18 days), which was deemed to be prohibitive. The standard free energy for CaAl₂ was reported to be ≈ 35 kJ/g atom (considering a working temperature of ≈ 500 °C). Veleckis also tested the reversible reaction of CaAl₂ with hydrogen during 25 cycles and pointed out a stable 2.13 wt% of hydrogen capacity throughout the cycling concluding that CaAl₂ was a favourable material for high temperature thermal storage up to 600 °C.

Investigation reports of Ca(AlH₄)₂ began to appear in the end of the 20th century, potentially inspired by the success of NaAlH₄.²⁴³ The synthesis uses tetrahydrofuran (THF) to react with CaH₂ and AlCl₃; Schwarz *et al.* stated that removing the solvent by filtration resulted in material decomposition.²⁴⁴ Fichtner managed to synthesise Ca(AlH₄)₂ with various starting compounds such as CaCl₂ and NaAlH₄ and was the first to solve calcium aluminium hydride's crystal structure.²⁴⁵ In the meantime, Lovvik, calculated the theoretical hydrogen capacity for the 3 step dehydrogenation reaction as 7.9 wt% H₂. Since the complete decomposition of calcium hydride is known to require high temperature, he also proposed to use the 2 first steps (1 and 2), which could offer 5.9 wt% of hydrogen.²⁴⁶,



In 2007, Kabbour *et al.* managed to directly synthesis Ca(AlH₄)₂ by ball milling 2AlH₃ + CaH₂ at 500 rpm.²⁴⁷ A 3 hour milling time was found to be the most efficient to obtain a large amount of Ca(AlH₄)₂. Hanada *et al.* investigated the slow kinetic barrier of desorption by

using additives such as Si, MgH₂ or 2LiNH₂.²⁴⁸ Under 3 bars of hydrogen back pressure, DSC measurements revealed decomposition of Ca(AlH₄)₂ at 150°C and a decomposition of CaAlH₅ to CaH₂+Al+3/2H₂ at ≈ 250°C. It is noted that the Si additive did not react with calcium despite a similar reaction enthalpy to calcium with Al. The proposed explanation was that the reaction kinetics of Ca with Al is better, therefore calcium reacts with aluminium preferentially.

Wolverton *et al.* extensively investigated the thermodynamics of calcium alanate and found the first decomposition step to be slightly exothermic, less than 10 kJ/mol H₂.²⁴⁹ While the second is endothermic and has a reaction enthalpy of 32 kJ/mol H₂ as well as the third with ΔH equal to 72 kJ/mol H₂ (decomposition of CaH₂ being strongly thermodynamically destabilised by presence of Al).²⁴⁹ Losub *et al.* studied the direct synthesis of CaAlH₅ by ball milling CaH₂ and AlH₃ for 3h with a ball to powder ratio of 80:1.²⁵⁰ A yield of 92% of CaAlH₅ was achieved, and a TPD of this compound revealed the second step previously mentioned (2) comprised of two additional steps via the formation of a new complex such as Ca₃(AlH₆)₂, but the bulk of the reaction released 3 wt% of hydrogen. DSC and TPD measured an activation energy of 161 kJ/mol and an enthalpy of 26 kJ/mol H₂.

The first step decomposition from Ca(AlH₄)₂ to CaAlH₅ (1) was proven to be experimentally irreversible by Li *et al.*²⁵¹ Their starting materials were NaAlH₄ + CaCl₂ and reported successful use of additives with an activation energy required for the second step reduced by a factor 3 by doping with TiF₃ to reach ≈ 50 kJ/mol.

In 2013, Liu investigated a hydrogen storage system involving LiBH₄ with Ca(AlH₄)₂, at different molar ratios.²⁵² Isothermal desorption of 1:6 (molar ratio of LiBH₄ and Ca(AlH₄)₂ respectively) revealed a release of 8.4 wt% of H₂ at 450°C followed by an uptake capacity of 4.5 wt% under 40 bar H₂. The reaction kinetics were reported to be as fast as 30 min for total desorption and ≈ 3 h to reabsorb 4 wt% of hydrogen. This showed calcium could offer attractive characteristics if more additives are investigated with an adjusted stoichiometrie.

More recently, Ward *et al.* reported a successful cycling of CaAl₂ prepared from CaH₂ (Sigma Aldrich) and AlH₃ (ATK).⁷⁵ Ball milling at 500 rpm with a cooling period every 15 min, for a non-reported overall time, using 2.6 mm stainless steel balls and a ball to powder ratio of 1:30. Annealing at 600 °C, for 6 hours under dynamic vacuum resulted in the production of CaAl₂ with minimal amounts of CaAl₄. Cycling at 600 °C (3) between 24 and 2 bar of hydrogen for absorption and desorption respectively revealed a consistent 1.9 wt% of hydrogen capacity with a reaction enthalpy of 83 kJ/mol H₂. Thermal conductivity

measurements of a cold pressed pellet of CaAl_2 presented a value as high as 20 W/m.K, which is 20 times more than that of other common hydrides.

Even though calcium based hydrides possess a series of features that are attractive, the use of hydrogen at temperature of 600 °C and above introduces additional safety concerns due to an operating temperature above the self-ignition point, which is 585 °C.²⁵³ Moreover, the solubility and permeability of hydrogen in steel above 500 °C implies supplementary challenges concerning the reactor.²⁵⁴ Some solutions have been developed such as ceramic coating or the use of silicon carbide reactor cells, but these are not affordable for a large lab scale experimentation at this stage.^{203, 207}

3.3.2. Sodium based

With a 1 bar equilibrium pressure at 425 °C, a hydrogen capacity of 4.2 wt% and an enthalpy of 117 kJ/mol H_2 , sodium hydride offers attractive characteristics for high temperature thermal energy storage.²³⁵ However, the decomposition of NaH leads to a molten form of Na (above 100 °C) and hydrogen absorption creates a layer of NaH on the surface that hinders the reversibility of the reaction.²³⁴ This issue may have led to the investigation of complex compounds based on sodium hydrides, such as sodium alanate (NaAlH_4), which were shown to display reversible hydrogen uptake at ≈ 150 °C by Bogdanović *et al.*^{237, 243} NaBH_4 offers an attractive 10.7 wt% of hydrogen capacity but also displays a poor reversibility with 3.1 wt% H_2 re-absorbed at 405 °C under 13.3 bar H_2 .²³⁶ The use of appropriate additives could improve the reversibility, however, investigations are directed towards low temperature hydrogen storage.²⁵⁵ Despite extensive research, no additives have displayed attractive enhancement yet.²⁵⁶ The perovskite NaMgH_3 has also received extensive attention, its low pressure desorption plateau at ≈ 450 °C motivated further investigations during this project. A detailed review is presented in the dedicated section 3.3.3.1 further in this chapter.²⁵⁷

3.3.3. Magnesium based

With virtually limitless quantities of magnesium available (i.e. 0.13 wt% in sea water and 2.7 wt% in the earth crust),⁸⁷ magnesium is a very attractive base metal for hydrides. The

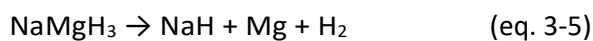
production technology is well established and the resulting cost of material is relatively low. Moreover, MgH₂ has a high theoretical hydrogen capacity of 7.6 wt%, therefore this hydride has received extensive interest from researchers.^{87, 210, 258} Recent reviews demonstrate interesting advances towards destabilisation and kinetic improvement aiming at using magnesium as a viable hydrogen storage material.^{259, 260} Successful additives, such as nickel, iron or titanium, showed impressive lowering of desorption temperatures and kinetics enhancements.^{228, 261}

In the 1990's, magnesium hydride was considered as a suitable material for thermal energy storage, when Bogdanović *et al.* demonstrated the feasibility of a magnesium hydride based steam generator.²⁶² In 2009, Felderhoff *et al.* further investigated the concept by evaluating the hydrogen capacity upon cycling at temperatures of ≈ 500 °C.²²⁷ It was revealed a consistent decrease in hydrogen capacity, which was deemed to be the results of magnesium sintering at temperatures above 450 °C. Since then, two magnesium based hydrides remained attractive for operating at temperature up to 600 °C: NaMgH₃ and Mg₂FeH₆.^{74, 234} They are further investigated in the following sections.

3.3.3.1. NaMgH₃

3.3.3.1.1. Introduction

The reasonably flat equilibrium pressure plateau upon hydrogen absorption and desorption displayed by the perovskite sodium magnesium hydride suggests an ease of reaction trigger and control.⁹⁵ Bouamrane *et al.* first determined its standard enthalpy of formation to be $\Delta H_f = -231$ kJ/mol,^{263,264} while Ikeda *et al.* identified a two-step decomposition pathway, the overall reaction released 6.0 wt% H₂ (eqs 3-5 and 3-6).²⁶⁵ They determined the hydride density to be 1.47 kg/m³. Sheppard *et al.* performed detailed thermodynamic investigations using pressure composition isotherms and calculated the enthalpy and entropy for the each of the reaction steps.⁹⁵ They were determined to be $\Delta H = 86.6$ kJ/mol H₂ with $\Delta S = 132.2$ J/mol H₂.K and $\Delta H = 117$ kJ/mol H₂.K with $\Delta S = 168$ J/mol H₂.K, respectively.



Sheppard et al. also demonstrated the reversible hydrogen uptake and release from NaMgH₃ into NaH, Mg and H₂ (eq. 3-5).⁹⁵ The irreversibility of the second step (eq. 3-6) was also exposed, the reaction leads to a macroscopic segregation of metallic Na and Mg, which impedes the hydrogen capacity. Therefore only the first decomposition step should be considered for long term application.

Recently, efforts to improve the sorption kinetics of NaMgH₃ have been undertaken. S.Tao et al. replaced 10 wt% of the sodium in NaMgH₃ with potassium and in the process lowered the activation energy of the first step from 180.2 kJ/mol to 141.3 kJ/mol.⁹⁴ This modification also reduced the onset of the decomposition temperature by approximately 50 °C and improved the desorption kinetics by a factor of two at 365 °C. Wang et al. doped NaMgH₃ with K₂TiF₆ (0.042 wt%) and reduced the activation energy to 153.35 kJ/mol,²⁶⁶ allowing desorption of 90% of the hydrogen capacity in 20 min at 365 °C, compared to only 60% for the pristine material in the same timeframe. The addition of 2.5 wt% carbon nanotubes or graphene oxide by ball milling also reduces the activation energy of the first step to 113.8 kJ/mol, while also allowing 90% dehydrogenation in 20 min at 365 °C.²⁶⁷

NaMgH₃ recently displayed low variation in hydrogen capacity for 10 cycles at ≈ 500 °C, which is instrumental for success as a high temperature energy storage material.²⁶⁸ Therefore, it was selected to be used as a large scale thermal energy storage material. Details of its usage in a 150 g lab scale reactor will be given in chapter 5.

3.3.3.1.2. Synthesis of NaMgH₃

A variety of successful synthesis processes have been reported to form NaMgH₃, including cryo-milling followed by annealing under hydrogen, and ball-milling followed by annealing, as well as reactive ball milling under hydrogen pressure.^{264, 269} The synthesis involves the use of magnesium hydride as a base product, which requires hydrogenation of magnesium prior NaMgH₃ production. Direct synthesis from NaH and pure magnesium is not reported in literature. Therefore, a comparative study on the feasibility of using pure Mg instead of MgH₂ as a starting material has been performed herein.

A mixture of NaH (Sigma-Aldrich, 95%), MgH₂ or Mg (Sigma-Aldrich, 98%) was used for NaMgH₃ synthesis. MgH₂ was synthesised within the laboratory by hydrogenating Mg powder at 400 °C under 30 bar H₂ for 18 h. The hydrogenated Mg was then ball milled (BM)

for 3 hours with a ball-to-powder mass ratio of 10:1 in a Shaker Mill (Turbula T2C shaker-mixer) and annealed once again under identical conditions (400 °C, 30 bar H₂, 18 h). The equimolar mixture of reactants (NaH and Mg/MgH₂) was first ball milled, for 240 min, under an argon atmosphere, in a stainless steel vials (150 ml in volume) using an equal number of 1 g and 0.6 g stainless steel balls. The ball to powder ratio was 30:1. The contents were then annealed at 500 °C under 20 bar H₂ to obtain the NaMgH₃ orthorhombic structure.

Comparison of yield using various synthesis methods was performed via XRD analysis and Rietveld refinement. XRD patterns are shown Figure 3-4Figure 3-3. When the precursors used are NaH and MgH₂, quantification through Rietveld analysis reveals a 90 % yield of NaMgH₃, with negligible starting material remaining. When Mg replaces MgH₂, an 80 % yield can be attained with a higher quantity of remaining starting material. If the precursors are hand ground instead of ball milled prior to the above described annealing procedure (under hydrogen), only 8 % of NaMgH₃ is formed. These results show the necessity of the ball milling step that reduces the particles size and demonstrate the feasibility of NaMgH₃ using pure magnesium as a reagent.

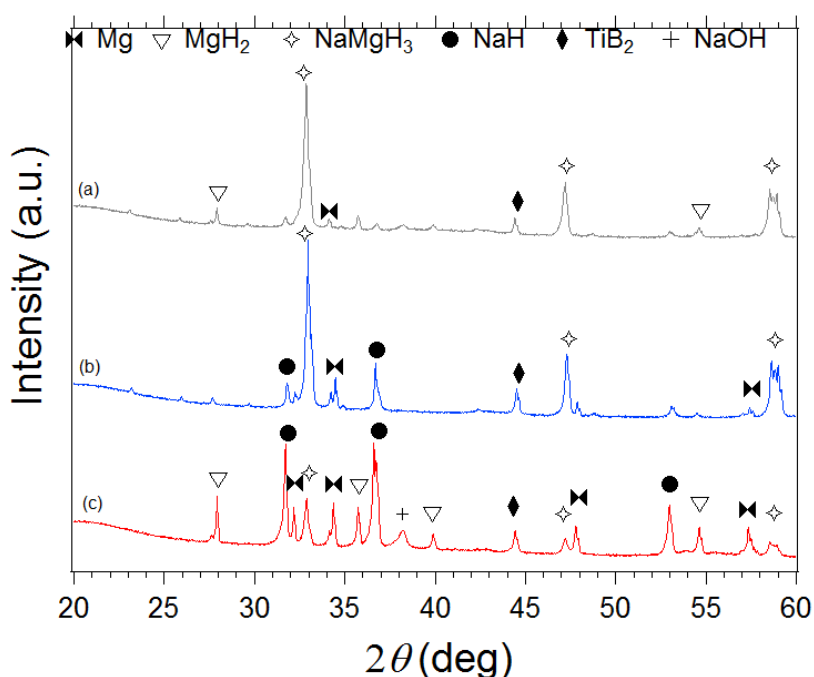


Figure 3-3 - . X-ray diffraction pattern of synthesised NaMgH₃ after milling and annealing. (a) Ball-milled with a MgH₂ precursor, (b) Ball-milled with a Mg precursor, (c) hand-ground with a Mg precursor; $\lambda = 1.5418 \text{ \AA}$.

The NaMgH₃ mixture developed to investigate this hydride in a thermal energy storage reactor is formed with an equimolar mixture of NaH and Mg. 2 mol % titanium diboride (TiB₂, Sigma-Aldrich, <10 μm) was added as an anti-sintering agent and to improve the kinetics of MgH₂ as demonstrated by Pitt et al.⁹⁰ An addition of 20 wt% of ENG (2.5–10 μm, SGL carbon), previously outgassed for 12 h at 500 °C under dynamic vacuum, was used to improve the thermal conductivity.^{91, 98}

3.3.3.1.3. Thermodynamics of NaMgH₃

Figure 3-4 details the pressure-composition isotherms (PCI) of the Reactor Mix (RM = NaMgH₃, 0.02TiB₂, ENG (20 wt%)), for a temperature range between 418 to 466 °C. Each curve represents the first decomposition step of NaMgH₃ into NaH and Mg. The RM offers a total hydrogen capacity of 2.6 wt%, which considering the additional 20 wt% of ENG is proportional to the 3.3 wt% H₂ reported capacity of pristine NaMgH₃.⁹⁵ Between 0.5 and 2.5 wt%, the desorption plateau is quasi flat for temperatures up to 444 °C. Desorption PCIs at higher temperature reveal a slope that may signify hindrance in the hydrogen desorption.

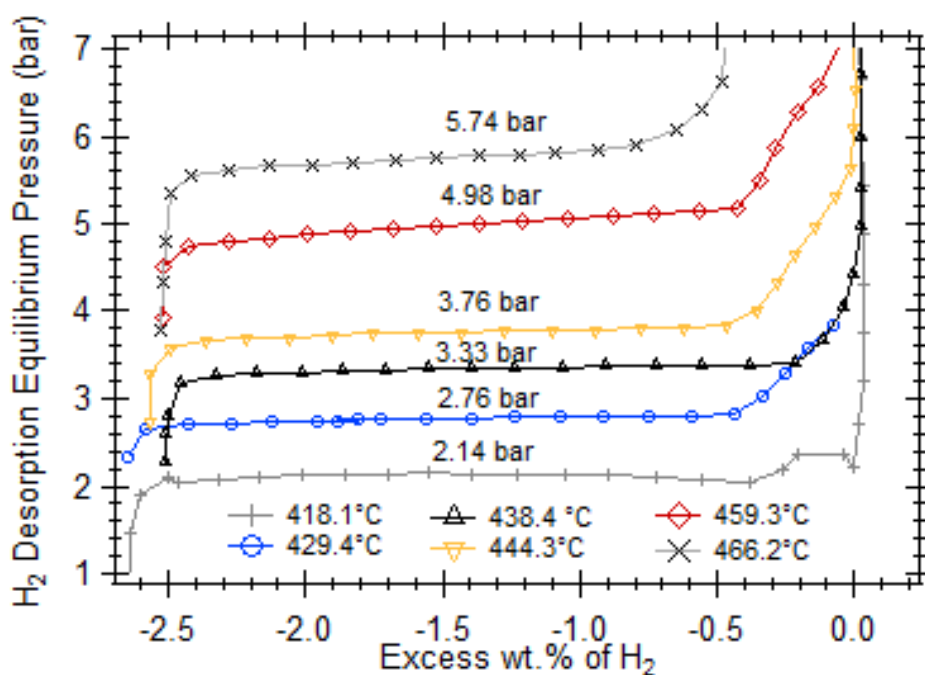


Figure 3-4 - Pressure composition isotherm of RM between 418 °C and 466 °C.

A van 't Hoff plot derived from the PCI data, shown Figure 3-5, allows for the determination of the thermodynamics of hydrogen desorption, such as enthalpy and entropy. They are found to be $\Delta H = 86.4 \pm 1.3$ kJ/mol H_2 and $\Delta S = 131.4 \pm 1.6$ J/K.mol H_2 , respectively. As shown in Table 3-3, the values calculated for the RM are similar to those reported by Sheppard *et al.*⁹⁵ This indicates that the addition of the TiB_2 additive and ENG doesn't have a significant impact on the thermodynamics of hydrogen release from $NaMgH_3$. Figure 3-6 shows the absorption PCIs alongside their associated desorption PCIs, and reveals a negligible hysteresis phenomenon for temperatures below 444 °C, becoming significant ($\Delta P = 0.5$ bar) at 459.3 °C. This could relate to a magnesium sintering effect.⁹⁰ Therefore, to guarantee a long cycle stability, it is recommended to operate $NaMgH_3$ at temperatures below 450 °C.

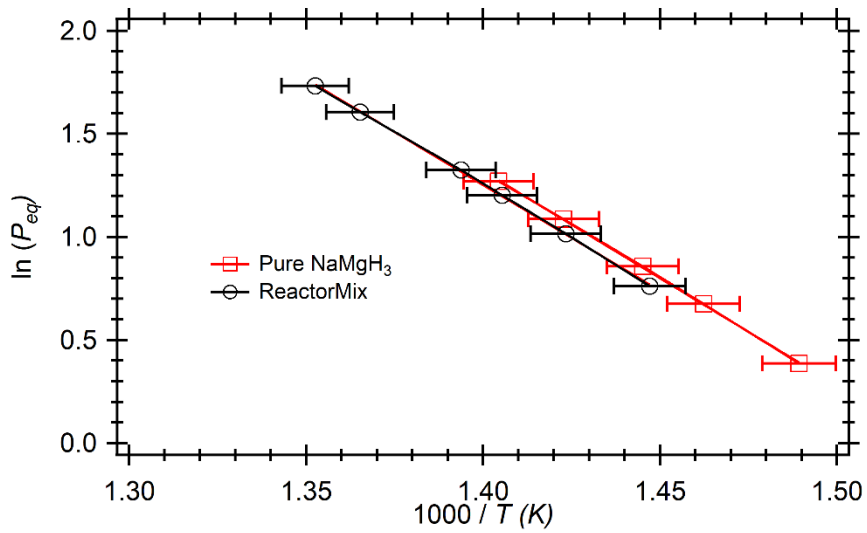


Figure 3-5 - van 't Hoff plot of the Reactor Mix compared with pristine NaMgH₃.

Table 3-3 - Comparison of enthalpy and entropy of hydrogen desorption.

Enthalpy (kJ/mol H ₂)	Entropy (J/mol H ₂ .K)	Reference
86.6 ± 1.0	132.2 ± 1.3	95
92	123	270
94	140	269
88	116.2	271
86.4 ± 1.3	131.4 ± 1.6	This work

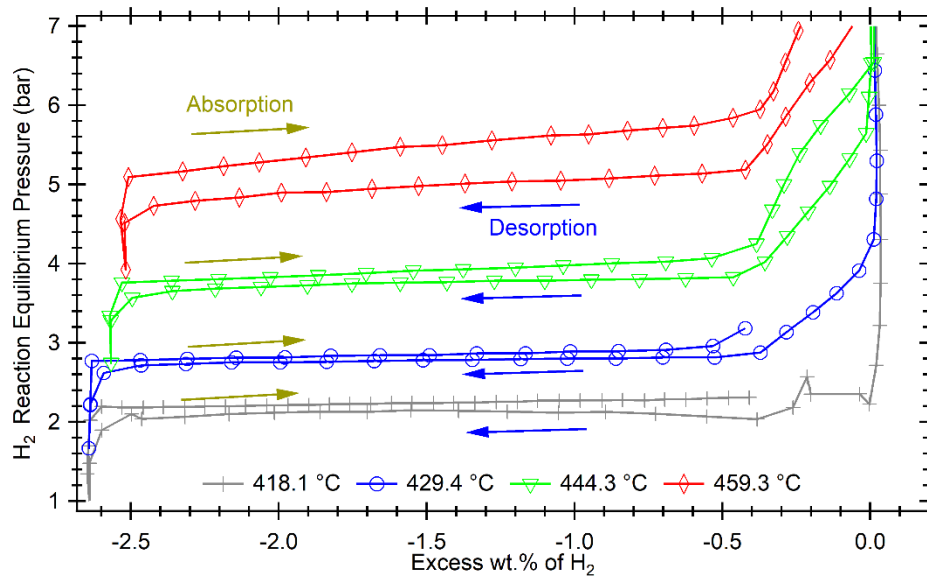


Figure 3-6 - Pressure - composition isotherms of NaMgH_3 with additives upon desorption and absorption between 418 °C and 459 °C.

3.3.3.1.4. Reaction kinetics of NaMgH_3

A comparative investigation on the influence of the additives (TiB_2 and ENG) on the hydrogen release was performed through DSC. Figure 3-7 presents the patterns obtained for pure NaMgH_3 (a) and the Reactor Mix (b) at different heating rates. The desorption process occurs at the onset temperature at which the plots starts to drop, showing that the hydrogen release generates a peak of energy required to maintain the heating rate of the sample.

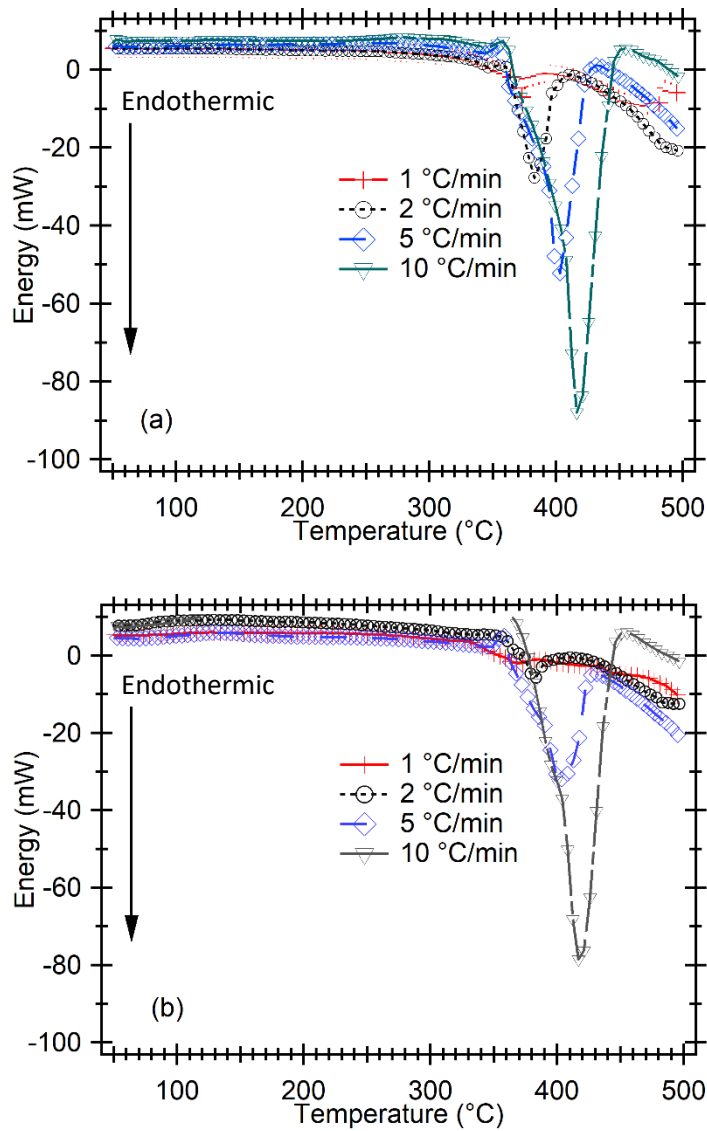


Figure 3-7 - Differential scanning calorimetry pattern of (a) pure NaMgH₃ and (b) Reactor Mix.

The Kissinger method, described in section 2.5.1 is used to determine the activation energy of both the pure NaMgH₃ and the Reactor Mix. Figure 3-8 displays the onset temperature for both materials and each heating rate. The results are similar for both materials, however at low temperature ($1000/T \approx 1.55$) a slight variation appears, but it remains within the uncertainty range. Each data set are fitted with a linear function to retrieve the coefficient and determine the activation energy.

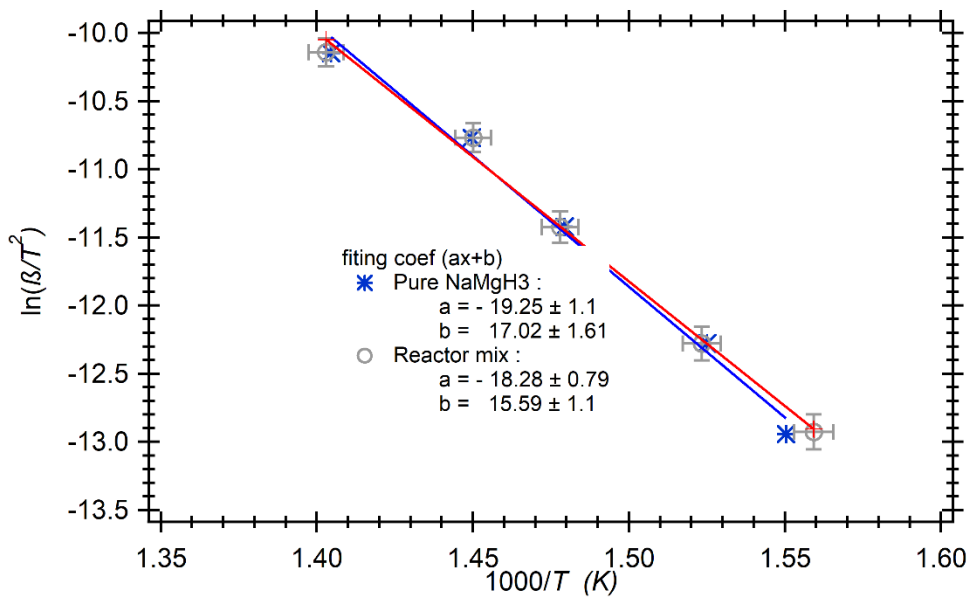


Figure 3-8 - Kissinger plot for the Reactor Mix (black circle) and pure NaMgH₃ (blue stars).

The activation energy E_a for pristine hydride is calculated to be 160 ± 9 kJ/mol, where the Reactor Mix exhibits a slightly lower activation energy of 151.9 ± 6.6 kJ/mol, which is within the uncertainty. Meanwhile, this lower results tends to corroborate previous reports on the kinetics provided by Ti based alloys.^{90, 269} It is comparable with the 153.3 kJ/mol previously obtained when NaMgH₃ is mixed with K₂TiF₆, but not as effective as when carbon nanotubes are incorporated.^{266,267}

Since the hydrogen absorption corresponds to a thermal energy release, it is of interest to gather information on the hydrogen uptake kinetics. For this purpose, the custom made Sieverts apparatus, described in chapter 2, offers the possibility of supplying various hydrogen inlet pressure at a fixed temperature and monitoring the time required for absorption. Figure 3-9 reveals the reacted fraction of the reactor mix upon hydrogen uptake for temperatures between 390 °C and 450 °C. In all cases, 90 % of the hydrogen capacity is absorbed within 5 min; moreover, the increase of the hydrogen supply pressure induces an acceleration of the reaction rate. However, a limited kinetic improvement is observed when the hydrogen supply pressure increases from 6 bar to 8 bar. This suggests the existence of a maximum reaction rate. For temperatures of 410 °C and higher, at a hydrogen supply pressure of 6 bar, the reaction attains 80 % completion in approximately 2 minutes. This rate is enhanced for the highest temperature tested, 450 °C, when the hydrogen supply pressure is increased from 6 bar to 8 bar.

Because the equilibrium pressure progresses with temperature increase; i.e. at 410 °C the equilibrium pressure is 1.96 bar and at 450 °C equilibrium pressure it is 4.46 bar; it seems that an overpressure of hydrogen supply can improve hydrogen uptake of NaMgH₃ for up to 5 bar above the equilibrium pressure. For higher overpressures, another limiting factor such as the formation of an hydride layer as suggested by Spatz *et al.* for MgH₂ seems to impede further reaction rate acceleration.²⁷²

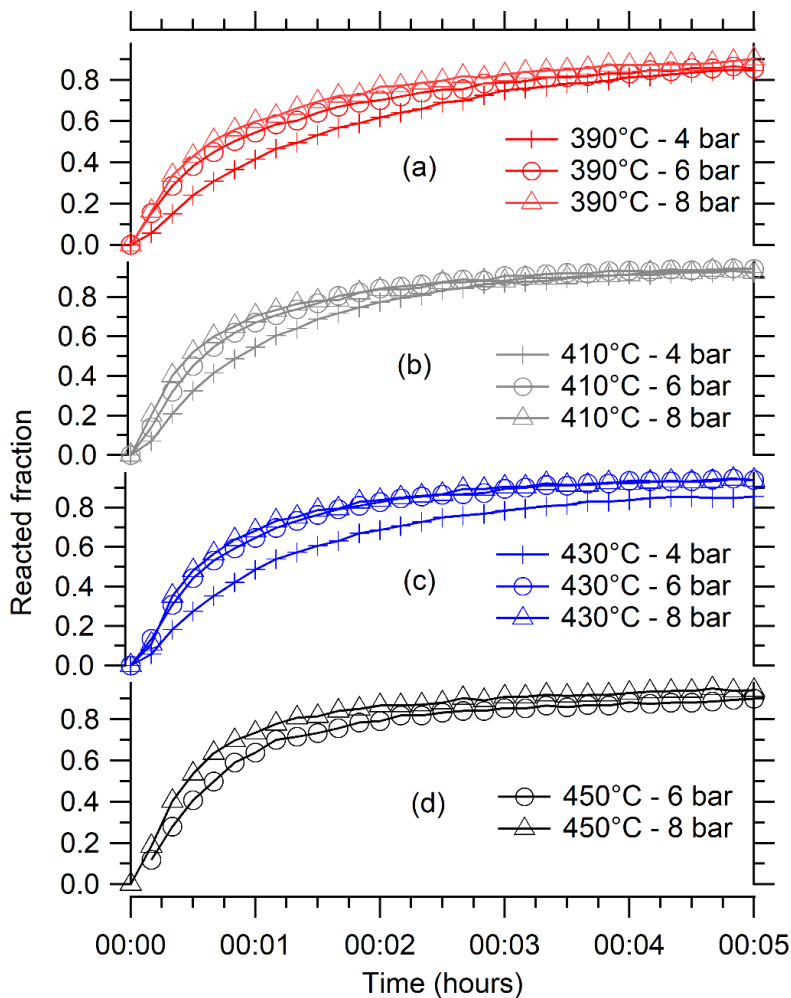


Figure 3-9 - Hydrogen absorption kinetic plots for the reactor mix at various supplied pressures for temperatures: (a) 390 °C, (b) 410 °C, (c) 430 °C and (d) 450 °C.

3.3.3.1.5. Thermal conductivity

The ability of a thermochemical heat storage material to transfer heat to a heat transfer fluid is instrumental to guarantee an efficient energy accumulation, diffusion and release. Metal hydrides inherently display low thermal conductivity values due to their powdered nature.²⁷³ Their compaction into pellets reduces voids between particles and improves heat transfer capacity, however this morphology doesn't sustain repetitive high temperature and pressure cycling.²⁷⁴ Another option is the addition of neutral thermal conductivity enhancers. Expanded natural graphite (ENG) has already demonstrated excellent results on thermal conductivity improvement.^{89, 91, 275} As shown Table 3-4, the addition of ENG almost triples the thermal conductivity of the Reactor Mix.²⁷⁶

Table 3-4 - Thermal conductivity of pristine NaMgH₃ and Reactor Mix, measured by TPS (Section 2.5.4). (Reprinted from co-authored paper ²⁷⁶)

Sample ID	Thermal Conductivity (W/mK)	Thermal Diffusivity (mm ² /s)	Volumetric Specific Heat (MJ/m ³ .K)
NaMgH ₃	1.84 (±0.02)	3.2 (±0.2)	0.58 (±0.04)
NaMgH ₃ -ReactorMix	5.15 (±0.07)	2.2 (±0.1)	2.4 (±0.2)

3.3.3.1.6. Summary

The developed NaMgH₃ based reactor mix is synthesised by ball-milling and annealing, using pure magnesium as a reagent. It offers a consistent 2.6 wt% of hydrogen capacity with an enthalpy of reaction $\Delta H = 86.6$ kJ/mol H₂. Hence the practical gravimetric energy density equates to 1120 kJ/kg.

The reaction rate of the mix attains 90 % hydrogenation in a few minutes, and the thermal conductivity has an improved value of 5.15 W/m.K.

This positions the developed material as an excellent candidate to be tested in a thermal energy storage prototype to investigate further feasibility. A complete presentation of the experimental set up and its results is given in Section 2.8 and Chapter 5, respectively.

3.3.3.2. Mg₂FeH₆

3.3.3.2.1. Introduction

Dimagnesium iron hexahydride (Mg₂FeH₆) is also an advantageous material for high temperature thermal storage compared to magnesium hydride (MgH₂) due to a higher operating temperature (550 °C) and lower price of Fe metal.²²⁷ This explains why the material has been discussed as a high temperature thermal energy storage. In 2002, thermodynamic investigations reported by Bogdanović *et al.* indicated a practical hydrogen capacity around 5.2 wt%, almost reaching the theoretical value of 5.47 wt%.⁷⁴ The pressure-composition isotherms also revealed a relatively flat plateau for hydrogen desorption and absorption, accompanied by a negligible hysteresis effect. The enthalpy determination for the reversible reaction was 77.4 kJ/mol H₂ resulting in an energy density of 2100 kJ/kg.

In 2016, Urbanczyk *et al.* demonstrated successful high temperature thermal energy storage feasibility of Mg₂FeH₆ for 23 cycles.⁹⁹ Based on the hydrogen mass uptake, ≈ 1500 kJ/kg of thermal energy was released at operating temperatures ranging between 395 °C and 515 °C. However, issues with the molten salts used as a heat transfer fluid prevented additional analysis. More recently, Polanski *et al.* successfully synthesised the hexahydride from plain steel and magnesium hydride opening a path to cheap hydride formation.²⁷⁷

Mg₂FeH₆ is an attractive candidate for future development of thermochemical high temperature thermal energy storage. It justifies further developments and investigations towards an industrial application.

3.3.3.2.2. Synthesis of Mg₂FeH₆

The literature shows that Mg₂FeH₆ synthesis can be achieved by various methods. Didisheim *et al.*, mixed 2 moles of Mg with one mole of Fe, compressed it into a pellet, which was then placed in a furnace at temperatures between 450 °C and 520 °C under

hydrogen pressures up to 120 bar.²⁷⁸ After 2 to 10 days, the product was suspended in chloroform. The magnetic stirrer sequestered unreacted iron molecules. The remaining Mg and MgH₂ was then removed through a suspension of 1,2-dibromoethane that allowed the Mg₂FeH₆ to sink while the reactants were floating.²⁷⁸ A procedure with this many steps offered a high yield of ≈ 90 %, but required extended time. In 1998, Huot *et al.*, improved the synthesis method by using mechanical milling during 20 hours under a hydrogen atmosphere and annealed at 350 °C under 50 bar of hydrogen.²⁷⁹ This method offered a 65 % yield, better than when the reactants were milled under argon. A year after, Huot *et al.*, reported a direct synthesis by milling Fe metal and magnesium hydride with a 53 % yield.²⁸⁰ The team showed the capacity of the hydrogen present in the MgH₂ phase to migrate and form Mg₂FeH₆. In 2010, Polanski *et al.*, achieved a 90 % yield by milling MgH₂ and Fe for 1 hour followed by high temperature (500 °C) and hydrogen back pressure above 80 bar.²⁸¹ More recently, Witek *et al.* created a synthesis efficiency map depending on the milling time of MgH₂ with Fe and heat treatment temperature for the subsequent annealing process under 100 bar H₂.²⁸² A 90 wt% yield was obtained after 2 hours of milling followed by heat treatment at 460 °C.

For this project, these findings were compiled and applied to synthesise the hexahydride with Mg and Fe as reactants. After 2 hours of ball milling in an argon atmosphere, the Mg-Fe mixture was annealed at high temperature (between 450 °C and 500 °C) and various hydrogen pressure (between 40 bar H₂ and 80 bar H₂) for one hour, and dehydrogenated at identical temperature under 1 bar H₂. This cycle was performed three times before cooling down under the high hydrogen pressure used for annealing. The samples were then analysed using XRD to determine the synthesis yield. Figure 3-10 presents diffraction patterns for 3 different heat treatment temperatures and pressures. The Rietveld refinement technique reveals that at 500 °C and 80 bar H₂, more than 85% of the sample is Mg₂FeH₆. An identical yield is obtained at a temperature of 460 °C under 60 bar H₂ with 80 % of targeted hydride formation. In contrast, when the sample is annealed at 450 °C under 40 bar H₂, only 22 wt% of Mg₂FeH₆ is found, displaying predominant formation of MgH₂. Hence the synthesis procedure at 460 °C under 60 bar hydrogen pressure was selected for producing larger quantities of Mg₂FeH₆.

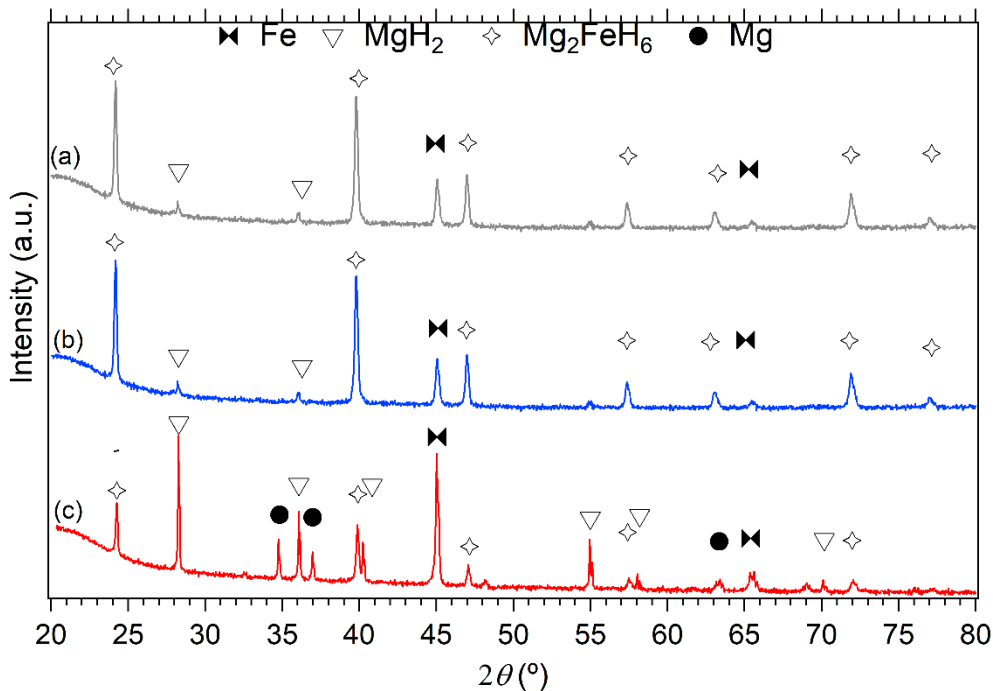


Figure 3-10 - X-ray diffraction pattern of different Mg_2FeH_6 annealing parameters; (a) 500 °C - 80 bar, (b) 460 °C - 60 bar, (c) 450 °C- 40 bar; $\lambda = 1.5418 \text{ \AA}$.

3.3.3.2.3. Thermodynamics of Mg_2FeH_6

The thermodynamic data for Mg_2FeH_6 has already been reported with an enthalpy of reaction of 77.4 kJ/mol H_2 .⁷⁴ It was deemed necessary to validate the results as applicable to our material.

Measurements were carried out in a conventional manner, on a sample weight of typically half a gram, using the custom made Sieverts apparatus presented in section 2.5.3. The pressure-composition isotherms for absorption were performed using a reference volume of $\approx 100 \text{ cm}^3$ and pressure steps based on a 2 bar addition every 2 hours. Figure 3-12 displays the pressure-composition isotherms for temperatures ranging between 410 °C and 490 °C. Each plot shows a relatively flat equilibrium pressure of absorption. Despite slight variations of the total hydrogen capacity, it can be averaged to 5 wt% H_2 which is 90 % of the theoretical capacity. The van 't Hoff plot Figure 3-11, compares the measured data to

those previously reported by Bogdanović *et al.* in 2002.⁷⁴ In the present case, the enthalpy of reaction and entropy are found to be 74.3 ± 1.3 kJ/mol H₂ and 132.2 ± 0.8 J/mol H₂.K respectively. A slight and consistent offset appears that can be accounted for by temperature measurement uncertainty (0.7 %). Moreover, it is to note that the Bogdanović *et al* value of 77.4 kJ/mol H₂ was determined from the slope of their two extreme experimental temperatures, 350 and 525 °C. The reported value is lowered to 76 kJ/mol H₂ when all the experimental data reported are used to determine the slope and the associated enthalpy.

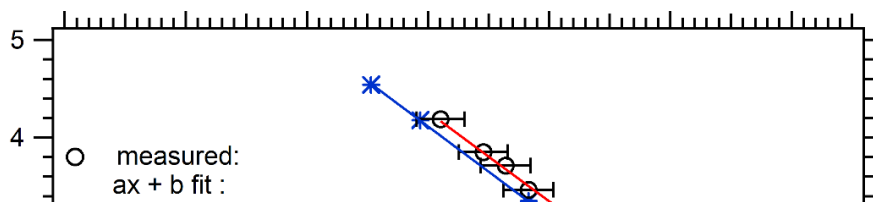


Figure 3-12 - Pressure-composition isotherms of Mg_2FeH_6 upon hydrogen absorption for temperature from 410 °C to 490 °C.

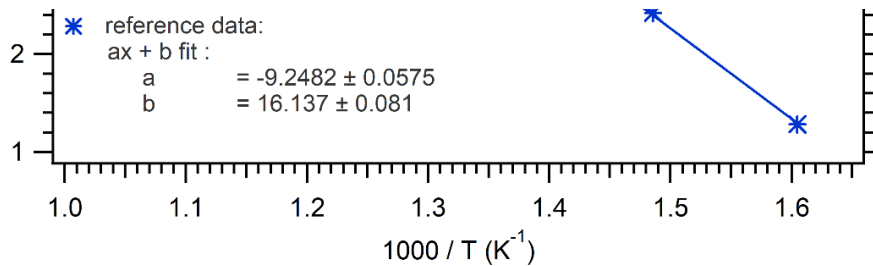


Figure 3-11 - Van 't Hoff plot of hydrogen absorption for Mg_2FeH_6 .

3.3.3.2.4. Reaction kinetics of Mg_2FeH_6

Kinetics of hydrogen absorption were measured using the custom-made Sievert apparatus, at operating parameters targeted for larger scale (≈ 1 kg of material) investigations. The hydrogen absorption curves of Mg_2FeH_6 at 430 °C and 450 °C are shown in Figure 3-13. For each test, the reaction is nearly completed under 15 min. A total absorption can be reached in less than 5 minutes, at 430 °C and 50 bar of supplied hydrogen pressure, which is 30 bar higher than the equilibrium pressure for this operating temperature. When the supplied hydrogen pressure is set at 42 bar, or 22 bar above equilibrium, the hydrogen up-take is almost complete in ≈ 7 minutes. The same result is found for a hydrogen absorption at 450 °C and 50 bar, which also corresponds to a 22 bar overpressure compared to the equilibrium pressure (28.5 bar). This shows, for operating temperatures ranging between 430 °C and 450 °C, that the kinetics of absorption can be tailored by the difference between equilibrium and supplied hydrogen pressure regardless the temperature level.

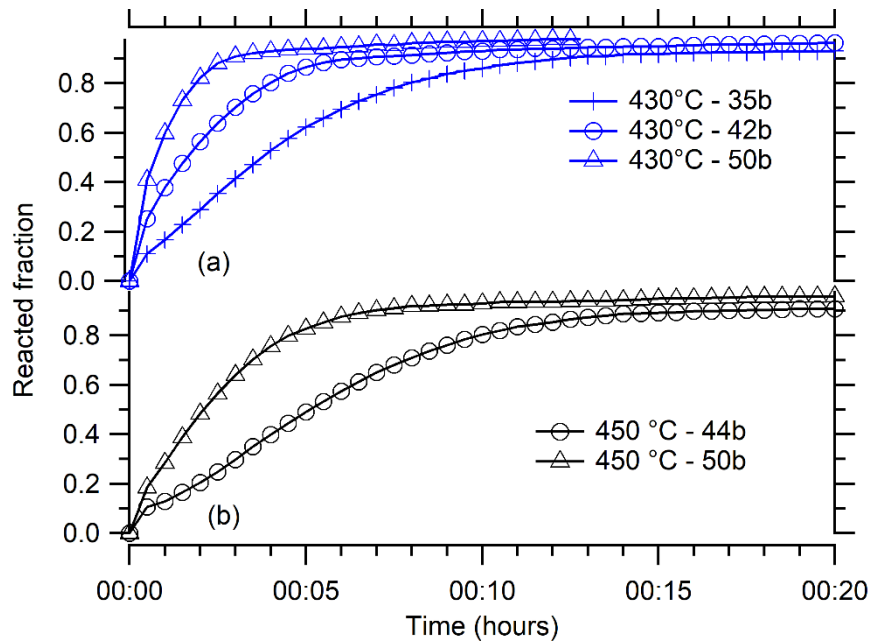


Figure 3-13 - Mg_2FeH_6 absorption kinetics for different hydrogen supply pressure at (a) 430 °C and (b) 450 °C.

Figure 3-14 displays an absorption kinetics plot for pure Mg_2FeH_6 and Mg_2FeH_6 with a 10 wt% of ENG added. For operating temperatures of 430 °C and 450 °C, a hydrogen over pressure of ≈ 13 bar above the equilibrium pressure was applied. In both cases, the time required to complete hydrogenation is greater for the sample containing ENG. Therefore, in large scale usage of this material, the addition of ENG shall be discarded.

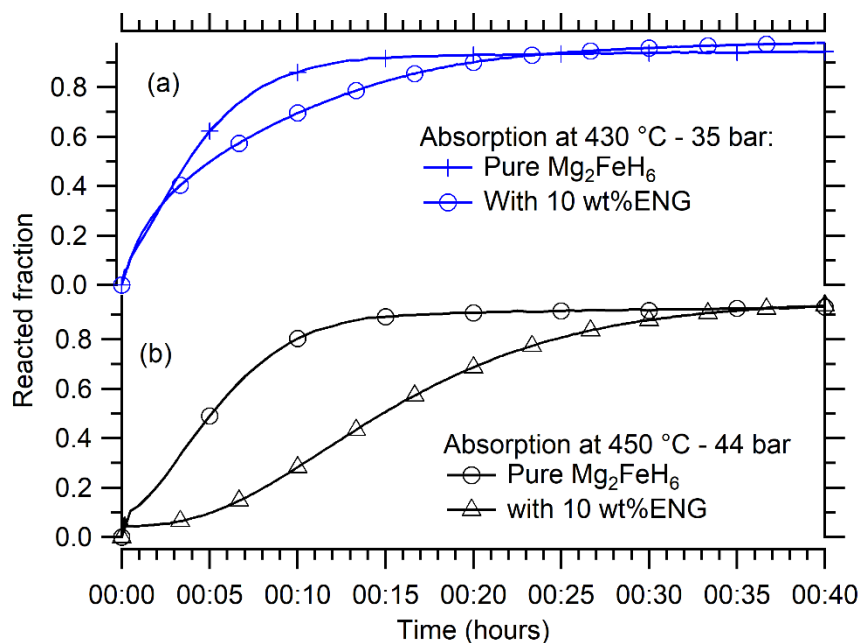


Figure 3-14 - Kinetics of Mg_2FeH_6 absorption at (a) 430 °C and (b) 450 °C for the pure hydride and with 10 wt% ENG added.

3.3.3.2.5. Thermal conductivity

Examinations of thermal properties were achieved using the TPS method described in chapter 2. As for the previous material, NaMgH₃, the pristine Mg₂FeH₆ exhibits a low thermal conductivity of 1.80 ± 0.02 W/m.K. Table 3-5 displays results obtained when Mg₂FeH₆ is mixed with additional iron metal, due to its high value of ≈ 80 W/m.K, or ENG that has already showed ability to tailor thermal conductivity.⁸⁹

The addition of iron metal, up to 25 wt%, doesn't provide any conductivity enhancement. The possible explanation may be found in the materials densities, with the iron density being 3 times higher than that of magnesium hydride (7.87 kg/m³ and 2.74 kg/m³, respectively). The small volume of added iron, less than 9 % for 25 wt%, doesn't provide significant pathways to induce enhanced heat diffusion. In contrast, the inclusion of a small mass of ENG reveals a significant improvement of the thermal conductivity with a value reaching 4.43 ± 0.05 W/m.K with a 5 wt% of ENG added, which is more than double the value for that of pure Mg₂FeH₆. However, as it was shown previously (section 3.3.3.2.4), the latter presents a hindering effect on the hydrogen absorption kinetics, which is the reason why ENG was not added in the larger scale experiments presented in Chapters 4 and 6.

Table 3-5 - Thermal conductivity for mixtures of Mg₂FeH₆ measured by TPS (Section 2.5.4). (Partly reprinted from co-authored paper ²⁷⁶)

Sample ID	Thermal Conductivity (W/mK)	Thermal Diffusivity (mm ² /s)	Specific Heat (MJ/m ³ .K)
Mg ₂ FeH ₆	1.80 (±0.02)	1.3 (±0.1)	1.39 (±0.08)
Mg ₂ FeH ₆ -10wt% Fe	1.72 (±0.03)	1.4 (±0.1)	1.3 (±0.1)
Mg ₂ FeH ₆ -25wt% Fe	1.73 (±0.03)	1.4 (±0.1)	1.2 (±0.1)
Mg ₂ FeH ₆ -5wt% ENG	4.43 (±0.05)	2.6 (±0.1)	1.73 (±0.07)
Mg ₂ FeH ₆ -10wt% ENG	6.76 (±0.04)	1.8 (±0.2)	3.7 (±0.3)

3.3.3.2.6. Summary

The thermodynamic study of Mg_2FeH_6 revealed slightly lower values than reported in the literature and the gravimetric energy density of 1850 kJ/kg shall be considered for later investigations. The kinetic study of hydrogen absorption revealed fast rates for operating temperatures at ≈ 450 °C and 50 bar of hydrogen pressure. Despite a favourable impact of ENG addition on the thermal conductivity, the kinetic hindrance observed motivated the decision of not using this additive for large scale investigations presented in chapter 6.

Chapter 4 High temperature metal hydride paired with a low temperature metal hydride

“Experiment is the sole source of truth. It alone can teach us something new; it alone can give us certainty.”

Henri Poincaré, [Science and Hypothesis](#).

4.1. Introduction

As seen in the previous chapters, metal hydrides offer attractive characteristics as thermal energy storage materials and could be an adequate alternative to sensible thermal energy storage at high temperatures. The targeted applications such as waste heat recovery or energy storage from CSP involves large storage capacity and, therefore, a substantial amount of hydride and hydrogen. For example, if magnesium iron hydride was used to replace the 13200 GJ of thermal energy storage of the Crescent Dunes power plant in Nevada,²⁸³ the mass of heat storing material could be reduced from 32,000 tons to 6,300 tons (based on the enthalpy of reaction) and would also involve ≈ 350 tons of hydrogen.^{74,}

284

The hydrogen desorbed during heat storage has to be stored and remain available for the subsequent heat discharge or hydrogen absorption. To limit operational costs, a hydrogen gas storage solution at ambient temperature matching the operational pressure seems essential. Amongst the hydrogen storage possibilities, it was shown that interstitial metal hydrides, such as LaNi_5 or TiFe , were able to comply with such a requirement.²⁸⁵ Nonetheless, material cost or troublesome activation procedure have impeded their usage. In this chapter, a brief overview of coupled hydrides systems is presented, followed by the selection strategy of materials. Then, an experimental study of a high temperature metal hydride (HTMH) paired with a low temperature metal hydride (LTMH) as a hydrogen store, is presented with an analysis of operational capabilities and limits.

4.2. Coupling principle

The principle of a coupled metal hydride system for thermal energy storage is based on a HTMH releasing hydrogen, which is absorbed by a low temperature metal hydride (LTMH). Ideally, the absorption of hydrogen by the LTMH would allow the system to have negligible gas pressure variations during cycles. The hydrogen should be able to flow autonomously involving no moving parts, which represents an excellent robustness advantage during operation. In the initial stage, the HTMH shall be fully hydrogenated at lowest operating temperature and the LTMH fully dehydrogenated at ambient temperature (≈ 25 °C). During

heat storage, the HTMH temperature is increased, which induces hydrogen desorption. The hydrogen released increases the system gas pressure while thermal energy is being stored. When the system gas pressure reaches the level of the LTMH equilibrium pressure (based on thermodynamics), it begins to absorb hydrogen. This means that the pressure required for the LTMH to absorb hydrogen must be at an equivalent level to that of the HTMH when it is at the low operational temperature. For example, as seen in Chapter 3, for an operational temperature of 450 °C for Mg_2FeH_6 , the equilibrium pressure of the LTMH should be around 30 bar H_2 . When the HTMH has fully completed dehydrogenation, the system pressure shall remain equal to the HTMH equilibrium pressure corresponding to its temperature level. As soon as the HTMH temperature decreases (e.g. night time), its equilibrium pressure drops accordingly and hydrogen shall flow back causing an exothermic reaction to occur. When the system gas pressure drops below the equilibrium pressure of the LTMH, the hydrogen desorption is initiated and allows the stored gas to flow back into the HTMH to generate heat. As long as the generated energy doesn't maintain temperature level, the equilibrium pressure of the HTMH continues to decrease and induce further hydrogen absorption until the LTMH reaches a fully hydrogenated state once again.

It should be noted that the LTMH also endures thermal variations due to hydrogen uptake and release. The reaction enthalpy creates these variations, and heat should be dissipated and/or provided according to enthalpy value. For the LTMH, as opposed to the HTMH, a low enthalpy of reaction is preferable to limit the thermal energy exchange requirement (for example, one kilo of hydrogen absorbed in a LTMH that has an enthalpy of reaction of 25 kJ/mol H_2 would generate nearly 12500 kJ that would need to be discarded .

4.3. Literature review

The first coupled metal hydride system was investigated by Nagel *et al.*, who paired a LaNi_5 based hydride with a mischmetal (typically made of minimum 50 wt% of cerium) based hydride as the LTMH.²⁸⁶ LaNi_5 was heated up to 150 °C to obtain about 70 % of the hydrogen capacity flowing and revealed the importance of the pressure-composition relationship. A numerical study of the same materials was later developed by Bjurström *et al.* and improved By Gambini.^{287, 288} Their heat and mass transfer investigations led to the establishment of the crucial influence of heat transfer performance to enhance the system

efficiency. It was also underlined by Isselhorst, who developed a model to link the hydrogenation state with the metal hydride's local temperature.²⁸⁹

Even though coupling two metal hydrides has attracted several research studies, the applications were mainly directed towards hydrogen storage alone, and therefore the aim was to limit the operational temperatures (< 150 °C). Bogdanović *et al.* were the first to report successful coupling of Ni doped MgH₂, as a heat storage material, with a Ti-Mn alloy coded 5800.⁸⁴ They reported 1600 cycles at the maximum temperature of 350 °C without hydrogen capacity losses. Wierse *et al.* also reported the design of small scale coupled thermal energy storage based on a Ni doped magnesium hydride.²⁹⁰ However, no results on the experiments were published. It was in 2017 that d'Entremont *et al.* reported the modelling of a coupled hydride system for high temperature thermal energy storage, at operating temperatures between 400 °C and 500 °C.²³³ Magnesium iron hydride was used as a HTMH and the LTMH gas storage was sodium aluminium hexahydride (Na₃AlH₆, also called sodium hexa-alanate). The simulation showed an attractive 83% energy efficiency on the HTMH at ≈ 450 °C with the LTMH at ≈ 160 °C. The thermal management of the LTMH in the study was not considered even though the LTMH seemed to divert a substantial part of the overall energy supplied from an external source.

A year later d'Entremont *et al.* reported a simulation study on a coupled system involving a low temperature hydrogen storage material operating at near ambient temperature.²⁹¹ The pair were NaMgH₂F as the HTMH and TiCr_{1.6}Mn_{0.2} as the LTMH and offered a storage capacity 1416 kJ/kg. However, a slow hydrogen absorption by the HTMH was admitted to be a hindrance. Moreover, experimental studies on fluoride substitution on sodium or magnesium reported a rapid decrease of the hydrogen capacity when cycled at ≈ 500 °C.^{96, 292} The capacity drop was attributed to the metallic sodium vaporisation, which the fluoride addition was unable to prevent. Experimental operation of a coupled metal hydride system for high temperature energy storage has been little studied, therefore the present chapter describes the operation of an experimental system and validates its feasibility.

4.4. Material election

4.4.1. High temperature metal hydride (HTMH)

The investigations on the suitable HTMH presented in Chapter 3 led to the election of a mixture of pure magnesium and iron to form Mg₂FeH₆ as a suitable material to perform the

following experimental study of a coupled system. The hydride presents in its pure form, shows satisfactory reversibility, rapid kinetics and operating temperatures up to 550 °C.⁷⁴

4.4.2. Low temperature hydride for storing hydrogen from HTMH

Storing hydrogen at near ambient temperature has been the aim of many researchers on metal hydrides for decades.^{159, 231, 293, 294} As presented in Chapter 1, different technologies are under investigation to address this challenge. Amongst them, Intermetallic metal hydrides present a wide range of compounds that offer consistent hydrogen capacity upon cycling at near ambient temperature.²⁸⁵ Though, this type of hydride generally displays a low gravimetric capacity of ≈ 2 wt%, as shown in Figure 4-1.¹⁵⁵

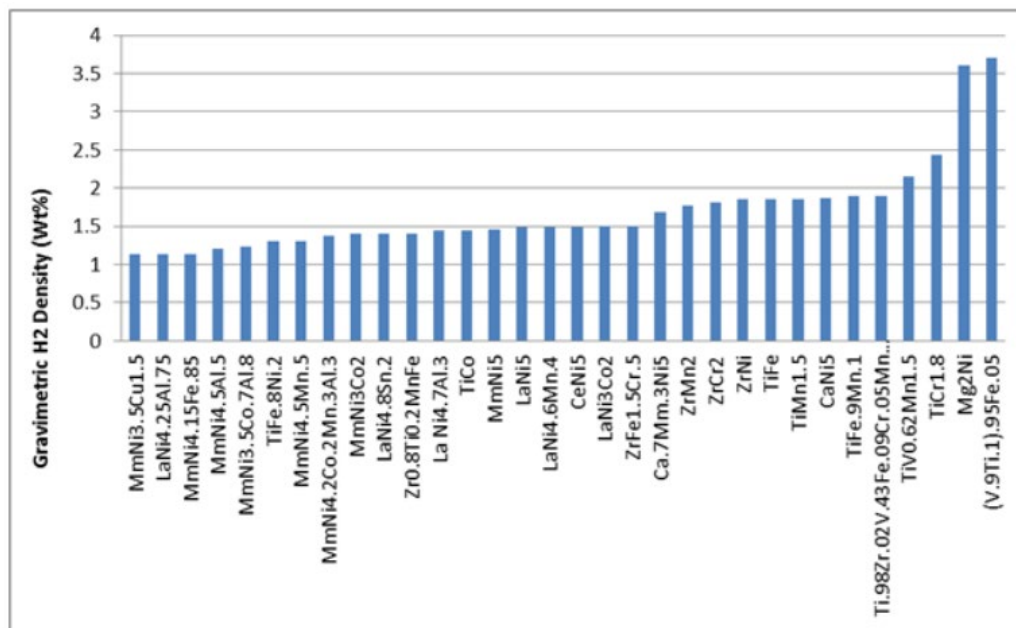


Figure 4-1 - Example of intermetallic metal hydrides for near-ambient hydrogen storage.¹⁵⁵

The specific behaviour of a coupled system demands the LTMH paired with a HTMH to comply with, not only consistent hydrogen capacity, but also with a series of properties to be a successful applicant. Primarily, the operating pressure (equilibrium pressure at ambient temperature) should match that of the HTMH at its high operating temperature. The reaction kinetics should be fast enough to not be a limiting factor for the HTMH to

absorb and release hydrogen. The heat involved in the reaction with hydrogen gas should remain low to minimise the need for thermal management. The hydrogen capacity, as well as the price of the material, must also be taken into consideration. Table 4-1 presents a list of hydrogen capacities of potential LTMHs to be paired with Mg_2FeH_6 as a HTMH, along with their equilibrium pressure at ambient temperature, enthalpy of reaction, and cost of raw material to store 10 kg of hydrogen.

Table 4-1 - List of potentially suitable LTMH.

Compound	H ₂ wt% capacity	Equilibrium pressure for 25 °C (bar)	Enthalpy (kJ/ mol H ₂)	Minimum mass required to store 10 kg of H ₂ (kg)	Raw material cost to store 10 kg of H ₂ (USD)	Ref
TiFe	1.9	4.1	29	526.3	3,610	295, 296
TiFe _{0.8} Mn _{0.1}	1.9	2.6	29.3	531.9	3,730	295, 297
V	3.8	2.1		263.2	103,930	295
LaNi ₅	1.5	1.8	30.8	666.7	41,340	295, 298
LaNi _{4.7} Al _{0.3}	1.4	0.4	33.9	714.3	44,570	295, 297
CaNi ₅	1.2	0.5	31.8	833.3	19,760	295, 297, 299
TiCr _{1.8}	2.4	182	20.2	416.7	5,980	295, 300
TiMn _{1.5} (alloy)	1.9	8.4	21.7	526.3	4,050	295, 301
MmNi ₅	1.5	23	21.1	666.7	6,670	300, 302
NaAlH ₄	3.7	0.7	38.4	270.3	1,030	237, 295

Table 4-1 shows some compounds offering hydrogen capacity above 3 wt%, and others between 1.2 and 2.4 wt%. The operating (or equilibrium) pressure at ≈ 25 °C ranges between 0.4 bar and 23 bar, excluding TiCr_{1.8} with an equilibrium pressure of 182 bar, which is prohibitive. The enthalpies of reaction are mostly ≈ 30 kJ/mol H₂ apart from TiCr_{1.8}, TiMn_{1.5} and MmNi₅ which are ≈ 20 kJ/mol H₂. Prices of raw materials are also an interesting indication regarding the applicability of these hydrides on an industrial scale and the variations are not negligible. However, as previously stated, the main parameter to couple

a LTMH to Mg_2FeH_6 is the operating pressure. As the HTMH operational temperature targeted for this experiment is ≈ 400 °C and above, the equilibrium pressure of the LTMH should be at least 7 bar at ambient temperature (25 °C), as shown in Figure 4-2, which prevents the need for active cooling of the LTMH.

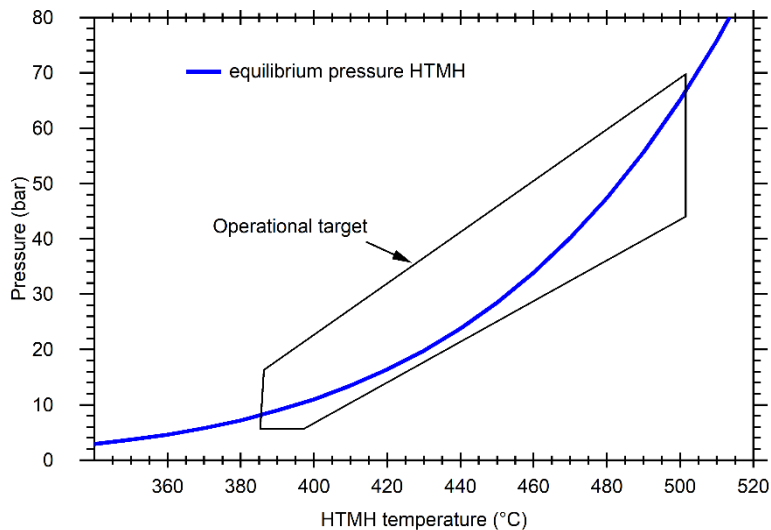


Figure 4-2 - Equilibrium pressure for Mg_2FeH_6 as the HTMH and operational target.

$TiMn_{1.5}$ and $MnNi_5$ display equilibrium pressure at 25 °C of 8.4 bar and 23 bar respectively.^{300, 301} For this study, preference was given to $TiMn_{1.5}$ (alloy) due to its superior hydrogen capacity (1.9 wt%) and a lower cost of the raw material. However, this material displays (as most intermetallic hydrides do) a substantial hysteresis effect (Figure 4-3) between the absorption and desorption equilibrium pressure.³⁰¹ It is also noticeable that the hydride offers a variable reversible hydrogen capacity depending on temperature, i.e. 1.5 wt% and 1.6 wt% of hydrogen at 40 °C and 25 °C respectively.

Figure 4-4 illustrates the correlation between the HTMH and LTMH equilibrium pressure based on operating temperature. It shows that for a system pressure of 8 bar, the LTMH is fully dehydrogenated for temperatures of 20 °C and higher, when the equilibrium temperature of the HTMH is ≈ 380 °C. To fully hydrogenate the LTMH at a temperature of 25 °C, the system pressure needs to reach ≈ 34 bar H_2 . The equilibrium temperature of the HTMH at a pressure of 34 bar is ≈ 460 °C. This implies that it is possible to cycle the HTMH between 380 °C and 460 °C and use the full hydrogen capacity of both hydrides.

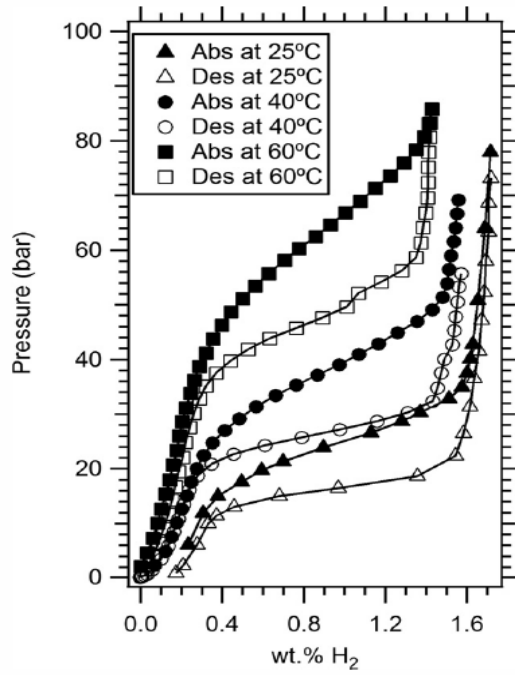


Figure 4-3 - Pressure composition isotherm of $TiMn_{1.5}$.³⁰¹ (Reprinted with permission of Elsevier)

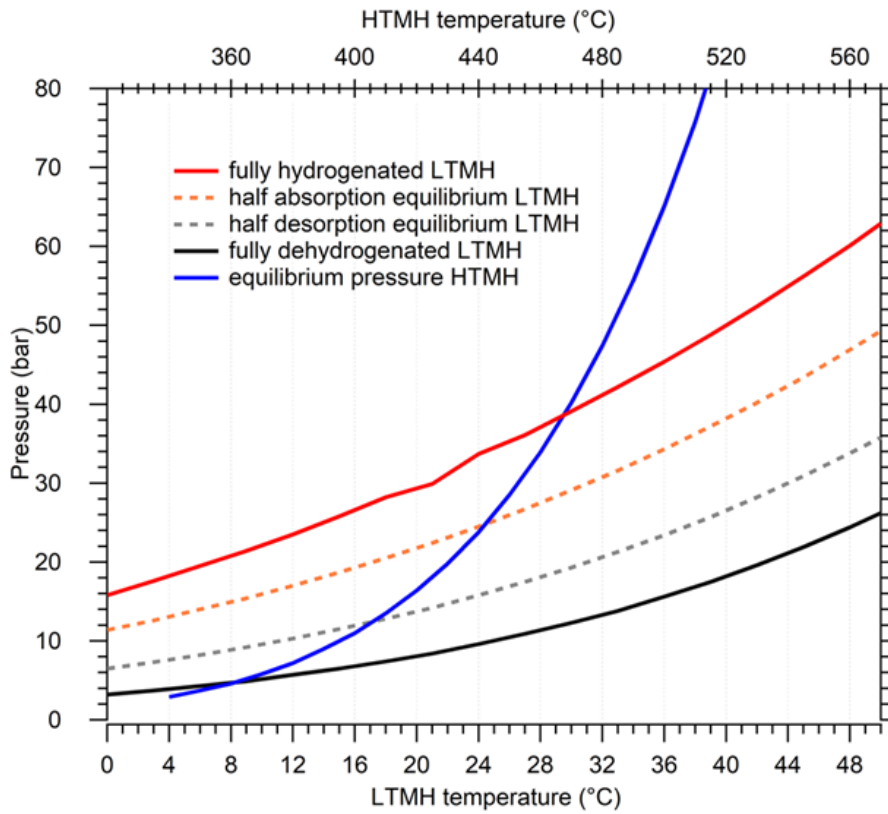


Figure 4-4 - Equilibrium pressure curves for Mg_2FeH_6 as HTMH and $TiMn_{1.5}$ as LTMH.³⁰¹

4.5. Cycling investigations

4.5.1. Cycling HTMH thermally with LTMH at ambient temperature

The initial state of the coupled thermal energy storage was set according to the analysis made from Figure 4-4, the HTMH temperature was elevated to 350 °C, and the closed system was loaded with 8 bar of hydrogen. The HTMH was then heated to 450 °C (10 °C/min) to simulate heat storage and promote hydrogen desorption. Figure 4-5 displays seven thermally driven cycles of the HTMH hydrogen desorption and absorption between 350 °C and 450 °C, along with the LTMH temperature variations induced by the gas storage and the overall system gas pressure evolution.

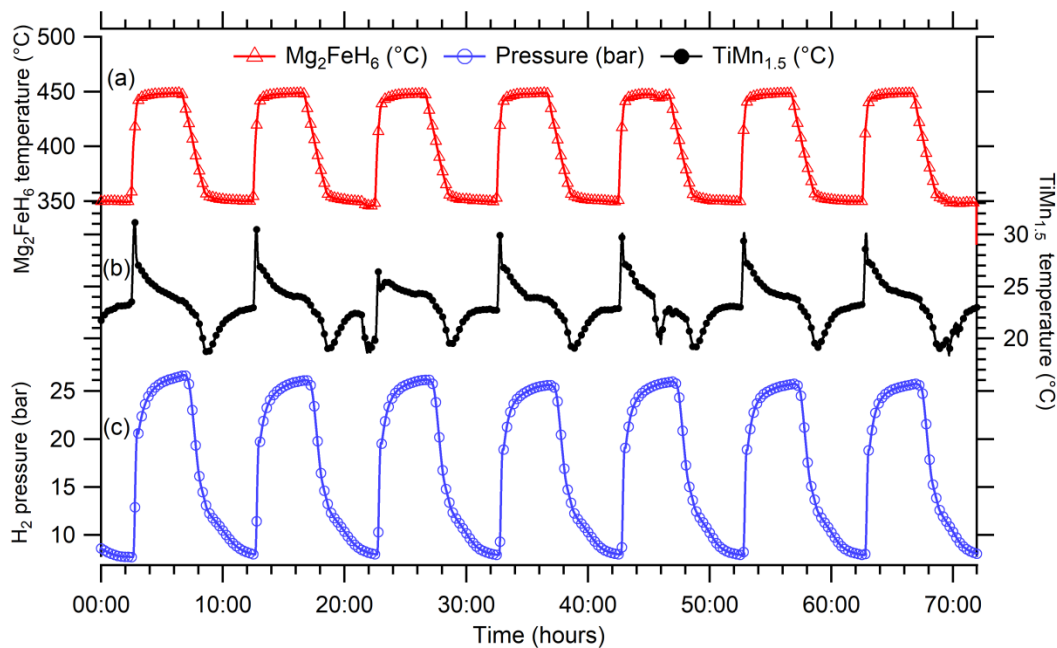


Figure 4-5 - (a) Cycling of HTMH between 350 °C and 450 °C, (b) associated temperature excursion of LTMH and (c) associated system pressure evolution.

The LTMH pattern reveals an increase in temperature from 22 °C to 27 °C with a short peak at 31 °C; this rise is caused by the absorption of the hydrogen into the LTMH that was released by the HTMH. It demonstrates the fast absorption kinetics of the LTMH. Likewise, when the HTMH starts to cool down, the LTMH also endures a temperature decrease caused by its hydrogen desorption. In these cycles the LTMH temperature drops to \approx 18 °C, which is below the ambient temperature.

The system gas pressure also fluctuates with cycles. During the heat storage process (HTMH desorption) it reaches ≈ 26 bar H_2 . When the hydrogen is reabsorbed by the HTMH, the system pressure returns to the original level of 8 bar H_2 .

The pattern in Figure 4-5 reveals the LTMH temperature and the system pressure remain relatively consistent during cycling, which testifies to the feasibility of such a pair. However, to further determine the thermal energy stored in the HTMH, an assessment of the quantity of hydrogen involved in the reactions is required.

Figure 4-6 displays three thermally driven cycles, identically thermally managed with the HTMH ranging between 350 °C and ≈ 450 °C. The temperature of both hydrides is depicted ((a), (b)), the system pressure (c) and the calculated hydrogen flow is illustrated (d).

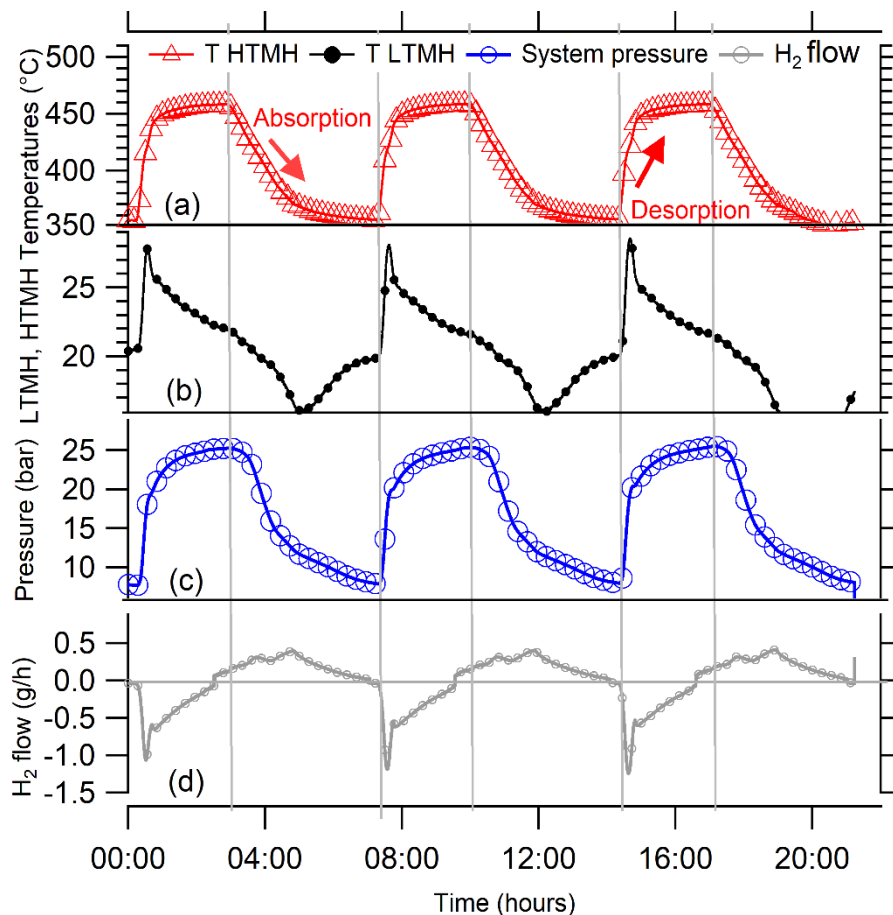


Figure 4-6 - (a) HTMH temperatures, (b) LTMH temperatures, (c) system pressure, (d) hydrogen flow 3 cycles when HTMH temperature oscillate between 350 °C and 450 °C.

During the HTMH desorption, the hydrogen flow peaks at 1 g/h and quickly drops by half before slowly declining to zero over the course of 3 hours. The integration of this repeatable pattern allows for the determination of the total mass of hydrogen flowing between both hydrides. Only 0.90 g of hydrogen was desorbed from the HTMH, while 0.15 g was held in the free gas volume to raise the system pressure. It is approximately half the expected hydrogen capacity of the HTMH. The gas pressure of 26 bar H₂ reached by the system corresponds to the Mg₂FeH₆ equilibrium pressure at 450 °C. Thus additional hydrogen release is prevented by the inherent thermodynamics of the HTMH. This system gas pressure also coincides relatively to the half absorption equilibrium pressure of the LTMH at ≈ 24 °C (Figure 4-4). Considering the LTMH absorbed between 0.75 - 0.80 g of the 0.90 g of hydrogen desorbed by the HTMH, the hydride absorbed about 50 % of the expected capacity. To achieve full LTMH hydrogenation, the system pressure should exceed 30 bar H₂. This emphasises the limitation caused by the pressure excursion required to operate TiMn_{1.5} alloy as a LTMH. It is thus imperative to tune the system to improve the mass flow of the hydrogen and therefore the thermal energy capacity of the HTMH. In addition, the hydrogen flow absorbed by the HTMH remained below 0.5 g/h, which didn't create any noticeable thermal event in the reactor. This flow equates to a power generation of 5 W, which rose the question of the possibility to extract such low power value.

4.5.2. HTMH working temperature optimisation

The temperature increase reached by the HTMH induces an elevation of the equilibrium pressure. Therefore, the hydride will desorb more hydrogen until approaching this equilibrium pressure. Moreover, a higher system gas pressure also allows the LTMH to absorb a significant fraction of hydrogen. Table 4-2 presents four representative HTMH desorption events (heat storage) with different maximum HTMH temperatures. It reveals the LTMH temperature excursions, the system gas pressure and the hydrogen mass flow in the system. The HTMH maximum temperature was evaluated from 410 °C to 500 °C. The gas pressure in the system as well as the LTMH maximum temperature increased accordingly. Furthermore, the hydrogen mass that was desorbed from the HTMH or absorbed by the LTMH also escalated with increased operating temperature. With the HTMH operating between 350 °C to 500 °C, the hydride desorbs 1.65 g of hydrogen which

almost equals the 4.4 wt% expected hydrogen capacity (from the yield obtained with the selected synthesis procedure, Chapter 3). Within this temperature range, the system gas pressure elevates to 37.5 bar H₂, which enables the LTMH to absorb a greater hydrogen mass. Indeed, the latter consequently absorbs 1.45 g of hydrogen which is \approx 95 % of its capacity.³⁰¹

This shows that the significant temperature differential is able and necessary to overcome the hysteresis involved in the LTMH hydrogen uptake and release.

Table 4-2 - Comparison of variables affected by the extension of the operating temperature range.

HTMH temperature (°C)			LTMH temperature (°C)		Gas pressure (bar)		HTMH Desorbed mass of H ₂ (g)	Hydrogen mass causing a system pressure increase (g)	LTMH Absorbed H ₂ mass (g)
min	max	DT	min	max	min	max			
350	410	60	18	22	7.2	14.5	0.40	0.05	0.35
350	455	105	15	27	7.5	26.0	0.90	0.13	0.75
350	480	130	17	32	8.5	30.0	1.30	0.16	1.10
350	500	150	14	32.5	8.5	37.5	1.65	0.21	1.45

(Temperatures and pressures have a 2% uncertainty; hydrogen masses have a 5% uncertainty).

4.5.3. Effect of free gas volume

The volume of free gas in the system can also alter the efficiency of the paired hydride thermal storage system. For each cycle, this free volume encounters pressure variations caused by a mass of hydrogen. Acting as a buffer, it inhibits the gas pressure rise in the system. The previous results demonstrated that this particular combination of metal hydrides requires a substantial pressure differential to operate thoroughly, due to the LTMH hysteresis phenomenon. Accordingly, a minimised free gas volume suggests an advancement of the system performances. The experimental set up was designed for a minimal free gas volume and a further reduction was impossible; therefore, a volume of 56.8 ml was appended to the set up and loaded with 8 bar of hydrogen. Some previous experiments were reproduced using the parameters displayed in Table 4-2.

Figure 4-7 illustrates a van 't Hoff style plot of the thermal cycle of the HTMH between 350 °C and \approx 500 °C, as well as the subsequent thermal response of the LTMH. The profile displayed by the HTMH and the LTMH is very similar whether the free gas volume is

enlarged or not. The extension of the free gas buffer limits the pressure rise in the system from 37.5 bar H₂ to 32.5 bar H₂ effectively diverting more gas to the larger volume.

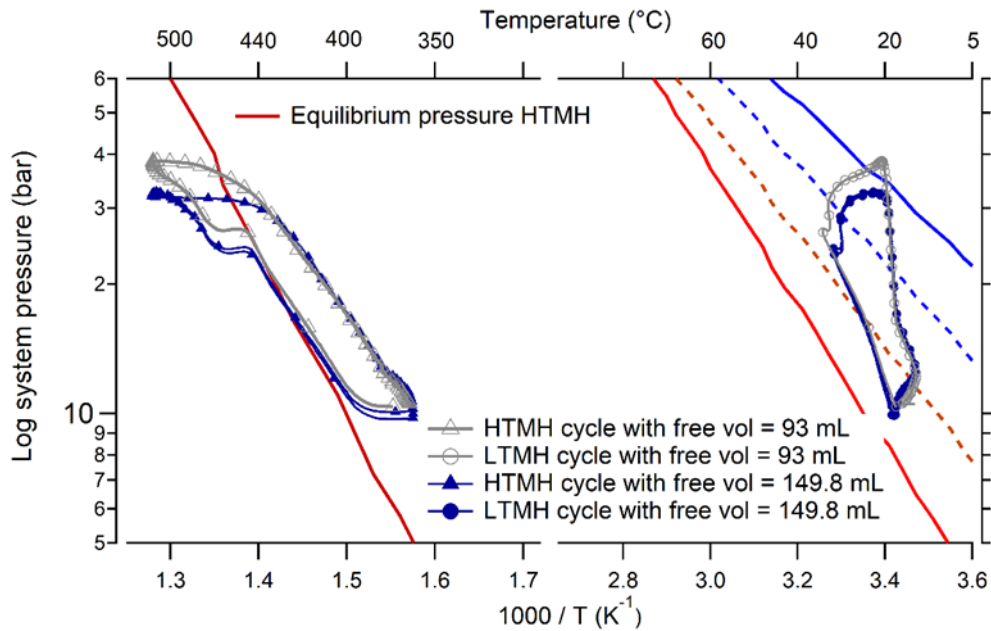


Figure 4-7 - HTMH cycling between ≈ 350 °C and ≈ 500 °C (left) and LTMH (right) with original and added volume; with their respective calculated equilibrium pressure plots. (Blue line: fully hydrogenated, blue dash: half hydrogenated, red line: fully dehydrogenated, red dash: half dehydrogenated).

Table 4-3 compares the system variables with two different free gas volumes for the HTMH cycling between 350 °C and a maximum temperature of 455 °C or 500 °C. It also shows that the increase of the free gas volume slightly limits the hydrogen release from the HTMH, and as the larger volume stores more gas the LTMH hydrogen uptake is lowered. Therefore, in a system exempt of free gas volume (or if this volume is negligible compared the overall gas volume involved in such thermal storage), a lower HTMH temperature variation would be required to obtain similar efficiency obtained as with the 150 °C temperature differential required with this current setup.

Table 4-3 - Comparison of variables affected by variations in a free gas volume. (Temperatures and pressures have a 2% uncertainty; hydrogen masses have a 5% uncertainty).

Free volume (ml) (approx.)	HTMH temperature (°C)		LTMH temperature (°C)		Pressure (bar)		HTMH	Hydrogen causing system pressure raise (g)	LTMH
	min	max	min	max	min	max	Desorbed H ₂ mass (g)		Absorbed H ₂ mass (g)
93	350	455	15	27	7.5	26	0.90	0.14	0.75
150	350	455	16	26.5	8	23.5	0.80	0.19	0.60
93	350	500	14	32.5	8.5	37.5	1.65	0.22	1.45
150	350	500	15	32.5	10	32.5	1.60	0.28	1.30

4.5.4. Cycling HTMH thermally with elevated LTMH temperature

Another parameter that can affect the coupled metal hydride performance is the LTMH operating temperature. Theoretically, the increase of the LTMH operating temperature induces an increase in the equilibrium pressures. For example, as seen in Figure 4-4, if the LTMH temperature is averaging ≈ 40 °C, it can be fully hydrogenated and dehydrogenated at 15 bar and 50 bar H₂ respectively. Some experiments can further validate the behaviour of the paired hydrides under a heated LTMH. For this purpose the water bath, in which the LTMH vessel was submerged, was controlled at different temperature levels.

Figure 4-8 depicts temperature cycling of the HTMH fluctuating between ≈ 350 °C and ≈ 450 °C with a LTMH temperature regulated at ≈ 20 °C, 30 °C and 40 °C. The thermoregulation of the LTMH at increased temperature tends to smooth the temperature variations during cycling. Figure 4-8(a) refers to thermal anomalies caused by the thermo-regulation.

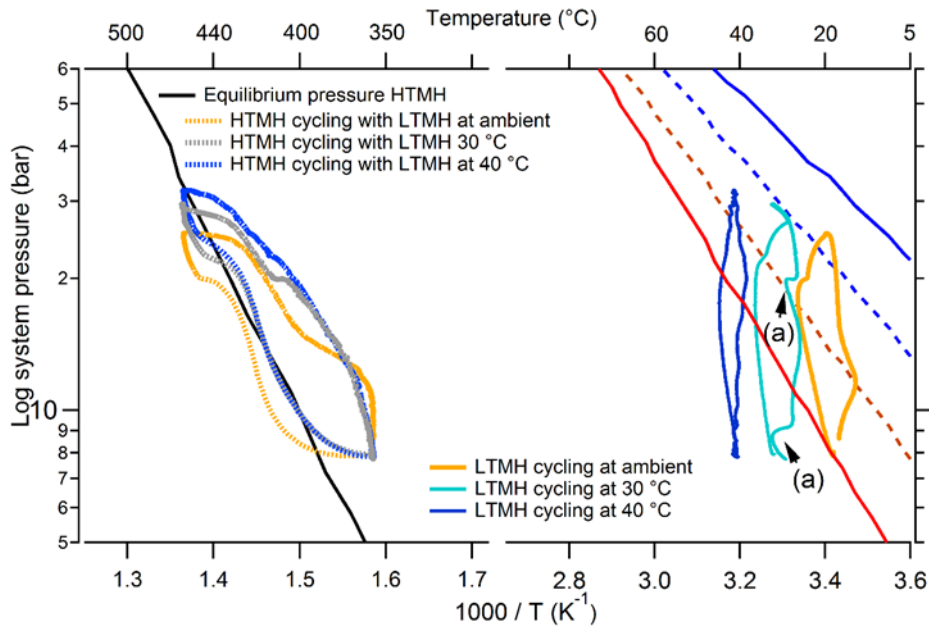


Figure 4-8 - HTMH (right) and LTMH (left) for different LTMH regulated temperatures (ambient, 30 °C, 40 °C). (Blue line: fully hydrogenated, blue dash: half hydrogenated, red line: fully dehydrogenated, red dash: half dehydrogenated). (a) points an anomaly caused by the water heater.

As revealed in Table 4-4, the increase of the LTMH average temperature for similar thermal cycles of the HTMH slightly increases the maximum pressure reached within the system. However, it diminishes the hydrogen mass desorbed during thermal energy storage as well as the hydrogen mass absorbed by the LTMH. This is due to a higher gas pressure required by the LTMH to reach full absorption. Therefore, a higher thermal energy storage temperature is necessary to adapt the HTMH equilibrium temperature.

HTMH temperature (°C)		LTMH temperature (°C)		Gas Pressure (bar)		HTMH Desorbed H ₂ mass (g)	Hydrogen for system pressure raise (g)	LTMH Absorbed H ₂ mass (g)
min	max	min	max	min	max			
350	455	15	27	7.5	26	0.9	0.15	0.75
350	460	25	35	8	30	0.8	0.17	0.63
350	460	36	42.5	8	33	0.65	0.19	0.46

Table 4-4 - Effect of average LTMH temperature change on the system variables.

Figure 4-9 depicts HTMH cycles with a maximum temperature of 450 °C or 520 °C with the associated LTMH cycles when thermo-regulated at 30 °C. The system reaches a gas pressure of ≈ 30 bar H_2 for the HTMH at 450 °C. The latter corresponds to the equilibrium pressure of the HTMH (Figure 4-4). It implies that the Mg_2FeH_6 can no longer release hydrogen unless its temperature increases. Indeed, when the HTMH cycles to a maximum temperature of 520 °C, a system pressure of 40.5 bar H_2 is attained revealing a greater mass of hydrogen released. This is verified by the calculated hydrogen mass released which approximates 1.7 g, which is almost 95 % of the expected mass released.

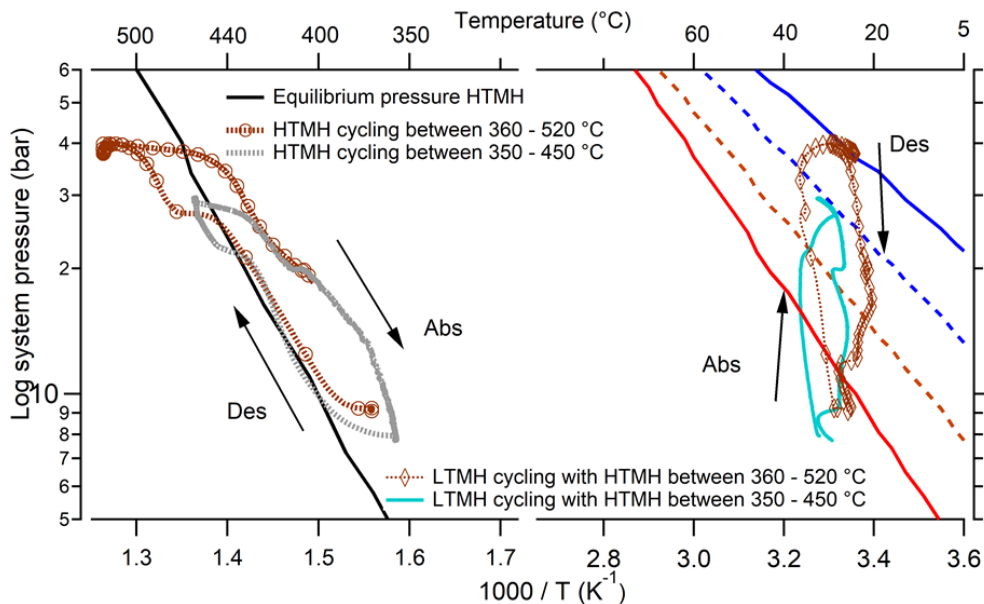


Figure 4-9 - HTMH (right) and LTMH (left) for different HTMH maximum temperatures (450 °C and 520 °C). (Blue line: fully hydrogenated, blue dash: half hydrogenated, red line: fully dehydrogenated, red dash: half dehydrogenated).

4.5.1. Cycling thermally the LTMH with the HTMH maintained ≈ 450 °C

An experiment was performed with the HTMH (Mg_2FeH_6) being maintained at a constant operating temperature (≈ 450 °C) while varying the LTMH (tiMn_{1.5} alloy) temperature. The test was initiated with the LTMH at 50 °C and the system loaded with 30 bar of hydrogen gas. These parameters were set so that the HTMH was fully hydrogenated and the LTMH in its metal form (as shown in Figure 4-3). Figure 4-10(a) displays the LTMH cooling to ambient temperature, before being heated up to ≈ 80 °C followed by cooling back to

ambient temperature. Consequently, the HTMH endured a hydrogen desorption followed by an absorption and another desorption, which were driven by the LTMH temperature management. The HTMH temperature evolution is also displayed in Figure 4-10(a) and reveals that it experiences a temperature drop of 5 °C on desorption whilst the gas absorption causes a 7 °C raise. The subsequent system pressure sustain variations that are also presented along with the dynamic equilibrium pressure of the HTMH (Figure 4-10 (b)). Initially, the system pressure of hydrogen was slightly above that of Mg_2FeH_6 equilibrium, the temperature drop of the LTMH induced a gas absorption that caused the system pressure to fall below the averaged HTMH equilibrium pressure but matches the equilibrium pressure of the coolest part of the reactor. Indeed, at 435 °C, the HTMH equilibrium pressure is approximately 23 bar H_2 , which may be the reason why the HTMH was desorbing 1.3 g of hydrogen (Figure 4-11(c)) instead of the 1.8 g corresponding to full dehydrogenation.

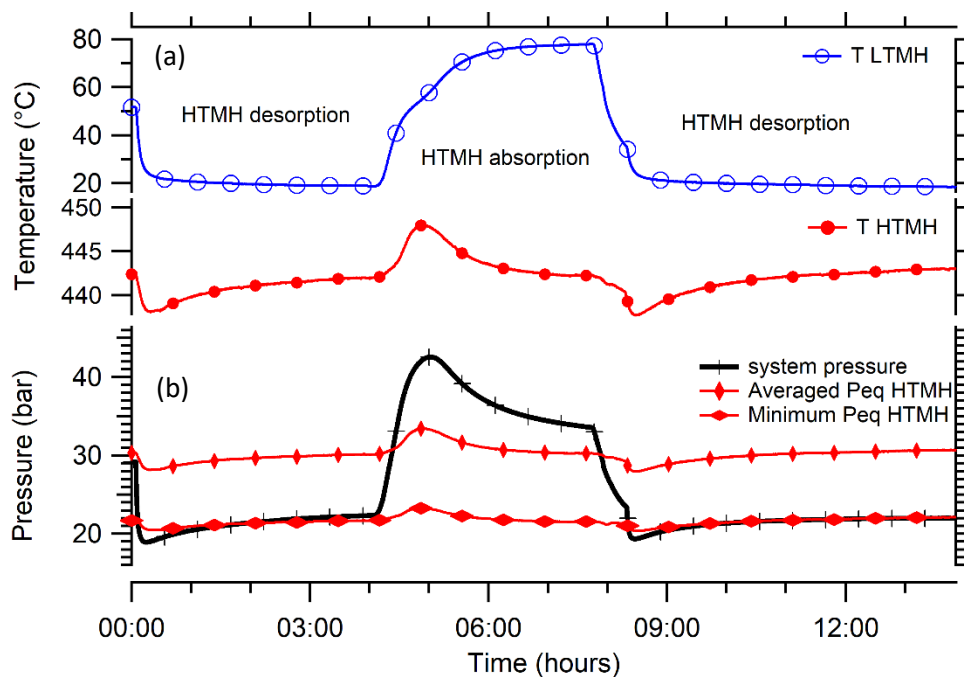


Figure 4-10 - Temperature evolutions of the LTMH and HTMH along with the system pressure and the HTMH equilibrium pressure (Peq, averaged and minimum).

Figure 4-11 (a) presents the system gas pressure compared with the equilibrium pressure of the LTMH when in hydrogenated and metal form. These 2 equilibrium pressure plots are displayed due to the combined sloping plateau and hysteresis phenomenon presented in Figure 4-3. The hydrogen flow (Figure 4-11(b), from differential pressure measurement)

and mass absorbed by the LTMH (Figure 4-11(c)) are also displayed. The initial 30 bar H_2 was slightly over the pressure required to start with a fully dehydrogenated LTMH. It was determined that approximately 0.3 g of hydrogen was still trapped in the LTMH. The LTMH temperature drop led to an absorption of nearly 1 g of H_2 . The following temperature increase up to 75 °C allowed to almost fully desorb 1.3 g H_2 from the LTMH and the subsequent cool down to ambient temperature enabled an absorption of that entire mass. Considering this mass of 1.3 g H_2 as the maximum mass available to be absorbed by the HTMH, it means that the energy density available in the Mg_2FeH_2 equates to 1180 kJ/kg. It designates the LTMH as the limiting factor in this operational mode, implying that its mass ratio should be 3 times higher compared to the HTMH to allow the hydrogen supply of full HTMH capacity (1.8 g H_2). Due to the specific heat and the enthalpy of hydrogen absorption and release, the LTMH diverts a part of the thermal energy that is being generated. The observed practical capacity of the HTMH and LTMH were 4.5 and 1.5 wt%, respectively. If the LTMH had a specific heat capacity of 500 J/kg.K and an enthalpy of reaction of 22 kJ/mol H_2 ,³⁰¹ this operational mode would need to provide to the LTMH around 610 kJ per kilogram of HTMH in order to generate the 1180 kJ/kg of high temperature thermal energy from the HTMH.

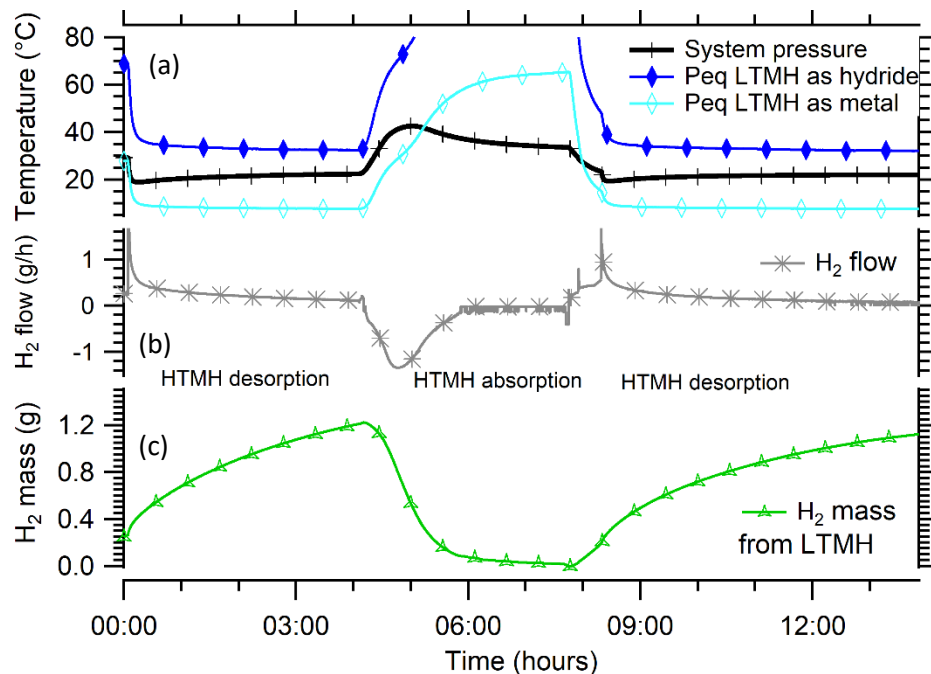


Figure 4-11 - System pressure evolution along with the LTMH equilibrium pressure when fully hydrogenated and fully dehydrogenated. Hydrogen flow and hydrogen mass flowing from the LTMH.

4.6. Summary

In this chapter, a coupled metal hydride system was designed to investigate the operation of a near ambient hydrogen gas storage system, which would autonomously pair with a HTMH. TiMn_{1.5} alloy, an interstitial metal hydride was chosen as the LTMH due to its hydrogen capacity, operating parameters and cost. The experimental investigation revealed an attractive pairing feasibility with the LTMH able to absorb the bulk of the hydrogen released by the HTMH. However, limitations due to the TiMn_{1.5} alloy specifications were exposed, more precisely the hysteresis phenomenon between hydrogen absorption and desorption. It was possible to overcome this hindrance by tuning the HTMH operating temperature range and restricting the free gas volume existing in the system. Moreover, adequate thermal management of the LTMH allows to adjust, to some degree, the maximum operating temperature of the HTMH.

An experiment was performed with the temperature management of LTMH as the hydrogen flow driving force. It was shown that the LTMH mass in this set up was insufficient to reach the HTMH energy density determined when the high temperature hydride was leading the hydrogen exchange. However, in a tuned design with the LTMH mass three times that of the HTMH, the energy required by the LTMH to drive the energy released by the HTMH would be around 40% of that generated.

During the investigation, ≈ 1.7 g of hydrogen was released and absorbed by the high temperature thermal energy storage operating between 360 °C and 520 °C with the LTMH temperature averaging 30 °C. Considering the 74.3 kJ/mol H₂ offered by Mg₂FeH₆, the experimental energy storage capacity is 1480 kJ/kg.⁷⁴ A comparable value of 1430 kJ/kg was obtained with the LTMH remaining at ambient temperature (≈ 20 °C) and a HTMH cycle between 350 °C and 500 °C. In the case of the Crescent Dunes CSP plant, operating in Nevada desert, 32000 tons of molten salts are required to store 13200 GJ of thermal energy that drives a steam turbine with an average efficiency of 30%. The capacity determined for Mg₂FeH₆ would allow energy storage between ≈ 350 and 500 °C to be reduced in mass to 8500 tons of HTMH.²⁸⁴ However, given the 1.5 wt% capacity displayed by the LTMH, this plant would require ≈ 22000 tons of LTMH to store the hydrogen involved in the heat storing process. This mass of LTMH would cost $\approx 170,000$ USD.²⁹⁵

Chapter 5 A sodium magnesium hydride reactor prototype to store thermal energy

“We must trust to nothing but facts: These are presented to us by Nature, and cannot deceive. We ought, in every instance, to submit our reasoning to the test of experiment, and never to search for truth but by the natural road of experiment and observation.”

Antoine Lavoisier, [Elements of Chemistry](#)

5.1. Introduction

In the early 1980s, a thermal energy storage system using Mg_2Ni hydride was investigated. Almost 6.3 kg of this powder producing 8.3 MJ at 300 °C revealed the dependence of the reaction mechanism on the heat transfer parameters.³⁰³ Since then, numerical modelling of reactors for low temperature hydrogen storage have concentrated most efforts to improve the hydride bed design in the aim to amend kinetics of hydrogen uptake and release. For a high temperature thermal energy storage using metal hydrides, it is also important to govern the absorption speed to control the heat generation in accordance with the energy demand of the end user. In the model of a three-dimensional heat and mass transfer reactor, Mat *et al.* identified the heat transfer within the hydride bed as a potential hindrance of the sorption kinetics.³⁰⁴ They also determined, for cylindrical reactors, a radius to height ratio of 0.1 as essential to mitigate the heat transfer constraint. Bao *et al.* showed, by three-dimensional modelling, that HTF flow, contact resistance and effective thermal conductivity were critical to improve the efficiency of a metal hydride reactor.³⁰⁵ In a comparison of different reactor designs, Shafiee and McCay documented the influence of heat exchange between the hydride bed and heat transfer fluid (HTF). They designated the fin equipped spiral as the HTF channel to best provide a fast hydrogenation reaction.³⁰⁶ Meanwhile, Chaise *et al.*, added 20 wt% of expanded natural graphite (ENG) to the powder bed and recorded sorption kinetics similar to that using a finned tubular heat exchanger.⁹¹ The results were linked to the thermal conductivity increase from 1 W/m.K for pure MgH_2 to 7.5 W/m.K for an addition of 10 wt% of ENG. The absorption was later improved by compacting the hydride with ENG into discs, which enhanced radial thermal conductivity.³⁰⁷ Other powdered additives were shown to offer attractive kinetics improvements. Pitt *et al.* described a positive effect of 2 mol% titanium based alloy addition,⁹⁰ and Shunjun *et al.* revealed a kinetics improvement by adding borohydride to a magnesium based hydride.³⁰⁸ At Curtin University, the experimental path in reactor design started in 2015; Paskevicius *et al.* produced a unique tubular reactor filled with 19 g of a magnesium hydride mixture and reported consistent hydrogen absorption and desorption.⁹⁷ However, large radiated heat losses were responsible for removing the greatest part of the energy generated during hydrogen absorption, and thermal energy extraction was not observed. This introduced the necessity for a larger scale apparatus. Later, a 36 g MgH_2 reactor was built with an

embedded HTF coil, and Dong *et al.* reported consistent cycling at ≈ 350 °C.⁹⁸ The embedded coil was shown to be beneficial to reduce the thermal transfer distance and improve thermal efficiency, but thermal losses were still a major issue which prevented any energetic analysis and effective thermal battery operation. Urbanczik *et al.* presented a reactor filled with 200 g of 2Mg + Fe, which consistently released and absorbed 3.8 wt% of hydrogen while operating at temperatures up to 500 °C.⁹⁹ This success was followed, in 2017, by the construction and testing of a tube bundle reactor as a heat storage tank filled with ≈ 5 kg of Mg_2FeH_6 .³⁰⁹ Urbanczik *et al.* managed to release 146.4 grams of hydrogen, corresponding to 1.5 kWh of stored thermal energy. Extreme difficulties regarding the thermal management were reported, which hindered cycling and further feasibility validation. The molten salts used as the HTF froze and destroyed parts of the HTF loop. They underlined heat losses due to insufficient insulation as a key parameter to drive the experimentation efficiently.

Experimental investigations of medium sized reactors are required to approach the operation of an industrial high temperature thermal storage system, and therefore to investigate the efficiency improvement of the heat recovery process.

As presented in Chapter 3, sodium magnesium hydride is amongst the most promising material for high temperature thermal energy storage. In this chapter an experimental investigation is presented on its feasibility by designing a reactor containing 150 grams of NaMgH_3 based material equipped with an embedded heat transfer fluid (HTF) coil. This set up underlines the operational parameters and limitations involved with this hydride and offers the first energy distribution analysis.

5.2. Operating parameter tuning

To prevent the irreversible decomposition of NaH into $\text{Na} + \frac{1}{2} \text{H}_2$, the initial operating parameters must be finely tuned. Figure 5-1(a) depicts the equilibrium pressure versus operating temperature for the decomposition of NaMgH_3 into $\text{Mg} + \text{NaH} + \text{H}_2$ and NaH into $\text{Na} + \frac{1}{2} \text{H}_2$.²³⁴ For example, at a temperature of 450 °C, NaMgH_3 decomposes at a gas pressure of ≈ 4.5 bar, where NaH decomposes when the gas pressure is 2 bar or below. Hence, when the thermal energy storage material reaches a maximum temperature of 450 °C, the system is designed so that the pressure does not drop below 2 bar of hydrogen pressure.

Different operating temperatures were investigated to determine suitable parameters to maintain consistent hydrogen capacity throughout cycling. Figure 5-1(b) shows thermal cycling investigations for temperatures ranging between 390 °C and 525 °C. Cycling experiments involving a temperature of 490 °C or higher invariably displayed extensive hydrogen capacity losses. Moreover, visual analysis of the sample repeatedly revealed an agglomerate of molten metal signifying the segregation and partial vaporisation of the Na in the sample. It was determined that a maximum operating temperature of 475 °C must

be maintained to achieve consistent hydrogen capacity. However, this capacity remains strongly dependent on the initial system gas pressure. It was determined that for operating temperature ranging from 390 °C to 465 °C, an initial system pressure of 3 bar hydrogen must be loaded in the system to avoid NaH decomposition and maintain consistent gas uptake and release through cycles. This verifies the previous maximum operating temperature recommendation in section 3.3.3.1.3 of ≈ 450 °C for NaMgH₃.

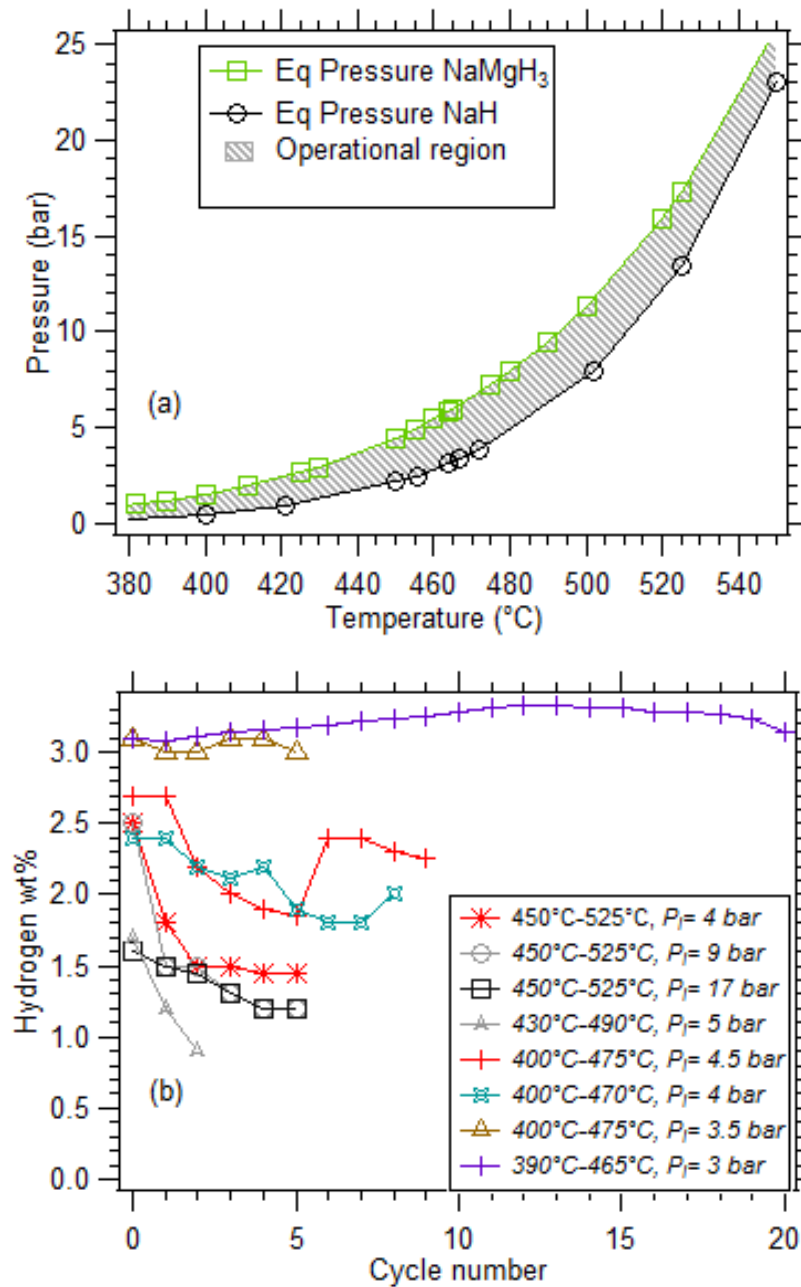


Figure 5-1 - (a) calculated equilibrium curves for NaH decomposition (Black circles) and NaMgH₃ decomposition (squares). (b) Hydrogen capacity versus cycle number for varying initial pressure and operating temperatures.

5.3. Lab scale thermal battery operation

5.3.1. Temperature cycling

The ideal operation of a large scale thermal battery is driven by the temperature of the HTF flowing in the reactor. To mimic a storage device for a CSP plant, the high temperature reached during the day elevates the reactor temperature, inducing hydrogen desorption which flows towards the gas tank. During the night, the HTF inlet temperature drops causing a temperature decline within the reactor. The associated equilibrium pressure then drops below the gas storage pressure, which triggers the absorption of hydrogen into the HTMH and generates thermal energy. This energy is then harvested by the HTF, maintaining a steady temperature at the outlet of the reactor. To simulate this operation, during this study, the HTF temperature was allowed to fluctuate periodically between 380 °C - 480 °C, while the system pressure was set to 2.35 bar when the thermal battery was at its minimum operating temperature (≈ 370 °C).

Figure 5-2 depicts the reactor's temperature evolution induced by the HTF temperature fluctuations, as well as the system gas pressure and the calculated hydrogen flow. The position of the thermocouples can be found in Figure 2-17. The hydrogen flow was determined from a differential pressure measurement according to the procedure explained in Section 2.6. The plots (Figure 5-2) show that the initial pressure level is reached after each absorption/desorption cycle, which testifies of the consistency of the system behaviour through cycles. It is, therefore, possible to select one desorption or absorption to further examine the thermal energy charge and discharge. It is noticeable that T_{s1} and T_{s2} , reflecting the reactor skin temperature, are at a significantly higher temperature than the powder bed. It is likely due to the 16.3 W/m.K thermal conductivity of the stainless steel, which is ≈ 3 times higher than the 5.15 W/m.K of the reactor mix (Section 3.3.3.1.5).

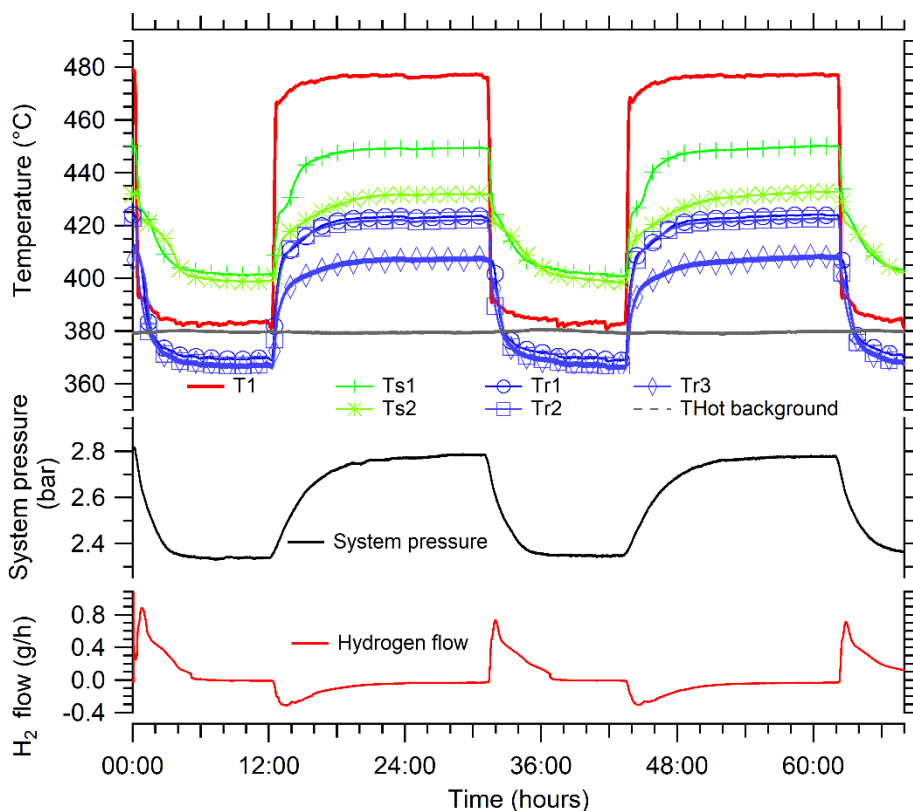


Figure 5-2 - Hydrogen absorption and desorption cycles with HTF flowing at 8 ml/min between 480 °C and 380 °C.

5.3.2. Temperature driven desorption

A more detailed presentation of the data acquired during a desorption (or heat storage) process is shown in Figure 5-3. Despite a HTF inlet temperature of ≈ 475 °C, the temperature inside the reactor reaches a maximum of 420 °C (Tr1, Tr2, Tr3), while the skin temperature averages 435 °C (Ts1 and Ts2) and reaches a peak of 445 °C. The bottom of the reactor is inherently cooler than the top showing that the energy provided by the HTF doesn't entirely counteract the heat losses, even with a hot background (HB) at 380 °C. However, hydrogen desorption raises the system pressure from 2.35 bar H_2 to 2.78 bar H_2 after 8 hours. Given the 50 litre volume for gas storage, this pressure increase equates to 1.75 g of hydrogen desorbed or 1.16 wt% H_2 , while the HTMH fully desorbed should release 3.9 g of hydrogen. As revealed by the thermocouple "Tr3", the bottom part of the reactor remains at ≈ 400 °C, a temperature at which the equilibrium pressure of $NaMgH_3$ is 1.5 bar H_2 (Chapter 3). This infers that a part of the reactor doesn't reach a sufficient temperature level to exceed the associated equilibrium pressure, a necessary condition for desorbing

the hydrogen. It is, therefore, possible to introduce the concept of active reactor mix mass, which is hot enough to host a desorption of 2.6 wt% H₂ previously obtained during the PCTs (Section 3.3.3.1.3). In this case, the active mass of material is \approx 68 g.

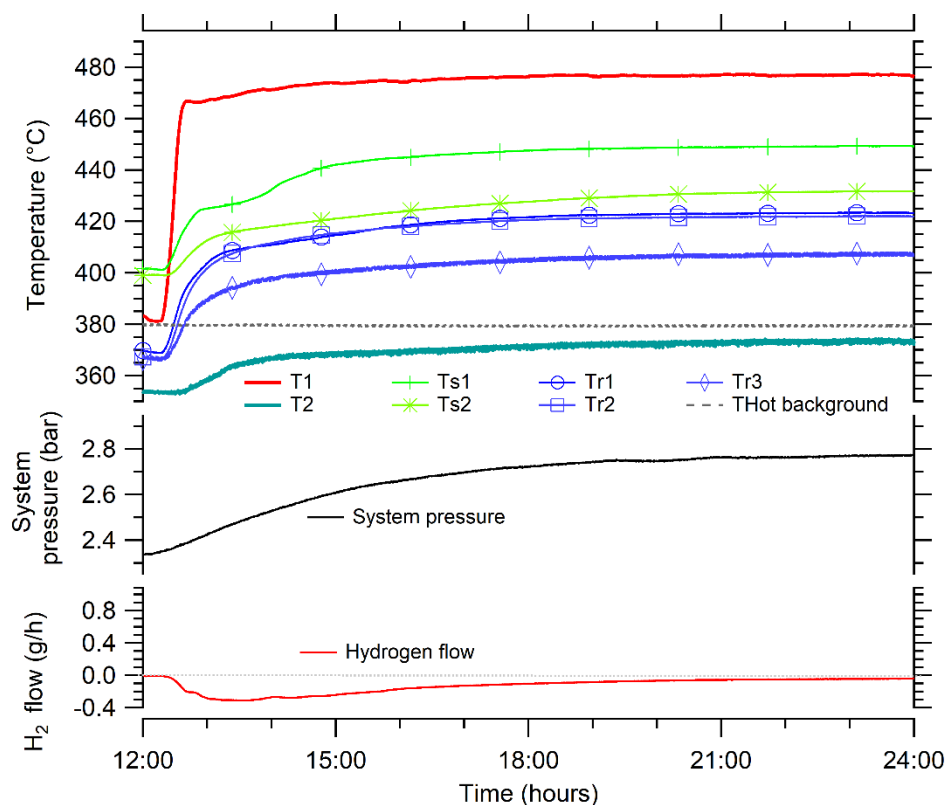


Figure 5-3 - Detailed view of various measurements in the system during desorption.

The mass of active material can be increased by raising the reactor temperature or lowering the initial system pressure. However, the thermal gradient in the reactor creates complications. Indeed, as explained previously, the decomposition of NaH into Na + H₂ must be avoided to preserve hydrogen capacity during cycling. Hence the system gas pressure should not drop below the NaH equilibrium pressure. For NaH, at 440 °C, the highest temperature measurement in this experiment, the equilibrium pressure is 1.8 bar H₂.²³⁴ It is, therefore, imperative for the reactor to remain above this pressure during high temperature desorption. This restriction highlights the difficulty associated with the operation of a multi-step reaction, which in the case of NaMgH₃, can lead to damaging the thermal battery.

The lab-scale system was tuned to optimise the mass of desorbed hydrogen and thus the mass of active hydride. Thermal insulation adjustments were performed in an attempt to

reduce the thermal gradient. The initial hydrogen pressure in the system was also lowered to trigger the desorption process at a lower temperature. Table 5-1 displays the various attempts to increase the active hydride mass. It reveals that the gain inherited from the insulation improvement, for an identical initial pressure of ≈ 2.45 bar, the desorbed hydrogen mass increased from 1.08 g to 1.58 g. The decrease of the initial gas pressure in the system also allowed up to 2.2 g of hydrogen to be desorbed. The quantity relates to ≈ 85 g of active reactor mix or 57 % of the total mass. Further improvement was prevented by the risk of NaH decomposition, which would cease any additional investigations.

Starting gas pressure (bar)	Final gas pressure (bar)	H ₂ mass desorbed (g)	Corresponding active Reactor Mix mass (g)	Average Temperature (°C)	
				Hydride	Skin
2.43	2.7	1.08	41.5	421	430
2.46	2.85	1.58	60.0	428	436
2.35	2.81	1.75	67.8	419	434
2.01	2.47	1.99	76.7	418	440
1.99	2.54	2.2	84.9	430	440
1.54	2.08	2.2	84.5	420	445

Table 5-1 - Hydrogen desorption optimisations, inlet HTF at 480 °C and 8 ml/min.

5.3.3. Temperature driven absorption

When the thermal battery is temperature driven, the hydrogen absorption is induced by the temperature drop within the reactor. This drop leads to an equilibrium pressure decrease within the material, which triggers a hydrogen absorption when the equilibrium pressure passes below the system gas pressure. In this set up, the reactor temperature decrease follows a reduction of the HTF inlet temperature. To secure a complete absorption, the HTF temperature was decreased to 380 °C, which corresponds to an equilibrium pressure of 1 bar H₂ for NaMgH₃.

Figure 5-4 shows a typical absorption step when the HTF temperature drops from 480 °C and 380 °C. The HTF (T1, T2) and reactor (Tr1, Tr2, Tr3 and Ts1, Ts2) temperatures are depicted along with the system pressure evolution as well as the calculated hydrogen flowing from the gas storage to the reactor. It is noted that the reactor skin temperature (Ts1 and Ts2) is consistently ≈ 20 °C higher than the powder bed temperature (Tr1, Tr2 and Tr3). This is attributed to the higher thermal conductivity of the stainless steel skin compared to that of the reactor powder mix.

As supported by the plot of hydrogen flow, absorption doesn't start directly when the HTF temperature decreases. It commences once the bulk of the reactor temperature decreases below 425 °C (Tr1 and Tr2), which is the equilibrium temperature for 2.8 bar H₂ (which also corresponds to the system pressure at the start of the absorption step). The hydrogen flow rises rapidly to a value of 1 g/h then slowly decreases over a 3 hour period. During the period of hydrogen flow increase, temperature humps are displayed by the sensors in the reactor, more specifically Tr1 and Ts1, which are the thermocouples situated closest to the hydrogen inlet. Despite the use of a hydrogen porous rod in the centre of each reactor, the hydrogen doesn't seem to diffuse evenly throughout the reactor length. Moreover, the effect of the exothermic reaction is not apparent on the HTF, as the outlet temperature (T2) decreases along with the reactor temperature.

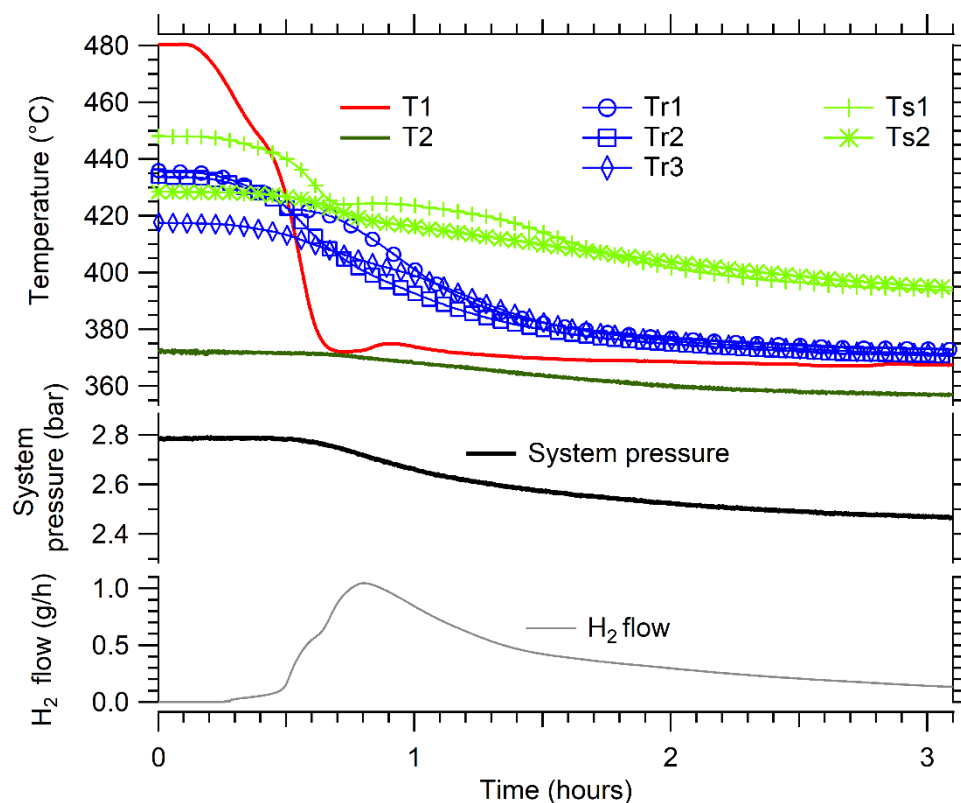


Figure 5-4 - Temperature driven absorption for HTF temperature dropping from 480 °C to 380 °C with a 8 ml/min flow.

During the 6 hour absorption cycle, 1.7 g of hydrogen was absorbed, which considering the enthalpy of reaction (86.4 kJ/mol H₂) equates to 72.8 kJ released or approximately 3.3 W. This low power value is the reason for not observing a clear thermal event in the thermal battery. Indeed, even if the first hour of reaction is considered, when a large portion of the hydrogen mass is absorbed (0.78 g of H₂), the average produced heat of 9.3 W doesn't create an evident heat release phenomenon. For the maximum hydrogen flow rate, the generated power is not enough to cover the heat diversions and losses.

It is, therefore, essential to increase the thermal power generated by the reactor. Bao *et al.* demonstrated through computer simulations that the reaction kinetics are one of the main parameters influencing reactor efficiency.³¹⁰ The reaction kinetics are generally determined by intrinsic hydride parameters such as hydrogen diffusivity, thermal conductivity or compaction, which were not adjustable in this case. The remaining available leverage was the hydrogen supply pressure, which would accelerate the absorption rate upon an increase of the differential pressure between the gas store and the equilibrium pressure of the hydride.

5.3.4. Over pressurised absorption

A high temperature thermal battery should be able to generate enough power to transmit the energy generated to the HTF. To improve the power generation, the absorption kinetics were optimised by increasing the initial hydrogen pressure available in the gas tank at the start of the absorption process.

Figure 5-5 depicts the calculated hydrogen flow (from differential pressure) during heat generation (absorption) for various starting gas pressures. Each absorption was performed at similar HTF thermal management, the temperature was dropped from 480 °C to 380 °C, at a flow of 8 ml/min. The valve that enables the hydrogen release from the gas tank was opened when the HTF temperature reached 400 °C, which was previously noted to be the temperature at which the reactor started to absorb on a thermally driven operation. The initial gas pressure directly affects the maximum hydrogen flow, rising with the increased pressure up to 10 g/h for the highest test pressure of 8 bar H₂. After the first 30 minutes of reaction, when the majority of the hydrogen had been absorbed, the hydrogen flows are similar at 1.2 ± 0.4 g/h, independent of the supplied pressure. After one hour the flow

drops below 1 g/h for all tests, which was shown to be inadequate to transfer substantial power to the HTF.

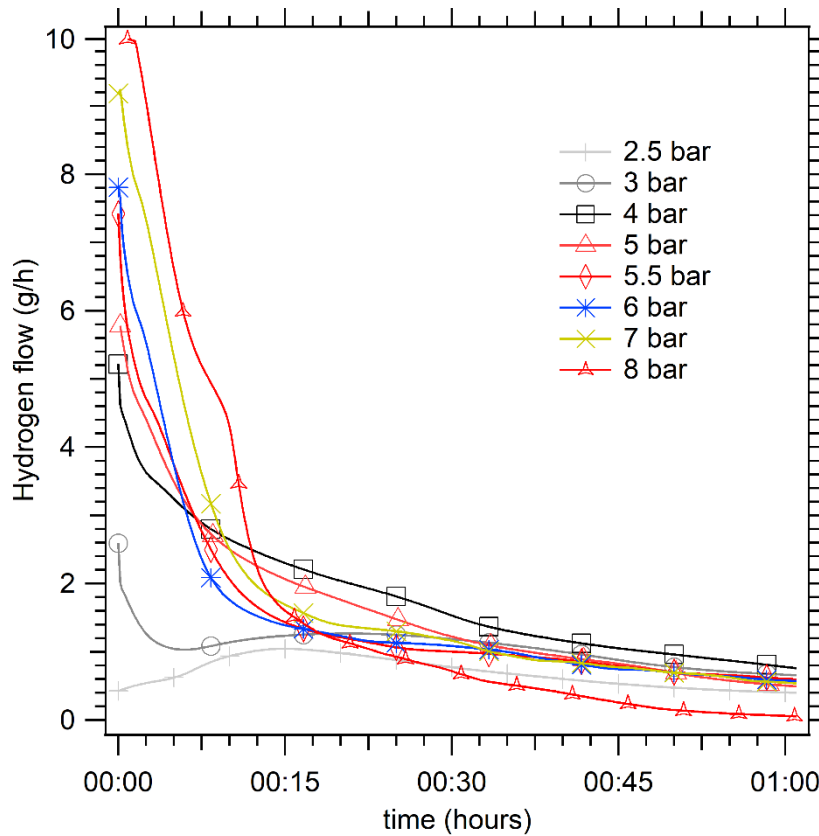


Figure 5-5 - Absorbed hydrogen flow for a range of initial hydrogen pressure

The initial hydrogen pressure also influences the overall time for the absorption to be completed. Table 5-2 reveals the substantial time decrease for increasing hydrogen starting pressures and reports the maximum hydrogen flow obtained. The time for full absorption required slightly more than an hour at a pressure of 8 bar where it required more than 6 hours when the absorption was thermally driven.

Table 5-2 - Time required for absorption, maximum hydrogen flow for a range of initial hydrogen pressures and subsequent theoretical maximum power generated.

Starting hydrogen pressure (bar)	2.5	3	4	5	5.5	6	7	8
Time (min)	378	238	167	150	148	128	115	68
Maximum hydrogen flow (g/h)	1.0	2.6	5.2	6.1	7.4	7.8	9.2	10.0
Theoretical maximum power generated (W)	10.7	27.7	55.5	65.1	78.9	83.2	98.1	106.6

Increasing the hydrogen supply pressure induces higher gas flows and therefore also increases the power generation within the hydride bed. Indeed, as shown in **Error! Reference source not found.**, the embedded temperature measurements at Tr1 and Tr3 reveal a sudden 20 °C gain for an initial hydrogen pressure of 4 bar. Tr2 data points don't harmonise with the two previously mentioned sensors, but it is likely that this thermocouple is in contact with the HTF coil, and therefore, relates to the local HTF temperature. The skin temperature of the reactor also sustains a rapid temperature increase by approximately 10 °C. These are clear manifestations of the exothermic reaction, which takes places in the reactor bed.

The phenomenon is tempered on the HTF outlet temperature due to the thermal interfaces between the powder and the fluid. However, the increased HTF temperature, up to 383 °C, compared to the initial level of 377 °C, testifies to an energy retrieval by the HTF.

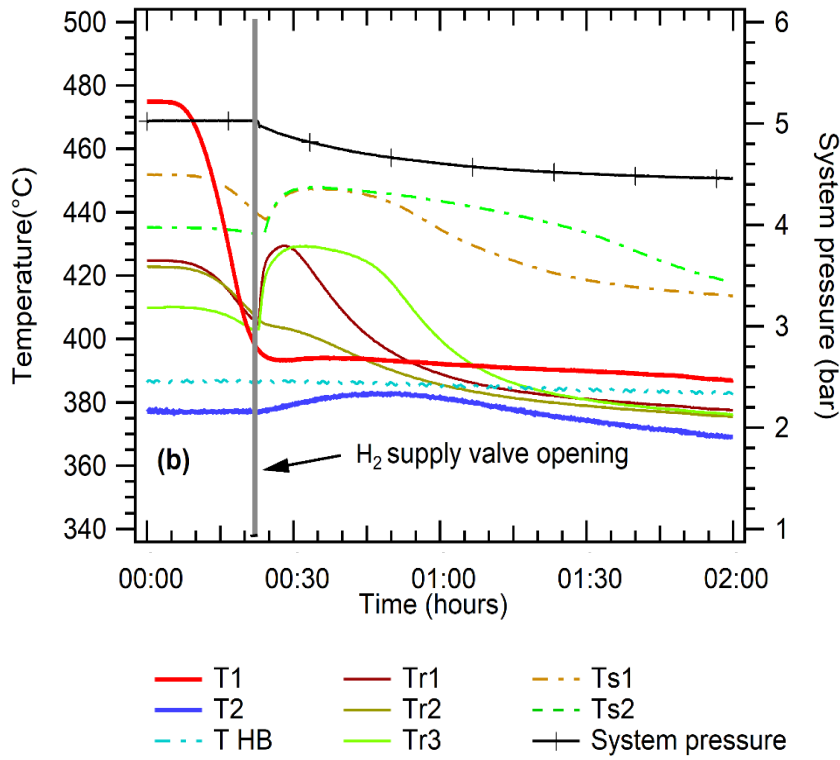


Figure 5-6 - Thermal response of the reactor set up for an absorption initially at 5 bar H₂.

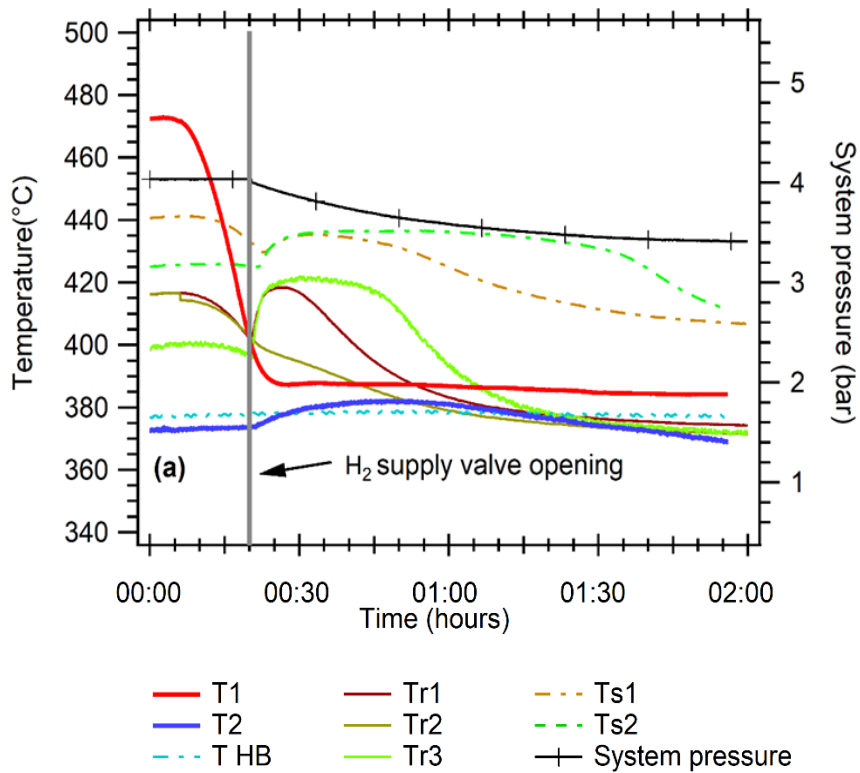


Figure 5-7 - Thermal response of the reactor set up for an absorption initially at 4 bar H₂.

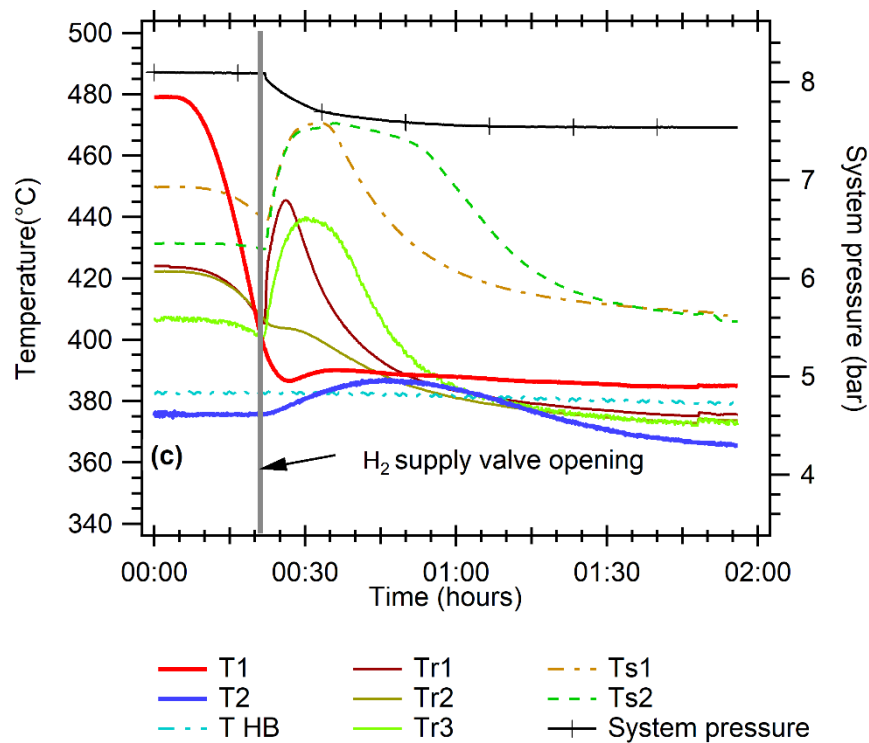


Figure 5-8 - Thermal response of the reactor set up for an absorption initially at 8 bar H₂.

Figure 5-6 and Figure 5-8 also show the thermal response of the reactor and HTF for a hydrogen supply pressure of 5 bar and 8 bar, respectively. The global behaviour is identical to that presented previously in **Error! Reference source not found.** The maximum temperature reached increases as the inlet pressure increases. At 5 bar H₂ supplied, the reactor bed temperature increases by 30 °C to 430 °C with the skin temperature reaching 450 °C, which almost correspond to the equilibrium pressure of 5 bar H₂. At 8 bar H₂, the HTMH temperature increases by approximately 40 °C, while the skin temperature reaches 475 °C, which almost relates to the equilibrium pressure of 8 bar H₂. The effect is also perceivable on the HTF outlet temperature, which reaches more than 10 °C higher than its original temperature level (Figure 5-8). Considering the water properties flowing at 8 ml/min under 140 bar at 25 °C, it is equal to 9 W of extracted power by the HTF. Despite the low power values, these results allow further examination of the thermal battery by determining the energy practically extracted and the energy lost.

5.3.5. Energy consideration

Considering the mass of hydrogen absorbed at each cycle, $\approx 2.0 \pm 0.2$ g, and given the determined enthalpy of reaction of 86.4 kJ/mol H₂, the heat released is approximately 85 kJ. Ideally, this energy would be harvested by the HTF to supply the end user. However, all the reactor components eventually divert a proportion of the generated heat.

To assess the energy balance of the system, it is possible to separate four subsystems that are sinking the generated heat during hydrogen absorption.

5.3.5.1. Heat transfer fluid energy

The HTF extracts the heat from the reactor. The extracted heat was calculated for each acquisition time step using the HTF properties at operating temperature and pressure. The flow of the 140 bar pressurised water, was consistent at 8 ml/min (at 25 °C) throughout the experimental study, which results in a mass flow of 0.13 g/s with a specific heat of 3.8 kJ/kg.K at a temperature of 400 °C.³¹¹

A reference cycle was performed without hydrogen sorption and similar thermal management (HTF temperature dropping from 480 °C to 380 °C) to determine the sensible thermal energy storage of the reactor (Figure 5-9 - Example of HTF temperature comparison between no reaction and a hydrogen absorption. Figure 5-9). This quantity of energy can then be retrieved from the power calculation so that only the thermo-chemical heat generated is considered.

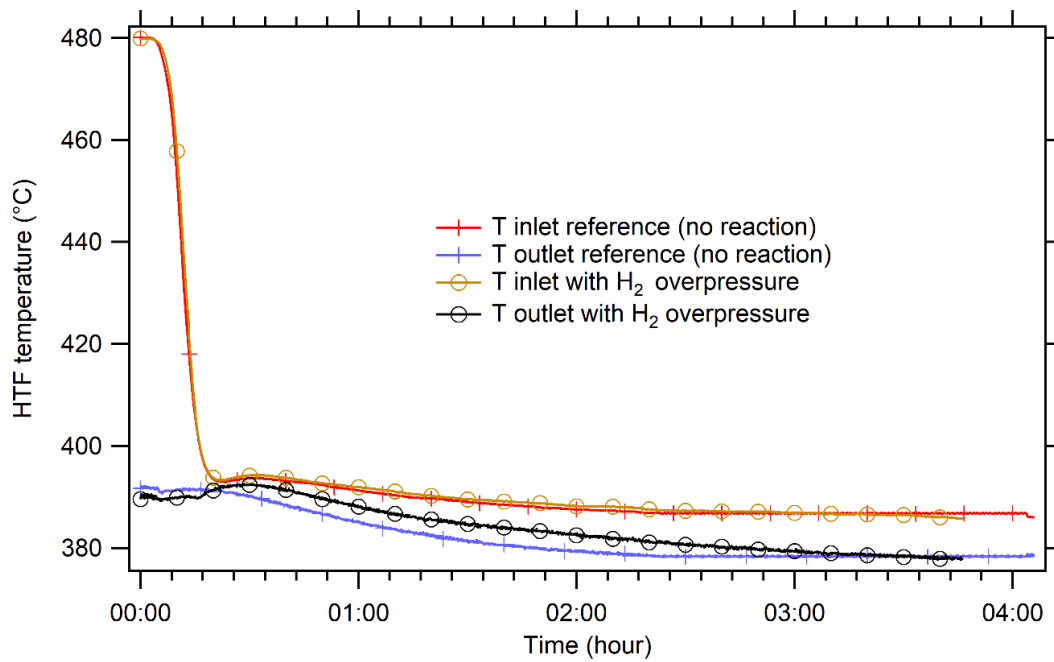


Figure 5-9 - Example of HTF temperature comparison between no reaction and a hydrogen absorption.

The reference test determined that a maximum of 43 W losses when the HTF inlet is at a temperature of 480 °C, dropping to 10 W when the HTF inlet is at 380 °C. The integration over a 5 hours period of each data acquisition results in 65 kJ of energy. It corresponds to sensible heat transferred from the hydride bed to the HTF, and was retrieved from the energy harvested by the HTF during a hydrogen absorption.

Figure 5-10 depicts the power extracted by the HTF; the reference was subtracted so that the value obtained only accounts for the exothermic hydrogen absorption process. The peak of extracted power increases as the initial hydrogen supplied pressure rises. The peak of extracted power was generally observed 30 minutes after the reaction commences. A maximum of 9 W was measured for the maximum test pressure of 8 bar H₂. Despite the modest values, this showed that the supply pressure is an excellent lever to adjust the thermal power delivered by the thermal storage material.

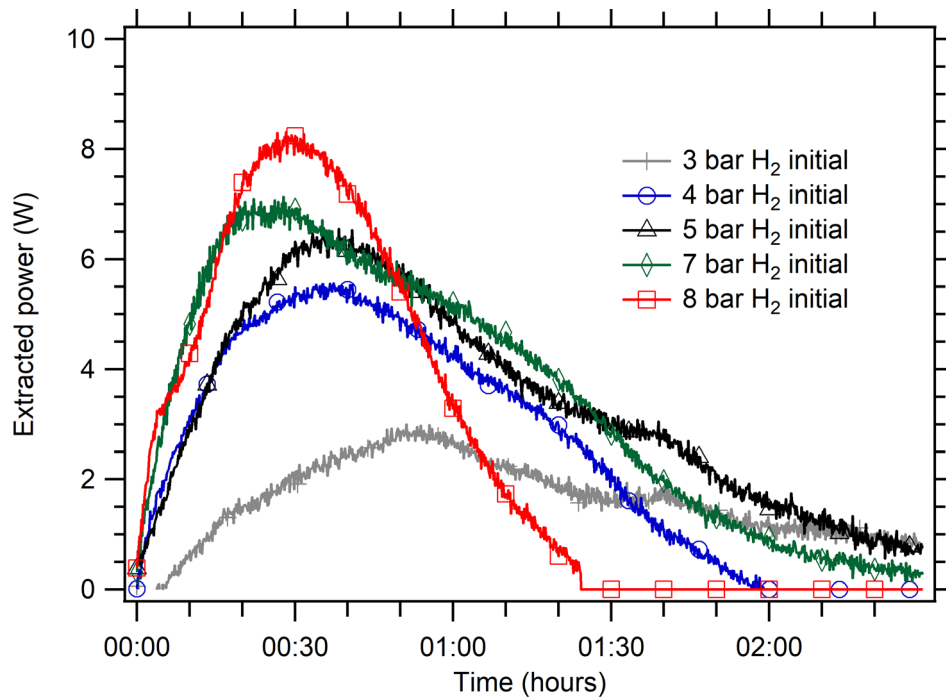


Figure 5-10 - Power extracted by the HTF during hydrogen absorption with various initial pressures.

5.3.5.2. Metal hydride energy

The metal hydride bed temperature increases as hydrogen absorption occurs. Hence, some heat is used as sensible energy to fuel this temperature rise. To quantify the energy diverted, the specific heat capacity (C_p) of the reactor mix was determined from the C_p of NaMgH₃ and the ENG.⁶⁶

For the hydride, the specific heat can be derived from the Gibbs energy following:

$$C_p = - \frac{d^2G}{dT^2} \cdot T \quad \text{eq. 5-1}$$

With T , the operating temperature and G , the Gibbs energy of NaMgH₃ which is defined as a function of temperature (for $298.15 \text{ K} \leq T \leq 2000 \text{ K}$) as follows:⁶⁶

$$G_{\text{NaMgH}_3} = -157905.85 + 185.83 T - 33.6 T * \ln(T) - 61.27 * 10^{-3} * T^2 \quad \text{eq. 5-2}$$

For the ENG, the equation of the C_p is written:⁶⁶

$$C_p = 15.912 + 10.2 * 10^{-3} * T - 14.831 * 10^5 * T^{-2} - 3.02 * 10^{-6} * T^2 \quad \text{eq. 5-3}$$

Considering an average temperature of 425 °C, the specific heat of NaMgH₃ is 2372.2 J/kg.K, and the C_p of graphite equal to 18.52 J/mol.K. The specific heat of the hydride mixture is then found to be equal to 3914 J/kg.K. The three thermocouple placed within the reactor (Tr1, Tr2, Tr3) allow for the assessment of the average bed temperature prior to hydrogen uptake as well as the maximum temperature reached due to the exothermic hydrogen absorption. The temperature difference can be associated with a quantity of thermal energy diverted. For example, if the powder bed is at 400 °C when the hydrogen absorption initiates and reaches a maximum temperature of 430 °C. The thermal energy diverted by 80 g of material considered active is 9.4 kJ.

5.3.5.3. Stainless steel reactor energy

The stainless steel reactor casing also sustains a temperature rise and therefore, disperses a portion of the generated thermal energy. The mass of the housing was approximately 3000 g and its specific heat is calculated from the equation:⁶⁶

$$C_p = 107.17 + 12.59 * 10^{-3} * T + 0.021 * 10^5 * T^{-2} - 0.017 * 10^{-6} * T^2 \quad \text{eq. 5-4}$$

which at 425 °C results in 116 J/mol.K or 646 J/kg.K. The temperature sensors placed on the outer skin of the reactor (Ts1 and Ts2) provide an average temperature of the overall stainless steel mass. As for the metal hydride bed, the temperature rise induced by the hydrogen absorption relates to a quantity of diverted thermal energy. For example, if the averaged skin temperature is 435 °C at the start of the reaction and reaches a temperature of 450 °C, the energy required is 29 kJ.

5.3.5.4. The environmental losses

Despite the assistance of the hot background (HB) to limit the heat losses to the environment, the reactor remains, at all times, at a higher temperature than the set temperature of the HB so that it doesn't interfere with the generated thermo-chemical energy. In this case, the environmental losses account for the energy that is neither used by the hydride bed or stainless steel nor extracted by the HTF.

5.3.5.5. Synopsis

Considering the energy distribution for each experiment with various initial hydrogen supply pressures, this allows for the identification of which part of the system is the most energy intensive diverter.

Figure 5-11 depicts a summary of the energy distribution for each test performed with hydrogen supply pressures ranging from 2 - 8 bar. The major part of the energy generated is lost into the environment despite all precautions taken. On average, 28 kJ/g H₂ account for losses, which is $\approx 65\%$ of the expected thermal energy released by this storage. The specific heat of the hydride mixture (≈ 4 kJ/kg.K) is responsible for diverting a maximum of 5 kJ/g H₂ even allowing for the maximum rate of heat generation under 8 bar hydrogen. It diverts a little over 10 % of the generated heat. The stainless steel reactor casing uses a large amount of heat, which amplifies greatly when the hydrogen supply pressure is increased. Despite a low specific heat (≈ 650 J/kg.K), the mass of steel (3 kg) diverts up to 17 kJ/g H₂ for the experiment under 8 bar of hydrogen. In this case, it corresponds to 40 % of the generated heat. This result infers that the mass ratio between the reactor casing and the heat storage material is an essential parameter that should be lowered. In this set up, the heat storage material to stainless steel mass ratio was $\approx 1:20$. This issue should be considered and alleviated upon prototype scale up.

The HTF was also able to retrieve a portion of the energy generated. However, despite the addition of ENG which increased the thermal conductivity from 1.84 W/m.K to 5.15 W/m.K, the maximum heat retrieval was 1.4 kJ/g H₂. This value illustrates the need for designing a

superior heat exchanger between the hydride bed and the HTF. The helical tube has received interests and was shown to increase the heat transfer area and provide short thermal energy transfer distance.^{98, 312, 313} However, more efficient heat transfer design should be investigated. For example, heat pipes are a well-known technology and have been shown to favourably enhance the heat transfer in metal hydride tanks.³¹⁴⁻³¹⁶

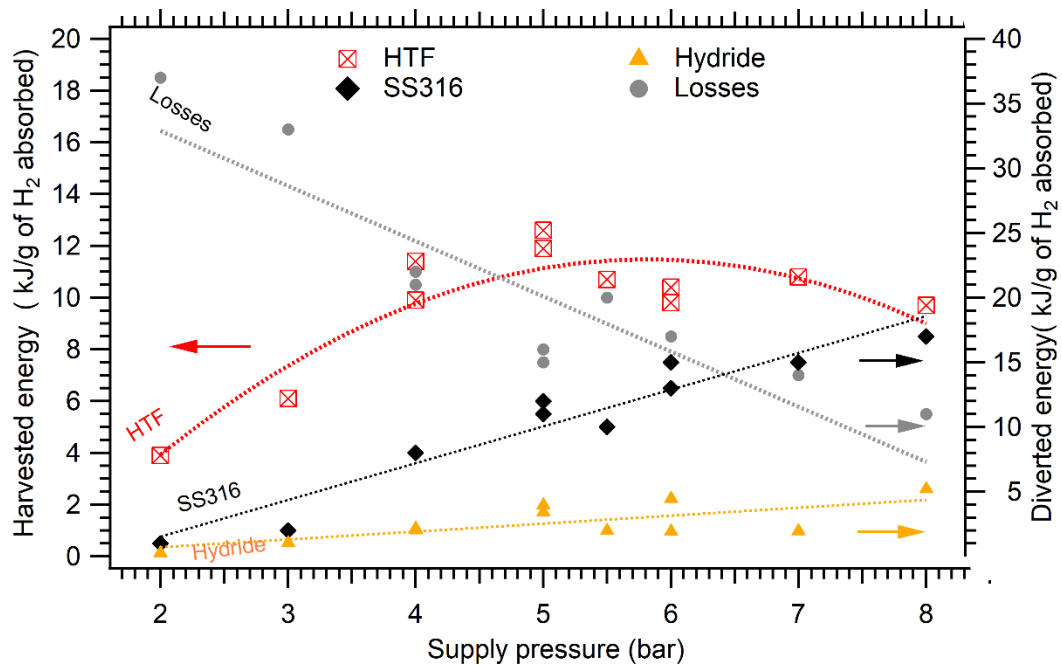


Figure 5-11 - Thermal energy distribution during hydrogen absorption in the 4 subsystems (HTF, SS316 reactor, hydride and losses) for various initial hydrogen pressures.

5.3.6. Post cycle analysis

After a final absorption, the reactor set up was dismantled, and the reactor mix analysed using XRD. A small amount of powder was taken from different places across the length of one reactor's cylinder, at the top of the reactor, 5 cm from the top, 15 cm from the top, 25 cm from the top and at the bottom of the reactor (or 40 cm from the top). Figure 5-12 reports the quantity of various materials found using the Rietveld refinement method. No more than 70 wt% of NaMgH₃ was detected, which correspond to the 80 % yield defined with the elected synthesis procedure in chapter 3, when considering the ENG addition. However a slightly lower mass ratio of NaMgH₃ is observed at the top and bottom of the reactor, which can be associated with the undesired mass of Na identified at these

respective places. Despite extensive precautions, these parts of the reactor may have been subjected to metallic NaH decomposition.

Additionally, a reduction of the graphite (or ENG) mass ratio is perceived at the top of the reactor. The pressurised absorption cycles may have engendered a migration of this fine powder through the bed toward the bottom.

A non-negligible mass ratio of magnesium oxide was revealed, distributed evenly across the five samples. However, this contamination may have occurred during the experimental set up or during the XRD measurements.

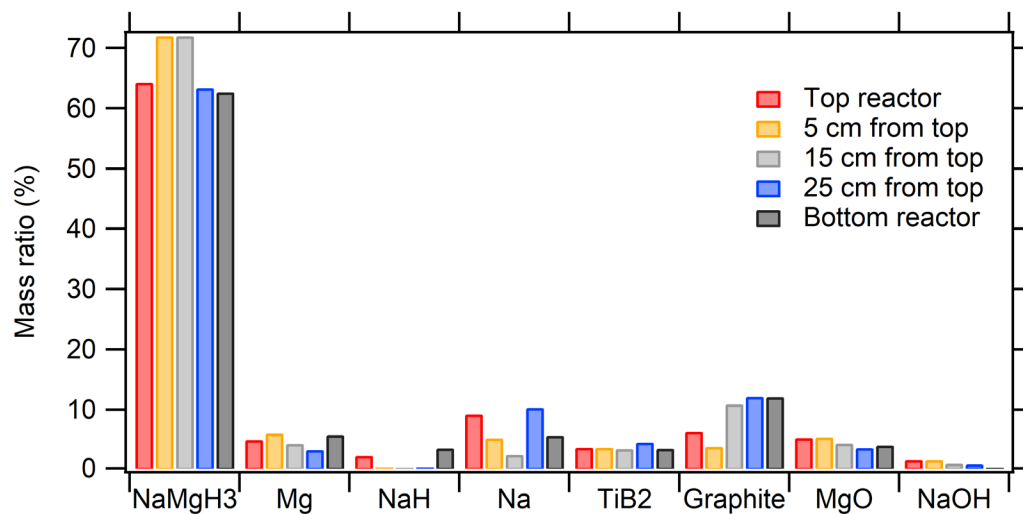


Figure 5-12 - Quantity analysis of the Reactor Mix at various places across the length of the reactor.

5.3.7. Summary

A scaled up experimental apparatus was designed and built to investigate the feasibility of a sodium magnesium based hydride imitating real operating conditions. A heat transfer fluid was implemented to provide and retrieve the high temperature thermal energy from the thermal battery. The set up revealed the capacity of the material to store and release heat on a 150 g scale. However, some limitations were exposed. A consistent hydrogen capacity during cycling was shown to be practicable for operating temperatures below 475 °C. As the decomposition of sodium hydride is non-reversible and the operating temperature and pressure windows (equilibrium pressure of RM at 444 °C is 3.9 bar H₂ where the decomposition temperature of NaH at this pressure is around 470 °C) are

narrow, NaMgH_3 has limitations as a thermal battery. The thermal gradient inherent to a large scale thermal energy storage hinders the usage of the material's heat capacity and threatens irreversible damage to the thermal battery. The post cycling XRD analysis supported this difficulty, since despite meticulous operation to avoid NaH decomposition, up to 10 wt% was found in the post cycles analysed samples.

The temperature driven absorption was shown to be insufficiently powerful to generate harvestable heat. i.e. Only a slight heating up phenomenon was observed in a part of the hydride mix itself.

An increase of the initial hydrogen supply pressure allowed for the generation of enough power to counteract the heat losses and pointed to the reactor casing as an important energy diverter. Even if this was a consequence of the small scale reactor, the mass ratio of metal hydride and casing must be reduced in future designs to alleviate the issue.

A part of the generated energy was harvested by the HTF, and the results suggest the presence of an optimal hydrogen supply pressure to obtain the best efficiency.

Chapter 6 An operational prototype to store thermal energy using magnesium iron hydride

“He who loves practice without theory is like the sailor who boards ship without a rudder and compass and never knows where he may cast.”.

Leonardo Da Vinci.

6.1. Introduction

As explained in the introduction of Chapter 5, high temperature thermal energy storage has rarely been experimentally investigated in an operating reactor. Most prototypes reported in the literature rely on latent energy involved in phase changes of materials.^{54, 56, 317} However, they often present an operating temperature below 300 °C. The development of thermochemical energy storage systems (i.e. metal hydrides) allows for ramping up that operating temperature and potentially increasing the energy density of thermal batteries.³¹⁸ In the past decade, metal hydrides for thermal energy storage have received growing interest from the scientific community in an attempt to develop and/or characterise a suitable material for high temperature heat storage.^{65, 87, 126, 153} Few materials have been reported to comply with all the constraints involved in such applications; these constraints were detailed in Chapter 3, Section 3.2. Magnesium iron hydride is, nowadays, amongst the most attractive candidates to be used in thermal energy storage between 400 and 600 °C.^{74, 277} The aim of the project detailed in this chapter was to develop a prototype that could approach a real case application and investigate the potential limitations involved in the use of Mg_2FeH_6 in a large scale (≈ 1 kg) high temperature thermal energy storage. The prototype was paired with a compressed hydrogen gas store as this solution had been recently proven to be financially attractive by Sheppard *et al.*³¹⁹ The presentation of the experimental setup is available in Chapter 2, Section 2.9.

6.2. Operating investigation

6.2.1. Thermal energy charging

Thermal energy charging consists of applying thermal energy to promote hydrogen desorption from magnesium iron hydride, provided that the hydrogen pressure in the reactor is maintained below the equilibrium pressure of the hydride at such an operating temperature. For a set reactor temperature and HTF parameters (temperature, flow and pressure), the gas compressor activation diminishes the hydrogen pressure in the hydride reactor to a level that can be set to a constant value (by control software). When the system gas pressure drops below the equilibrium pressure of the hydride, hydrogen

desorption occurs. The experimental setup enabled activating the gas compressor when the reactor gas pressure is greater than a given level, therefore inducing a quasi-stepwise desorption between a given pressure window.

For the following typical thermal energy storage experiment, the TES900 material was fully hydrogenated at the initial state. Additional hydrogen gas was kept pressurised in the gas store at 68 bar (Figure 6-1). The average reactor temperature was maintained at 430 °C, due to a 35 ml/min HTF flow with an inlet temperature of \approx 485 °C. The reactor pressure was set to be regulated at \approx 10 bar H₂. As this pressure is below the equilibrium pressure of Mg₂FeH₆ at 430 °C (22 bar H₂), hydrogen desorption was induced. The furnace, heating the reactor surroundings, ensured a “hot background” (HB) regulated at 400 °C to minimise heat losses to the environment.

To initiate hydrogen desorption, the gas pressure was dropped to 10 bar by opening valve Vm₂ (Figure 2-25). The compressor transferred the gas removed from the reactor volume to the gas store as soon as the pressure surpassed 10 bar. Figure 6-1 illustrates the gas store (bottle) pressure, the pressure in the reactor volume and the mass of hydrogen desorbed during the thermal energy storage process. This mass was calculated by integration of the gas flow over time (q_{H_2}) determined from eq. 2-29. The calculated hydrogen mass could also be validated from the gas store pressure variations based on its known volume. In this case, the pressure of the 50 L store increased from 68 bar to 79 bar, while the gas pressure in the reactor fluctuated between 12 bar and 8 bar. It allowed desorption of \approx 44 g of hydrogen within 6 hours. Considering the 900 g of Mg₂FeH₆, this

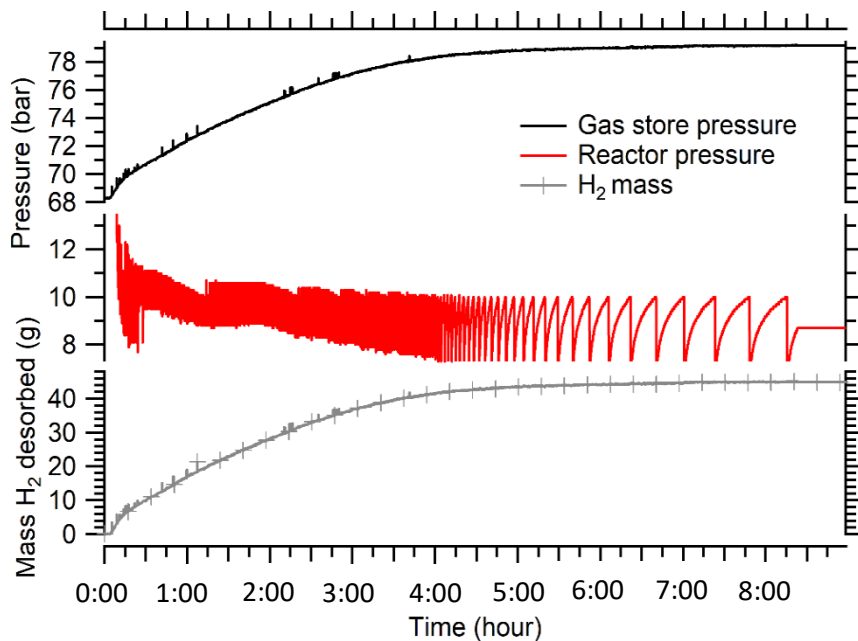


Figure 6-1 - Gas store and reactor hydrogen pressure during desorption, along with the hydrogen mass desorbed from the hydride. Average reactor temperature 430 °C, HTF flow of 35 ml/min, and hydrogen pressure set to 10 bar.

equates to ≈ 4.9 wt% or 90 % of the theoretical (5.47 wt%) hydrogen capacity.

The corresponding HTF and reactor temperature data are presented in Figure 6-2. The inlet HTF temperature was stable at 485 °C. The temperatures of T1 to T6 reflect the local temperature across the reactor, close to the HTF coil. Temperature sensors T1, T2 and T3, represent the wall temperature of an external cell of the reactor whereas T4, T5 and T6 reflect the wall temperature of a middle cell. In the reactor, apart from T1, which was located close to the HTF inlet, the average initial temperature equated to 430 °C. However, the thermal gradient observed in the external cell (between T1 and T3) approached 50 °C, while the thermal gradient within the middle cell remained at ≈ 10 °C. This demonstrated that there were significant heat losses endured by the lab-scale thermal battery despite the operation of a hosting furnace (hot background). These losses were taken into account when discussing the energy supply below.

At the start of the endothermic dehydrogenation reaction, the reactor and the HTF outlet endured a sharp temperature drop. Both temperatures monitored reactor cells displayed a 20 °C drop upon initiation of desorption before returning to their original levels after 6 hours. This exemplifies the thermal energy storage during hydrogen desorption and implies

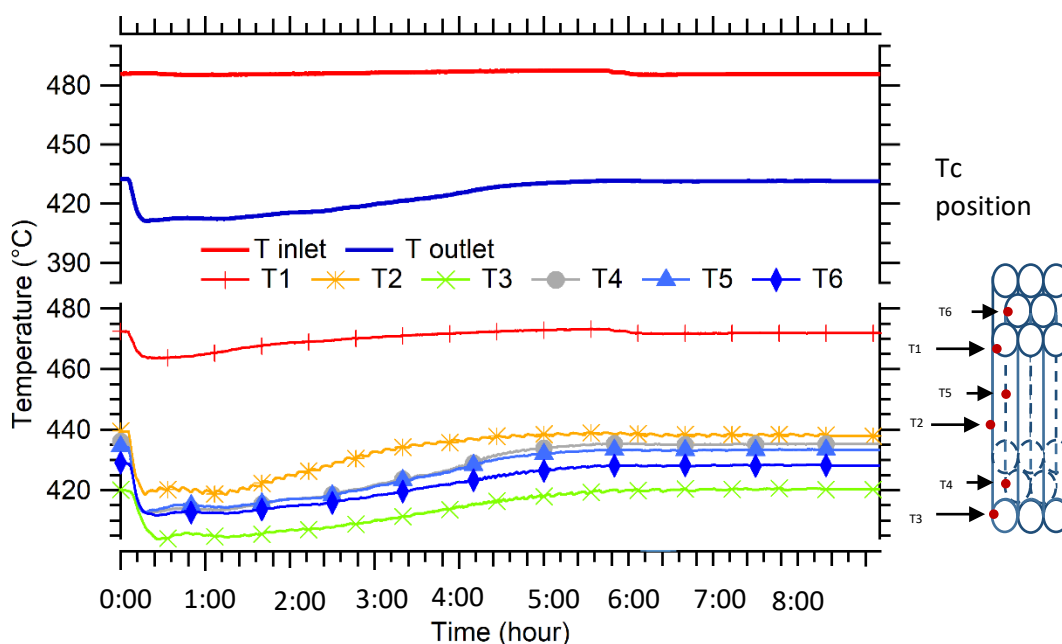


Figure 6-2 - Temperature of inlet and outlet HTF as well as inside the reactor during desorption. Average reactor temperature 430 °C, HTF flow of 35 ml/min, and hydrogen pressure set to 10 bar. T1 to T6 follow the HTF flow direction (T inlet was 10 cm before T1 and T outlet was 10 cm after T6).

that the energy supplied by the HTF is complemented by sensible heat from the material and housing.

From the recorded temperatures and hydrogen mass flow, it was possible to determine the thermal energy stored during the desorption event. The temperature difference (ΔT) between the HTF inlet and outlet allowed for a calculation of the power (P_{HTF} , in kW) delivered by the HTF to the thermal energy store using eq. 6-1. Its integration over time determines the total energy provided by the HTF; the temperatures were recorded every 10 s.

$$P_{HTF} = q_v \cdot \rho \cdot C_p \cdot \Delta T \quad \text{eq. 6-1}$$

Where,

q_v = the volumetric HTF flow (m^3/s),

ρ = the HTF density (kg/m^3) at the temperature (T_a , in K) where the volumetric flow was measured under 200 bar, determined from:³¹¹

$$\rho = -0.0028119 \cdot T_a^2 + 1.3691 \cdot T_a + 847.72 \quad \text{eq. 6-2}$$

C_p = the HTF specific heat ($\text{kJ}/\text{kg}\cdot\text{K}$) at the average reactor temperature (T_H in K) and 200 bar, determined from:³¹¹

$$C_p = 0.00023918 \cdot T_H^2 - 0.37593 \cdot T_H + 150.84 \quad \text{eq. 6-3}$$

Due to the inherent heat losses caused by the reactor's surface to volume ratio and the location of the thermocouples monitoring the HTF temperature at the HTF inlet and outlet, the HTF temperature at the outlet was consistently at a lower level than that at the inlet. The evaluation and retrieval of these losses was possible when it was assumed that the fluid should undergo no or negligible heat losses when no reaction occurred in the thermal battery. In this case, the losses were determined at the initial steady state of the system

before engaging the desorption process. The use of eq. 6-1 determined the general heat loss to the environment as 144 W, which was considered consistent throughout the desorption process.

Given the hydrogen mass flow (q_{H_2} , in g/s) at each time step, the power (P_{H_2} , in kW) required to desorb hydrogen from Mg_2FeH_6 can be determined from the enthalpy of reaction (ΔH) that was previously calculated to be 74.3 kJ/mol H_2 (section 3.3.3.2.3) using eq. 6-4.

$$P_{H_2} = q_{H_2} \cdot \frac{1}{2.016} \cdot \Delta H \quad \text{eq. 6-4}$$

Integration over time of eq.6-4 also allowed for the determination of the total energy used to complete hydrogen desorption, hence the practical thermal energy stored in the battery.

The power and energy involved in this typical hydrogen desorption (thermal energy storage) process are plotted in Figure 6-3. The start of desorption induced a large hydrogen flow that corresponds to a ≈ 300 W peak of consumption. The HTF provided ≈ 80 W at this time, whilst the remaining was eventually provided by the specific heat of the hydride bed, the stainless steel casing (which justifies the 20 °C drop previously observed) and the furnace.

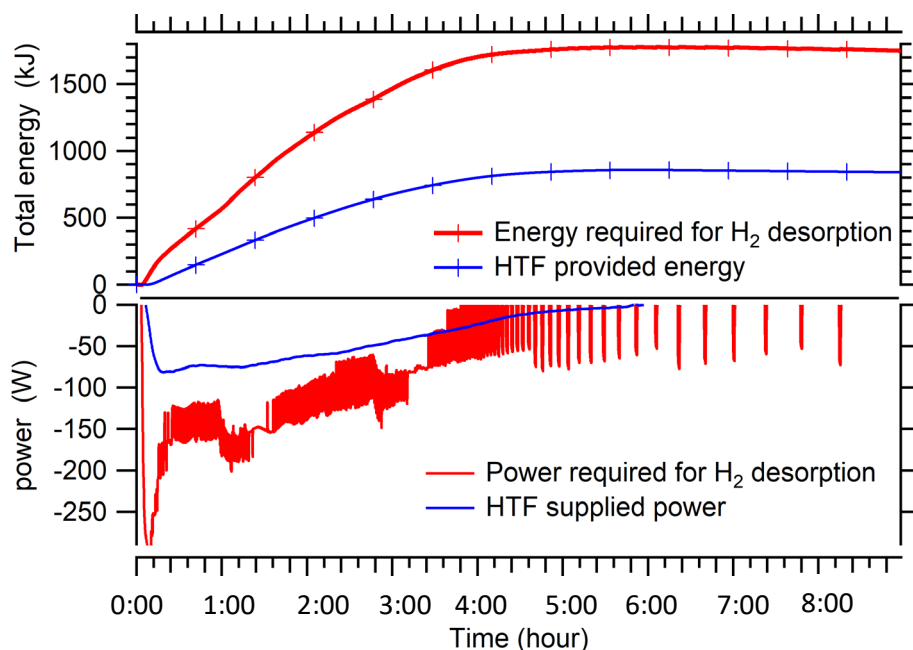


Figure 6-3 - Energy and power required for hydrogen desorption. Average reactor temperature 430 °C, HTF flow of 35 ml/min, and hydrogen pressure set to 10 bar.

The total energy required for hydrogen desorption was determined from the integration of the power curve produced from eq. 6-4 and was found to be ≈ 1710 kJ. The integration of the power delivered by the HTF resulted in ≈ 850 kJ, which is half the energy required. Sensible energy from the material and housing as well as the furnace on PID mode contributed to the energy supply as described below.

During desorption, the hydride bed temperature dropped from an average of 430 °C to 412 °C. Considering the specific heat at 430 °C (determined from the HSC chemistry software to be 2420 J/kg.K),⁶⁶ Mg_2FeH_6 released ≈ 32 kJ of specific heat to promote hydrogen desorption. The stainless steel reactor casing (8 cylindrical cells) was considered to undergo an identical temperature drop. With a specific heat determined in chapter 5 (Section 5.3.5.3) of 645.9 J/kg.K and a total mass estimated at 6 kg, the housing supplied ≈ 72 kJ to the chemical reaction. The furnace which was programmed to maintain 400 °C to the reactor surroundings was actively providing thermal energy to counteract the decrease in the reactor's temperature. It was estimated to supply ≈ 680 kJ over the six first hours of the desorption event.

Table 6-1 presents a summary of the energy contribution provided by the various components of the thermal battery.

Table 6-1 - Energy breakdown (kJ) of the different supplies (with 10 % uncertainty). Hydride and vessel energy are based on their specific heat, furnace energy was estimated from PID control, HTF energy from temperature and mass flow, and required energy was determined from hydrogen mass and enthalpy.

Hydride (Mg_2FeH_6) (kJ)	Vessel (SS316) (kJ)	Furnace (kJ)	HTF (kJ)	Total supplied energy (kJ)	Required energy for reaction (kJ)
32	72	680	870	1650	1710

6.2.2. Thermal energy discharge

When the thermal battery is fully charged (i.e. hydrogen fully desorbed, Mg and Fe remaining), a hydrogen absorption induces thermal energy generation, which can be restored to the HTF. In the following typical case, the parameters from the previously described thermal energy storage experiment were kept identical: HTF heated up to ≈ 490 °C flowing at 35 ml/min, and furnace set to maintain 400 °C on the reactor's surroundings.

However, the valve allowing hydrogen to flow through the compressor was closed, and the valve allowing the hydrogen to flow from the gas store to the reactor was opened. The pressure regulator was set to 45 bar H₂, which is \approx 23 bar over the equilibrium pressure of Mg₂FeH₆ at 430 °C (22 bar). This was to ensure full hydrogenation of the hydride.

Figure 6-4 shows the pressures measured in the hydrogen gas store (bottle) and reactor throughout the thermal energy discharge event, as well as the cumulated hydrogen mass absorbed by the hydride (determined by mass flow). The regulated hydrogen supply pressure started at 44 bar, increasing slowly to 45 bar as absorption slowed. The absorption of \approx 44 g of hydrogen was completed within 6 to 7 hours and induced a gas pressure drop in the store from 79 to 68 bar H₂. The mass of hydrogen absorbed was similar to the mass previously desorbed (44 g), demonstrating the reversibility of the thermochemical reaction in the reactor, at these operating temperature and pressure conditions.

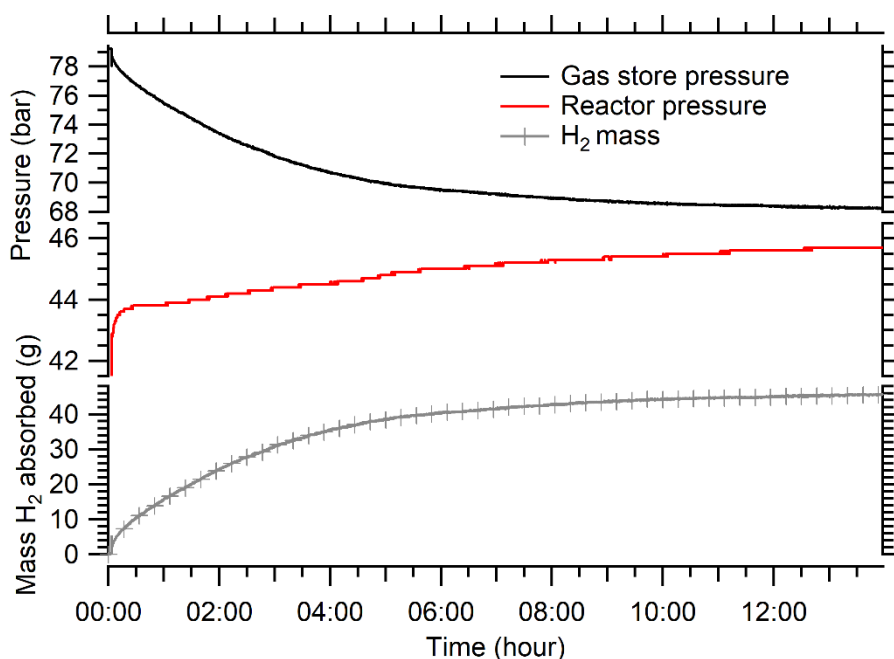


Figure 6-4 - Gas store and reactor hydrogen pressure evolution, along with the hydrogen mass absorbed by the hydride. Average reactor temperature 430 °C, HTF flow of 35 ml/min, and hydrogen pressure set to 45 bar.

The energy generated from the hydrogen absorption caused a temperature increase within the thermal battery. As shown in Figure 6-5, apart from T1, all thermocouples display a sudden 30 °C increase and return to original levels after 6 of 7 hours. The temperature of the HTF outlet also increased from 430 °C to \approx 460 °C. Previous reports mentioned scale, heat losses or thermal management issues, which hindered the observation of such thermal energy extraction at this temperature level.^{93, 97, 98, 309}

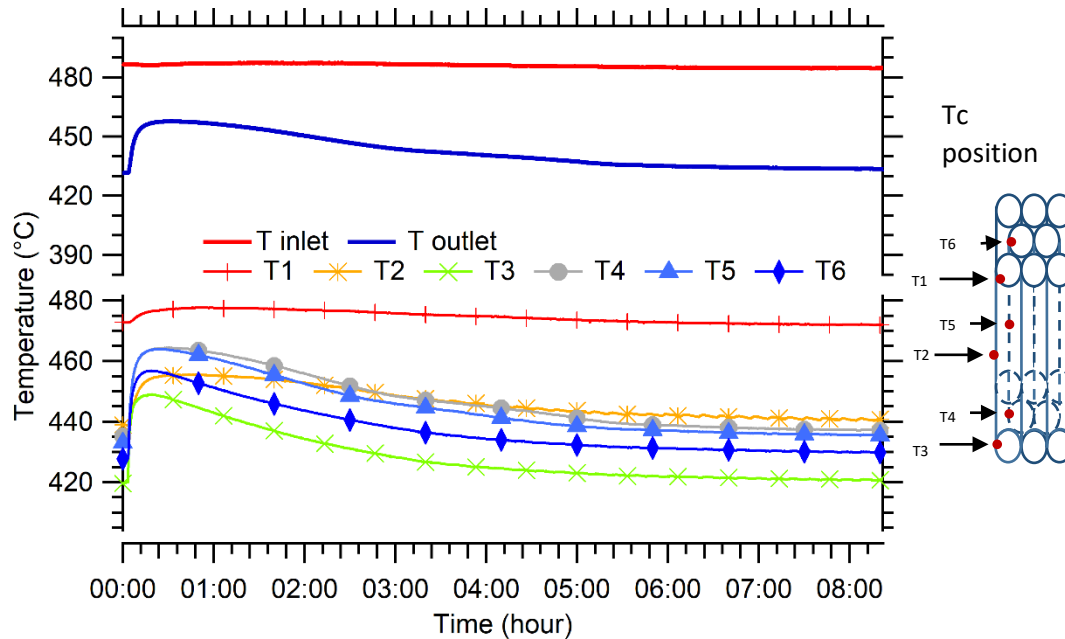


Figure 6-5 - Temperature of inlet and outlet HTF as well as inside the reactor during H_2 absorption. Average reactor temperature 430 °C, HTF flow of 35 ml/min, and hydrogen pressure set to 45 bar. T1 to T6 follow the HTF flow direction (T inlet was 10 cm before T1 and T outlet was 10 cm after T6).

Following the same procedure as described in the previous section the energy and power generated by the absorption were determined and plotted alongside the energy harvested by the HTF (Figure 6-6). As the hydrogen mass absorbed was similar to the previously desorbed mass, the total energy generated by this thermochemical reaction was identical (\approx 1710 kJ). Additionally, with 23 bar H_2 of overpressure supplied compared to the equilibrium pressure of 22 bar H_2 at 430 °C, the hydrogen flow absorbed and its related power generated is virtually identical to the pattern observed during hydrogen desorption under 10 bar H_2 . The power generation determined from the hydrogen absorption spiked as the reaction initiated and the HTF was not able to extract as much power. Better control of the hydrogen supply would prevent this effect. The energy and power level harvested by the HTF was, however higher compared to that supplied for hydrogen desorption. Indeed, \approx 1 MJ was retrieved by the HTF (as opposed to 850 kJ supplied) with a peak power slightly

over 80 W. The explanation may lie in the contribution made by other parts of the experimental system.

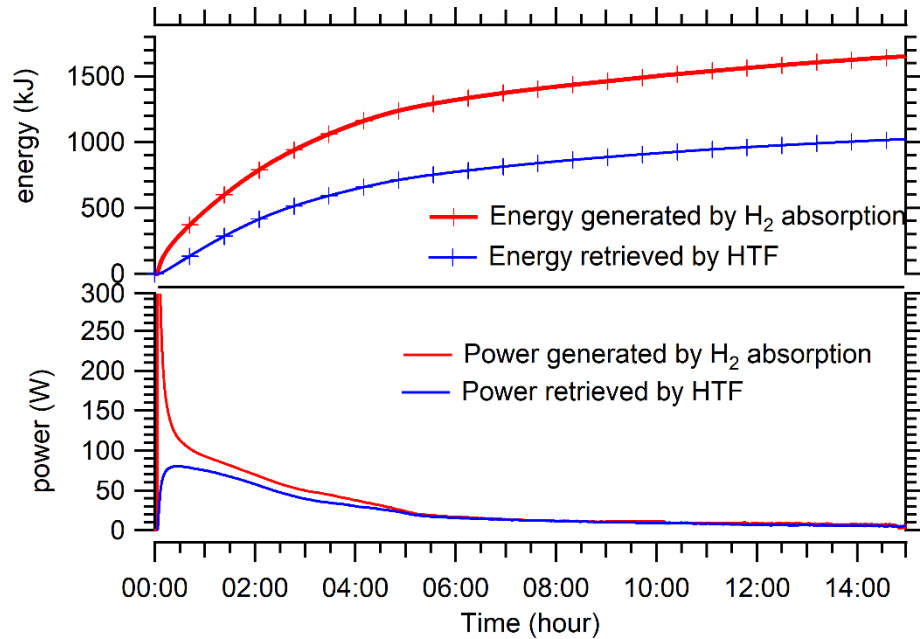


Figure 6-6 - Energy and power generated by the hydrogen absorption. Average reactor temperature 430 °C, HTF flow of 35 ml/min, and hydrogen pressure set to 10 bar.

In Table 6-2, the energy determined to be consumed by different parts of the system is summarised. As the magnitude of the temperature excursion caused by the hydrogen absorption was more substantial than that caused by the desorption event, the energy diverted by the hydride and the stainless steel increased from 32 kJ to 46 kJ and from 72 kJ to 104 kJ, respectively. However, the furnace diverted only 450 kJ during the thermal energy discharge, which is less energy than it supplied for the loading (680 kJ). This is the main reason why the HTF was able to retrieve > 1 MJ of the generated energy.

Table 6-2 - Energy breakdown (kJ) of the different components (with 10 % uncertainty). Hydride and vessel energy are based on their specific heat, furnace energy was estimated from PID control, HTF energy from temperature and mass flow, and required energy was determined from hydrogen mass and enthalpy.

Hydride (Mg ₂ FeH ₆) (kJ)	Vessel (SS316) (kJ)	Furnace (kJ)	HTF (kJ)	Total energy harvested (kJ)	Generated energy by reaction (kJ)
46	105	450	1080	1680	1710

The study of this standard cycle of hydrogen desorption and absorption revealed the possibility of generating $\approx 90\%$ of the theoretical energy provided by the thermochemical reaction of hydrogen with Mg_2FeH_6 . However, the scale of this experimental setup doesn't allow for harvesting all of the heat, as the furnace, acting as the environment, still contributes significantly to the energy supply and dissipation. Indeed, as Paskevicius *et al.* mentioned in their small scale prototype study, the surface radiating to the environment compared to the mass of heat storing material is an inherent issue of lab scale prototype that should be alleviated upon up scaling.⁹⁷ Considering the 8 cm outer diameter of this thermal battery, the surface to hydride mass ratio was $\approx 0.9 \text{ cm}^2/\text{g}$. A reduction of this ratio seems instrumental to overcome this issue inherent to small scale systems. The power loss (P_l), determined in Section 6.2.1 to be 144 W for a 30 °C difference between the reactor and its environment, can be determined from eq. 6.5.³²⁰

$$P_l = \frac{T_i - T_e}{R_{\text{reac}}} \cdot H \quad \text{eq. 6-5}$$

where T_i is the temperature inside the reactor (705 K), T_e is the temperature of the reactor's surroundings (675 K), H is the reactor height (0.3 m) and R_{reac} is the local thermal resistivity (in m.K/W). Hence, the thermal resistivity for this setup was determined to be 0.0625 m.K/W. A larger thermal battery would involve a thick layer of insulation, improving the thermal resistivity as:³²⁰

$$R_{\text{tot}} = R_{\text{reac}} + \frac{\ln(r_i/r_r)}{2\pi \cdot \lambda_i} \quad \text{eq. 6-6}$$

Where r_r is the radius of the reactor, r_i is the radius of the insulated reactor and λ_i is the thermal conductivity of the insulating layer.

For a cylinder of 4 m height and 10 m in diameter, the surface to hydride mass ratio reduces to $0.014 \text{ cm}^2/\text{g}$, considering a similar apparent hydride density of $640 \text{ kg}/\text{m}^3$. Such a thermal battery would have a capacity of $103 \text{ MWh}_{\text{th}}$ (eq.3-1), with an insulation of 0.5 metres (conductivity of $0.08 \text{ W}/\text{m.K}$), the thermal resistivity determined from eq.0-6 becomes $0.16 \text{ m.K}/\text{W}$. An operating temperature of 450 °C induces 10.65 kW or $255.6 \text{ kWh}_{\text{th}}$ of heat losses over 24 hours, which is $\approx 0.2\%$ of the energy storage. Following the same calculations, Figure 6-7 provides an estimation of the heat losses as a function of the

thermal energy capacity based on the thermal resistance and hydride density observed in the presented setup Improved with an additional 30 cm of insulation (0.08 W/m.K). It shows that a 250 kWh_{th} thermal battery as a 1 m high cylinder would lose 10 % of its storage capacity over 24 hours.

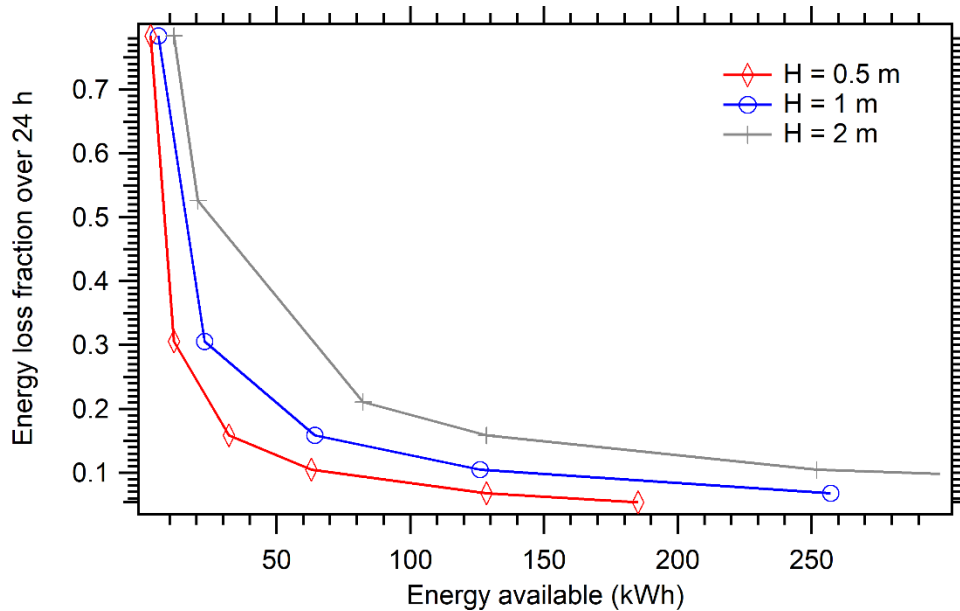


Figure 6-7 - Energy losses fraction versus energy storage capacity based on the thermal resistivity and apparent hydride density determined in this setup. Three different heights (H) are displayed.

6.2.3. Operating pressure variations

6.2.3.1. Operating at $T = 430\text{ }^{\circ}\text{C}$

In the typical cycle presented above, the supply pressure for hydrogen absorption by the hydride was set to 45 bar H_2 to ensure full absorption. However, investigations on the influence of this pressure level seemed necessary. Similar experimental parameters were fixed to compare the role of the hydrogen supply pressure: host furnace maintaining the reactor's environment at $400\text{ }^{\circ}\text{C}$ and HTF flowing at 35 ml/min under 200 bar back pressure with a temperature at the inlet of the reactor at $\approx 490\text{ }^{\circ}\text{C}$. The average reactor temperature was stable at $430\text{ }^{\circ}\text{C}$, which corresponds to an equilibrium pressure of 22 bar H_2 .

The hydrogen pressure supplied was varied between 30 – 50 bar H_2 , which equates to 8 to 28 bar of overpressure compared to the experimental 22 bar equilibrium pressure of

Mg₂FeH₆ formation at 430 °C. The absorption kinetics (based on hydrogen mass flow) are displayed in Figure 6-8 with the plots revealing that a minimum of 45 bar H₂ was required to reach over 80 % hydrogen capacity, whereas if 35 bar H₂ was applied, absorption only reaches 60 % of the reacted fraction. As shown in Figure 6-2 and Figure 6-5, a thermal gradient is observed within the reactor, with T1 (at the top of the reactor) ≈ 470 °C and T3 (at the bottom of the reactor) remaining at ≈ 420 °C. The equilibrium pressure of Mg₂FeH₆ at 470 °C is 40 bar H₂, implying that below this pressure, a part of the reactor cannot undergo hydrogen absorption. The increase of the supplied pressure also allowed for faster kinetics, since for 50 bar supplied hydrogen pressure, 80 % of the reacted fraction was reached within 3 hours, whereas at 40 bar H₂, this value was only attained in 9 hours. This demonstrates the ability of the pressure supply to control the hydrogen mass flow during absorption by the hydride, and the time required to complete the reaction.

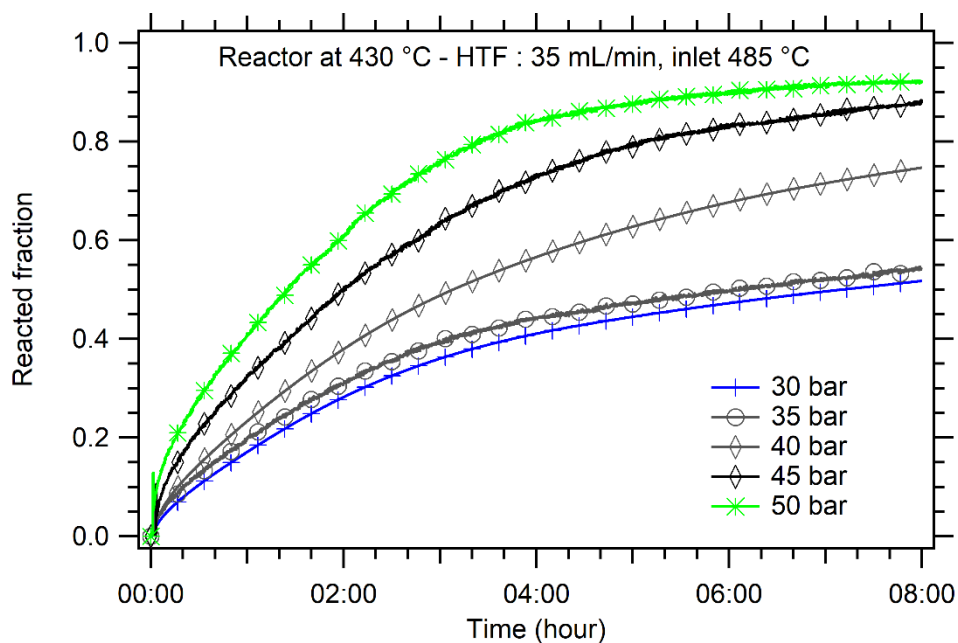


Figure 6-8 - Hydrogen absorption kinetics for varied H₂ supply pressures for an operating temperature of 430 °C.

Table 6-3 presents a summary of the energy diverted by the different components of the system for various hydrogen supply pressures. It shows that for this setup, a substantial overpressure of hydrogen is required to approach full hydrogen capacity. Even if it allows more energy to be harvested by the HTF, the vessel and hydride divert an increased proportion of the generated energy with an increase in the supplied hydrogen pressure. The furnace exerts less energy as the maximum temperature reached by the thermal

battery increases with the hydrogen pressure rise. The results shows that the energy extracted by the HTF ($\approx 50 - 60\%$) doesn't significantly vary with the gas pressure supply in this setup (final column).

Table 6-3 - Energy breakdown at an operating temperature of 430 °C and HTF flow of 35 ml/min for different hydrogen pressure supplies (uncertainty of 10 %). Hydride and vessel energy are based on their specific heat, the furnace energy was estimated from PID control, HTF energy from temperature and mass flow, and required energy was determined from hydrogen mass and enthalpy.

Hydrogen pressure supply (bar)	Hydrogen mass absorbed (g)	Energy generated by reaction (kJ)	Energy diverted by hydride (kJ)	Energy diverted by vessel (kJ)	Energy diverted by furnace (kJ)	Energy harvested by HTF (kJ)	Ratio of harvested and generated (%)
30	21.5	825	20	40	270	475	58
30	31	1190	25	58	315	545	46
35	32	1230	30	65	450	600	49
35	33	1270	25	60	380	675	53
40	40	1540	40	90	410	870	57
40	41.5	1590	40	90	515	790	50
45	44	1690	45	105	455	1045	62
50	46	1770	60	140	510	960	55
50	44	1690	60	130	485	1010	60

6.2.3.2. Operating at $T = 410\text{ °C}$

A series of absorption experiments were conducted at a lower operating temperature under a variety of hydrogen supply pressures. The average reactor temperature was kept at $\approx 410\text{ °C}$. The HTF flow and pressure were sustained at 35 ml/min and 200 bar, respectively, but the inlet temperature required was 430 °C. To maintain the 30 °C temperature difference between the reactor and background, the host furnace was set to maintain 380 °C. The hydrogen pressure supply was varied between 25 and 40 bar H_2 , or 7 to 22 bar of overpressure compared to the 18 bar H_2 of equilibrium pressure for the hydride at 410 °C (Section 3.3.2.3). As previously observed, the absorption kinetics were improved by the elevation of the hydrogen supplied pressure (Figure 6-9). For 40 bar H_2 , or 22 bar overpressure, 80 % of hydrogen capacity was achieved after 2 hours. For 25 bar H_2 , or 7 bar overpressure, 80 % of the reacted fraction was also reached, after 8 hours. The thermal gradient within the reactor in steady state was much lower with an 18 °C difference

between the top and bottom (instead of 50°C) and a maximum temperature measured at 421 °C. At this temperature, the equilibrium pressure of Mg₂FeH₆ remains at 20 bar H₂; therefore, the whole reactor was able to undergo hydrogen absorption, even at the lowest pressure tested.

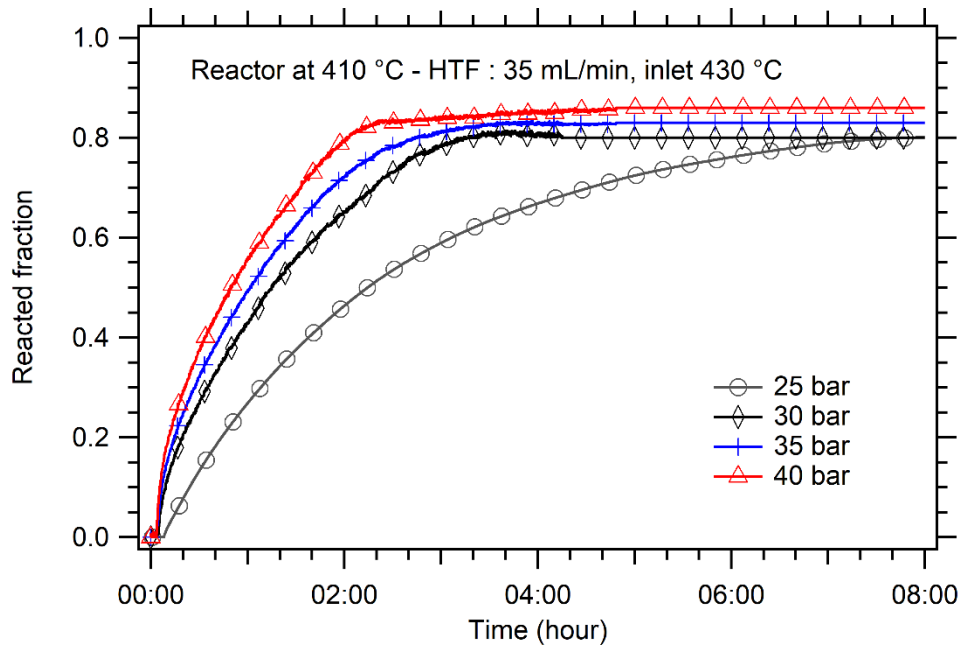


Figure 6-9 - Hydrogen absorption kinetics for different supply pressures for an operating temperature of 410 °C. HTF flow of 35 ml/min and hot background temperature regulated at 380 °C.

These pressure experiments illustrate that keeping the reactor cell isothermal is a crucial parameter to help decrease the difference between the equilibrium pressure and the supplied pressure required to perform a hydrogen absorption with an optimised capacity.

6.2.4. Operating temperature variations

Hydrogen absorption experiments were performed at various average reactor temperatures between 410 °C and 450 °C (note that the thermal gradient is not constant in each case). The HTF flow was set to 35 ml/min and 200 bar backpressure. The host furnace PID was set to maintain the background at ≈ 30 °C colder than the average reactor temperature. The HTF inlet temperature was set to maintain the reactor at an operating

temperature when no reaction should occur. Figure 6-10 displays the reacted fraction during the hydrogen absorption event at various operating temperatures and an overpressure of hydrogen set at ≈ 17 bar (overpressure = gas pressure – equilibrium pressure).

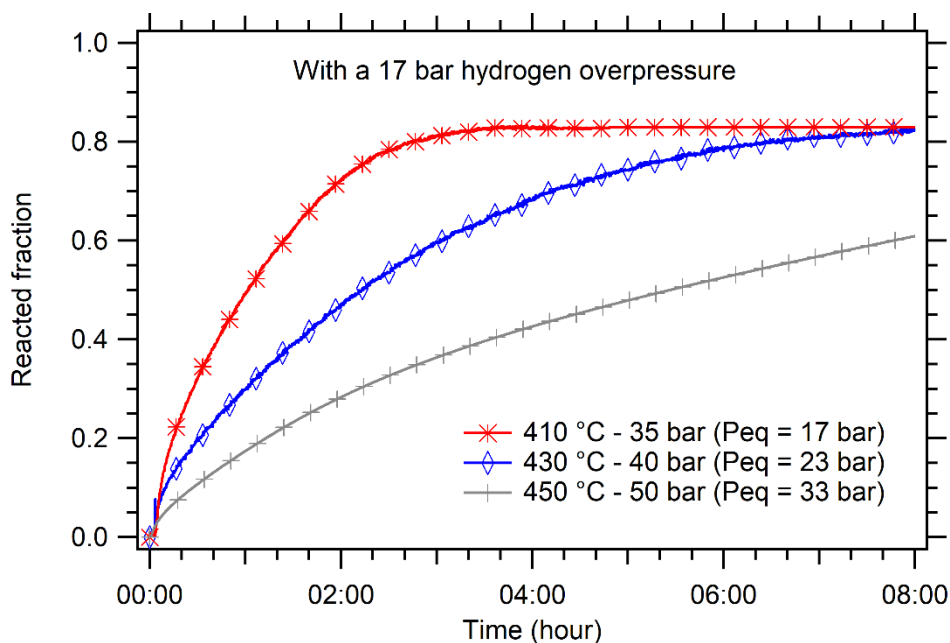


Figure 6-10 - Absorption kinetics at varied operating temperatures and a hydrogen supply pressure of 17 bar over the equilibrium pressure. The HTF flow was 35 ml/min.

The plots show that 80 % of absorption capacity was reached in less than 3 hours at the operating temperature of 410 °C, whereas it required 6 hours at 430 °C. When operating at 450 °C, a 17 bar hydrogen overpressure was not sufficient to complete the absorption in 8 hours and reached only 72 % completion in 14 hours. However, the thermal gradient observed in the reactor when operating at an average of 450 °C was ≈ 60 °C, with the highest temperature measured at T1 being slightly below 500 °C. The equilibrium pressure at this temperature would be 65 bar H₂. Therefore, part of the reactor was not at a condition that allowed hydrogen absorption to occur. From this data, it is apparent that the thermal gradient may impact the absorption kinetics more than the actual operating temperature. Nonetheless, the thermal gradient occurrence was inherent to the setup and the scale of the reactor. For future designs, this observation shall be assessed to limit that gradient to ≈ 10 °C, implying that the density of energy provided or extracted will be optimised.

In the present setup, only one control parameter could alleviate or diminish that gradient, which is the HTF flow. Hence, the following section presents an investigation into the effects of a HTF flow increase.

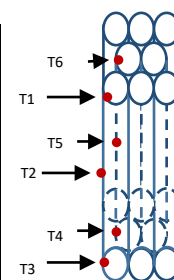
6.2.5. HTF flow variations

To evaluate the effect of the HTF flow rate on the thermal gradient in the thermal battery, hydrogen absorption experiments were performed at three different HTF flow rates: 35, 50 and 65 ml/min. The thermal battery operating temperature target was an averaged 430 °C, and the furnace was again set to maintain the environment at 400 °C.

Table 6-4 illustrates the temperatures measured by each of the thermocouples placed in the thermal battery, along with the inlet and outlet HTF temperatures for each of the flows tested. These temperatures were measured when no hydrogen flow was occurring. A 50 °C gradient in the reactor was observed with a 35 ml/min HTF flow rate with a maximum temperature recorded at T1 of 468 °C. This difference was decreased to 35 °C with a flow of 50 ml/min with a maximum of 455 °C. The increase of the HTF flow to 65 ml/min further reduced the thermal gradient to 30 °C with a maximum temperature of 450 °C at T1.

Table 6-4 - Local temperatures measured in a steady state reactor (no chemical reaction, with 0.75% uncertainty).

HTF flow (ml/min)	Inlet HTF Temp (°C)	T1 (°C)	T2 (°C)	T3 (°C)	T4 (°C)	T5 (°C)	T6 (°C)	Outlet HTF Temp (°C)
35	480	468	437	419	427	432	433	430
50	459	455	432	419	428	432	431	429
65	451	449	432	418	427	432	430	428



The maximum temperatures observed at the sensor T1 also constrain the minimum gas pressure required to reach total hydrogen capacity, hence also limiting the optimum gravimetric energy density. For the HTF flowing at 35 ml/min this minimum pressure correlates to the 468 °C and is 43 bar H₂, whereas for 50 and 65 ml/min, it drops to 40 and 33 bar H₂ respectively.

The plots shown in Figure 6-11, also support this observation as the reacted fraction obtained with 40 bar H₂ at a HTF flow of 35 ml/min remains slightly below 80 % even after 8 hours, showing that not all the material was hydrogenated. Moreover, the absorption kinetics were improved with an increased HTF flow for both hydrogen supply pressures tested. Improved heat removal during the gas absorption process results in an increased power generation. However, the absorption kinetics displayed for 50 bar H₂ are similar, whether the HTF flow rate is 50 ml/min or 65 ml/min, which implies that another factor is limiting the absorption process.

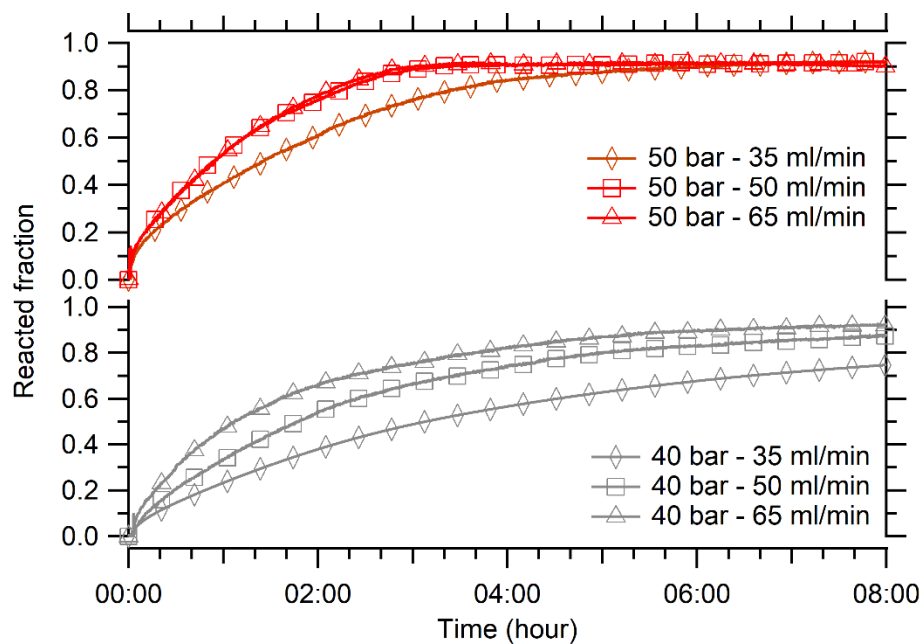


Figure 6-11 - Reacted fraction evolution for various HTF flow at the operating temperature of 430 °C with 40 and 50 bar H₂ supplied.

The power extracted by the HTF was also improved by increasing the flow rate. As shown in Figure 6-12(a), the power extracted reached a peak of ≈ 150 W at 50 bar H₂ and 65 ml/min of HTF flow, whereas for a flow rate of 35 ml/min, the power peaked at ≈ 100 W. With a hydrogen supply pressure of 40 bar (Figure 6-12(b)), the absorption and heat generation were not so vigorous. As the reaction kinetics decreased, the thermal energy extraction was reduced. A 100 W peak extracted for a HTF flow of 65 ml/min was determined, as opposed to 150 W when 50 bar of hydrogen pressure was applied.

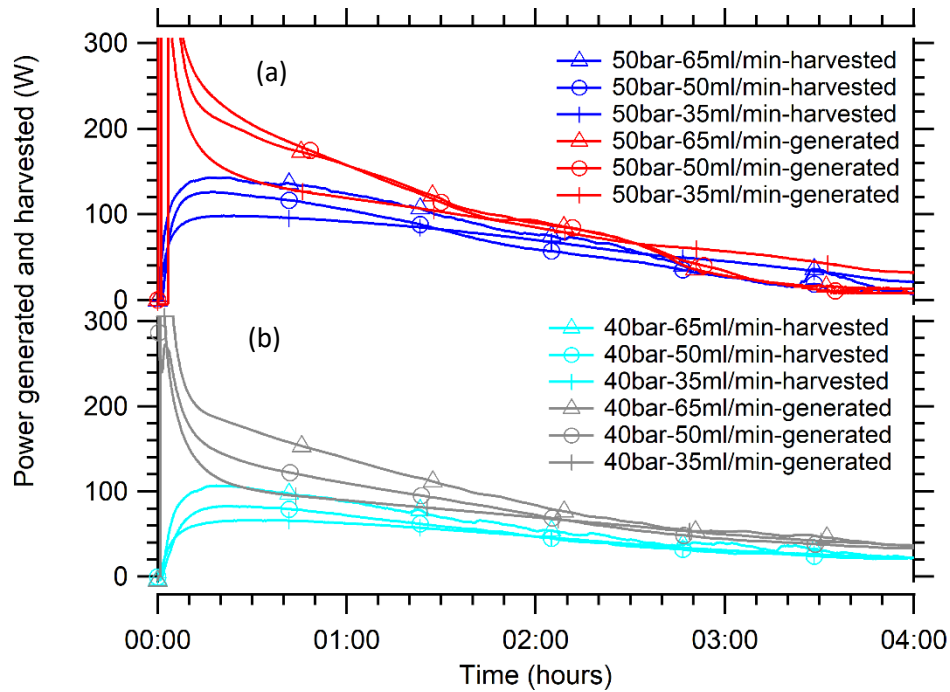


Figure 6-12 - Power generated and harvested for various HTF flow rates at the operating temperature of 430 °C with 40 and 50 bar H₂ supplied.

The integration of the power extracted from the system over time allows the determination of the overall energy extracted. Table 6-5 presents a summary of the energy generated and harvested by the HTF for various HTF flow rates at 40 and 50 bar H₂. It shows that an increase in HTF flow rate tends to improve total energy generated and the harvested heat also increases. Hence the efficiency of the thermal battery compared to the theoretical capacity was greatly enhanced, reaching > 60 %.

Table 6-5 - Energy generated and harvested for thermal energy discharge at 430 °C with 40 and 50 bar H₂ supplied for various HTF flows (uncertainty on energy calculation is 10%). Hydride and vessel energy are based on their specific heat, the furnace energy was estimated from PID control, HTF energy from temperature, mass flow and required energy were determined from hydrogen mass and enthalpy.

HTF flow (ml/min)	Hydrogen pressure supply (bar)	Energy generated (kJ)	Energy harvested by HTF (kJ)	Efficiency (%)
35	40	1520	870	48
50	40	1670	950	52
65	40	1650	990	54
35	50	1690	1010	56
50	50	1670	1110	61

65	50	1710	1120	62
----	----	------	------	----

6.2.6. Thermal battery supplying consistent power

Eventually, if a thermo-electric engine (e.g. Stirling engine) was to be utilised to transform the thermal energy produced, it would require a steady level of power supply to ensure the production of baseload electric power. Three parameters can be regulated to provide consistent thermal energy output at a fixed temperature: the HTF flow, the hydrogen pressure and the HTF inlet temperature. As the HTF flow and hydrogen pressure regulator are manually operated in the present case, the HTF inlet temperature remains the parameter that can be varied to determine if this system can provide steady power output.

6.2.6.1. HTF outlet temperature regulation between 430 °C – 425 °C with 40 bar H₂, HTF flow of 50 ml/min

To assess the ability of this thermal battery to provide consistent power, the HTF inlet temperature was varied between 470 °C (to simulate day time heat charging) and 440 °C (to simulate night time heat discharge). At a steady HTF flow of 50 ml/min, when the inlet temperature was at 470 °C and no hydrogen reaction occurred, the temperature of the HTF outlet reached 438 °C. The steady heat losses determined from eq. 6-1,2,3 were \approx 100 W. When the inlet temperature was at 440 °C and no hydrogen reaction occurred, the HTF outlet reached 418 °C, which implied heat losses of 140 W. These temperature differences in a steady state that accounted for the heat losses may be due to the thermal battery scale (radiating surface to hydride mass ratio) and HTF temperature sensor positions. The calculated heat losses were, therefore, retrieved from power and energy calculations.

Figure 6-13 presents the inlet HTF temperature along with the regulated outlet temperature between 430 °C and 425 °C by the operation of the thermal battery. The regulation of the HTF outlet temperature was performed automatically by supplying hydrogen when the HTF temperature dropped below 425 °C or by evacuating hydrogen when the temperature was $>$ 430 °C. An adjustment of the period at which the inlet temperature remains high (470 °C, promoting hydrogen desorption) or low (440 °C,

promoting hydrogen absorption) allows the thermal battery to successfully provide the energy required to maintain the HTF outlet temperature at $T > 425$ °C. Thermal energy can also be stored while limiting the outlet temperature at 430 °C.

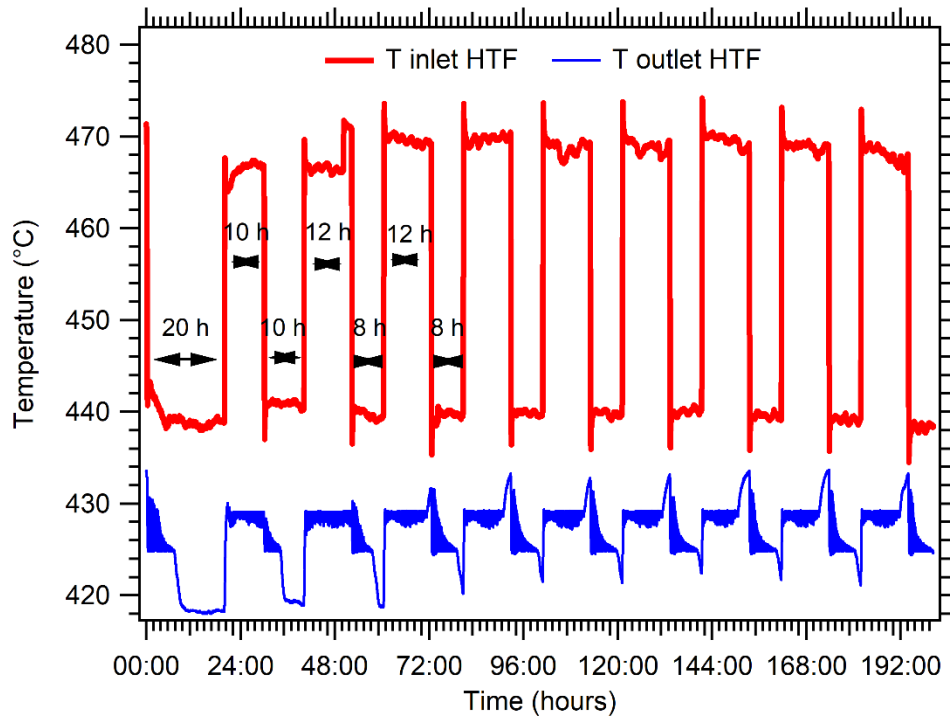


Figure 6-13 - Inlet and outlet HTF temperature history during thermal energy charge and discharge when the flow rate is 50 ml/min.

Figure 6-14 describes the hydrogen pressures in the gas store and the reactor corresponding to the HTF temperature regulation depicted in Figure 6-13. The hydrogen mass exchanged is also displayed. It reveals the consistency of the absorption and desorption reaction throughout the cycles. The two first cycles differed in the times used to perform heat charging (10 h and 12 h) and discharging (20 h and 10 h) but didn't have an impact on the subsequent overall capacity, which was consistently ≈ 44 g of hydrogen (or 4.9 wt%). Therefore the thermal battery does not exhibit charging memory.

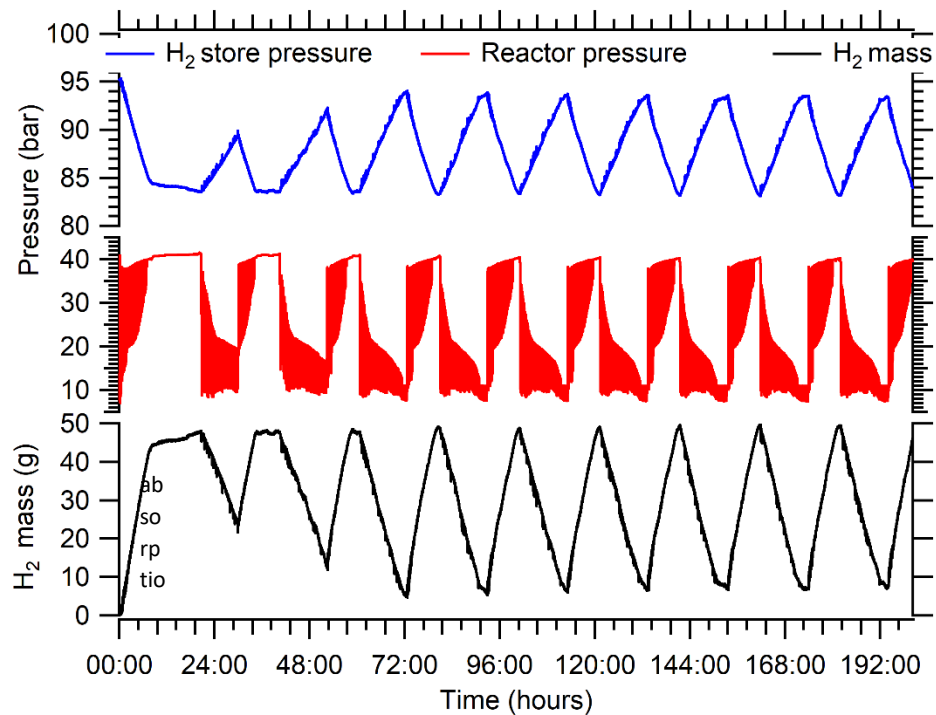


Figure 6-14 - History of hydrogen cylinder pressure, reactor pressure and mass of hydrogen absorbed by the hydride during thermal energy charge and discharge. (HTF flow rate 50 ml/min, hydrogen pressure 40 bar)

The temperature variation of the HTF allows for the determination of the power retrieved and supplied to the thermal battery. Figure 6-15 illustrates the power exchange fluctuations between the HTF and the thermal battery. During energy discharge, an average of 39 W was extracted by the HTF over 8 hours, which equates to ≈ 1.1 MJ. The energy storage process used an average of 26 W during 12 hours, which also relates to ≈ 1.1 MJ. Figure 6-16 depicts the energy involved in the hydrogenation reaction, which directly correlates to the hydrogen mass flowing in and out of the reactor and the energy supplied or extracted by the HTF. After the initial test cycles, the thermal battery showed a consistent energy storage capacity of 1.65 MJ. The 1.1 MJ extracted by the HTF corresponds to an efficiency of 67 %.

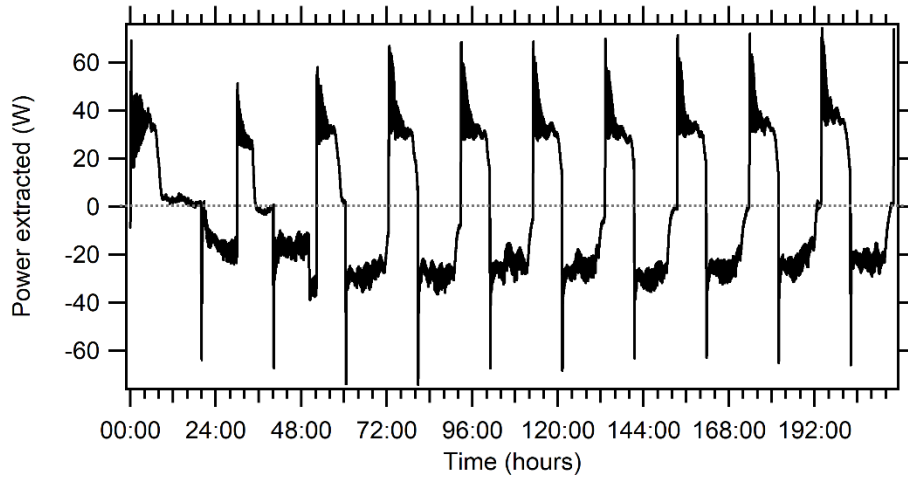


Figure 6-15 - Power exchanged between the HTF and the thermal battery during thermal cycles (HTF flow 50 ml/min, hydrogen pressure 40 bar).

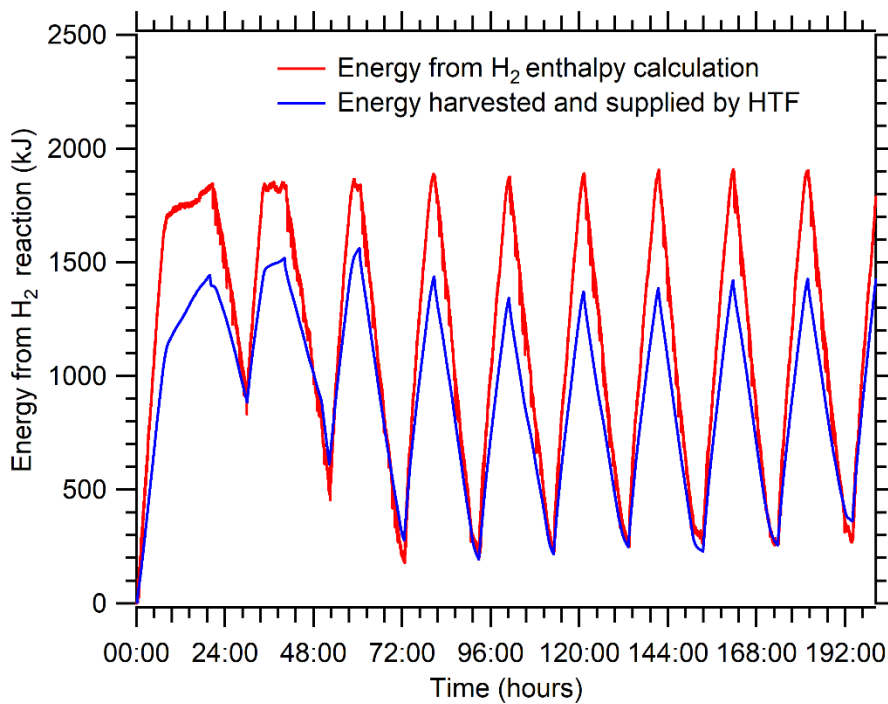


Figure 6-16 - Energy generated and absorbed by the hydrogen reaction along with the energy harvested and supplied by the HTF (HTF flow 50 ml/min, hydrogen pressure 40 bar)

A detailed view of the reactor temperature (thermocouples T2 to T6) is presented in Figure 6-17(a). Figure 6-17(b) displays the gas cylinder pressure to compare the thermal sensor response with hydrogen desorption and absorption events. Despite their various locations

in the thermal battery, all thermal sensors displayed identical responses during cycling. Their similar reactivity demonstrates the capacity of hydrogen gas to be absorbed independently from the distance between the material and the hydrogen inlet. Due to the high hydrogen permeability of iron at these temperatures, the iron strip placed in the centre of each reactor cell seems to enable the hydrogen gas to be distributed evenly

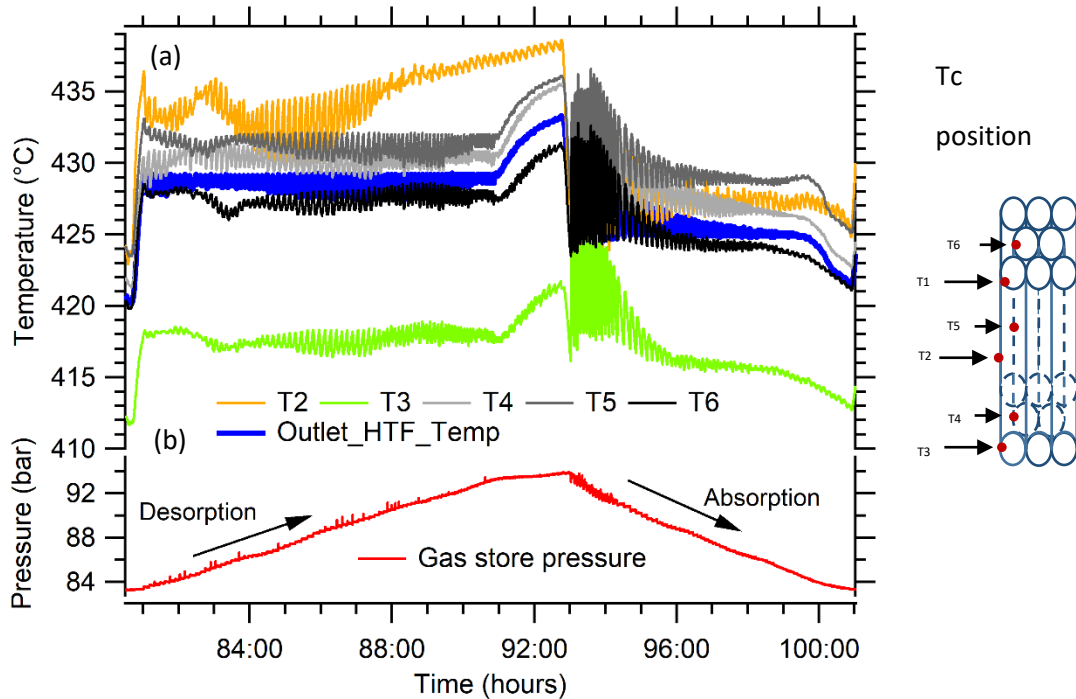


Figure 6-17 - (a) Temperature measured at each thermocouple and (b) related gas store pressure during one of the cycles presented in Figure 6-14, 6.15, 6.16.

throughout the length of the reactor.²⁰¹

6.2.6.2. HTF outlet temperature regulation between 430 °C – 425 °C with 35 bar H₂, HTF flow of 50 ml/min

A similar experiment of HTF temperature regulation was performed with a lower hydrogen supply pressure to assess the effect on the operation of the thermal battery. The HTF flow was once again set to 50 ml/min with a backpressure of 200 bar. For the hydrogen desorption (or heat charge) the inlet temperature was set to \approx 480 °C and slightly above 440 °C for the hydrogen absorption (or heat discharge). Figure 6-18 shows the HTF temperature inlet variation along with the temperature regulated HTF outlet. The hydrogen mass cycled over time, the power harvested and supplied by the HTF are also depicted. The

first heat discharge lasted 8 hours, in which time 27 g of hydrogen was absorbed. The subsequent heat charge, which was set to 12 hours, required only 3 hours to complete. When energy was not required for the hydrogen desorption, the HTF outlet temperature raised to 438 °C. The extension of the heat discharge time to 12 hours allowed to utilise \approx 35 g of hydrogen (on the fourth and fifth heat discharge). An average of 25 W was harvested by the HTF over the 12 hours, which shows the capacity of the supplied pressure to regulate the power generated and retrieved. However, at the end of the hydrogen absorption events, the remaining 12 % of the hydrogen mass absorbed didn't allow the HTF

outlet to maintain 425 °C (Figure 6-18 (dashlines)), underlining the limitation induced by slow reaction kinetics.

The reduced hydrogen mass involved in the thermal cycling of the battery produced less energy during the absorption event. As shown in Figure 6-19, ≈ 1.42 MJ was attained. The energy harvested by the HTF was slightly lowered to 1 MJ, which is in the same vicinity as

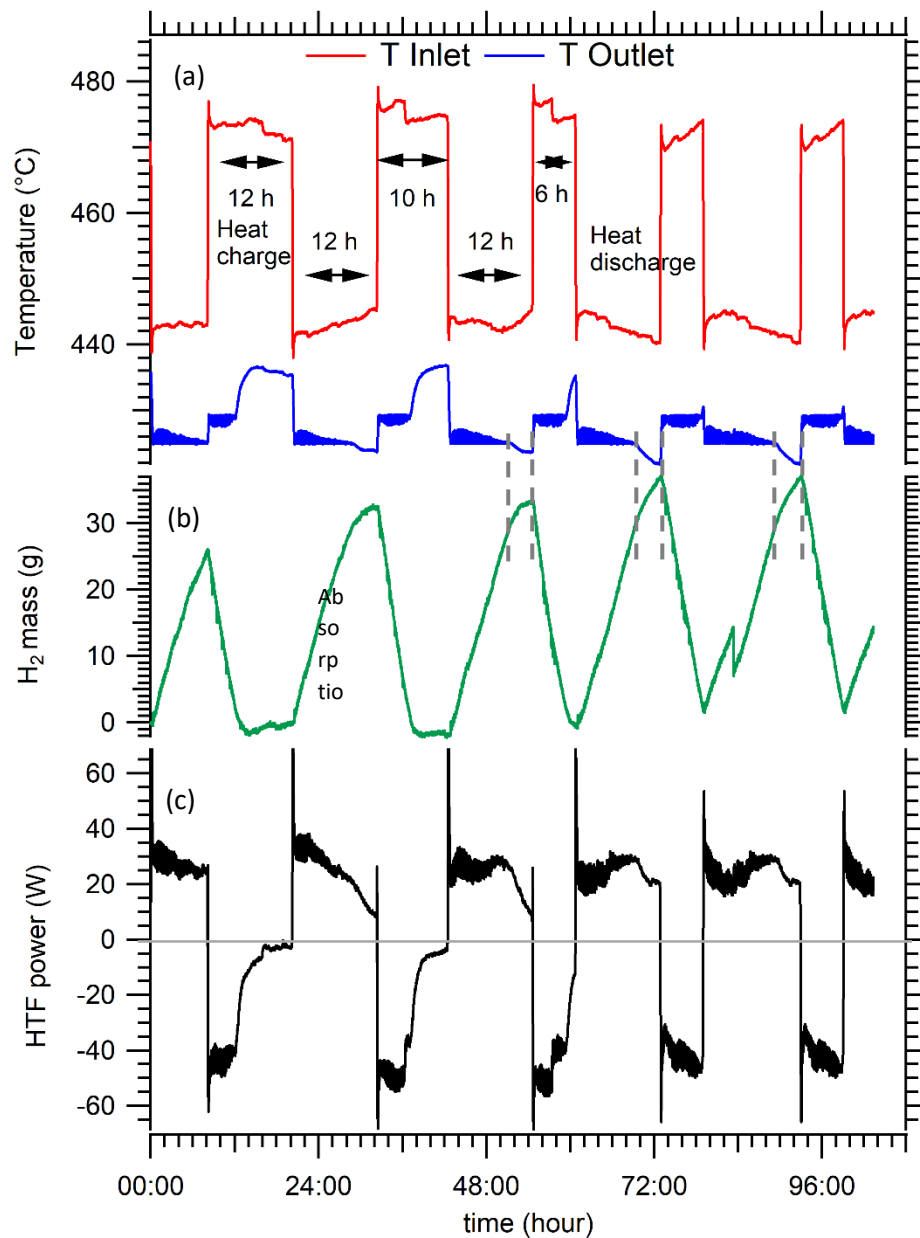


Figure 6-18 (a) Inlet and regulated HTF outlet temperature between 430 and 425 °C and flowing at 50 ml/min, (b) Hydrogen mass absorbed and desorbed and (c) power extracted and supplied by the HTF, with 35 bar H₂ supplied.

that of the previous experiment.

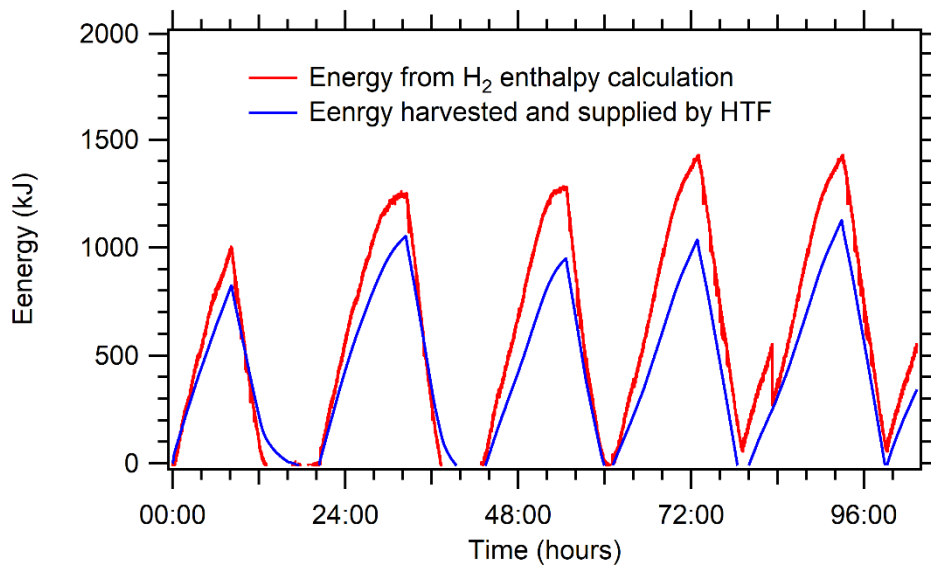


Figure 6-19 - Energy generated and absorbed by the hydrogen reaction along with the energy harvested and supplied by the HTF (HTF flow 50 ml/min, hydrogen pressure 35 bar).

6.2.6.3. HTF outlet temperature regulation between 430 °C – 425 °C with 35 bar H₂, HTF flow of 65 ml/min

As discussed previously, the observed thermal gradient was a hindrance when attempting to reach the maximum hydrogen capacity with a hydrogen pressure supply near equilibrium. Since a higher HTF flow diminishes the thermal gradient, an experiment replicating the previous parameters with a HTF flowing at 65 ml/min instead of 50 ml/min was performed.

Figure 6-20 presents the HTF inlet temperature variations along with the temperature regulated HTF outlet of the thermal battery; the hydrogen mass involved in each absorption and desorption event; and the power harvested and supplied by the HTF. The charging of the thermal battery was achieved with a HTF temperature inlet of ≈ 465 °C, with 12 hours required to complete the desorption of 44 g of hydrogen. This process used an average of 37 W. The heat discharged when the HTF temperature was lowered to 440 °C caused the reaction to take 10 hours to complete with an averaged 44 W being retrieved

by the HTF. Even though the previously observed hydrogen capacity of 4.9 wt% was reached with 44 g hydrogen involved when the cycles were tuned, the absorption of the last 20 % of the hydrogen mass was not generating enough power to maintain the HTF outlet at 425 °C (Figure 6-20 (dashlines)). This shows that the kinetics of absorption with 35 bar of hydrogen was limiting the energy generation. Despite a reduction in the thermal gradient of the reactor caused by the increased flow rate of the HTF an increased gas pressure should be supplied to allow operation of the thermal battery between 430 and 425 °C under the 65 ml/min HTF flow.

The energy collected during this experiment is presented in Figure 6-21, and shows that it

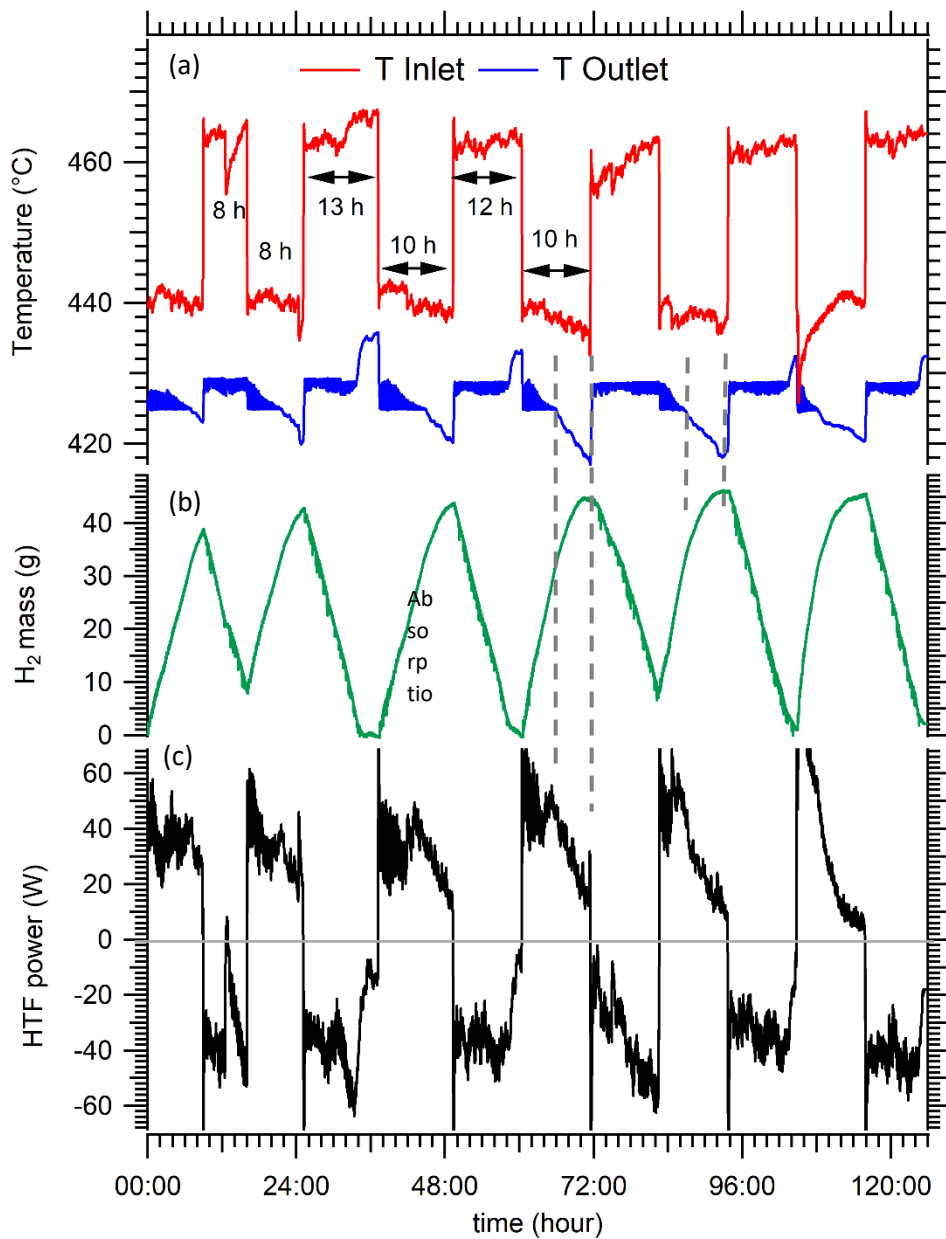


Figure 6-20 - (a) Inlet and regulated HTF outlet temperature between 430 and 425 °C with flow rate of 65 ml/min, (b) Hydrogen mass absorbed and desorbed, and (c) power extracted and supplied by the HTF), with 35 bar H₂ supplied.

reached 1.5 MJ when 1.7 MJ was generated. It shows that even if the temperature level was not maintained, the setup achieved almost 90% efficiency when the heat losses are not taken into account. If the energy harvested by the HTF below the set temperature level of 425 °C was not considered, that energy was ≈ 1.05 MJ, which dropped the efficiency to 62 %.

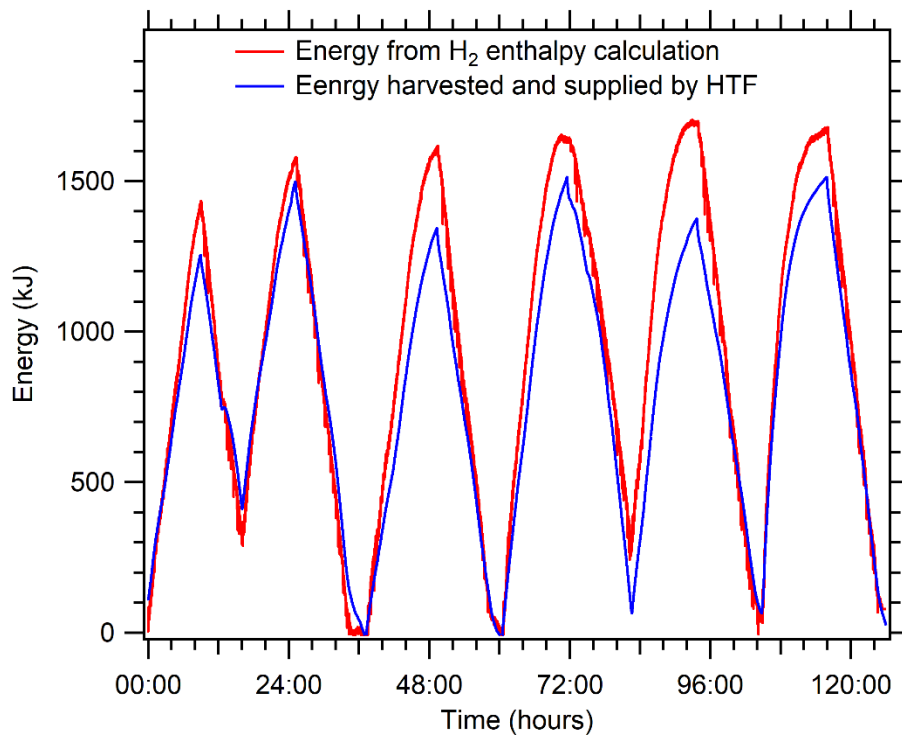


Figure 6-21 - Energy generated and absorbed by the hydrogen reaction along with the energy harvested and supplied by the HTF (HTF flow 65 ml/min, hydrogen pressure 35 bar)

6.3. Summary

A magnesium iron hydride thermal energy storage prototype was designed and built with pressurised water acting as the heat transfer fluid. A compressed hydrogen tank was connected to the thermal battery so that hydrogen charge and discharge could be automated. A detailed investigation was carried out using this setup to investigate the influence of various parameters (HTF flow rate, HTF temperature, hydrogen pressure supply, etc.) at an operating temperature of 430 °C. The thermal battery displayed similar cycle reversibility between 410 and 450 °C. The small scale material studies suggest that

this hydride could be used at temperatures up to 600 °C if the corresponding equilibrium hydrogen pressure is supplied.⁷⁴

During the experiment, it was noted that that reducing the thermal gradient throughout the reactor (thermal battery) was crucial to achieving optimum hydrogen absorption with a minimum difference between supplied hydrogen pressure and equilibrium pressure. Increasing the HTF flow improved the heat retrieval. The tuning of these parameters allowed absorption of up to 44 g of hydrogen, which equates to 90 % of the theoretical capacity. The maximum energy density of the thermal battery was found to be ≈ 1650 kJ/kg, which is 90 % of the theoretical value (1800 kJ). Considering the heat losses were inherent to the small scale of the thermal battery, they were retrieved from the energy calculations. In this case, the maximum energy that could be extracted by the HTF was ≈ 1500 kJ, which corresponds to 82 % efficiency based on the theoretical energy available. For a consistent power extraction (or regulated HTF temperature outlet), the thermal battery efficiency was dependent on the heat extraction capacity (or HTF flow) and hydrogen supplied pressure.

The reaction kinetics were found to be sufficient to maintain a consistent power level when the gas supply was twice the equilibrium pressure of the operating temperature. This thermal battery has shown the necessary versatility to supply adaptive power output by varying the hydrogen pressure supplied and/or the HTF flow rate. Further scaling up would address the heat loss issue. It was determined that the heat losses over a 24 hour period for a 100 MWh_{th} thermal battery wrapped in a thickness of a half metre of insulation, with similar thermal resistance to the environment, would be limited to 0.2 % of the theoretical energy available.

Chapter 7 Conclusions and future work

In the context of ongoing climate change, the need to develop alternative energy sources to conventional coal and oil has pressed the research community to explore new technologies. Renewables are deemed to be an attractive solution due to their potential in limiting CO₂ emissions associated with energy production. However, these sources are hindered by their fluctuations over time and require efficient energy storage technologies to provide base-load power.

Alternative energy storage technologies include high temperature thermal energy storage, which could assist in storing renewable energy, particularly in concentrated solar power plants or in the recovery of waste heat from high temperature industrial processes, such as concrete production. This thesis has focused on the development and investigation into high temperature thermal energy storage using the thermochemical reaction between metals and hydrogen gas to form metal hydrides. As this reaction involves large quantities of thermal energy, the scientific community has studied a vast list of potential reactions, determining their thermodynamics on gram-scale samples. However, the implementation of this type of thermal battery on an operating scale has rarely been reported. The work presented herein explored the scaling up of this technology.

A detailed literature examination was performed to assess different materials that offered all the qualities required to operate as thermochemical energy stores on a large scale. Several calcium based hydrides were shown to display attractive characteristics to operate between 600 and 800 °C. However, material development such as destabilisation, reversibility and kinetics improvement are necessary to allow investigations as a large scale heat storage prototype. The screening led to the selection of NaMgH₃ and Mg₂FeH₆ as candidates to function as a thermal battery between 350 and 600 °C, mainly due to their encouraging reaction reversibility. These thermochemical materials were synthesised through a ball milling technique of 3 hours followed by heating at temperatures up to 500 °C under hydrogen pressure, which on an industrial scale could be performed during the commissioning of the plant.

An experimental feasibility study on a pair of hydrides to store high temperature thermal energy as well as the associated hydrogen gas involved in the process was performed. Such a thermal battery was interesting due to a quasi-autonomous operation with a flow of

hydrogen solely driven by thermal energy inputs. Mg_2FeH_6 was used at temperatures up to 520 °C while a $\text{TiMn}_{1.5}$ alloy was employed as the solid-state gas store. The pair displayed satisfying operation when the HTMH was operating between 400 and 500 °C and returned an experimental thermal energy density of 1500 kJ/kg. However, some limitations were exposed, mainly correlated with the use of an intermetallic LTMH. Indeed, the fugacity of their hydrogen uptake and release imposed a large temperature excursion on the HTMH, which may be a hindrance for the final application. The design of such a thermal battery was revealed to be crucial for an optimised efficiency, where the volume of gas in the system between both hydrides had to be minimised. The mass ratio between hydrides was determined according to the operational mode of the thermal battery (HTMH kept at a set temperature with thermal energy supplied to LTMH or HTMH temperature varying as the hydrogen reaction driver). The low gravimetric capacity of LTMH's unfortunately requires large quantities of material, which can drastically increase the cost of the storage technology. Moreover, as the hydrogen absorption by the HTMH is solely driven by the equilibrium pressure at the operating temperature, the reaction kinetics are slow, and such a system may not generate the power required by the end user.

Thermal battery prototypes were designed and set up to investigate their operation in a real case scenario. A pressurised gas reservoir replaced the LTMH, and this was used to supply the hydrogen gas required for the exothermic absorption event. A heat transfer fluid, i.e. pressurised steam, was implemented to act as a thermal energy carrier. This HTF remains an excellent fluid choice for lab scale prototypes due to its safety, low temperature of fusion, and well-known behaviour. However, the implementation cost on a large scale induced by the operating pressure (≈ 200 bar) should motivate investigations on a substitute. The first prototype used 150 g of a NaMgH_3 based compound, and a heat transfer coil was embedded in the heat storing powder. Despite successful cycling operations, the thermal management of the battery was shown to be difficult to operate efficiently due to large thermal losses. Moreover, the threat posed by the irreversible NaH decomposition (if the hydrogen pressure became too low) was found to hinder an optimised thermal battery operation. It is clear that a material that presents such irreversibility is not suited for long term application and therefore should be avoided. The mass of the housing (≈ 3 kg of stainless steel) was found to divert a large part of the generated energy, up to 25 % in this setup. Therefore the mass ratio between the hydride and the housing shall be taken into account and minimised in future designs to maximise the gravimetric energy density of the heat storage. As the reactor envelop thickness is

often increased to sustain high pressures, the use of a metal hydride based thermal battery should aim at low operating pressure at high temperature to reduce this mass and cost.

A second prototype was designed as a bundle of 8 stainless steel tubes (total empty mass \approx 6 kg) containing 900 g of Mg_2FeH_6 with a theoretical energy storage capacity of 1.8 MJ. This prototype ran continuously for more than 3 months at operating temperatures between 400 and 450 °C. The thermal battery displayed a hydrogen capacity of 4.9 wt%, which corresponds to an experimental thermal energy capacity of 1.65 MJ (or 1.8 MJ/kg). Over a hundred absorption and desorption cycles were performed without any issues or hydrogen capacity losses. When tuned adequately, this prototype was able to regulate the HTF temperature at the thermal battery outlet between 425 and 430 °C, which extracted almost 1.5 MJ if the heat losses were neglected. A hydrogen gas tank backed by a pneumatically driven hydrogen compressor allowed the setup to function in a closed loop with a minimal volume required to store the hydrogen gas. Since the supplied hydrogen pressure had a clear impact on the hydrogen flow during hydrogen absorption, and those kinetics dictate the power generation, the thermal power extracted by the HTF is directly controlled by hydrogen pressure. This implies that for a given heat exchange design, the regulation of the hydrogen pressure during absorption is suitable to provide adaptive thermal power output. The use of a pressurised hydrogen store coupled with the thermal battery is therefore preferred over the use of a LTMH.

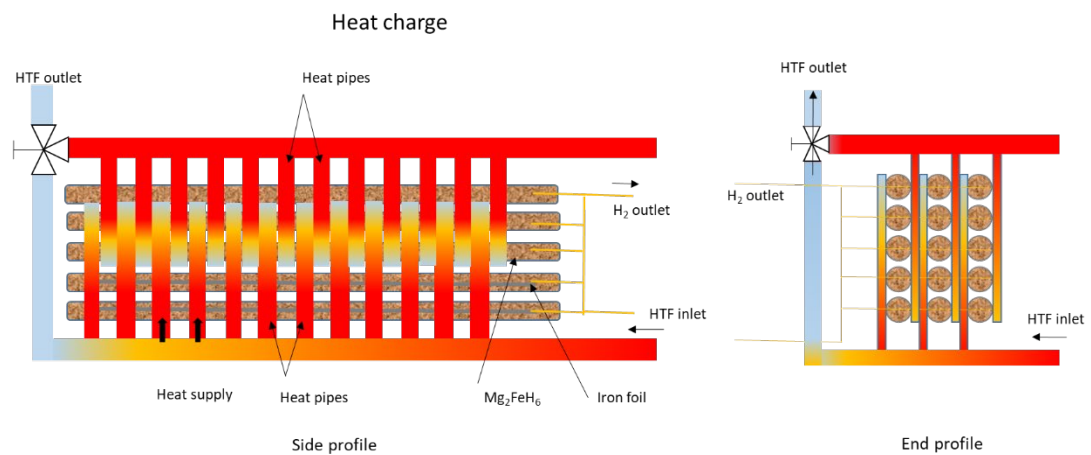
The Mg_2FeH_6 study showed the thermal gradient observed in the battery at low HTF flow to be a hindrance to achieve optimal hydrogen absorption, and hence limit the energy density of the thermal battery. That gradient was diminished with increased HTF flow. Moreover, a high HTF flow was required to guarantee an efficient energy retrieval. This emphasises the need for a HTF that has a high energy density due to a high fluid density or large specific heat.

The tubes bundle design, equipped with a thin iron foil in their centre (for H_2 diffusion), displayed an excellent thermal battery response to the hydrogen gas supply as the heating events were observed throughout the reactor with no observed delay. The automation of hydrogen supply pressure proved to be successful in using the metal hydride thermal energy storage as a thermal battery that can ensure baseload power.

Future scale up of this technology should be directed towards further improvement of the heat exchange between the material and the HTF. Other fluids should be investigated to avoid the cost induced by the use of high pressure water, although this may be a necessary

compromise. Eventually, high temperature heat pipes could be envisaged as an efficient heat transfer device to supply or collect thermal energy from the metal hydride bed. Heat pipes would exchange heat with an external steam circuit that is already commonly used in industry. The thermal battery segmentation in small diameter tubes (≈ 2 cm) showed satisfying energy transfer, avoiding the potential issues arising from the low thermal conductivity of the hydride powder (1.85 W/m.K). The modularity offered by such a design should motivate further research for its use as a base design. On a scale of several kg or tons, this segmentation would allow for a dedicated regulation of hydrogen supply pressure to each sub-reactor based on their local temperature and diminish the thermal gradient issues inherent to thermal energy storage.

Figure 7.1 is a design concept of a Mg_2FeH_6 based thermal battery that uses a bundle of tubes containing the hydride. These tubes are in contact with 2 sets of heat pipes, one for the heat charge and the other for the heat discharge. The hydrogen manifold allows supplying H_2 to each row with a dedicated H_2 pressure regulator during absorption (heat discharge) and desorption (heat charge). Based on the research in this thesis it is the author's opinion that Figure 7.1 depicts an optimised thermal energy design for the next generation prototype of a metal hydride thermochemical energy store.



Appendices

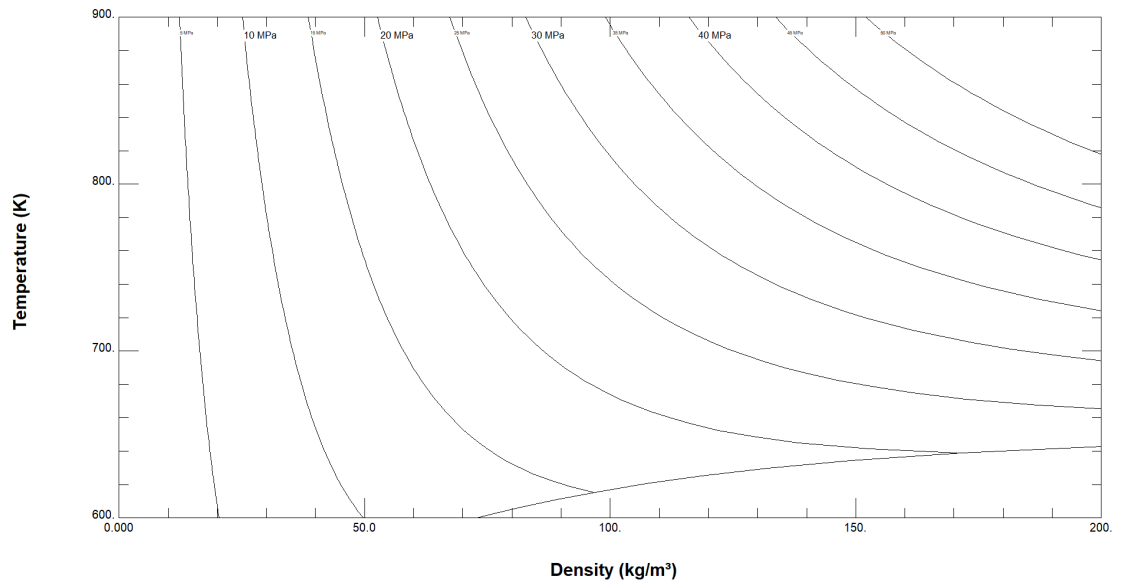


Figure A. 2 – Graph of water density for temperatures ranging from 600 to 900 K.

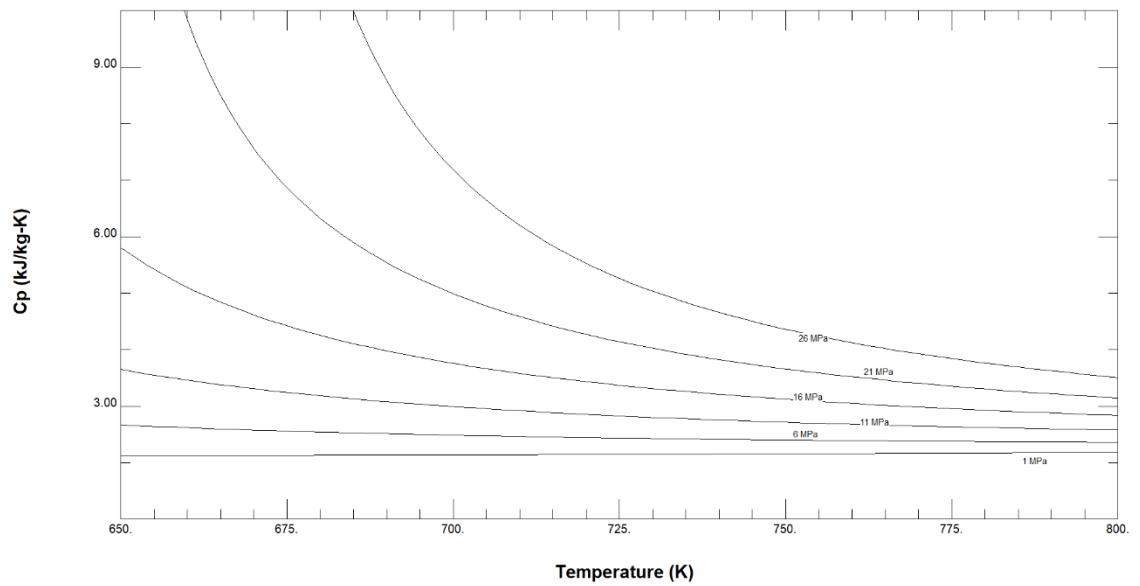


Figure A. 1 - Graph of water specific heat for temperatures ranging from 650 to 800 K

Discharge coefficient C for orifice plates

Purpose: defines the relation of jet flow diameter to orifice diameter and distance to pressure tapplings.

$$C = 0,5961 + 0,0261 \cdot \beta^2 - 0,216 \cdot \beta^8 + 0,000521 \cdot \left(\frac{10^6 \cdot \beta}{Re_D}\right)^{0,7} + (0,0188 + 0,0063 \cdot A) \cdot \beta^{3,5} \cdot \left(\frac{10^6}{Re_D}\right)^{0,3} + (0,043 + 0,080 \cdot e^{-10L_1} - 0,123 \cdot e^{-7L_1}) \cdot (1 - 0,11 \cdot A) \cdot \frac{\beta^4}{1 - \beta^4} - 0,031 \cdot (M_2 - 0,8 \cdot M_2^{1,1}) \cdot \beta^{1,3}$$

Data on pipe orifice plate medium

Data on upstream pressure tapplings

Data on downstream pressure tapplings

$\beta = \frac{d}{D}$ relation between orifice and pipe diameter

A function of β and Re_D

$$A = \left(\frac{19000 \cdot \beta}{Re_D}\right)^{0,5}$$

M_2 function of β and L_2

$$M_2 = \frac{2 \cdot L_2}{1 - \beta}$$

Reader-Harris Gallagher Equation

SP Technical Research Institute of Sweden

Figure A. 4 - Expression of discharge coefficient C for hydrogen flow through an orifice calculation.

Standards are updated from time to time

ISO 5167 (1991) & ASME MFC-3M (2004)
ISO 5167 (1991)

Discharge coefficient

$$C = 0,5961 + 0,0261 \cdot \beta^2 - 0,216 \cdot \beta^8 + 0,000521 \cdot \left(\frac{10^6 \cdot \beta}{Re_D}\right)^{0,7} + (0,0188 + 0,0063 \cdot A) \cdot \beta^{3,5} \cdot \left(\frac{10^6}{Re_D}\right)^{0,3} + (0,043 + 0,080 \cdot e^{-10L_1} - 0,123 \cdot e^{-7L_1}) \cdot (1 - 0,11 \cdot A) \cdot \frac{\beta^4}{1 - \beta^4} - 0,031 \cdot (M_2 - 0,8 \cdot M_2^{1,1}) \cdot \beta^{1,3}$$

Reader-Harris Gallagher equation

$$C = 0,5959 + 0,0312 \beta^{2,1} - 0,1840 \beta^8 + 0,0029 \beta^{2,5} \cdot \left(\frac{10^6}{Re_D}\right)^{0,75} + 0,0900 L_1 \cdot \beta^4 \cdot (1 - \beta^4)^{-1} - 0,0337 L_2 \cdot \beta^3$$

Stolz equation

Expansibility factor

$$\epsilon = 1 - (0,351 + 0,256 \cdot \beta^4 + 0,93 \cdot \beta^8) \cdot \left[1 - \left(\frac{p_2}{p_1}\right)^{\frac{1}{\kappa}}\right]$$

$$\epsilon = 1 - (0,41 + 0,35 \cdot \beta^4) \cdot \frac{\Delta p}{\kappa \cdot p_1}$$

SP Technical Research Institute of Sweden

Figure A. 3 - Expression of expansibility factor for hydrogen flow calculation.

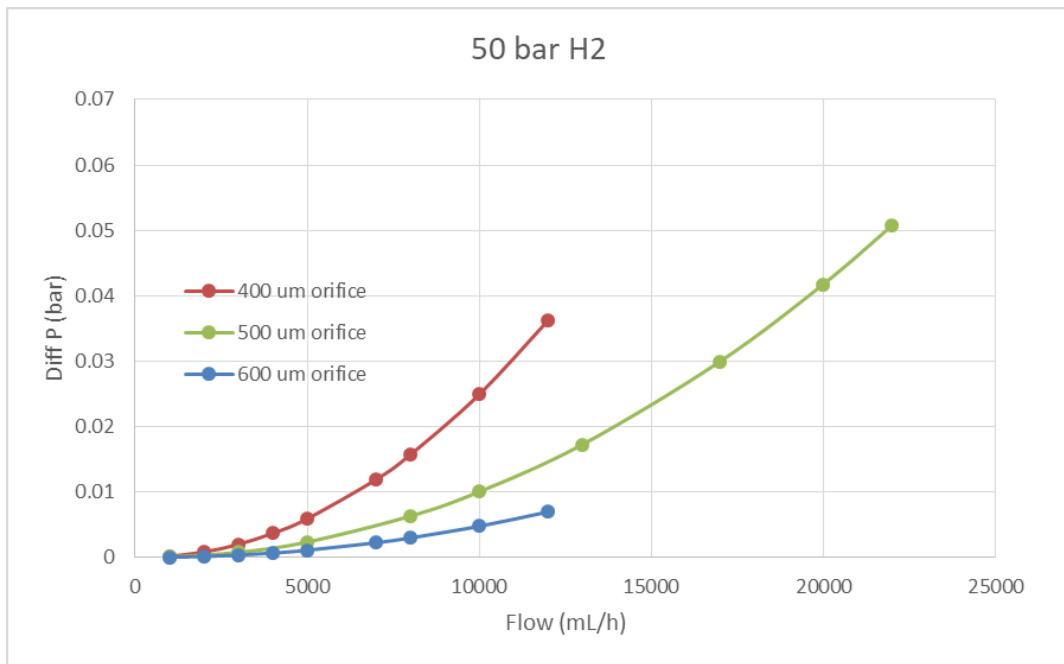


Figure A. 5 - Graph example used for determination of orifice size to measure pressure differential and calculate hydrogen flow.

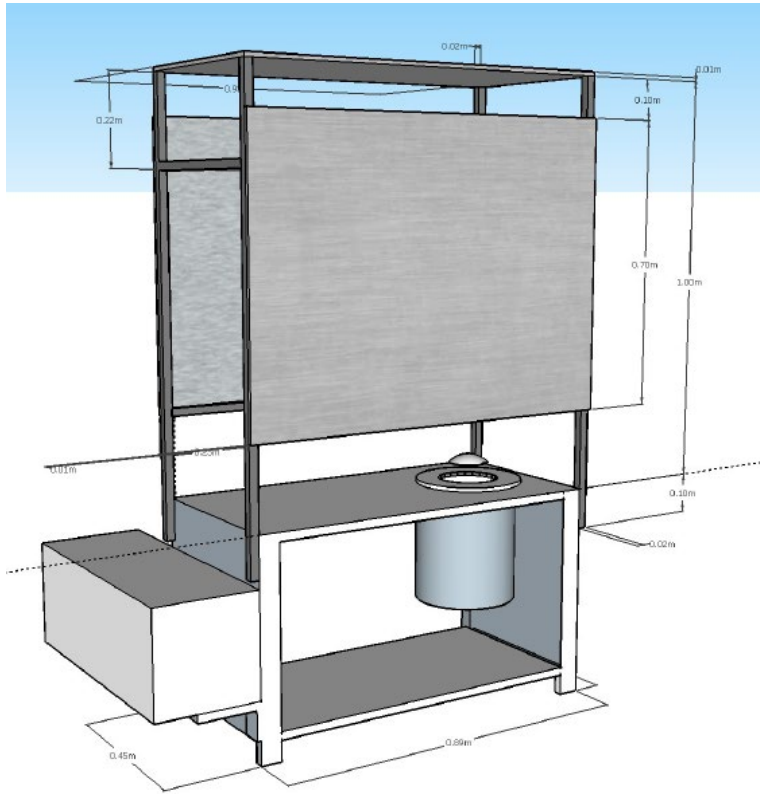


Figure A. 6 - Drawing of the front face of automated large scale experimental apparatus.

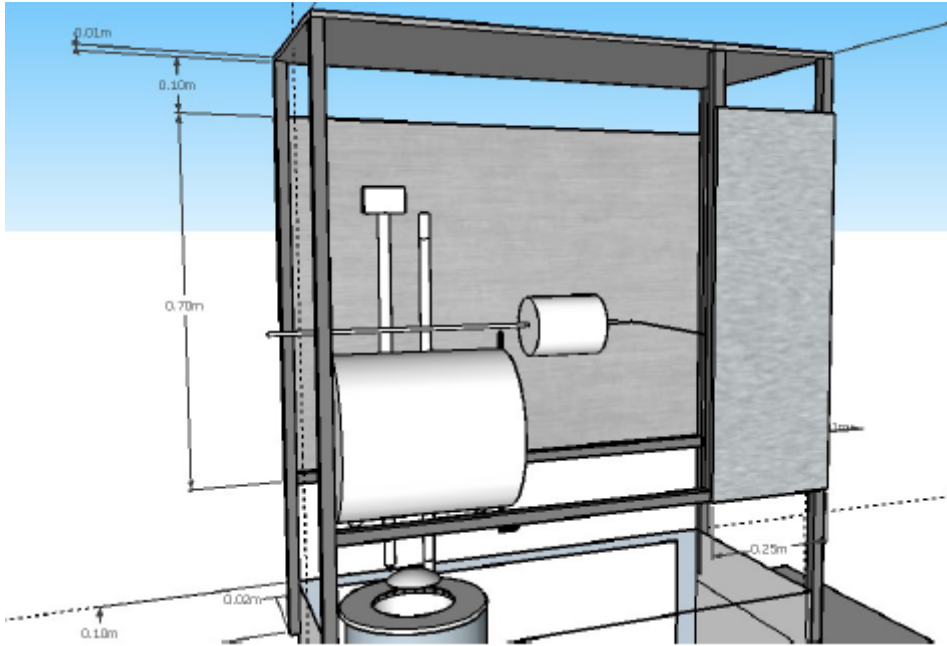


Figure A. 7 - Drawing of the back face of automated large scale experimental apparatus.

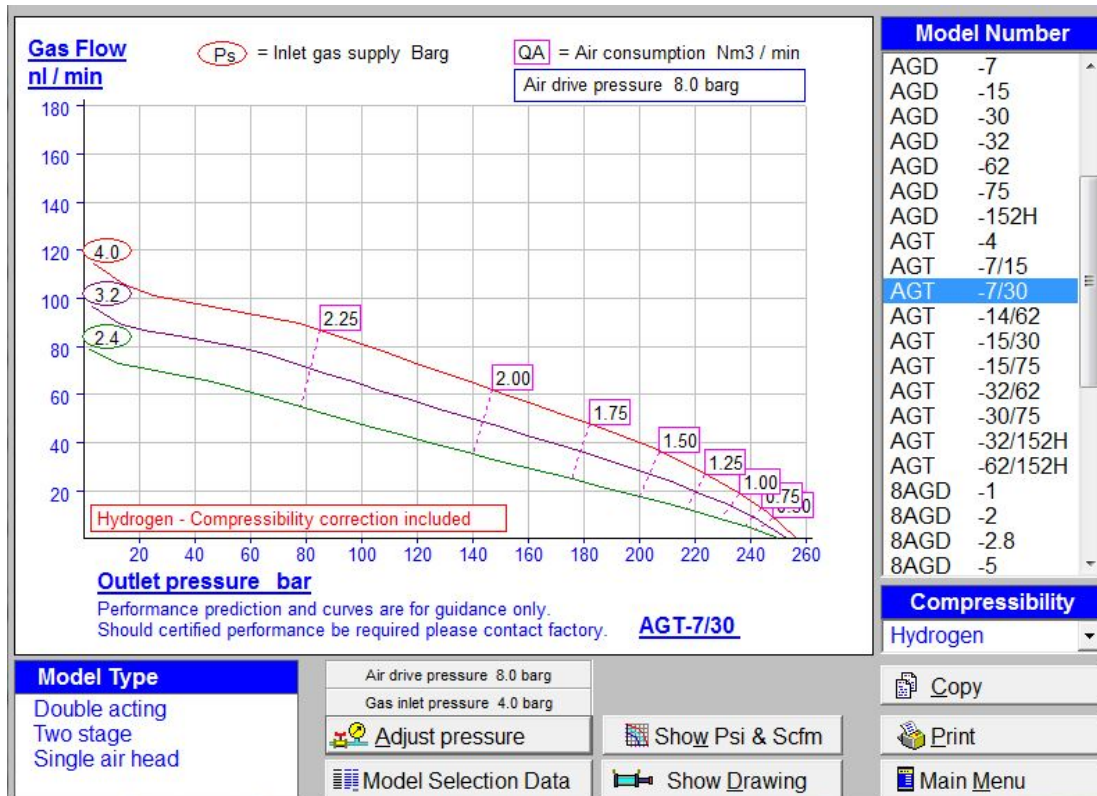


Figure A. 8 - Compression characteristics of hydrogen compressor AGT 7/30.

Data acquisition wiring table

		HTF FLOW												
		(ml/min)	1	2	5	8	10	20	30	50	100			
Cp		kg/s	1.6E-05	3.3E-05	8.2E-05	1.3E-04	1.6E-04	3.3E-04	4.9E-04	8.2E-04	1.6E-03			
NaMgH3		Mg2FeH6												
1708.0		1679.229												
Energy provided by hydride reactor		Temp difference IN/Out based on flow and 600 W/m2.K and all power generated is extracted												
metal hydride		Temp difference base HTF massique flow and all power generated is extracted												
Overall mass		2000 g	Coil area (0.077m2)											
NaMgH3		1600 g	dt											
Density powder		1.16 kg/m3	ml/min											
Cp		1379.31 L												
H2 capacity		4 % wt	Absorption time	generated power (W)	hydrogen flow (l/s)	hydrogen flow (g/h)								
64 g		30	1504.4	0.395	142.2	32.6	2193	1097	731	439	219			
31.7 mol		60	752.2	0.198	71.1	16.3	1097	548	366	219	110			
DH		85.3 kJ/molH2	120	376.1	0.099	35.6	8.1	548	274	183	110			
energy available		2707.9 kJ	180	250.7	0.066	23.7	5.4	366	183	122	73			
			210	214.9	0.056	20.3	4.7	313	157	104	63			
			240	188.1	0.049	17.8	4.1	274	137	91	55			
			300	150.4	0.040	14.2	3.3	219	110	73	44			
SS316			360	125.4	0.033	11.9	2.7	183	91	61	37			
Mass		35 kg	420	107.5	0.028	10.2	2.3	157	78	52	31			
cp		646 J/Kg.K	600	75.2	0.020	7.1	1.6	110	55	37	22			
dT		30 °C												
22610 J/K														
678300														
HTF														
Cp water		4800 J/Kg.K												
rho water		0.1 kg/l												
k steel		20 W/m.K												
coef exchange w		600 W/m2.K												
desired DT		15 °C												
Max power exch		177.2 W												
Coil		Heat energy to dump												
length		11 m	from 450 to 400°C		450 to 50°C					Total				
De		0.00057 m	generated	from MH	From SS316	From H2O								
surface		0.0196878 m2	Energy (J/s)	30	10ml/min	20ml/min	50ml/min	10ml/min	Exchange arr	20ml/min	Exchange a	50ml/min	Exchange a	
Reactor + insulation			1504.4	45.5	376.83	672.9	1345.9	2018.8	2599.7	0.0108	3272.7	0.0136	3945.6	0.0164
Working temp		420 °C	752.2	34.6	188.42	672.9	1345.9	2018.8	1648.1	0.0069	2321.1	0.0097	2994.0	0.0125
Ambiant temp		380 °C	376.1	13.1	94.21	672.9	1345.9	2018.8	1156.4	0.0048	1829.3	0.0076	2502.2	0.0104
length		0.4 m	250.7	3.3	62.81	672.9	1345.9	2018.8	989.8	0.0041	1662.7	0.0069	2335.7	0.0097
De		0.2 m	214.9	0.7	53.83	672.9	1345.9	2018.8	942.4	0.0039	1615.3	0.0067	2288.3	0.0095
surface		0.2512 m2	188.1	0.1	47.10	672.9	1345.9	2018.8	908.2	0.0038	1581.2	0.0066	2254.1	0.0094
Insl length		0.1 m	150.4	0.0	37.68	672.9	1345.9	2018.8	861.1	0.0036	1534.0	0.0064	2206.9	0.0092
Insl conductivity		0.05 W/m.K	125.4	0.0	31.40	672.9	1345.9	2018.8	829.7	0.0035	1502.6	0.0063	2175.6	0.0091
Insl De		0.4 m	107.5	0.0	26.92	672.9	1345.9	2018.8	807.3	0.0034	1480.2	0.0062	2153.2	0.0090
Rth		6.31 K/W	75.2	0.0	18.84	672.9	1345.9	2018.8	767.0	0.0032	1439.9	0.0060	2112.9	0.0088
Heat loss		6.3 W												

Figure A. 9 - Spreadsheet example for large scale experiment design.

Statement from the co-authors

Chapter 4 is based on a co-authored paper, the details of the paper are:

Poupin, L., Humphries, T. D., Paskevicius, M. & Buckley, C. E. (2020). An experimental high temperature thermal battery coupled to a low temperature metal hydride for solar thermal energy storage. *Sustainable Energy & Fuels*, 4(1), 285-292.

My contribution to the related paper involved:

- Literature analysis
- Material synthesis and characterisation
- Experimental design and construction
- Data acquisition and critical analysis
- Draft the manuscript
- Accommodate manuscript to co-author comments
- Finalise manuscript

(Lucas POUPIN, Candidate)

(T. D. Humphries)

(M. Paskevicius)

(C. E. Buckley)

Chapter 5 is based on a co-authored paper, the details of the paper are:

Poupin, L., Humphries, T. D., Paskevicius, M. & Buckley, C. E. (2019). A thermal energy storage prototype using sodium magnesium hydride. *Sustainable Energy & Fuels*, 3(4), 985-995.

My contribution to the related paper involved:

- Literature analysis
- Material synthesis and characterisation
- Experimental design and construction
- Data acquisition and critical analysis
- Draft the manuscript
- Accommodate manuscript to co-author comments
- Finalise manuscript

(Lucas POUPIN, Candidate)

(T. D. Humphries)

(M. Paskevicius)

(C. E. Buckley)

To whom it may concern I, Lucas Poupin, contributed significantly to all components of the paper/publication entitled:

“Thermal properties of thermochemical heat storage materials”, (Phys. Chem., Chem. Phys., (2020), 22, 4617 – 4625.

(Lucas POUPIN, Candidate)

I, as a co-author, endorse that the level of contribution by the candidate indicated above is appropriate.

(J. Bird)

(T. D. Humphries)

(M. Paskevicius)

(C. E. Buckley)

Licence agreement for Figure 1.5

ELSEVIER LICENSE TERMS AND CONDITIONS

Jul 28, 2020

This Agreement between Mr. Lucas poupin ("You") and Elsevier ("Elsevier") consists of your license details and the terms and conditions provided by Elsevier and Copyright Clearance Center.

License Number	4874520601834
License date	Jul 22, 2020
Licensed Content Publisher	Elsevier
Licensed Content Publication	Elsevier Books
Licensed Content Title	Encyclopedia of Electrochemical Power Sources
Licensed Content Author	A. Züttel
Licensed Content Date	Jan 1, 2009
Licensed Content Pages	19
Start Page	440
End Page	458
Type of Use	reuse in a thesis/dissertation
Portion	figures/tables/illustrations
Number of figures/tables /illustrations	1
Format	both print and electronic
Are you the author of this Elsevier chapter?	No
Will you be translating?	No
Title	development of metal hydride system for thermal energy storage applications
Institution name	Curtin university
Expected presentation date	Aug 2020
Portions	figure 3

Licence agreement for Figure 1.8

ELSEVIER LICENSE TERMS AND CONDITIONS

Jul 28, 2020

This Agreement between Mr. Lucas poupin ("You") and Elsevier ("Elsevier") consists of your license details and the terms and conditions provided by Elsevier and Copyright Clearance Center.

License Number	4874481384028
License date	Jul 22, 2020
Licensed Content Publisher	Elsevier
Licensed Content Publication	Solar Energy
Licensed Content Title	Screening of high melting point phase change materials (PCM) in solar thermal concentrating technology based on CLFR
Licensed Content Author	Akira Hoshi,David R. Mills,Antoine Bittar,Takeo S. Saitoh
Licensed Content Date	Sep 1, 2005
Licensed Content Volume	79
Licensed Content Issue	3
Licensed Content Pages	8
Start Page	332
End Page	339
Type of Use	reuse in a thesis/dissertation
Portion	figures/tables/illustrations
Number of figures/tables /illustrations	1
Format	both print and electronic
Are you the author of this Elsevier article?	No
Will you be translating?	No
Title	development of metal hydride system for thermal energy storage applications
Institution name	Curtin university
Expected presentation date	Aug 2020
Portions	figure 1 and 2

Licence agreement for Figure 1.9

ELSEVIER LICENSE TERMS AND CONDITIONS

Jul 28, 2020

This Agreement between Mr. Lucas poupin ("You") and Elsevier ("Elsevier") consists of your license details and the terms and conditions provided by Elsevier and Copyright Clearance Center.

License Number	4874490274567
License date	Jul 22, 2020
Licensed Content Publisher	Elsevier
Licensed Content Publication	Journal of Power Sources
Licensed Content Title	Fuel cell vehicles: Status 2007
Licensed Content Author	Rittmar von Helmholt,Ulrich Eberle
Licensed Content Date	Mar 20, 2007
Licensed Content Volume	165
Licensed Content Issue	2
Licensed Content Pages	11
Start Page	833
End Page	843
Type of Use	reuse in a thesis/dissertation
Portion	figures/tables/illustrations
Number of figures/tables /illustrations	1
Format	both print and electronic
Are you the author of this Elsevier article?	No
Will you be translating?	No
Title	development of metal hydride system for thermal energy storage applications
Institution name	Curtin university
Expected presentation date	Aug 2020
Portions	figure 4

Licence agreement for Figure 1.13

ELSEVIER LICENSE TERMS AND CONDITIONS

Aug 03, 2020

This Agreement between Mr. Lucas poupin ("You") and Elsevier ("Elsevier") consists of your license details and the terms and conditions provided by Elsevier and Copyright Clearance Center.

License Number	4881300459797
License date	Aug 03, 2020
Licensed Content Publisher	Elsevier
Licensed Content Publication	Renewable and Sustainable Energy Reviews
Licensed Content Title	Review of energy storage systems for electric vehicle applications: Issues and challenges
Licensed Content Author	M.A. Hannan,M.M. Hoque,A. Mohamed,A. Ayob
Licensed Content Date	Mar 1, 2017
Licensed Content Volume	69
Licensed Content Issue	n/a
Licensed Content Pages Start Page	19
End Page	771
Type of Use	reuse in a thesis/dissertation
Portion	figures/tables/illustrations
Number of figures/tables /illustrations	1
Format	both print and electronic
Are you the author of this Elsevier article?	No
Will you be translating?	No
Title	development of metal hydride system for thermal energy storage applications
Institution name	Curtin university
Expected presentation date	Aug 2020
Portions	figure 6

Licence agreement for Figure 4.3

ELSEVIER LICENSE TERMS AND CONDITIONS

Jul 28, 2020

This Agreement between Mr. Lucas poupin ("You") and Elsevier ("Elsevier") consists of your license details and the terms and conditions provided by Elsevier and Copyright Clearance Center.

License Number	4874560602178
License date	Jul 22, 2020
Licensed Content Publisher	Elsevier
Licensed Content Publication	International Journal of Hydrogen Energy
Licensed Content Title	Structure, morphology and hydrogen storage properties of a Ti _{0.97} Zr _{0.019} V _{0.439} Fe _{0.097} Cr _{0.045} Al _{0.026} Mn _{1.5} alloy
Licensed Content Author	J.A. Murshidi, M. Paskevicius, D.A. Sheppard, C.E. Buckley
Licensed Content Date	Jul 1, 2011
Licensed Content Volume	36
Licensed Content Issue	13
Licensed Content Pages	7
Start Page	7587
End Page	7593
Type of Use	reuse in a thesis/dissertation
Portion	figures/tables/illustrations
Number of figures/tables /illustrations	1
Format	both print and electronic
Are you the author of this Elsevier article?	No
Will you be translating?	No
Title	development of metal hydride system for thermal energy storage applications
Institution name	Curtin university
Expected presentation date	Aug 2020
Portions	figure 4

References

1. M. Arbabzadeh, R. Sioshansi, J. X. Johnson and G. A. Keoleian, *Nat Commun*, 2019, **10**, 3413.
2. M. Beaudin, H. Zareipour, A. Schellenberglobe and W. Rosehart, *Energy Sustain Dev*, 2010, **14**, 302-314.
3. J. S. L.M.Lombrana, These massive renewable energy project are powering chilean mines, Bloomberg businessweek, 2018
4. A. G. Olabi, *Energy*, 2017, **136**, 1-6.
5. M. S. Guney and Y. Tepe, *Renew Sust Energ Rev*, 2017, **75**, 1187-1197.
6. S. Ould Amrouche, D. Rekioua, T. Rekioua and S. Bacha, *Int J Hydrogen Energy*, 2016, **41**, 20914-20927.
7. M.Higgins, A.Nagoshi, J.Noack and S. P. K.Kairies, K.Pullen,O.Schmidt, *IRENA*, 2017, 30.
8. D. A. D. Prasad, K. Jain and A. Gairola, *Int J Comput Appl*, 2013, **81**, 41-48.
9. E. Barbour, I. G. Wilson, J. Radcliffe, Y. Ding and Y. Li, *Renew Sust Energ Rev*, 2016, **61**, 421-432.
10. T. Hino and A. Lejeune, 6.15 - Pumped Storage Hydropower Developments, 2012.
11. M. E. Nazari, M. M. Ardehali and S. Jafari, *Energy*, 2010, **35**, 4092-4101.
12. B. Lu, M. Stocks, A. Blakers and K. Anderson, *Appl Energy*, 2018, **222**, 300-312.
13. S. Feifei, China's State Grid to Spend \$5.7 Billion on Pumped Hydro Plants, Bloomberg News, 2019
14. G. Kear and R. Chapman, *Renew Energy*, 2013, **57**, 249-261.
15. P.Gordon, 22 million GWh of pumpd hydro energy storage potential worldwide., smart-energycom, 2019.
16. S. E. Council, *Australian Energy Storage, market Analysis*, 2018.
17. F. R. Kalhammer and T. R. Schneider, *ANRE*, 1976, **1**, 311-343.
18. Y. Kim, J. Lee, S. J. Kim and D. Favrat, *Entropy*, 2012, **14**, 1501-1521.
19. H. Chen, T. N. Cong, W. Yang, C. Tan, Y. Li and Y. Ding, *Prog Nat Sci*, 2009, **19**, 291-312.
20. M. Budt, D. Wolf, R. Span and J. Yan, *Appl Energy*, 2016, **170**, 250-268.
21. F. Crotagino, K.-U. Mohmeyer and R. Scharf, presented in part at the Solution Mining Research Institute (SMRI) Spring Meeting, Orlando, Florida, USA, 2001, 351-362.
22. Q. Yu, Q. Wang, X. Tan, G. Fang and J. Meng, *J Renew Sustain Ener*, 2019, **11**, 1-12.
23. A. Colthorpe, Energy stored in underground caverns joins megabatteries in South Australia, Energy storage news, 2019
24. R. Östergård, Flywheel energy storage : a conceptual study, 2011
25. F. Faraji, A. Majazi and K. Al-Haddad, *Renew Sust Energ Rev*, 2017, **67**, 477-490.
26. K. Murakami, M. Komori and H. Mitsuda, *IEEE Trans Appl Supercond*, 2007, **17**, 2146-2149.
27. P. M. Cronk and J. D. Van de Ven, *International Journal of Fluid Power*, 2018, **19**, 69-79.
28. E. M. Amiryar and R. K. Pullen, *Applied Sciences*, 2017, **7**.
29. A. Volta, *Philos Trans Royal Soc*, 1800, **90**, 403-431.
30. P. Kurzweil, *J Power Sources*, 2010, **195**, 4424-4434.
31. M. A. Hannan, M. M. Hoque, A. Mohamed and A. Ayob, *Renew Sust Energ Rev*, 2017, **69**, 771-789.

32. John B. Goodenough, M Stanley Whittingham and A. Yoshino, The nobel prize, N. m. AB2020, DOI: <https://www.nobelprize.org/prizes/chemistry/2019/goodenough/facts/>).
33. J. Gao, S.-Q. Shi and H. Li, *Chinese Physics B*, 2016, **25**, 018210.
34. K. Chayambuka, G. Mulder, D. L. Danilov and P. H. L. Notten, *Adv Energy Mater*, 2018, **8**, 1800079.
35. C.-X. Zu and H. Li, *Energy Environ Sci*, 2011, **4**, 2614-2624.
36. D. E. Fenton, J. M. Parker and P. V. Wright, *Polymer*, 1973, **14**, 589.
37. A. Manthiram, X. Yu and S. Wang, *Nat Rev Mater*, 2017, **2**, 16103.
38. H.S.Williams, *the beginnings of modern science*, gutenber.org, 2009.
39. M. Fukuhara, T. Kuroda and F. Hasegawa, *Appl Phys Lett*, 2014, **105**, 202904.
40. J. R. Miller, *Appl Surf Sci*, 2018, **460**, 3-7.
41. A.-L. Allègre, A. Bouscayrol, P. Delarue, P. Barrade, E. Chattot and S. El-Fassi, *IEEE Trans Ind*, 2010, **57**, 4001-4012.
42. H. A. Kiehne, *Battery technology handbook*, CRC Press, 2003.
43. M. G. Molina, in *Dynamic Modelling*, IntechOpen, 2010.
44. M. G. Molina, presented in part at the 2012 Sixth IEEE/PES Transmission and Distribution: Latin America Conference and Exposition (T&D-LA), 2012, 1-7.
45. G. Alva, Y. Lin and G. Fang, *Energy*, 2018, **144**, 341-378.
46. S. Kalaiselvam and R. Parameshwaran, in *Thermal Energy Storage Technologies for Sustainability*, eds. S. Kalaiselvam and R. Parameshwaran, Academic Press, Boston, 2014, DOI: <https://doi.org/10.1016/B978-0-12-417291-3.00003-7>, pp. 57-64.
47. S. Izquierdo, C. Montanes, C. Dopazo and N. Fueyo, *Energy Policy*, 2010, **38**, 6215-6221.
48. M. T. Islam, N. Huda, A. B. Abdullah and R. Saidur, *Renew Sust Energ Rev*, 2018, **91**, 987-1018.
49. E. González-Roubaud, D. Pérez-Osorio and C. Prieto, *Renew Sust Energ Rev*, 2017, **80**, 133-148.
50. U. Pelay, L. Luo, Y. Fan, D. Stitou and M. Rood, *Renew Sust Energ Rev*, 2017, **79**, 82-100.
51. X. Xu, K. Vignarooban, B. Xu, K. Hsu and A. M. Kannan, *Renew Sust Energ Rev*, 2016, **53**, 1106-1131.
52. A. I. Fernandez, M. Martínez, M. Segarra, I. Martorell and L. F. Cabeza, *Sol Energy Mater Sol Cells*, 2010, **94**, 1723-1729.
53. P. Pardo, A. Deydier, Z. Anxionnaz-Minvielle, S. Rougé, M. Cabassud and P. Cognet, *Renew Sust Energ Rev*, 2014, **32**, 591-610.
54. B. Xu, P. Li and C. Chan, *Appl Energy*, 2015, **160**, 286-307.
55. A. Hoshi, D. R. Mills, A. Bittar and T. S. Saitoh, *SEJ*, 2005, **79**, 332-339.
56. J. P. Da Cunha and P. Eames, *Appl Energy*, 2016, **177**, 227-238.
57. R. Jacob and F. Bruno, *Renew Sust Energ Rev*, 2015, **48**, 79-87.
58. N. Pflieger, T. Bauer, C. Martin, M. Eck and A. Wörner, *Beilstein J Nanotechnol*, 2015, **6**, 1487-1497.
59. H. Kerskes, in *Storing Energy*, Elsevier, Oxford, 2016, DOI: <https://doi.org/10.1016/B978-0-12-803440-8.00017-8>, pp. 345-372.
60. X. Chen, Z. Zhang, C. Qi, X. Ling and H. Peng, *Eng convman*, 2018, **177**, 792-815.
61. K. Lovegrove, A. Luzzi, I. Soldiani and H. Kreetz, *SEJ*, 2004, **76**, 331-337.
62. C. Chen, H. Aryafar, G. Warriar, K. M. Lovegrove and A. S. Lavine, *AIP Conf Proc*, 2016, **1734**, 050010.
63. D. A. Sheppard, M. Paskevicius, T. D. Humphries, M. Felderhoff, G. Capurso, J. Bellosta von Colbe, M. Dornheim, T. Klassen, P. A. Ward, J. A. Teprovich, C. Corgnale, R. Zidan, D. M. Grant and C. E. Buckley, *Appl Phys A*, 2016, **122**, 395.

64. T. D. Humphries, K. T. Møller, W. D. A. Rickard, M. V. Sofianos, S. Liu, C. E. Buckley and M. Paskevicius, *J Mater Chem A*, 2019, **7**, 1206-1215.
65. E. C. E. Rönnebro, G. Whyatt, M. Powell, M. Westman, F. R. Zheng and Z. Z. Fang, *Metal Hydrides for High-Temperature Power Generation.*, 2015.
66. A. Roine, *HSC chemistry 6*, 2016, 6.12, 04/2018
67. M. Benitez-Guerrero, B. Sarrion, A. Perejon, P. E. Sanchez-Jimenez, L. A. Perez-Maqueda and J. M. Valverde, *Sol Energy Mater Sol Cells*, 2017, **168**, 14-21.
68. S. Tescari, C. Agrafiotis, S. Breuer, L. Oliveira, M. Puttkamer, M. Roeb and C. Sattler, *Thermochemical Solar Energy Storage Via Redox Oxides: Materials and Reactor/Heat Exchanger Concepts*, 2013.
69. T. Block, N. Knoblauch and M. Schmücker, *Thermochim Acta*, 2014, **577**, 25-32.
70. L. André, S. Abanades and L. Cassayre, *J Solid State Chem*, 2017, **253**, 6-14.
71. J. S. Prasad, P. Muthukumar, F. Desai, D. N. Basu and M. M. Rahman, *Appl Energy*, 2019, **254**, 113733.
72. Z. Pan and C. Y. Zhao, *Energy*, 2015, **82**, 611-618.
73. D. A. Sheppard, C. Corgnale, B. Hardy, T. Motyka, R. Zidan, M. Paskevicius and C. E. Buckley, *RSC Adv*, 2014, **4**, 26552-26562.
74. B. Bogdanovic, A. Reiser, K. Schlichte, B. Spliethoff and B. Tesche, *J Alloys Compd*, 2002, **345**, 77-89.
75. P. A. Ward, J. A. Teprovich, Y. Liu, J. He and R. Zidan, *J Alloys Compd*, 2018, **735**, 2611-2615.
76. I. G. Fernández, G. O. Meyer and F. C. Gennari, *J Alloys Compd*, 2007, **446-447**, 106-109.
77. E. Y. Ivanov, I. Konstanchuk, A. Stepanov, Y. Jie, M. Pezat and B. Darriet, *Inorg Chem*, 1989, **28**, 613-615.
78. A. P. Muroyama, A. J. Schrader and P. G. Loutzenhiser, *SEJ*, 2015, **122**, 409-418.
79. A. Bayon, R. Bader, M. Jafarian, L. Fedunik-Hofman, Y. Sun, J. Hinkley, S. Miller and W. Lipiński, *Energy*, 2018, **149**, 473-484.
80. F. Schaube, L. Koch, A. Wörner and H. Müller-Steinhagen, *Thermochim Acta*, 2012, **538**, 9-20.
81. F. Schaube, L. Koch, A. Wörner and H. Müller-Steinhagen, *Thermochim Acta*, 2012, **538**, 9-20.
82. S. Funayama, H. Takasu, M. Zamengo, J. Kariya, S. T. Kim and Y. Kato, *Energy Storage*, 2019, **1**, e53.
83. N. Uchiyama, H. Takasu and Y. Kato, *Appl Therm Eng*, 2019, **160**, 113893.
84. B. Bogdanović, B. Spliethoff and A. Ritter, presented in part at the Z Phys Chem (Muenchen, Ger), 1989, 1497.
85. B. Bogdanović, K. Bohmhammel, B. Christ, A. Reiser, K. Schlichte, R. Vehlen and U. Wolf, *J Alloys Compd*, 1999, **282**, 84-92.
86. A. Reiser, B. Bogdanović and K. Schlichte, *Int J Hydrogen Energy*, 2000, **25**, 425-430.
87. J.-C. Crivello, B. Dam, R. V. Denys, M. Dornheim, D. M. Grant, J. Huot, T. R. Jensen, P. de Jongh, M. Latroche, C. Milanese, D. Milčius, G. S. Walker, C. J. Webb, C. Zlotea and V. A. Yartys, *Appl Phys A*, 2016, **122**, 97.
88. G. Liang, J. Huot, S. Boily, A. Van Neste and R. Schulz, *J Alloys Compd*, 1999, **292**, 247-252.
89. J.-H. Shim, M. Park, Y. H. Lee, S. Kim, Y. H. Im, J.-Y. Suh and Y. W. Cho, *Int J Hydrogen Energy*, 2014, **39**, 349-355.
90. M. P. Pitt, M. Paskevicius, C. J. Webb, D. A. Sheppard, C. E. Buckley and E. M. Gray, *Int J Hydrogen Energy*, 2012, **37**, 4227-4237.
91. A. Chaise, P. de Rango, P. Marty, D. Fruchart, S. Miraglia, R. Olivès and S. Garrier, *Int J Hydrogen Energy*, 2009, **34**, 8589-8596.

92. M. Paskevicius, D. A. Sheppard and C. E. Buckley, *J Am Chem Soc*, 2010, **132**, 5077-5083.
93. L. Poupin, T. D. Humphries, M. Paskevicius and C. E. Buckley, *Sustain Energ Fuels*, 2019, **3**, 985-995.
94. S. Tao, Z. Wang, Z. Wan, J. Deng, H. Zhou and Q. Yao, *Int J Hydrogen Energy*, 2017, **42**, 3716-3722.
95. D. A. Sheppard, M. Paskevicius and C. E. Buckley, *Chem Mater*, 2011, **23**, 4298-4300.
96. M. S. Tortoza, T. D. Humphries, D. A. Sheppard, M. Paskevicius, M. R. Rowles, M. V. Sofianos, K. F. Aguey-Zinsou and C. E. Buckley, *Phys Chem Chem Phys*, 2018, **20**, 2274-2283.
97. M. Paskevicius, D. A. Sheppard, K. Williamson and C. E. Buckley, *Energy*, 2015, **88**, 469-477.
98. D. Dong, T. D. Humphries, D. A. Sheppard, B. Stansby, M. Paskevicius, M. V. Sofianos, A. L. Chaudhary, M. Dornheim and C. E. Buckley, *Sustain Energ Fuels*, 2017, **1**, 1820-1829.
99. R. Urbanczyk, M. Meggouh, R. Moury, K. Peinecke, S. Peil and M. Felderhoff, *Appl Phys A*, 2016, **122**, 315.
100. H. Cavendish, *Philos Trans Royal Soc*, 1766, 141-184.
101. J. Emsley, *Nature's building blocks: an AZ guide to the elements*, Oxford University Press, 2011.
102. C. M. White, R. R. Steeper and A. E. Lutz, *Int J Hydrogen Energy*, 2006, **31**, 1292-1305.
103. S. Dutta, *J Ind Eng Chem*, 2014, **20**, 1148-1156.
104. E. c. industry.org, Hydrogen, U. o. York).
105. A. Steinfeld, *SEJ*, 2005, **78**, 603-615.
106. H. Ahmad, S. K. Kamarudin, L. J. Minggu and M. Kassim, *Renew Sust Energ Rev*, 2015, **43**, 599-610.
107. I. Dincer and C. Acar, *Int J Hydrogen Energy*, 2015, **40**, 11094-11111.
108. C. Acar and I. Dincer, *J Clean Prod*, 2019, **218**, 835-849.
109. J. Snyder, Hydrogen fuel cells gain momentum in maritime sector, rivieramm.com, (accessed 2019/10/05, 2019).
110. R. Kothari, D. P. Singh, V. V. Tyagi and S. K. Tyagi, *Renew Sust Energ Rev*, 2012, **16**, 2337-2346.
111. L. Garcia, *Compedium of Hydrogen Energy*, 2015, 83-107.
112. M. Seitz, H. von Storch, A. Nechache and D. Bauer, *Int J Hydrogen Energy*, 2017, **42**, 26192-26202.
113. H. Ju, S. Badwal and S. Giddey, *Appl Energy*, 2018, **231**, 502-533.
114. T. Hisatomi, J. Kubota and K. Domen, *Chem Soc Rev*, 2014, **43**, 7520-7535.
115. B. Ipek and D. Uner, in *Water chemistry*, ed. intechopen, 2019, DOI: 10.5772/intechopen.89235.
116. H. Balat and E. Kirtay, *Int J Hydrogen Energy*, 2010, **35**, 7416-7426.
117. K. N. Das Debabrata, Veziroğlu Nejat T., *Chemical industry and Chemical Engineering Quarterly*, 2008, **14**, 57-67.
118. V. Vogl, M. Åhman and L. J. Nilsson, *J Clean Prod*, 2018, **203**, 736-745.
119. J. M. Modak and J. M. Modak, *Resonance*, 2002, **7**.
120. A. M. Abdalla, S. Hossain, O. B. Nisfindy, A. T. Azad, M. Dawood and A. K. Azad, *Eng convman*, 2018, **165**, 602-627.
121. Hydrogen, U. o. York, The Essential chemical Industry, (<http://www.essentialchemicalindustry.org/chemicals/hydrogen.html>).

122. H. Fayaz, R. Saidur, N. Razali, F. Anuar, A. Saleman and M. Islam, *Renew Sust Energ Rev*, 2012, **16**, 5511-5528.
123. Y. Ligen, H. Vrabel and H. Girault, *World Electric Vehicle Journal*, 2018, **9**, 3.
124. J. Yang, A. Sudik, C. Wolverton and D. J. Siegel, *Chem Soc Rev*, 2010, **39**, 656-675.
125. P. Colbataldo, S. B. Agustin, S. Campanari and J. Brouwer, *Int J Hydrogen Energy*, 2019, **44**, 9558-9576.
126. K. Manickam, P. Mistry, G. Walker, D. Grant, C. E. Buckley, T. D. Humphries, M. Paskevicius, T. Jensen, R. Albert, K. Peinecke and M. Felderhoff, *Int J Hydrogen Energy*, 2019, **44**, 7738-7745.
127. P. F. P. Franc, K. Kapoun, *Hydrogen technologies in Europe. Financial and technology outlook on the European sector ambition 2014–2020*, New Energy Word, 2011.
128. DOE, DOE Technical Targets for Onboard Hydrogen Storage for Light-Duty Vehicles, energy.gov, <https://www.energy.gov/eere/fuelcells/doe-technical-targets-onboard-hydrogen-storage-light-duty-vehicles>, 2019).
129. J. Zheng, X. Liu, P. Xu, P. Liu, Y. Zhao and J. Yang, *Int J Hydrogen Energy*, 2012, **37**, 1048-1057.
130. M. B. Ley, L. H. Jepsen, Y.-S. Lee, Y. W. Cho, J. M. Bellosta von Colbe, M. Dornheim, M. Rokni, J. O. Jensen, M. Sloth, Y. Filinchuk, J. E. Jørgensen, F. Besenbacher and T. R. Jensen, *Mater Today*, 2014, **17**, 122-128.
131. H. Barthelemy, M. Weber and F. Barbier, *Int J Hydrogen Energy*, 2017, **42**, 7254-7262.
132. R. von Helmolt and U. Eberle, *J Power Sources*, 2007, **165**, 833-843.
133. R. Tarkowski, *Renew Sust Energ Rev*, 2019, **105**, 86-94.
134. M. Panfilov, in *Compendium of Hydrogen Energy*, Elsevier, 2016, pp. 91-115.
135. O. Kruck, F. Crotonino, R. Prelicz and T. Rudolph, *KBB Underground Technologies GmbH*, 2013.
136. D. G. Caglayan, N. Weber, H. U. Heinrichs, J. Linßen, M. Robinius, P. A. Kukla and D. Stolten, *Int J Hydrogen Energy*, 2020, **45**, 6793-6805.
137. A. Le Duigou, A. G. Bader, J. C. Lanoix and L. Nadau, *Int J Hydrogen Energy*, 2017, **42**, 22987-23003.
138. A. Godula-Jopek, W. Jehle and J. Wellnitz, *Hydrogen storage technologies: new materials, transport, and infrastructure*, 2012, 97-170.
139. J. Sheffield, K. Martin and R. Folkson, in *Alternative Fuels and Advanced Vehicle Technologies for Improved Environmental Performance*, ed. R. Folkson, Woodhead 2014, DOI: 10.1533/9780857097422.1.117, pp. 117-137.
140. P. M. Modisha, C. N. M. Ouma, R. Garidzirai, P. Wasserscheid and D. Bessarabov, *Energy Fuels*, 2019, **33**, 2778-2796.
141. Daniel Teichmann, Wolfgang Arlt, Eberhard Schlücker and P. Wasserscheid, in *Hydrogen Science and Engineering : Materials, Processes, Systems and Technology*, 2016, DOI: 10.1002/9783527674268.ch33, pp. 811-830.
142. M. Niermann, S. Drünert, M. Kaltschmitt and K. Bonhoff, *Energy Environ Sci*, 2019, **12**.
143. M. Jang, Y. S. Jo, W. J. Lee, B. S. Shin, H. Sohn, H. Jeong, S. C. Jang, S. K. Kwak, J. W. Kang and C. W. Yoon, *ACS Sustain Chem Eng*, 2019, **7**, 1185-1194.
144. Y. He, W. Zhou, G. Qian and B. Chen, *Chem Soc Rev*, 2014, **43**, 5657-5678.
145. O. K. Farha, I. Eryazici, N. C. Jeong, B. G. Hauser, C. E. Wilmer, A. A. Sarjeant, R. Q. Snurr, S. T. Nguyen, A. Ö. Yazaydin and J. T. Hupp, *J Am Chem Soc*, 2012, **134**, 15016-15021.
146. N. L. Rosi, J. Eckert, M. Eddaoudi, D. T. Vodak, J. Kim, M. Keefe and O. M. Yaghi, *Science*, 2003, **300**, 1127.

147. H. W. Langmi, J. Ren, B. North, M. Mathe and D. Bessarabov, *Electrochim Acta*, 2014, **128**, 368-392.
148. E. N. Augustus, A. Nimibofa, I. A. Kesiye and W. Donbebe, *Am J Environ Prot*, 2017, **5**, 61-67.
149. I. Dimanta, M. Paiders, A. Gruduls and V. Nikolajeva, *Selection and modification of microorganisms and substrates for acquiring and separation of energy carriers*, 2019.
150. J. Huheey, *Inorganic Chemistry*, Harper and Row, Harper international SI edition, 3rd edn., 1983.
151. A. Züttel, in *Encyclopedia of Electrochemical Power Sources*, ed. J. Garche, Elsevier, Amsterdam, 2009, DOI: <https://doi.org/10.1016/B978-044452745-5.00325-7>, pp. 440-458.
152. J. Reilly, *Metal hydrides as hydrogen storage media and their applications*, 2018.
153. T. K. Møller, D. Sheppard, B. D. Ravnsbæk, E. C. Buckley, E. Akiba, H.-W. Li and R. T. Jensen, *Energies*, 2017, **10**, 1645.
154. B. Bogdanović, R. A. Brand, A. Marjanović, M. Schwickardi and J. Tölle, *J Alloys Compd*, 2000, **302**, 36-58.
155. T. Motyka, *DOE Materials-Based Hydrogen Storage Summit: Defining Pathways to Onboard Automotive Applications*, Golden, Colorado, Office of energy efficiency and renewable energy, 2015.
156. L. McKeehan, *Phys Rev Mater*, 1923, **21**, 334.
157. J. Smittenberg, *Nature*, 1934, **133**, 872.
158. G. G. Libowitz, H. F. Hayes and T. R. Gibb Jr, *Am J Phys Chem*, 1958, **62**, 76-79.
159. H. Buchner, *Int J Hydrogen Energy*, 1978, **3**, 385-406.
160. A. Züttel, *Mater Today*, 2003, **6**, 24-33.
161. W. M. Mueller, J. P. Blackledge and G. G. Libowitz, *Metal hydrides*, Elsevier, 2013.
162. K. Nogita, S. Ockert, J. Pierce, M. C. Greaves, C. M. Gourlay and A. K. Dahle, *Int J Hydrogen Energy*, 2009, **34**, 7686-7691.
163. B. Bogdanović, H. Hofmann, A. Neuy, A. Reiser, K. Schlichte, B. Spliethoff and S. Wessel, *J Alloys Compd*, 1999, **292**, 57-71.
164. T. J. Seebeck, *Poggendorff's] Annalen der Physik und Chemie*, 1826, **6**, 1-20.
165. J. S. Benjamin and T. E. Volin, *Metall Mater trans*, 1974, **5**, 1929-1934.
166. S.-i. Orimo, Y. Nakamori, J. R. Eliseo, A. Züttel and C. M. Jensen, *Chem Rev (Washington, DC, U S)*, 2007, **107**, 4111-4132.
167. V. Berube, G. Radtke, M. Dresselhaus and G. Chen, *Int J Energy Res*, 2007, **31**, 637-663.
168. J. Huot, D. B. Ravnsbæk, J. Zhang, F. Cuevas, M. Latroche and T. R. Jensen, *Prog Mater Sci*, 2013, **58**, 30-75.
169. D. Tabor, *The hardness of metals*, Oxford University press, 1951.
170. B. Wunderlich, *Thermal analysis*, New York academic press, 1990.
171. H. E. Kissinger, *J Res NBS 57*, 1956, 109-117.
172. S.A. Arrhenius, *Z Phys Chem*, 1889, **4**, 96-116.
173. S. Vyazovkin, *Macromol Rapid Commun*, 2002, **23**, 771-775.
174. R. E. Dinnebier and S. J. L. Billinge, in *Powder Diffraction: Theory and Practice*, RSC, 2008, pp. 1-19.
175. R. Jenkins, in *Encyclopedia of Analytical Chemistry*, 2006, DOI: 10.1002/9780470027318.a6801.
176. B. E. Warren, *X-ray Diffraction*, Courier Corporation, 1990.
177. J. K. Cockcroft and A. N. Fitch, *Powder Diffraction: Theory and Practice*, 2008, 20-57.
178. H. M. Rietveld, *Phys Scr*, 2014, **89**, 098002.
179. H. Rietveld, *J Appl Crystallogr*, 1969, **2**, 65-71.

180. R. W. Cheary and A. Coelho, *J Appl Crystallogr*, 1992, **25**, 109-121.
181. E. Poirier, R. Chahine, A. Tessier and T. K. Bose, *Rev Sci Instrum*, 2005, **76**, 055101.
182. R. Checchetto, G. Trettel and A. Miotello, *Meas Sci Technol*, 2003, **15**, 127-130.
183. T. Blach and E. M. Gray, *J Alloys Compd*, 2007, **446**, 692-697.
184. G. T. Manivasagam, K. Kiraz and H. L. P. Notten, *Crystals*, 2012, **2**, 1410-1433.
185. P. Atkins and J. De Paula, *Physical Chemistry*, W.H. Freeman and Company, 2006.
186. W. Greiner, L. Neise and H. Stöcker, in *Thermodynamics and Statistical Mechanics*, eds. W. Greiner, L. Neise and H. Stöcker, Springer New York, New York, NY, 1995, DOI: 10.1007/978-1-4612-0827-3_4, pp. 84-119.
187. T. Gamo, Y. Moriwaki, N. Yanagihara, T. Yamashita and T. Iwaki, *Int J Hydrogen Energy*, 1985, **10**, 39-47.
188. S. E. Gustafsson, *Rev Sci Instrum*, 1991, **62**, 797-804.
189. Y. He, *Thermochim Acta*, 2005, **436**, 122-129.
190. H. Zhang, M.-J. Li, W.-Z. Fang, D. Dan, Z.-Y. Li and W.-Q. Tao, *Appl Therm Eng*, 2014, **72**, 62-69.
191. D. Bernoullis, *Hydrodynamica*, 1738, Encyclopedia Britannica
192. M. Reader-Harris, *Orifice Plates and Venturi Tubes*, Springer international publishing, 2015.
193. Y. Amano, *The fukushima Daiishi Accident*, IAEA, 2015.
194. S. C. Weiner and L. L. Fassbender, *Int J Hydrogen Energy*, 2012, **37**, 17358-17363.
195. M.R. Louthan and G. Caskey, *Int J Hydrogen Energy*, 1976, **1**, 291-305.
196. N. Nanninga, A. Slifka, Y. Levy and C. White, *J Res Natl Inst Stand Technol*, 2010, **115**, 437-452.
197. M. R. Louthan, G. R. Caskey, J. A. Donovan and D. E. Rawl, *MAT SCI ENG*, 1972, **10**, 357-368.
198. J. G. Morlet, *the journal of the Iron and Steel Institute*, 1958, **189**.
199. M. Louthan, *JFAP*, 2008, **8**, 289-307.
200. J. J. Neuharth and M. N. Cavalli, *Eng Fail*, 2015, **49**, 49-56.
201. S. A. Steward, *Review of hydrogen isotope permeability through materials*, Lawrence Livermore National laboratory, 1983.
202. A. Turnbull, in *Gaseous Hydrogen Embrittlement of Materials in Energy Technologies*, eds. R. P. Gangloff and B. P. Somerday, Woodhead Publishing, 2012, vol. 1, pp. 89-128.
203. X. Xiang, X. Wang, G. Zhang, T. Tang and X. Lai, *Int J Hydrogen Energy*, 2015, **40**, 3697-3707.
204. R. A. Causey, R. A. Karnesky and C. San Marchi, *Tritium barriers and tritium diffusion in fusion reactors*, Sandia National Laboratories, 2012.
205. R. A. Causey, J. D. Fowler, C. Ravanbakht, T. S. Elleman and K. Verghese, *J Am Ceram Soc*, 1978, **61**, 221-225.
206. K. S. Forcey, D. K. Ross and C. H. Wu, *J Nucl Mater*, 1991, **182**, 36-51.
207. D. A. Sheppard, M. Paskevicius, P. Javadian, I. J. Davies and C. E. Buckley, *J Alloys Compd*, 2019, **787**, 1225-1237.
208. Sunshot 2030 goal, energy.gov, Solar energy technology office, <https://www.energy.gov/eere/solar/sunshot-2030>).
209. R. Izatt, S. Izatt, R. Bruening, N. Izatt and B. Moyer, *Chem Soc Rev*, 2014, **43**.
210. C. M. Stander, *J Inorg Nucl Chem*, 1977, **39**, 221-223.
211. J. Bloch and M. H. Mintz, *J Alloys Compd*, 1997, **253-254**, 529-541.
212. L.-P. Ma, P. Wang and H.-M. Cheng, *J Alloys Compd*, 2007, **432**, L1-L4.
213. S.-A. Jin, J.-H. Shim, J.-P. Ahn, Y. W. Cho and K.-W. Yi, *Acta Mater*, 2007, **55**, 5073-5079.

214. M. Medrano, A. Gil, I. Martorell, X. Potau and L. F. Cabeza, *Renew Sust Energ Rev*, 2010, **14**, 56-72.
215. K. Vignarooban, X. Xu, A. Arvay, K. Hsu and A. M. Kannan, *Appl Energy*, 2015, **146**, 383-396.
216. D. Leitch, SolarReserve still falling short at flagship solar tower project, *Renew Economy*, DOI: <https://reneweconomy.com.au/solarreserve-still-falling-short-at-flagship-solar-tower-project-13928/>).
217. M. L. H. E.W.Lemmon, M.O.McLinden, *NIST stdrefdat*, 2013.
218. M. B. Kermani and A. Morshed, *CORROSION*, 2003, **59**, 659-683.
219. J. Tan and K. S. Chan, *Understanding advanced physical inorganic chemistry: the Learner's approach*, World Scientific Publishing Company, 2010.
220. G. Cui, Z. Yang, J. Liu and Z. Li, *INT J Greenh Gas Con*, 2019, **90**, 102814.
221. A. San-Martin and F. D. Manchester, *Bull Alloy Phase Diagr*, 1987, **8**, 30-42.
222. W. E. Wang, *J Alloys Compd*, 1996, **238**, 6-12.
223. S. V. Alapati, J. K. Johnson and D. S. Sholl, *J Phys Chem B*, 2006, **110**, 8769-8776.
224. M. V. Sofianos, S. Randall, M. Paskevicius, K.-F. Aguey-Zinsou, M. R. Rowles, T. D. Humphries and C. E. Buckley, *J Alloys Compd*, 2020, **819**, 153340.
225. A. C. M. Griffond, Concentrating Solar Thermal storage using metal hydride: Study of destabilised calcium hydrides, Curtin University, 2019.
226. P. Chen, Z. Xiong, J. Luo, J. Lin and K. L. Tan, *Nature*, 2002, **420**, 302-304.
227. M. Felderhoff and B. Bogdanović, *Int J Mol Sci*, 2009, **10**, 325-344.
228. H. Liu, Z. Wang, J. Zhang, B. Tao and Q. Liu, *IOP Conf Ser: Earth Environ Sci*, 2019, **267**, 022042.
229. Z. A. Matysina, S. Y. Zaginaichenko, D. V. Shchur and M. T. Gabdullin, *RUSS PHYS J+*, 2016, **59**, 177-189.
230. R. Martínez-Coronado, M. Retuerto, B. Torres, M. J. Martínez-Lope, M. T. Fernández-Díaz and J. A. Alonso, *Int J Hydrogen Energy*, 2013, **38**, 5738-5745.
231. J. J. Reilly Jr and R. H. Wiswall Jr, *Inorg Chem*, 1968, **7**, 2254-2256.
232. G. Zepon, D. R. Leiva, R. B. Strozi, B. C. M. Terra, S. J. A. Figueroa, R. Floriano, A. M. Jorge and W. J. Botta, *Int J Hydrogen Energy*, 2017, **42**, 14593-14601.
233. A. d'Entremont, C. Corgnale, M. Sulic, B. Hardy, R. Zidan and T. Motyka, *Int J Hydrogen Energy*, 2017, **42**, 22518-22529.
234. D. A. Sheppard, T. D. Humphries and C. E. Buckley, *Appl Phys A*, 2016, **122**.
235. F. D. Manchester and A. S. M. International, *Phase diagrams of binary hydrogen alloys*, ASM International, Materials Park, OH, 2000.
236. L. Chong, J. Zou, X. Zeng and W. Ding, *J Mater Chem A*, 2015, **3**, 4493-4500.
237. B. Bogdanović, M. Felderhoff, A. Pommerin, F. Schüth and N. Spielkamp, *Adv Mater*, 2006, **18**, 1198-1201.
238. M. H. Sørby, H. W. Brinks, A. Fossdal, K. Thorshaug and B. C. Hauback, *J Alloys Compd*, 2006, **415**, 284-287.
239. E. Veleckis, *Am J Phys Chem*, 1977, **81**, 526-531.
240. P. Javadian, D. A. Sheppard, T. R. Jensen and C. E. Buckley, *RSC Adv*, 2016, **6**, 94927-94933.
241. A. E. Finholt, G. D. Barbaras, G. K. Barbaras, G. Urry, T. Wartik and H. I. Schlesinger, *J Inorg Nucl Chem*, 1955, **1**, 317-325.
242. E. Veleckis, *J Less Common Met*, 1981, **80**, 241-255.
243. B. Bogdanović and M. Schwickardi, *J Alloys Compd*, 1997, **253-254**, 1-9.
244. M. Schwarz, A. Haiduc, H. Stil, P. Paulus and H. Geerlings, *J Alloys Compd*, 2005, **404-406**, 762-765.
245. M. Fichtner, C. Frommen and O. Fuhr, *Inorg Chem*, 2005, **44**, 3479-3484.
246. O. M. Løvvik, *Phys Rev B*, 2005, **71**, 144111.

247. H. Kabbour, C. C. Ahn, S.-J. Hwang, R. C. Bowman and J. Graetz, *J Alloys Compd*, 2007, **446-447**, 264-266.
248. N. Hanada, W. Lohstroh and M. Fichtner, *J Phys Chem C*, 2008, **112**, 131-138.
249. C. Wolverton and V. Ozoliņš, *Phys Rev B*, 2007, **75**, 064101.
250. V. Iosub, T. Matsunaga, K. Tange and M. Ishikiriya, *Int J Hydrogen Energy*, 2009, **34**, 906-912.
251. C. Li, X. Xiao, P. Ge, J. Xue, S. Li, H. Ge and L. Chen, *Int J Hydrogen Energy*, 2012, **37**, 936-941.
252. D. M. Liu, C. Gao, Z. X. Qian, T. Z. Si and Q. A. Zhang, *Int J Hydrogen Energy*, 2013, **38**, 3291-3296.
253. J.H.Perry, *Chemical Engineer handbook*, 1963.
254. P. Flint, *The diffusion of hydrogen through materials of construction*, Knolls Atomic Power Lab., 1951.
255. J. Mao and D. H. Gregory, *Energies*, 2015, **8**, 430-453.
256. M. Paskevicius, L. H. Jepsen, P. Schouwink, R. Černý, D. B. Ravnsbæk, Y. Filinchuk, M. Dornheim, F. Besenbacher and T. R. Jensen, *Chem Soc Rev*, 2017, **46**, 1565-1634.
257. E. Rönnebro, D. Noréus, K. Kadir, A. Reiser and B. Bogdanovic, *J Alloys Compd*, 2000, **299**, 101-106.
258. V. A. Yartys, M. V. Lototskyy, E. Akiba, R. Albert, V. E. Antonov, J. R. Ares, M. Baricco, N. Bourgeois, C. E. Buckley, J. M. Bellosta von Colbe, J. C. Crivello, F. Cuevas, R. V. Denys, M. Dornheim, M. Felderhoff, D. M. Grant, B. C. Hauback, T. D. Humphries, I. Jacob, T. R. Jensen, P. E. de Jongh, J. M. Joubert, M. A. Kuzovnikov, M. Latroche, M. Paskevicius, L. Pasquini, L. Popilevsky, V. M. Skripnyuk, E. Rabkin, M. V. Sofianos, A. Stuart, G. Walker, H. Wang, C. J. Webb and M. Zhu, *Int J Hydrogen Energy*, 2019, **44**, 7809-7859.
259. X. Yao and G. Lu, *Chin Sci Bull*, 2008, **53**, 2421-2431.
260. K.-F. Aguey-Zinsou and J.-R. Ares-Fernández, *Energy Environ Sci*, 2010, **3**, 526-543.
261. K. Alsabawi, T. A. Webb, E. M. Gray and C. J. Webb, *Int J Hydrogen Energy*, 2017, **42**, 5227-5234.
262. B. Bogdanović, A. Ritter, B. Spliethoff and K. Straßburger, *Int J Hydrogen Energy*, 1995, **20**, 811-822.
263. A. Bouamrane, C. de Brauer, J. P. Soulié, J. M. Létoffé and J. P. Bastide, *Thermochim Acta*, 1999, **326**, 37-41.
264. A. Bouamrane, J. P. Laval, J. P. Soulie and J. P. Bastide, *Mater Res Bull*, 2000, **35**, 545-549.
265. K. Ikeda, Y. Kogure, Y. Nakamori and S. Orimo, *Scripta Mater*, 2005, **53**, 319-322.
266. Z. Wang, S. Tao, J. Deng, H. Zhou and Q. Yao, *Int J Hydrogen Energy*, 2017, **42**, 8554-8559.
267. Z. Wang, S. Tao, J. Li, J. Deng, H. Zhou and Q. Yao, *Metals*, 2017, **7**, 9.
268. P. A. Ward, C. Corngale, J. A. Teprovich, T. Motyka, B. Hardy, B. Peters and R. Zidan, *J Alloys Compd*, 2015, **645**, S374-S378.
269. K. Komiyama, N. Morisaku, R. Rong, Y. Takahashi, Y. Shinzato, H. Yukawa and M. Morinaga, *J Alloys Compd*, 2008, **453**, 157-160.
270. D. Pottmaier, E. R. Pinatel, J. G. Vitillo, S. Garroni, M. Orlova, M. Baró, G. B. M. Vaughan, M. Fichtner, W. Lohstroh and M. Baricco, *Chem Mater*, 2011, **23**, 2317-2326.
271. K. Ikeda, S. Kato, Y. Shinzato, N. Okuda, Y. Nakamori, A. Kitano, H. Yukawa, M. Morinaga and S. Orimo, *J Alloys Compd*, 2007, **446**, 162-165.
272. P. Spatz, H. Aebischer, A. Krozer and L. Schlapbach, *Z Phys Chem (Muenchen, Ger)*, 1993, **181**, 393-397.
273. E. Tsotsas and H. Martin, *Chem Eng Process*, 1987, **22**, 19-37.

274. D. Mirabile Gattia, A. Montone, I. Di Sarcina, M. Nacucchi, F. De Pascalis, M. Re, E. Pesce and M. Vittori Antisari, *Int J Hydrogen Energy*, 2016, **41**, 9834-9840.
275. C. Pohlmann, L. Röntzsch, S. Kalinichenka, T. Hutsch and B. Kieback, *Int J Hydrogen Energy*, 2010, **35**, 12829-12836.
276. J. E. Bird, T. D. Humphries, M. Paskevicius, L. Poupin and C. E. Buckley, *Phys Chem Chem Phys*, 2020, **22**, 4617-4625.
277. M. Polanski, D. Nawra and D. Zasada, *J Alloys Compd*, 2019, **776**, 1029-1040.
278. J. J. Didisheim, P. Zolliker, K. Yvon, P. Fischer, J. Schefer, M. Gubelmann and A. F. Williams, *Inorg Chem*, 1984, **23**, 1953-1957.
279. J. Huot, H. Hayakawa and E. Akiba, *J Alloys Compd*, 1997, **248**, 164-167.
280. J. Huot, S. Boily, E. Akiba and R. Schulz, *J Alloys Compd*, 1998, **280**, 306-309.
281. M. Polanski, T. Płociński, I. Kuncce and J. Bystrzycki, *Int J Hydrogen Energy*, 2010, **35**, 1257-1266.
282. K. K. K. Witek, M. Karpowicz, M. Polanski, *Crystals*, 2018, **8**, 94.
283. S. Kraemer, Crescent Dunes 24-Hour Solar Tower Is Online, clean technica, 2016
284. M. Fellet, C. E. Buckley, M. Paskevicius and D. A. Sheppard, *MRS Bulletin*, 2013, **38**, 1012-1013.
285. B. Sakintuna, F. Lamari-Darkrim and M. Hirscher, *Int J Hydrogen Energy*, 2007, **32**, 1121-1140.
286. M. Nagel, Y. Komazaki and S. Suda, *J Less Common Met*, 1986, **120**, 45-53.
287. H. Bjurström and S. Suda, *Int J Hydrogen Energy*, 1989, **14**, 19-28.
288. M. Gambini, *Int J Hydrogen Energy*, 1994, **19**, 67-80.
289. A. Isselhorst, *J Alloys Compd*, 1995, **231**, 871-879.
290. M. Wierse, R. Werner and M. Groll, *J Less Common Met*, 1991, **172-174**, 1111-1121.
291. A. d'Entremont, C. Corgnale, B. Hardy and R. Zidan, *Int J Hydrogen Energy*, 2018, **43**, 817-830.
292. T. D. Humphries, D. A. Sheppard, M. R. Rowles, M. V. Sofianos and C. E. Buckley, *J Mater Chem A*, 2016, **4**, 12170-12178.
293. D. J. Durbin and C. Malardier-Jugroot, *Int J Hydrogen Energy*, 2013, **38**, 14595-14617.
294. R. Moradi and K. M. Groth, *Int J Hydrogen Energy*, 2019, **44**, 12254-12269.
295. D. N. Harries, M. Paskevicius, D. Sheppard, T. Edward Cameron Price and C. E. Buckley, *Proc IEEE*, 2012, **100**, 539-549.
296. J. Reilly and R. Wiswall, *Inorg Chem*, 1974, **13**, 218-222.
297. E. L. Huston and G. D. Sandrock, *J Less Common Met*, 1980, **74**, 435-443.
298. A. Demircan, M. Demiralp, Y. Kaplan, M. Mat and T. Veziroglu, *Int J Hydrogen Energy*, 2005, **30**, 1437-1446.
299. G. Sandrock, J. Murray, M. Post and J. Taylor, *Mater Res Bull*, 1982, **17**, 887-894.
300. G. Sandrock, *J Alloys Compd*, 1999, **293-295**, 877-888.
301. J. A. Murshidi, M. Paskevicius, D. A. Sheppard and C. E. Buckley, *Int J Hydrogen Energy*, 2011, **36**, 7587-7593.
302. V. N. Verbetsky, R. A. Sirotina and E. A. Umerenko, *Int J Hydrogen Energy*, 1996, **21**, 935-938.
303. M. Kawamura, S. Ono and Y. Mizuno, *J Less Common Met*, 1983, **89**, 365-372.
304. M. D. Mat, Y. Kaplan and K. Aldas, *Int J Energy Res*, 2002, **26**, 973-986.
305. Z. Bao, Z. Wu, S. N. Nyamsi, F. Yang and Z. Zhang, *Appl Therm Eng*, 2013, **52**, 97-108.
306. S. Shafiee and M. H. McCay, *Int J Hydrogen Energy*, 2016, **41**, 9462-9470.
307. A. Chaise, P. de Rango, P. Marty and D. Fruchart, *Int J Hydrogen Energy*, 2010, **35**, 6311-6322.

308. S. Qiu, X. Ma, E. Wang, H. Chu, J. Huot, Y. Zou, C. Xiang, F. Xu and L. Sun, *J Alloys Compd*, 2017, **704**, 44-50.
309. R. Urbanczyk, Peinecke, K., Peil, S., Felderhoff, M., *Int J Hydrogen Energy*, 2017, DOI: 10.1016/j.ijhydene.2017.02.160.
310. Z. Bao, F. S. Yang, Z. Wu, X. Cao and Z. X. Zhang, *Appl Energy*, 2013, **112**, 1181-1189.
311. I. Bell, *NIST Reference Fluid Thermodynamic and Transport Properties Database (REFPROP) Version9 - SRD 23*, National Institute of Standards and Technology, 2017.
312. M. Raju and S. Kumar, *Int J Hydrogen Energy*, 2012, **37**, 2767-2778.
313. Z. Wu, F. Yang, Z. Zhang and Z. Bao, *Appl Energy*, 2014, **130**, 712-722.
314. C. A. Chung, S. W. Yang, C. Y. Yang, C. W. Hsu and P. Y. Chiu, *Appl Energy*, 2013, **103**, 581-587.
315. D. B. Sarraf and W. G. Anderson, *Heat Pipes for High Temperature Thermal Management*, Vancouver, British Columbia, Canada, 2007.
316. N. Hack, S. Unz and M. Beckmann, *EngProc*, 2017, **120**, 140-148.
317. H. Zhang, J. Baeyens, G. Cáceres, J. Degrève and Y. Lv, *Progr Energy Combust Sci*, 2016, **53**, 1-40.
318. J. Sunku Prasad, P. Muthukumar, F. Desai, D. N. Basu and M. M. Rahman, *Appl Energy*, 2019, **254**, 113733.
319. D. A. Sheppard and C. E. Buckley, *Int J Hydrogen Energy*, 2019, **44**, 9143-9163.
320. J. Kenneth, *Albright's chemical engineering handbook*, 2008.

“Every reasonable effort has been made to acknowledge the owners of copyright material. I would be pleased to hear from any copyright owner who has been omitted or incorrectly acknowledged.”